



Skolkovo Institute of Science and Technology

DEVELOPMENT OF LITHIUM-CONDUCTING POLYMER-CERAMIC  
MEMBRANES FOR LITHIUM-METAL HYBRID FLOW BATTERIES

*Doctoral Thesis*

by

NIKITA AKHMETOV

DOCTORAL PROGRAM IN MATERIALS SCIENCE AND ENGINEERING

Supervisor

Professor Keith Stevenson

Moscow – 2023

© Nikita Akhmetov 2023

I hereby declare that the work presented in this thesis was carried out by myself at Skolkovo Institute of Science and Technology, Moscow, except where due acknowledgement is made, and has not been submitted for any other degree.

Nikita Akhmetov

Prof. Keith Stevenson

## Abstract

Softening the discrepancy between produced and consumed energy is one of the most powerful solutions for a safe, sustainable, and economically beneficial energy supply. Inflexibility of conventional energy plants and intermittent generation from renewable sources demand specific energy storage buffers to accumulate overproduced electricity and release it in high demand. Redox flow batteries (RFBs) represent a promising class of safe energy storage devices with high efficiency, durability, and simple adaptability for power systems of different natures and configurations.

Lithium-metal hybrid flow batteries (Li-HFBs) are distinguished from conventional RFBs by improved energy density and the simplified architecture (anolyte tank is replaced by Li anode). The main limitation of Li-HFBs is a lack of a suitable solid electrolyte: a *membrane* with high ionic conductivity (IC) and selectivity, flexibility and integrity, stability in Li-HFB environment, etc. In this Thesis, we follow the ceramic-in-polymer approach in membrane design and develop a composite consisted of  $\text{Li}_{1.3}\text{Al}_{0.3}\text{Ti}_{1.7}(\text{PO}_4)_3$  (LATP) filler and poly(vinylidene fluoride) (PVdF) matrix. Not only does this approach combine the advantages of each component (i.e., high IC of ceramics and flexibility of polymer), but provides prominent protection of sensitive filler particles from the aggressive Li-HFB environment.

We found that porosity plays a crucial role in the membrane's final properties and the whole battery system performance: it defines permeability (active species crossover) that affects the cell's efficiency and capacity retention. Polymer's phase and microstructure

(globularity) together with ceramic particle agglomerates are the major factors influencing the membrane's porosity. Low components mixing and high solution casting temperatures as well as preliminary sonication of the solvent-filler suspension decrease the membrane's permeability from 6.6 to  $0.86 \cdot 10^{-7} \text{ cm}^2 \text{ min}^{-1}$ .

For the first time, we proved that the LATP ceramic filler mainly contributes to composite's IC. LATP structure comprises labile Li ions that are leached out after the membrane fabrication, but return during galvanostatic cycling within the hybrid cell. IC of all LATP+PVdF samples was  $>10^{-4} \text{ S cm}^{-1}$  that outperforms commercial alternatives — Nafion and Neosepta.

The Li-TEMPO hybrid flow cell equipped with the optimized membrane exhibits high coulombic efficiency ( $>95\%$ ), durability ( $>100$  cycles), and initial capacity ( $>93\%$ ), as well as its slight decay of  $0.4\% \text{ h}^{-1}$ . Based on extensive literature review and collected experimental data, we summarized the set of battery-related issues that should be further investigated for the continuous development of Li-HFBs.

## Publications

- 1) Akhmetov NO, Waris Z, Ryazantsev SV, Lipovskikh SA, Gvozdik NA, Pogosova MA, Stevenson KJ. Towards Durable and High-Power Li-Metal Hybrid Flow Battery: Composite LATP+PVdF Membrane Development, Cell Performance, and Perspective. *J. Mat. Chem. A*. 2023; 11, 19656–19668.  
*Personal impact:* synthesis of ion-conducting membranes; performing electrochemical measurements (EIS, CV, galvanostatic cycling, etc.); performing SEM; data analysis; writing original draft.
- 2) Waris Z, Akhmetov NO, Pogosova MA, Lipovskikh SA, Ryazantsev SV, Stevenson KJ. A Complex Investigation of LATP Ceramic Stability and LATP+PVdF Composite Membrane Performance: The Effect of Solvent in Tape-Casting Fabrication. *Membranes*. 2023; 13(2), 155.  
*Personal impact:* performing electrochemical measurements (EIS, CV); data analysis; reviewing original draft; supervision.
- 3) Akhmetov NO, Ovsyannikov NA, Gvozdik NA, Pogosova MA, Ryazantsev SV, Lipovskikh SA, Krasnikova IV, Stevenson KJ. Composite lithium-conductive LATP+PVdF membranes: Development, optimization, and applicability for Li-TEMPO hybrid redox flow batteries. *J. Mem. Sci.* 2022; 643, 120002.  
*Personal impact:* synthesis of ion-conducting membranes; performing electrochemical measurements (EIS, CV, galvanostatic cycling, etc.); performing SEM; data analysis; writing original draft.
- 4) Ovsyannikov NA, Romadina EI, Akhmetov NO, Gvozdik NA, Akkuratov AV, Pogosova MA, Stevenson KJ. All-Organic Non-Aqueous Redox Flow

Batteries with Advanced Composite Polymer-Ceramic Li-Conductive Membrane. *J. Energy Storage*. 2022; 46, 103810.

*Personal impact:* synthesis of ion-conducting membranes; data analysis; reviewing original draft.

- 5) Gandomi YA, Krasnikova IV, Akhmetov NO, Ovsyannikov NA, Pogosova MA, Matteucci NJ, Mallia CT, Neyhouse BJ, Fenton Jr. AM, Brushett FR, Stevenson KJ. Synthesis and Characterization of Lithium-Conducting Composite Polymer–Ceramic Membranes for Use in Nonaqueous Redox Flow Batteries. *ACS Appl. Mater. Interfaces*. 2021; 13(45), 53746–53757.

*Personal impact:* synthesis of ion-conducting membranes; measuring membrane's electrochemical stability; performing SEM; data analysis; writing the section of membrane fabrication optimization of the original draft.

## Conferences

- 1) Akhmetov NO, Stevenson KJ. Development of Polymer-Ceramic Li-Conducting Membranes for Li-Metal Hybrid Flow Batteries. 2023; *The 8<sup>th</sup> Asian Symposium on Advanced Materials (ASAM-8)*, Novosibirsk, Russia, Abstracts.
- 2) Stevenson KJ, Romadina EI, Akhmetov NO, Ovsyannikov NA, Gvozdik NA, Pogosova MA. Composite Lithium-Conductive Latp+Pvdf Membranes: Development, Optimization, and Applicability for Li-Hybrid Redox Flow Batteries. 2022; *ECS Meeting*, Atlanta, GA, USA, Abstracts, 48, 1994.
- 3) Akhmetov NO, Ovsyannikov NA, Pogosova MA, Krasnikova IV, Gvozdik NA, Stevenson KJ. Composite lithium-conductive membranes for lithium-hybrid redox flow batteries. 2021; *European-MRS 2021 Fall Meeting*, Warsaw, Poland, B.D1.3.
- 4) Akhmetov NO, Ovsyannikov NA, Krasnikova IV, Pogosova MA, Ryazantsev SV, Gvozdik NA, Stevenson KJ. Complex investigation of ceramic-polymer ion-conductive membranes for hybrid lithium-TEMPO redox flow batteries. 2021; *Mendeleev 2021: XII International Conference on Chemistry for Young Scientists*. Saint Petersburg, Russia, 693-694.
- 5) Akhmetov NO, Ovsyannikov NA, Krasnikova IV, Pogosova MA, Luchkin SV, Gvozdik NA, Stevenson KJ. Electrochemical impedance spectroscopy for complex studying lithium-conductive composite membranes. 2020; *14th International Workshop on Impedance Spectroscopy*. Leibniz, Germany.

## Acknowledgements

First of all, I would like to express the gratitude to my research advisor **Prof. Keith Stevenson**, who inspired and opened the wonderful world of battery science, material chemistry, and electrochemistry to me. He is an example of a hard-working, honest, and purposeful scientist and manager that I would like to resemble. A great thank to my PhD supervisor **Prof. Alexei Buchachenko** that assisted and supported me during the preparation to the Thesis Defense.

I am grateful to my PhD jury committee, **Prof. Evgeniy Antipov**, **Prof. Yongdan Li**, **Prof. Atif Alzahrani**, **Prof. Albert Nasibulin**, **Prof. Stanislav Fedotov**, **Dr. Daniil Itkis**, for careful evaluation of my progress and valuable ideas to improve the quality of my Thesis. A great thank to all the Skoltech instructors and alumni for their limitless education support and solid knowledge in material science and adjacent areas.

A special thank is for **Dr. Irina Krasnikova** — she invited me to obtain a PhD at Skoltech and gave essential but important theoretical and practical skills of working with battery membrane materials. She has set an ideological basis for this PhD research. I do appreciate the lessons from **Dr. Mariam Pogosova** on synthesis and characterization of ceramic materials. I will never forget her large assistance in preparation of our research articles and improving my PhD Thesis. I greatly thank **Dr. Nataliya Gvozdik** for teaching me the lab RFBs testing and other electrochemistry techniques, as well as for being a good friend, with whom I can always share my thoughts and ask for advice on both science and

life issues. I am happy to have worked with **Dr. Sergey Ryazantsev** and **Dr. Svetlana Lipovskikh**, who performed FTIR and microscopy experiments, assisted in their analysis, and contributed to our common manuscripts. We had a very productive and valuable collaboration. A big thank to master and PhD students, especially to **Nikolay Ovsyannikov** and **Zainab Waris** — guiding and helping each other made us better and stronger.

I would like to express my gratitude to **Prof. Artem Abakumov** and all the employees of Skoltech Center for Energy Science and Technology for providing a unique research facility, along with the friendly and comfortable atmosphere. Thanks to Skoltech Advance Imaging Core Facility for an opportunity to perform high-quality microscopy analysis.

Thanks to **Mikhail Bulavskiy** for sharing the way of Skoltech PhD students, sincere friendship, large support, bright discussions, and other wonderful moments of the last 4 years. At the end, I am grateful to my beloved family: my parents, relatives, and my caring wife **Elizaveta**, who admire, inspire, support, and love me.

## Table of Contents

Abstract.....	3
Publications.....	5
Conferences.....	7
Acknowledgements.....	8
Table of Contents.....	10
Abbreviations.....	13
Introduction.....	16
Chapter 1. Literature Overview.....	18
1.1. Energy Storage Systems for Better Infrastructure.....	18
1.2. Rechargeable Batteries: From Invention to Modern Days.....	23
1.3. Lithium Batteries Family.....	27
1.3.1. Conventional Li-ion Batteries.....	27
1.3.2. All-Solid-State Batteries.....	30
1.3.3. Redox Flow Batteries.....	31
1.3.3.1. Non-aqueous all-flow batteries.....	36
1.3.3.2. Li-Metal Hybrid Flow Batteries.....	38
1.4. Membranes for RFBs.....	47
1.4.1. Types of Membrane Materials.....	48
1.4.1.1. Porous Polymer.....	48
1.4.1.2. Ion-Exchange.....	52
1.4.1.3. Dense Polymer.....	56
1.4.1.4. Inorganic.....	58
1.4.2. Polymer-Ceramic Composite Membranes.....	65

1.4.3. Composite Membrane Fabrication Methods.....	67
1.4.4. Membranes Porosity and the Ways of Its Suppression.....	71
1.5. Characterization Techniques: RFB Prototype and Membrane Performance Metrics.....	75
1.6. Conclusions from Chapter 1.....	84
1.7. Goal and Objectives of the Thesis.....	85
Chapter 2. Experimental Details.....	87
2.1. Synthesis of LATP Ceramic Filler.....	87
2.2. Fabrication of Composite Membranes.....	89
2.3. Characterization of Composite Membranes.....	93
2.3.1. Physicochemical Characterization.....	93
2.3.2. Electrochemical Characterization.....	96
2.4. Membrane Life Testing in Li-TEMPO Hybrid Cells.....	102
2.4.1. Static Cell.....	102
2.4.2. Flow Cell.....	103
Chapter 3. Optimization of Composite Membrane Properties.....	106
3.1. Composition Variation.....	106
3.1.1. Impact of Lithium Salt.....	106
3.1.2. Solvent Variation.....	107
3.1.3. Polymer-Solvent Ratio.....	113
3.1.4. Ceramic-Polymer Ratio.....	114
3.2. Fabrication Conditions Variation.....	121
3.2.1. Solution Mixing Temperature.....	121
3.2.2. Solution Casting Temperature.....	124
3.2.3. Samples Drying Conditions.....	127

3.2.4. Effect of Filler Distribution.....	129
3.3. Conclusions from Chapter 3.....	134
Chapter 4. Prototyping Li-Hybrid Flow Cell Equipped with Composite Membrane.....	137
4.1. Evaluation of Membranes Stability to Metallic Lithium.....	137
4.2. Performance of Li-TEMPO Static Cell .....	140
4.3. Performance of Li-TEMPO Flow Cell.....	144
4.4. Conclusions from Chapter 4.....	155
Chapter 5. Conclusions and Future Perspective .....	156
5.1. System Advances and Paths for Improvement.....	156
5.2. Conclusions of the Thesis.....	163
Bibliography .....	165
Appendices.....	185
A. Data Supporting Literature Overview .....	185
B. XRD Refinement .....	194
C. EIS Fitting Data .....	197
D. Pre-Treatment and Performance of Commercial Membranes .....	200

## Abbreviations

ACN — acetonitrile

AEM — anion exchange membrane

ASSB — all-solid-state battery

BenPh — N-benzylphthalimide

CCDC — The Cambridge Crystallographic Data Centre

CEM — cation-exchange membrane

CPE — constant phase element

CV — cyclic voltammetry

DBBB — 2,5-di-tert-butyl-1,4-bis(2-methoxyethoxy)benzene

DBMMB — 2,5-di-tert-butyl-1-methoxy-4-(2-methoxyethoxy)benzene

DPBQ — 2,5-dipropoxy-1,4-benzoquinone

DEC — diethyl carbonate

DEGDME — diethylene glycol dimethyl ether

DMC — dimethyl carbonate

DME — dimethoxyethane

DMF — dimethyl formamide

DMSO — dimethyl sulfoxide

DOL — dioxolane

DSC — differential scanning calorimetry

EC — ethylene carbonate

EDX — energy-dispersive X-ray spectroscopy

EIS — electrochemical impedance spectroscopy

EMC — ethyl methyl carbonate

ESS — energy storage system

ESW — electrochemical stability window

EV — electric vehicles

FEC — fluoroethylene carbonate

FTIR — Fourier-transform infrared spectroscopy  
GBL —  $\gamma$ -butyrolactone  
HFB — hybrid flow battery  
IC — ionic conductivity  
IEM — ion-exchange membrane  
LIB — Li-ion battery  
LICGC — Li-conducting glass ceramic  
(LI)NASICON — (Li) Na superionic conductor  
LiPON — Li phosphorus oxynitride  
LSV — linear sweep voltammetry  
MOF — metal-organic framework  
MPT — 10-methylphenothiazine  
MWCNT — multi-wall carbon nanotubes  
NAq — non-aqueous  
NMP — N-methyl pyrrolidone  
OCV — open-circuit potential  
PC — propylene carbonate  
PDDA — poly(diallyldimethylammonium chloride)  
PEO — polyethylene oxide  
PVC — polyvinyl chloride  
PVdF — poly(vinylidene fluoride)  
PVdF-HFP — poly(vinylidene fluoride-co-hexafluoropropylene)  
PVP — polyvinylpyrrolidones  
RFB — redox flow battery  
RT — room temperature  
SE — supporting electrolyte  
SEI — solid electrolyte interface  
SS — stainless-steel

SEM — scanning electron microscopy  
TBA — tetrabutylammonium  
TCR — total cell resistance  
TEA — tetraethylammonium  
TEM — transmission electron microscopy  
TEMPO — (2,2,6,6-tetramethylpiperidin-1-yl)oxyl  
TFSI — bis(trifluoromethane)sulfonimide  
TGA — thermogravimetric analysis  
TPP — tetraphenylporphyrin  
VC — vinylidene carbonate  
VRFB — all-vanadium redox flow batteries  
XRD — X-ray diffraction

## Introduction

The need for energy storage reservoirs is anticipated to rise over the next few years due to the continuous transition to alternative energy producers. In excess of energy, the energy storage systems (ESSs) accumulate it and release it when there is a shortage. Redox flow batteries (RFBs) are ideal for stationary applications due to their independent scale of capacity and power, durability, and quick recharge by means of changing tanks with used electrolytes with ones that are charged. Despite the fact that water-based vanadium RFBs are the most developed kind, their widespread application is constrained by uneven vanadium availability, water instability, and low power density. As an alternative, RFBs based on non-aqueous (NAq) media provide higher operating voltages and greater redox chemistries' solubility. Moreover, NAqRFBs can convert the device into a hybrid flow battery (Li-HFB) by using low-potential metal anodes such as lithium. Such systems can combine the benefits of metal batteries (high energy density) and RFBs (scalability, extended cycle life). However, to boost Li-HFBs' performance and improve their applicability, a new ion-conducting, dense, and highly stable membrane should be developed. Besides the material design, one should simultaneously develop better manufacturing and characterization methods to make an acceptable membrane.

A potential direction to advance membranes is the creation of composite materials. The currently existing single-component solutions are unlikely to be suitable for Li-HFBs. Commercially available materials (Li-ion battery separators) possess large permeability, resulting in a high rate of active species crossover. Ion-exchange membranes, traditionally

used in aqueous RFBs, show poor ionic conductivity (IC) and stability. Ceramics have a promising IC but remain unstable towards metallic lithium and/or air. The "filler-matrix", composite approach, combining the benefits of ceramic and polymer components, might generate a membrane product with potentially high IC, improved stability, flexibility, and integrity. To create the composite membrane appropriate for Li-HFBs, among the variety of materials we selected  $\text{Li}_{1.3}\text{Al}_{0.3}\text{Ti}_{1.7}(\text{PO}_4)_3$  (LATP) NASICON-type ceramic and poly(vinylidene fluoride) (PVdF) polymer. With a solid structure, adequate electrochemical stability, and a promising IC ( $>10^4 \text{ S cm}^{-1}$ ), LATP can be easily produced. The PVdF matrix, being simple to construct and handle, gives the system flexibility, improves its stability, and reduces crossover. To the best of our knowledge, no polymer-ceramic membranes for flow batteries have yet been suggested. Taking the prospect of the composite system for the Li-HFBs into consideration, we established the following **goal of the current Thesis**:

– to develop an ion-conductive, selective, and stable ceramic-in-polymer composite membrane for Li-metal hybrid flow batteries.

To accomplish this goal, a series of objectives based on the literature overview (Chapter 1) were further formulated in Section 1.7.

## **Chapter 1. Literature Overview**

In this chapter, we introduce energy storage systems — effective devices capable of maintaining the electrical energy generation/consumption balance for either conventional or renewable power plants. We start with a broad discussion of different types of ESSs. After the electrochemical type, we describe their historical development, and evaluate various current and emerging technologies. Later, we consider RFBs, prospective energy storage systems, elucidating their classification, operation principles, and components. Then, we focus on ion-conducting membranes — crucial RFB components retarding their development. We provide membrane common and emerging types, compare their properties, and analyze potential applicability in RFBs. Further, we discuss main principles and metrics for RFB and membrane characterization. We establish a Li-metal hybrid flow battery (Li-HFB) equipped with a polymer-ceramic membrane to be a promising solution for the high-power and high-energy energy storage. Finally, we draw conclusions from Literature Overview and formulate Goals and Objectives of the Thesis.

### **1.1. Energy Storage Systems for Better Infrastructure**

Since the start of the third decade of the 21<sup>st</sup> century, global authorities have been expecting a so-called energy transition to come soon [1]. In a specific sense, the “Energy Transition” can be explained as a global shift from production and consumption of fossil-originated energy (wood, coal, oil, natural gas) to renewable energy (solar, wind, geothermal heat, water). The global pandemic of COVID-19 started in 2020 clearly demonstrated the fragility of the current energy system based on traditional fuels.

Conventional plants usually have long start-up time and constant energy output that make them totally inflexible toward sudden or cyclic fluctuation of energy demand. Such production-consumption inconsistencies may lead to wasted energy generation, financial damages, and increasing pollution [2]. Moreover, the altering prices for hydrocarbon fuels and the danger of their supply shortage for importing regions require novel approaches enabling to improve energy security. As a result, the global communities are currently focused on developing alternative energy production technologies based on renewable resources and characterized by higher adaptability [2,3].

Although the renewable energy generators are more flexible and environmentally benign, their energy generation is intermittent — sun light intensity depends on time of day, wind power changes with weather. To overcome the described inconsistencies between the actual energy production and demand, the power stations should be coupled with ESSs. Such buffers would accumulate energy in the periods of overproduction and release it in the time of deficiency enhancing the system's safety, flexibility, efficiency, and durability. In an ideal scenario, the smart integration of ESSs and energy production plants of different scale and storage/generation mechanisms into a common grid system would bear many economic, social, and ecological benefits. The electricity generated can be stored through conversion to energy of a different nature. Accordingly, existing ESSs can be distinguished by mechanical, thermal, electrical, and electrochemical devices, different by capacity, power, time of response, efficiency, and application (Table 1.1).

Table 1.1. Characteristics and applications of energy storage technologies [4,5].

Technology	Capacity, MWh	Power, MW	Efficiency %	Response time	Application
Mechanical					
Flywheel	<10	<20	70-85	<10 ms	Small scale: load & voltage support. Customer management
Pumped hydro	5000- 15000	500- 1500	70-85	<1 min	Energy arbitrage. Frequency regulation.
Compressed air	<2700	<135	~70	<15 min	Renewable integration
Thermal					
Latent- and sensible-heat	<350	<50	<80	<10 min	Energy arbitrage
Electrical					
Double-layer capacitor	0.1-0.5	<1	~95	~10 ms	Short-term/emergency power supplying
Superconducting magnetic	1-3	<10	~95	~10 ms	
Electrochemical					
Lead-acid battery	0.25-50	<100	~85	~1 ms	Load following.
Li-ion battery	0.25-25	<100	~90	~1 ms	Small-scale arbitrage. Custom. management.
Vanadium redox flow battery	<250	<50	~85	1-10 min	Renewable integration

In mechanical ESSs, electricity transforms by a spinning rotor (*flywheel* storage), up-and-down water pumping (*pumped hydro* storage), or compressing air. The flywheel ESSs are self-sustain, durable, and ecological, but have a high self-discharge rate (up to  $20\% \text{ h}^{-1}$ ), high cost, and low capacity making them suitable specifically for small-scale ESS applications. The pumped hydro ESSs share the dominant position in the global stationary storage market (~95% or 210 GW) providing the gigawatt-sized energy arbitrage [6]. A technically unlimited lifetime is a plus, whereas a massive construction and specific topology requirements are disadvantages of this energy storage approach [7]. The compressed air-based technology is quite promising due to its scalability and low self-discharge, although it is currently expensive and requires further optimization [8]. Thermal ESSs are distinguished by the latent- and sensible-heat types [9]. The latent-heat ESSs employ the material's liquid-solid transition: during energy accumulation, the material (typically, NaOH) is transformed from solid to liquid state, during retrieval — vice versa. The heat is transferred by the circulation of specific fluids distributing the energy in the system. The sensible thermal storage utilizes no aggregate state transition, but heats/cooling the bulk material (e.g., molten sodium salts). The released heat is used to vaporize water that is fed to the turbo-alternator system. Other less common thermal storage approaches are geothermal, solar, and phase conversion systems [10].

Electrical ESS (double-layer and superconducting magnetic capacitors) can promptly release all the stored energy in seconds, but possess high self-discharge rate ( $5\% \text{ day}^{-1}$ ), so they are more suitable for emergency back-up or engine starting.

The electrochemical ESSs (rechargeable batteries) are currently the most intensively developing branch due to energy efficiency that overcomes the majority of other storage technologies. What is more, the batteries have wide limits of scalability — from milliwatt-hours for human wearable devices [11] to gigawatt-hours for the large-scale applications [4,5]. In a respect to ESSs, rechargeable batteries support ancillary service (stable transmission of power from a generator to a consumer), arbitrage (storing energy in the periods of its excess and low price), integration with renewable producers, and customer private usage (Table 1.1). Due to the rapid distribution of LIBs, the price per a pack decreased by 85% within ~20 years [12]. Therefore, it is not surprising that since 2016 more than 80% of newly installed stationary ESSs are powered by LIBs [13]. Of course, there are problems that still have to be resolved, i.e., cost-efficiency, durability, safety, sustainability, and integrity to specific ESSs. Therefore, other rechargeable battery concepts are now intensively investigated in parallel with LIBs.

Among the large variety of energy storage technologies mentioned in this section, rechargeable batteries can reasonably be considered the most attractive option for energy grid modification. Compared to other ESSs, the batteries possess general flexibility paired with high energy efficiency, so they can be integrated into power systems of various natures and scales. In the next section, we provide a brief insight into the current battery types: discuss their operational principles, advantages and limitations, functional features, and applicability for stationary energy storage purposes.

## 1.2. Rechargeable Batteries: From Invention to Modern Days

Rechargeable batteries are electrochemical energy storage devices enabled to accumulate and release electrical energy multiple times operating in a charge/discharge cycling manner. The first rechargeable accumulator type was a **Pb-acid battery** invented in 1859 by Gaston Planté. In this battery, lead, lead oxide, and concentrated sulfuric acid are used as anode, cathode, and electrolyte, respectively. In the fully discharged state, both electrodes take the form of lead sulphate, while the concentration of  $\text{H}_2\text{SO}_4$  in the electrolyte is reduced (Table 1.2). The modern Pb-acid batteries are low-cost, tolerant to low temperature, low self-discharging, and capable with high discharge currents. At the same time, the Pb-acid batteries require careful usage and specific utilization approaches to avoid an impact of harmful Pb on humans and environment. Short lifetime (<500 cycles; Figure 1.1), low charge speed, and low specific energy ( $\sim 40 \text{ Wh kg}^{-1}$ ; see brief description of battery performance metrics in Appendices, Table A1) currently make the Pb-acid batteries suitable for specific applications, e.g., internal combustion engine starting [14].

**Ni-Cd batteries**, explored by Waldemar Jungner in 1899, in contrast to the Pb-acid representatives, have longer cycle life, higher charge rates, and better compactness (Table 1.2). From the 1980s to the middle 1990s, the Ni-Cd batteries dominated the market of portable devices. In this type, Cd anode and NiO(OH) cathode are immersed in KOH electrolyte. Their main drawbacks are *memory effect* (capacity reduction due to partial discharging) and fast self-discharge (Figure 1.1b). Moreover, Cd is a toxic and expensive metal that demands much attention to battery production, application, and utilization.

Table 1.2. Performance comparison of Pb-acid, Ni-Cd, and Ni-MH batteries with LIBs [14–18].

Type	Electrode reactions	Specific energy, Wh kg <sup>-1</sup>	Energy density, Wh L <sup>-1</sup>	Voltage, V	Cycle life	Self-discharge, % month <sup>-1</sup>	In use since
Pb-acid	A: $\text{Pb} + \text{HSO}_4^- \leftrightarrow \text{PbSO}_4 + \text{H}^+ + 2\text{e}^-$ C: $\text{PbO}_2 + 3\text{H}^+ + \text{HSO}_4^- + 2\text{e}^- \leftrightarrow \text{PbSO}_4 + 2\text{H}_2\text{O}$	30-50	60-110	2.0	300-500	5	1800s
Ni-Cd	A: $\text{Cd} + 2\text{OH}^- \leftrightarrow \text{Cd}(\text{OH})_2 + 2\text{e}^-$ C: $\text{NiO}(\text{OH}) + \text{H}_2\text{O} + \text{e}^- \leftrightarrow \text{Ni}(\text{OH})_2 + \text{OH}^-$	40-60	150-190	1.2	1000	20	1950
Ni-MH	A: $\text{MH} + \text{OH}^- \leftrightarrow \text{M} + \text{H}_2\text{O} + \text{e}^-$ C: $\text{NiO}(\text{OH}) + \text{H}_2\text{O} + \text{e}^- \leftrightarrow \text{Ni}(\text{OH})_2 + \text{OH}^-$	60-120	140-300	1.2	500-2000	30	1989
LIB	A: $\text{C} + x\text{Li}^+ + \text{xe}^- \leftrightarrow \text{Li}_x\text{C}$ C: $\text{LiCoO}_2 \leftrightarrow \text{Li}_{1-x}\text{CoO}_2 + x\text{Li}^+ + \text{xe}^-$	155	400	3.6	500-2000	5	1991
	C: $\text{LiNMC} \leftrightarrow \text{Li}_{1-x}\text{NMC} + x\text{Li}^+ + \text{xe}^-$	>300	>700	3.8	800-3000	5	1999
	C: $\text{LiFePO}_4 \leftrightarrow \text{Li}_{1-x}\text{FePO}_4 + x\text{Li}^+ + \text{xe}^-$	150	325	3.3	3000-12000	5	1997

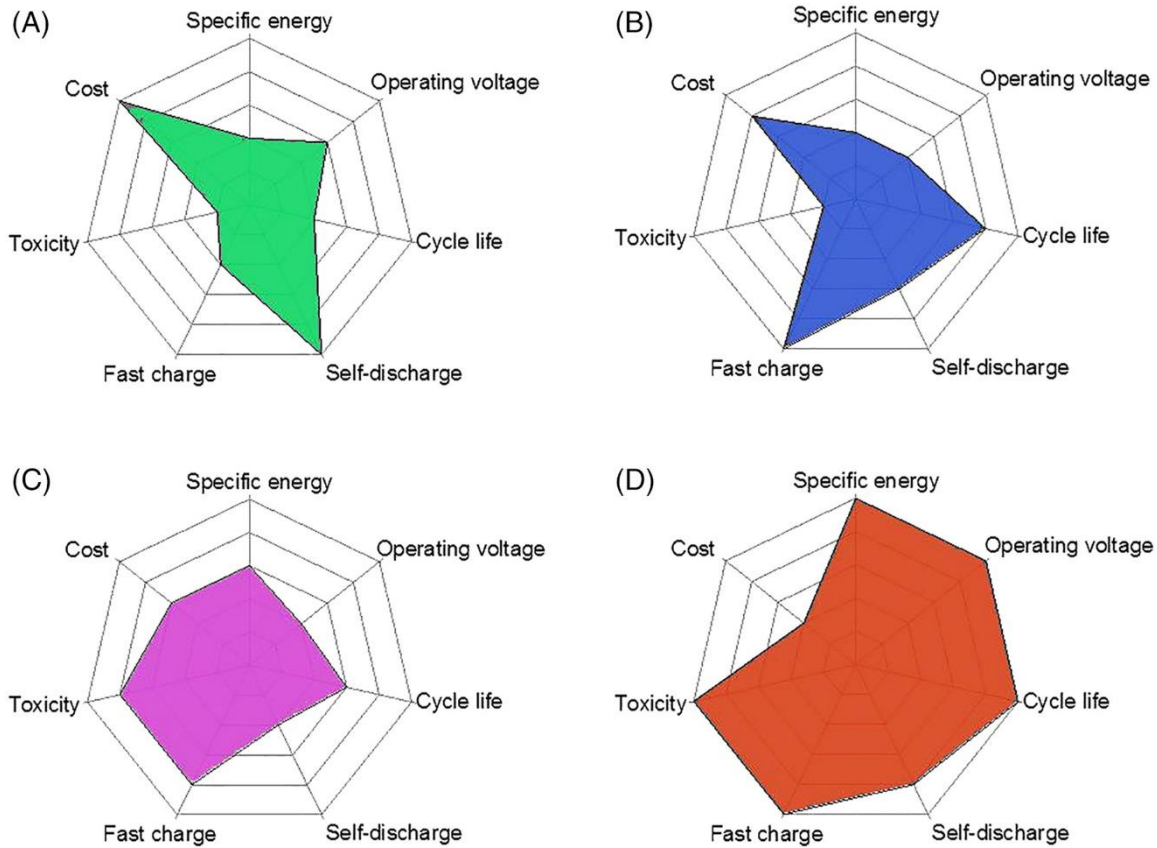


Figure 1.1. Qualitative performance comparison of (a) Pb-acid, (b) Ni-Cd, (c) Ni-MH, and (d) LIB [14].

**Ni-MH batteries**, commercially available from 1989, instead of Cd anode employ metal alloys (**M**) with a layer of adsorbed hydrogen (**H**) in the charged state. This diminished the memory effect and increased energy density and charge rates. The huge limitation of the Ni-MH batteries is the dramatic self-discharge process approaching one third of the battery's initial capacity. The Ni-MH batteries had been widely used in mobile phones, laptops, and even first hybrid electric vehicles before they gave the floor to LIBs.

**Na-S** batteries deserve attention due to their relatively high energy density (150–300 Wh L<sup>-1</sup>), low materials cost, and durability. Such batteries operate at 300-350 °C and utilize molten sodium and sulfur as an anode and cathode separated by  $\beta$ -alumina served as a sodium-ion conductor [18]. In spite of materials affordability, the annual operating cost of the Na-S batteries approaches 80 \$ kW<sup>-1</sup> year<sup>-1</sup> (vs. 6-16 for LIBs [19]) due to the heat supply required to the system. To overtake the cost problems, the room-temperature Na-S batteries with carbonate- or ester-based electrolytes are tested. However, poor cyclability, high irreversible capacity, self-discharging, dendrite growth, and slow reaction kinetics should be resolved prior to their commercialization [20]. Disregarding all the limitations, the Na-S batteries are already installed in several energy generation facilities for mitigating wind and solar power fluctuation and load levelling [18].

To mitigate the limitations of the battery types from above, a great attention has been devoted to investigating Li-ion batteries. In conventional LIBs, Li<sup>+</sup> as a charge carrier participates in redox processes through intercalation/deintercalation to electrode materials [21–24]. The use of Li is beneficial due to at least two reasons: Li is the lightest metal and has the lowest electrochemical potential (–3.04 V) among the others. The Li-involved battery weighs less and provides higher energy for the same capacity unit, which can dramatically enhance specific power and energy (Watt and Watt-hour, respectively, normalized to kg). This makes the Li-based batteries very promising for a broad range of electrical devices. Therefore, in the next section, we are going to estimate performance of current and emerging lithium battery types and evaluate their potential for stationary ESSs.

### 1.3. Lithium Batteries Family

#### 1.3.1. Conventional Li-ion Batteries

In 1991, LIB final commercialization by Sony Corporation opened up a new era of rechargeable batteries. During the charge process of a typical LIB, Li ions move from the  $\text{LiCoO}_2$  cathode to the graphite anode through a liquid electrolyte consisting of an organic carbonate solvent and lithium hexafluorophosphate as a salt (Figure 1.2a). This set-up brought an outstanding at that time performance:  $400 \text{ Wh L}^{-1}$  and  $155 \text{ Wh kg}^{-1}$  at 3.6 V nominal voltage [15]. Low self-discharge, light weight, and good cycling performance rapidly made LIB a dominant energy storage device for portable applications and beyond (EV, ESS). The substitution of electrolytes from liquid to polymer-based improved LIB's compactness, allowing the production of thin devices (ultrabooks, smartphones) and wearable electronics [14].

With time, several new materials have been introduced for LIBs to further improve their energy and power density, life span, etc. The cathode materials development is of special interest: the currently available diversity (layered, spinel, olivine structures; see Figure 1.2b) allows the adoption of the LIB for a specific use case. For example, the  $\text{LiNi}_x\text{Mn}_y\text{Co}_z\text{O}_2$  cathodes, providing moderate cycle life, give high power and energy density, whereas  $\text{LiFePO}_4$ , having lower energy density, shows supreme cycle and thermal durability (Figure 1.2c, Table 1.2).

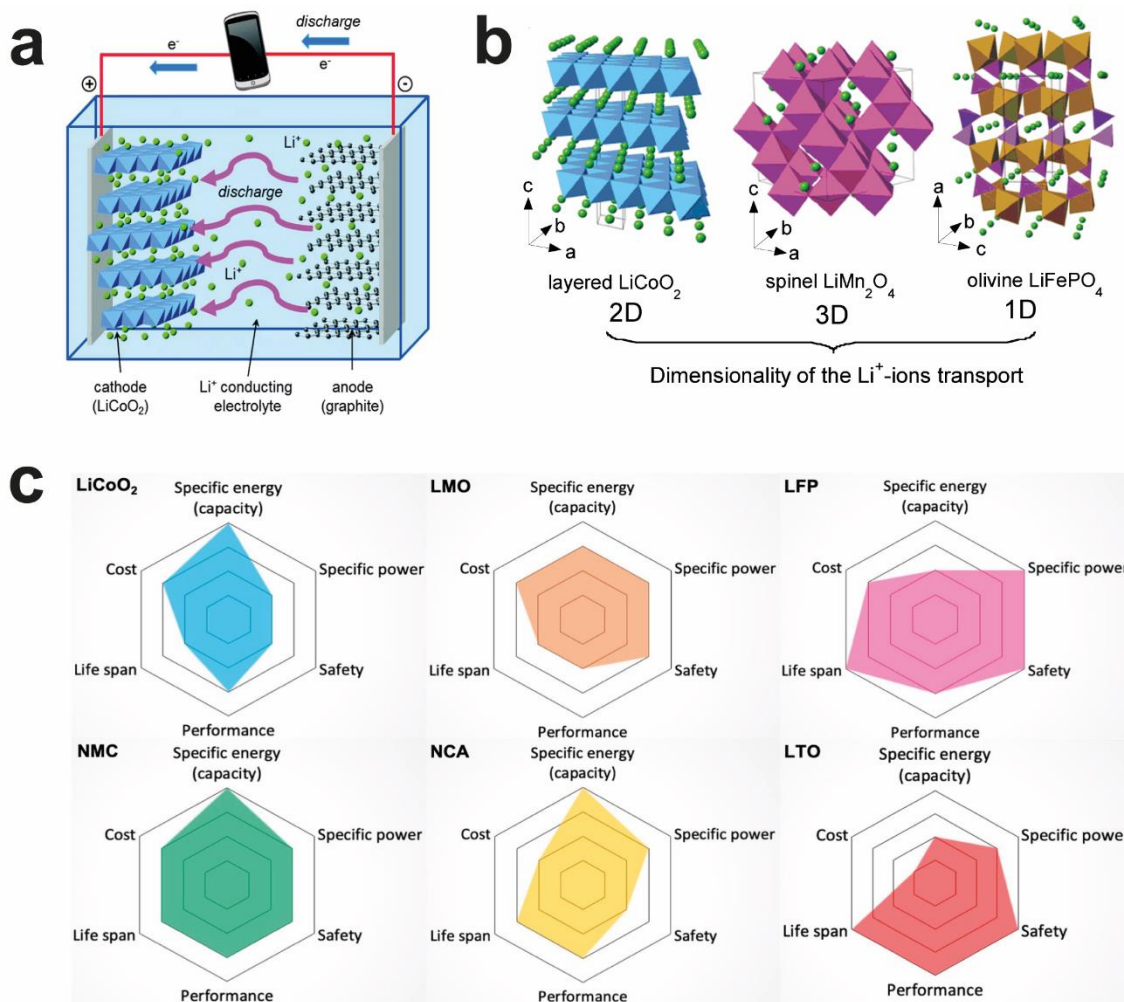


Figure 1.2. (a) Principal scheme of LIB operation; (b) crystal structure of three Li-insertion compounds and corresponding Li<sup>+</sup> mobility dimension; (c) qualitative characteristics of popular LIB cathodes [25,26].

In spite of the mentioned advantages, current LIB technology demands severe optimization to be more efficient for ESSs. The most crucial points are:

- Cost. LIBs are relatively cost-efficient for portable devices and EVs. For large-scale applications, the energy-specific storage cost is one of the main problems to resolve.
- Safety. Inflammation of LIBs caused by mechanical, thermal, and other damage is one of the main concerns for specialists [27]. More advanced and safe electrolytes should be developed to suppress the risk of thermal expansion, dendrite growth, and other reasons of LIB inflammation [28,29].
- Life cycle. Prolongation of LIB's cycle life would drastically diminish the cost of energy storage in LIBs. Their lifetime actually depends on the degradation processes occurring inside the cell. To prevent them, it is suggested to stabilize SEI, improve the contact between a cathode material and a current collector, and enhance the phase stability of the cathode active compound [30,31].
- Fast charging. For stationary applications, a fast LIB responding to the energy input is a necessity. Although this is a complex problem, it can be resolved by introducing new materials supporting fast and reversible redox processes [32].
- Sustainability. Mines and deposits of raw materials for the cathodes are localized in specific geographical places that makes their continuous supply to LIB plants challenging [33]. Taking into account the forecasted exponential growth of the LIBs demand [34], to avoid resource depletion, the infrastructure for the end-of-life LIB, recycling should be developed [35,36]. Finally, the technologies for materials extraction, cell manufacturing, and spent LIBs recycling are to maintain a low amount of CO<sub>2</sub> emission [37].

### *1.3.2. All-Solid-State Batteries*

To overtake the LIB's limitations stated above, new battery types are being investigated. In ASSBs, no liquid components are employed [11,38]: instead of liquified electrolyte, a solid Li-conducting membrane is used for a charge balance. The membrane not only prevents the LIB's leakage and electrolyte's thermal extension improving safety, but also makes the cell even more compact, improving its gravimetric characteristics. The dense membrane's structure blocks the growth of lithium dendrites enabling the application of a low-potential metallic Li anode. Together with the high-voltage cathodes (e.g., NMCs), the system can approach outstanding specific energy of up to 500 Wh kg<sup>-1</sup>, which is 2-2.5 times higher than of conventional LIBs [11,38]. Majority of ASSB's limitations, e.g., Li dendrites growth, high total cell resistance, are associated with the membrane issues. Hence, enhancing ASSB membrane's IC, robustness, and stability is the central task. Due to high specific power (directly related to energy density), ASSBs are expected to be used mainly for EVs, power tools, wearable devices, and for an easy start of large machines (tracks, ships, aircrafts).

Despite ASSBs will unlikely be applied for ESSs broadly, they revealed valuable benefits of Li-metal anode and solid-state ion-conducting membrane — the combination that can be also used in other ESSs. Development and optimization of these components can enhance the performance of batteries even beyond the all-solid-state set-up.

### *1.3.3. Redox Flow Batteries*

Calling to the history of RFB development, P. Pissoort originally reported a vanadium redox couple in 1933 [39], while W. Kango first patented a titanium chloride flow cell in 1954 [40]. Thaller et al. began systematic investigations on Fe-Ti and Fe-Cr electrolytes in the 1970s as a part of NASA space missions [41,42]. At the start of the 1980s, an interest in electrochemical energy storage began to grow in Japan, where the Electrotechnical Lab developed Fe-Cr redox systems using hydrochloric acid [43]. A. Pelligri and P. Spaziante reintroduced the vanadium concept in 1978 [44], but a little progress was made. Later in 1985, Skyllas-Kazacos successfully demonstrated and commercialized an all-vanadium RFB [45,46]. Simultaneously, new technologies of vanadium mining and refining were developed (e.g., from soot of heavy fuels and titanium production) which boosted the interest in this metal. Such success stimulated an increase in vanadium RFB research resulting in the first commercial installations in the 2000s and shifting the Fe-Cr RFB technology from the scene. In recent years, a number of research groups and companies focus on improving existing cell design and developing new chemistries. Nowadays, vanadium RFBs are successfully tested for voltage sag compensation, emergency power supply, load levelling, power stability, etc.

It can be said the RFB's main components are inverted in terms of aggregatory state compared with conventional LIBs. RFB's electroactive material is not embedded in solid electrodes, but dissolved in liquid solutions (**electrolytes** in the RFB notation) that are stored in two separate reservoirs (tanks; Figure 1.3a) outside and pumped through the cell.

This allows an independent control of power and capacity, strictly linked in other batteries, that makes RFBs flexible and cost-efficient for various applications. Increasing the volume of electrolytes (keeping redox moieties concentration the same) and maintaining the electrodes area, RFB's capacity scales regardless of power. Moreover, the tanks with the used electrolytes can be changed to that with charged ones in case of instant recharge emergence.

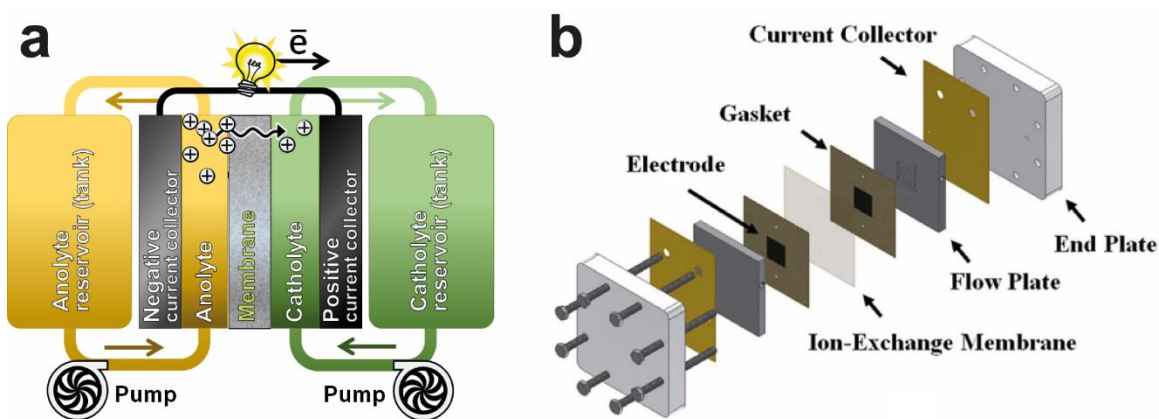


Figure 1.3 (a) General scheme of a RFB system and (b) illustration of electrochemical cell reflecting its main components [47,48].

The RFB cell is composed of two parts separated by a solid ion-conducting **membrane** (Figure 1.3b). In addition to charge balancing, the RFB membrane must block intermixing of the opposite electrolytes to avoid a crossover — a source of the battery capacity decay. Therefore, an ideal membrane for RFBs should have high IC, low electronic conductivity, low permeability to electroactive species, mechanical and chemical stability, and inexpensiveness (the membrane share in total RFB cost exceeds

40% [49]). Taking into account such a strong requirement set, the scientific communities developing RFBs should pay much attention to the membrane design [50].

In RFBs, **electrodes** (Figure 1.3b) are porous materials with high surface area, where redox species reactions take place. Electrode's morphology largely affects the transport and kinetics of redox processes. Graphite paper or felt are currently the most common materials for the RFB electrodes. Inert and flexible **gaskets** (made of Teflon or Viton; Figure 1.3b) fix the electrode position, protect the membrane, prevent leakage, and provide tightness for the assembled cell.

**Flow plates** (or bipolar plates; Figure 1.3b) in the RFB cell transfer electrons from the electrodes to current collectors and distribute the flowing electrolyte through the electrode surface. The flow plates are usually made of compressed modified graphite with high electrical conductivity and zero permeability to liquids to avoid cell leakage. The flow plate can optionally have a channel pattern to distribute the electrolyte more uniformly upon the electrode's surface.

**Current collectors** (Figure 1.3b), commonly made of electronically conductive Cu or Al, provide the electrons transport from the cell to an external circuit. Metal or plastic **end plates** (Figure 1.3b) allow in- and outlet flow of the electrolytes, distribute pressure, and tighten and complement the whole construction. Multiple cells can be connected serially into a stack for scaling the battery's power. Besides the reservoirs with electrolytes, the electrochemical cell, and the pumping system, the final RFB installation should also

include the electronic control system responsible for temperature and power tuning and components state monitoring.

Nowadays, commercially available and emerging membranes can balance the charge through conducting different cations ( $H^+$ ,  $TEA^+$ ,  $Li^+$ ,  $Na^+$ ) and anions ( $OH^-$ ,  $BF_4^-$ ). Even though there are different all-flow RFB systems employing specific charge carriers, the actual nature of balancing ions does not impact the battery's performance directly. However, *this impact increases drastically as soon as its solid, zero-charged form becomes involved in an electrochemical process:  $M^0/M^{n+}$  potential differentiates charge carriers by their nature. Introducing the  $M^0/M^{n+}$  redox couple into the flow system can boost the battery's working voltage and, hence, energy and power density.*

While Li-ion RFBs are only developing, all-vanadium and zinc-bromine aqueous systems have already received much investment and reached an early stage of commercialization as ESSs [51,52]. VRFBs are employed in pilot plants with the range of 1–200 MW power and 10–800 MWh energy. Using vanadium oxides at both compartments suppresses their intermixture and supports 20,000 charge/discharge cycles compared to 3,000-5,000 for typical LIB [53]. At the same time, VRFB are characterized with low cell voltage (1.26 V), low active compounds solubility, and, hence, only 40 Wh L<sup>-1</sup> energy density [54] (vs. 200 Wh L<sup>-1</sup> for LIB's). The limiting factor of increasing cell voltage is a water decomposition (1.2-1.6 V) that retards the implementation of vanadium and other aqueous RFBs. Accounting the fluctuating vanadium cost linked to the steel production and expensive Nafion membrane (\$500 m<sup>-2</sup> [55]), the capital cost of

typical VRFB varies within  $\$300\text{--}800 \text{ (kWh)}^{-1}$  — much higher than the established target of  $\$100 \text{ (kWh)}^{-1}$  [49,56].

Zn-Br RFB has been also scaled up: several  $0.6\text{--}2 \text{ MW h}^{-1}$  projects are installed for the load leveling service [52]. Zn-Br RFBs represent the hybrid flow structure — zinc deposits on a carbon anode during the charge and dissolves during the discharge. Zn-Br RFBs possess enhanced energy density ( $60\text{--}90 \text{ Wh L}^{-1}$ ) and cheaper materials comparing to VRFBs. However, the specific maintenance conditions (preventing Zn dendrite growth, sequestering agents, avoiding toxic Br emissions, etc.) level the capital costs of Zn-Br and VRFBs at *ca.*  $\$0.2 \text{ (kWh cycle)}^{-1}$  [57].

In order to decrease the RFB capital cost, organic redox-active couples can be used instead of metal-based compounds. Organic molecules are more abundant and can be synthesized from various sources. Some of them support the energy-beneficial multi-electron transfer; the structure can be synthetically tailored to provide better kinetics, solubility, and potential [58]. The most successful examples of aqueous RFBs can be found in Appendices, Table A2. Still, their performance is limited to low cell potential ( $<1.7 \text{ V}$ ), as well as to insufficient redox species' water solubility ( $<1 \text{ M}$ ) and slow kinetics.

Overall, to accelerate the RFB implementation in ESSs, its capital cost should approach an estimated  $\$100$  per kWh. This target can be achieved by increasing RFB's energy density through several modifications:

- Substitute electrolytes media from aqueous to non-aqueous that can broaden operation voltage and improve redox couples' solubility;

- Design low-cost redox couples with facile kinetics and high stability (e.g., organic-based moieties);
- Prioritize the metal cations as the charge carriers to further enhance RFB with solid materials, introduce a  $M^0/M^{n+}$  couple.

#### 1.3.3.1. Non-aqueous all-flow batteries

NAqRFBs were first described by Matsuda et al. in 1988 [59] and contained Ru-based active species dissolved in ACN. Besides noble metal complexes, in 2009 vanadium acetylacetonate was employed as an active component showing promising performance [60]. To resolve some of the organometallic compounds' issues (poor solubility, low stability), numerous organic molecules have been investigated as redox species since 2011 [61]. The resulting organic-based NAqRFBs operate at much higher cell voltages (up to 5-6 V), temperatures, and species concentrations that can theoretically increase RFBs energy and power density. At the same time, NAq solvents are more viscous than water, so one may expect lower IC.

The choice of a membrane for NAqRFBs is more challenging. The Nafion membranes, used for aqueous systems, even in the modified state show poorer IC in NAqRFBs. As a result, the current range applied for NAqRFBs is only 0.1–10 mA cm<sup>-2</sup> vs. 0.1–1 A cm<sup>-2</sup> for aqueous systems. High swellability of ion-exchange membranes may lead to severe crossover of active species. Membrane's stability in NAq media is also questioned [50]. Nevertheless, organic-based NAqRFBs have a huge potential to overtake VRFBs and approach LIBs in terms of performance. Below, we discuss the most promising

NAqRFBs relying on Li-ion transfer (the examples based on other supporting ions can be found in Appendices, Table A3).

Brushett et al. for the first time investigated an all-organic RFB system utilizing the DBBB-based catholyte, 2,3,6-trimethylquinoxaline anolyte, and ion-exchange Nafion 117 membrane soaked in  $\text{LiBF}_4$  in PC [62]. The authors discussed intriguing advantages that organic materials can provide such as tailorable redox potentials, solubilities, and kinetics of the species. The DBBB compounds showed reversible single electron transfer at 4 V vs.  $\text{Li/Li}^+$  and solubility at PC of up to 7 M. The proof-of-concept 1.7-1.8 V cell, assembled in a coin set-up ( $0.0625 \text{ mA cm}^{-1}$ ), demonstrated coulombic and energy efficiency of higher than 70% and 37%, respectively, during 30 cycles. Energy density was also lower than that for VRFBs (16 vs.  $40 \text{ Wh L}^{-1}$ ). In spite of insufficient performance reported, this work initiated a series of research focused on long-term stability and efficiency improvement through the active species tailoring, cell design, and searching for the membrane for Li-ion NAqRFBs.

Wei et al. continued the all-organic systems development and examined the 9-fluorenone-DBMMB NAqRFBs cell (2.4 V) [63]. The authors designed a flow cell operated by the Daramic porous membrane enabling the current density as high as  $15 \text{ mA cm}^{-2}$ . Despite the system approached  $11 \text{ Wh L}^{-1}$  energy density, it maintained only 86% coulombic efficiency and 20% of initial capacity after 100 cycles. The authors associated the decay with the fluorenone radical degradation and high Daramic membrane permeability dictated by its 57% porosity.

To further improve current density, the same research group introduced N-methylphthalimide instead of fluorenone [64]. Using the 1.0 M LiTFSI in DME electrolyte and the Daramic membrane, the battery cell (2.3 V) demonstrated 50 cycles at 35 mA cm<sup>-2</sup> and maintained 90 and 69% coulombic and energy efficiencies throughout the cycling. The membrane was chosen among several Daramic and Celgard commercial samples according to the lowest resistance. At the same time, their permeability was not addressed, even though it might grow opposite to porous membrane's resistance.

Overall, Li-ion NAqRFBs are quite promising due to their cell voltage going beyond the water decomposition potential. Organic redox active species are cost-beneficial and allow tuning their properties through the structural modification. Nevertheless, energy density of the all-flow NAqRFBs is still much lower than of VRFB counterparts, so either cell resistance, cell voltage, or both should be further improved. A significant portion of attention is to be addressed to membranes: there is little information regarding its stability in the NAq environment and the IC (resistance)/permeability correlation.

#### 1.3.3.2. Li-Metal Hybrid Flow Batteries

An intriguing approach to enhance the NAqRFB cell voltage and, hence, energy density is to couple a catholyte with a metallic anode (e.g., Zn, Na, Li, etc.). Li-metal hybrid flow batteries (Li-HFBs) are particularly interesting due to the lowest electrochemical potential of Li (-3.04 V). By its employment, the expected NAqRFB's cell voltage can be increased to 2.5–4 V approaching that of conventional LIBs. Additionally, such a hybrid system simplifies the RFB's architecture by replacing the anolyte tank with a thin Li plate

(Figure 1.4a). Combining the features of NAqRFBs and ASSBs this way, Li-HFBs have great potential to finally overtake the energy density of aqueous RFBs and even approach the LIB technology (Figure 1.4b). See examples of common Li-HFBs in Table 1.3.

In 2011, Senoh et al. reported the Li-HFB performance for the first time [65]. As a catholyte, they employed benzoquinone-based compounds dissolved in the 1 M LiClO<sub>4</sub> in GBL supporting electrolyte (SE). In the designed static-mode electrochemical cell, the authors used LICGC membrane to separate the anode part (Li metal in SE) from the cathode (active moieties in SE). The most efficient Li-DPBQ cell showed 2.6 V and 98% capacity retention after 25 cycles at 0.05 mA cm<sup>-2</sup>.

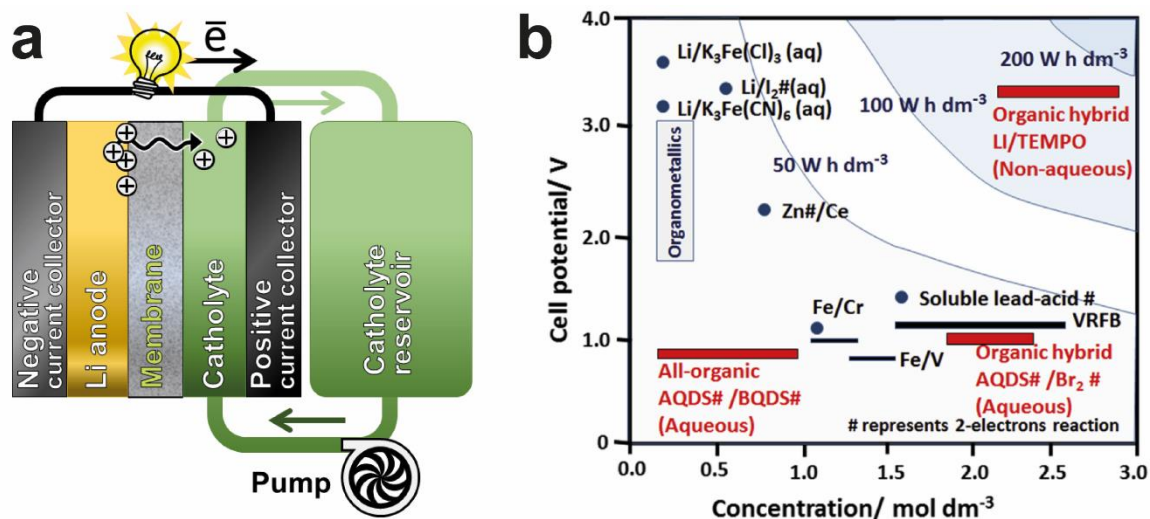
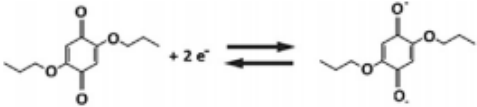
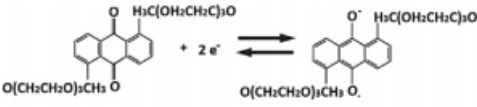
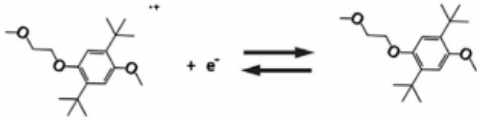
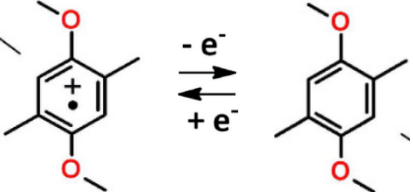


Figure 1.4. (a) Scheme of HFB with lithium-metal anode; (b) Performance comparison of Li-HFBs with common RFB solution [66].

Table 1.3. Performance of Li-metal HFBS.

Catholyte / Membrane	Positive redox couple	OCV, V	Energy density, Wh L <sup>-1</sup> / current density, mA cm <sup>-2</sup>	Coulombic / Energy efficiency, %	Ref.
0.1 M DPBQ + 1 M LiClO <sub>4</sub> in GBL / LiCGC		2.6	- / 0.05	-	[65]
0.25 M anthraquinone- based + 1.0 M LiPF <sub>6</sub> in PC / Celgard 3401		2.4	25 / 0.1	- / 82	[67]
1 mM DBMMB + 0.5 M LiBF <sub>4</sub> in PC / -		4.0	- / 0.1	- / 81	[68]
0.1 M 1,4-dimethoxy- 2,5-dimethylbenzene + 1 M LiTFSI in EC-PC- EMC / Daramic		3.9	16 / 7.5	95 / 79	[69]

2 M TEMPO + 1.0 M LiPF <sub>6</sub> in PC-EC-EMC/ polyethylene-based		3.6	126 / 5	99 / 86	[70]
1:1 MeO- TEMPO:LiTFSI + 17 wt.% H <sub>2</sub> O / LICGC		3.3	200 / 0.1	99 / 80	[71]
0.08 M Tetra- aminoanthraquinone + 1.0 M LiTFSI in DMSO / Nafion 115		3.8	22 / 20; theoretical energy is 1858 Wh kg <sup>-1</sup>	99 / 71	[72]
0.3 M MPT with Ketjenblack + 1.0 M LiPF <sub>6</sub> in EC:DEC / LAGP		3.5	190 / 0.2	99 / -	[73]

Later, Wang et al. proposed anthraquinone modified with triethylene glycol methyl ether groups as catholyte species [67]. Operated in the static mode at 2.45 V and 0.1 mA cm<sup>-2</sup>, the cell showed 25 Wh L<sup>-1</sup> energy density, which was never achieved before for NAqRFBs, and 82% energy efficiency that diminished though to 70% after 10 cycles due to possible oligomerization of radical anions.

To further increase Li-HFB cell voltage, Huang et al. explored several DBMMB-based compounds as positive moieties [68]. At 0.4 mA, the cell (4.0 V) showed 30 charge/discharge cycles maintaining *ca.* 80% energy efficiency. The liquid state of the DBMMB molecule allows the latter to be used as-received or co-dissolved for high-energy NAqRFBs. Unfortunately, there is a lack of information in the article regarding the cell assembling features, including the membrane used.

Later, Huang and co-authors reported light 1,4-dimethoxy-2,5-dimethylbenzene catholyte species that provided ultimate capacity of 161 mAh g<sup>-1</sup>. In their performance experiments, the authors used the hybrid anode consisting of the stacked Li foil and graphite felt. Worth mentioning the anode part as well as the catholyte reservoir were filled with comparable volumes of active compounds in SE. This set-up excludes the impact of crossover from the cell performance allowing to use low-resistant porous separators and, hence, higher currents. Although such specifics simplify proof-of-concept studies, in further HFB development, the crossover impact should be considered.

Using the same approach to the anode and cell design, Wei et al. for the first time investigated the Li-TEMPO flow cell [70]. Theoretical energy density of TEMPO-based

HFBs approaches outstanding  $200 \text{ Wh L}^{-1}$  primarily due to the high solubility of TEMPO in NAq electrolytes (2 M). In aprotic solvents, TEMPO is a stable radical showing reversible redox reaction within 3.4-3.9 V [74]. Using 2 M TEMPO dissolved in the  $\text{LiPF}_6$  PC-EC-EMC electrolyte, the authors achieved 86% energy efficiency and  $126 \text{ Wh L}^{-1}$  energy density (Figure 1.5a, b) reaching 67% of the theoretical value.

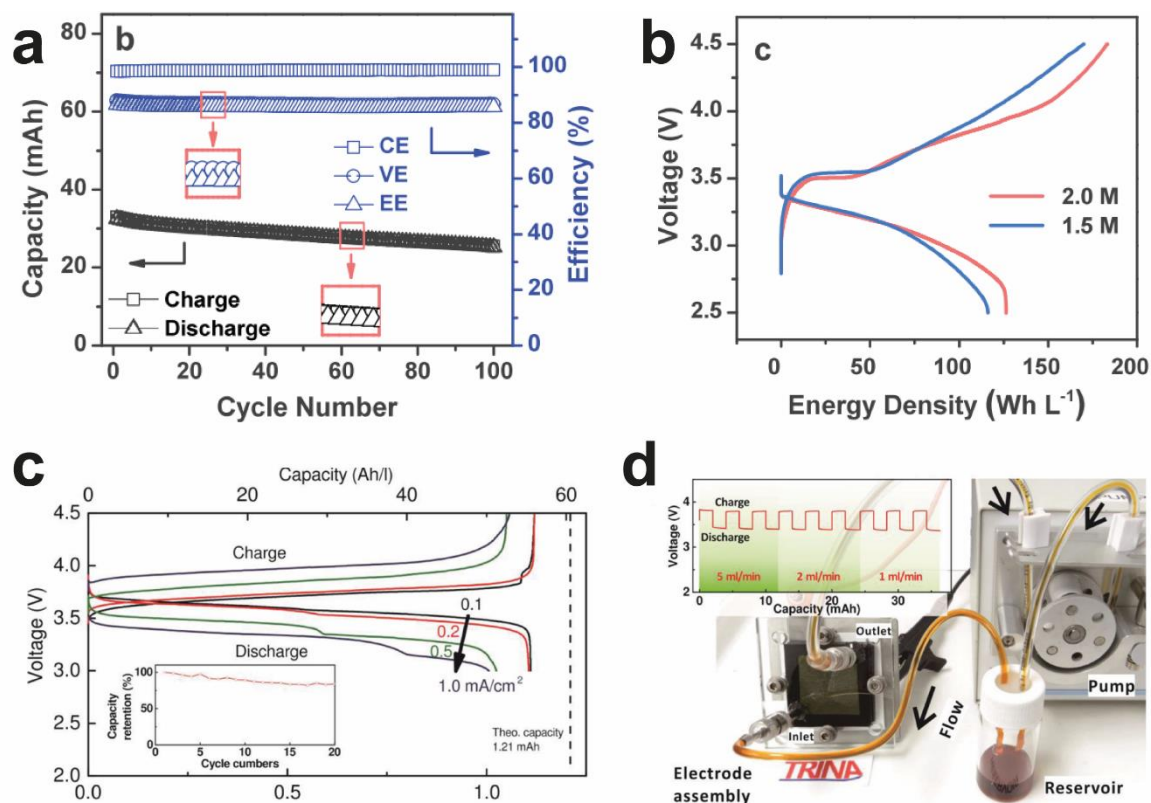


Figure 1.5. (a) Cycling performance of 0.1 M TEMPO + 1.0 M  $\text{LiPF}_6$  in PC-EC-EMC+15 wt.% FEC at  $5 \text{ mA cm}^{-2}$ ; (b) energy density voltage curves for Li|TEMPO cell; (c) Cycling behavior of Li|MeO-TEMPO flow cell during the 1<sup>st</sup> cycle at 0.1–0.5  $\text{mA cm}^{-2}$ ; (d) Flow cell demonstration and cycling behavior at 1 – 5  $\text{mL min}^{-1}$  flow rates [70,71].

Takeshi et al. reported the MeO-TEMPO catholyte to be able to provide even higher energy density —  $200 \text{ Wh L}^{-1}$  [71]. The authors' novel idea was to liquify MeO-TEMPO by mixing it with the LiTFSI supporting salt and small amount of water, thereby obtaining a supercooled ionic liquid. The static mode cell survived 20 charge/discharge cycles at  $0.1 \text{ mA cm}^{-2}$  showing 80% energy efficiency and 84% capacity retention (Figure 1.5c, d). However, the system's components stability to water was not evaluated.

Outstanding research was recently carried out by Pahlevaninezhad and co-workers [72]. As a catholyte active compound, they utilized tetra-aminoanthraquinone (DB-1) capable of a 4-electron charge transfer and high electrode potential ( $3.5 \text{ V vs. Li}$ ). Theoretically, DB-1 may achieve one of the highest specific energy values ever reported for RFBs —  $1858 \text{ Wh kg}^{-1}$ . According to DFT calculations (for the DMSO solvent) and the voltammetric studies, the molecule can not only experience the oxidation ( $4 \text{ e}^{-}$ ) but also the reduction process ( $2 \text{ e}^{-}$ ), thereby supporting the 6-electron transfer. The Li-HFB cell cycling with the  $1.0 \text{ M LiTFSI}$  in DMSO electrolyte, Nafion 115 membrane, and  $80 \text{ mM DB-1}$  concentration (solubility is *ca.*  $1 \text{ M}$ ) at  $20 \text{ mA cm}^{-1}$  showed energy efficiency of 71%, capacity retention of *ca.* 100%, and  $22 \text{ Wh L}^{-1}$  energy density (Figure 1.6a, b).

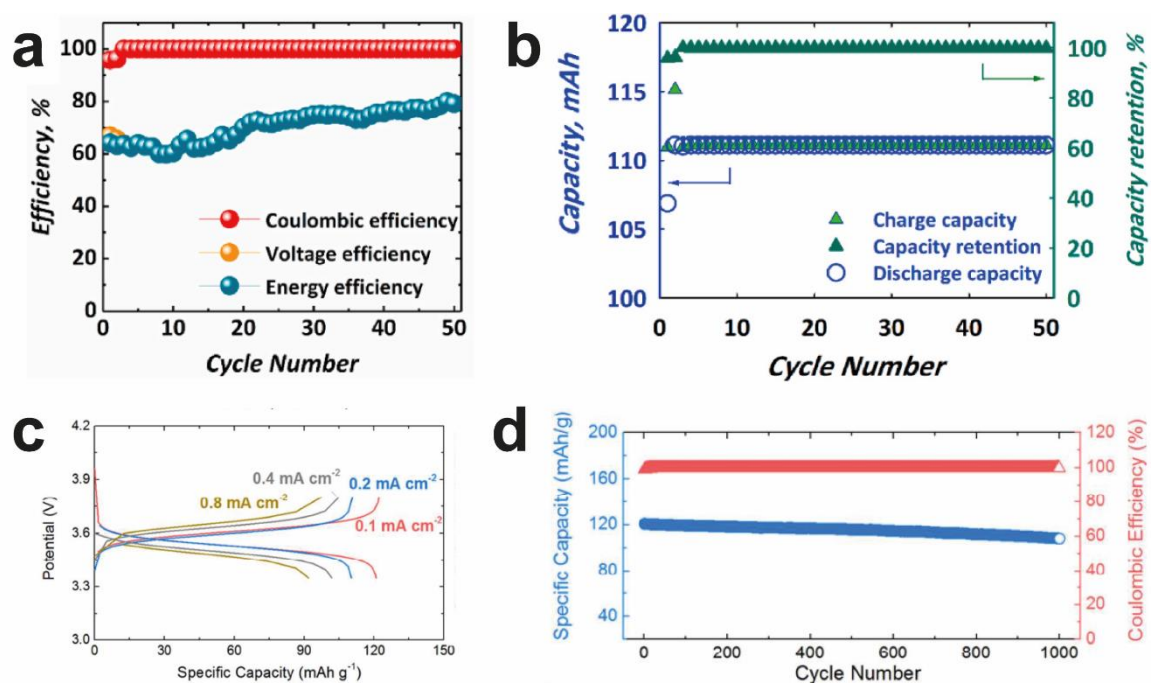


Figure 1.6. (a) Performance of 80 mM DB-1 + 1.0 M LiTFSI in DMSO in Li|DB-1 cell at 20 mA cm<sup>-2</sup>; (b) Capacity retention during 50 charge/discharge cycles; (c) First cycles of galvanostatic profile of 0.3 M MPT + 1 M LiPF<sub>6</sub> in EC:DEC (1:1 vol.) in Li|MPT cell at 0.1–0.8 mA cm<sup>-2</sup>; (d) Capacity retention and coulombic efficiency of Li|MPT cell at 0.1 mA cm<sup>-2</sup> [72,73].

Recently, Chiang et al. proposed the concept of semi-solid RFBs [75]. The addition of dispersed conductive material (solid boosters) into liquid electrolyte media can potentially enhance RFB's energy density. Among the diversity of such suspension-based flow systems [76], the research by Chen et al. is of a particular interest [73]. The authors combined Li-metal anode with the MPT-based catholyte suspended with conductive carbon (Ketjenblack) to drastically improve the battery's performance. As a Li-conducting

separating solution, the authors exploited  $\text{Li}_{1.5}\text{Al}_{0.5}\text{Ge}_{1.5}(\text{PO}_4)_3$  ceramic membrane placed between two Celgard separators. By introducing carbon, they increased cell's volumetric capacity from 7 to 55  $\text{Ah L}^{-1}$  and achieved energy density of 190  $\text{Wh L}^{-1}$  — close to LIBs. Moreover, the cell demonstrated outstanding cycling stability: 95% of initial capacity retains after 1000 cycles (Figure 1.6c, d). Suspended RFBs are now rapidly developing and deserve a separate study.

Overall, the organic-based Li-HFBs represent a promising class of electrochemical energy storage devices because of high operation voltage. Due to the intensive improvement of redox active species, electrolytes, and cell design in the last decade, some Li-HFBs characteristics (e.g., energy density) has approached that of conventional LIBs. At the same time, the performance of membranes for Li-HFBs is still underexplored. Passing through the most influential research published, we found that either porous, ion-exchange, or ceramic membranes were applied in various NAqRFBs. However, their IC, permeability, and stability were just briefly addressed (never all together) with no deeper analysis. Nevertheless, all these properties do impact energy density and long-term operation, which are the crucial parameters for ESSs. Willing to fulfill this niche, in the next section, we discuss the main types of Li-conducting membranes: evaluate their performance, limitations, and, the most important, potential applicability in Li-HFBs.

#### 1.4. Membranes for RFBs

Ion-conductive solid-state membranes are much safer than conventional liquid electrolytes (negligible thermal extension, no leakage). They can be cheaper (polymeric materials) and even more integrable because of low thickness and flexibility. In order to be suitable for Li-HFBs, a membrane should meet two sets of requirements at the same time: for all-flow and Li-metal batteries. An ideal Li-HFB membrane should exhibit mechanical robustness and flexibility, high IC and Li<sup>+</sup> selectivity (low redox species permeability), stability to NAq media and metallic Li anode, and low cost (Table 1.4).

Table 1.4. Main targets for membranes utilized in NAqRFBs.

Parameter	Target value
Ionic conductivity	$10^{-4}$ – $10^{-2}$ S cm <sup>-1</sup>
Permeability	$<10^{-6}$ cm <sup>2</sup> min <sup>-1</sup> [62]
Chemical stability	No degradation after long-term cycling
Mechanical strength	100 MPa [77]
Cost	$<40$ \$ m <sup>-2</sup> [55]

A membrane's IC and permeability, in fact, depend on a material's porosity and SE applied, so there is no uniform standard for this criterion. One can define typical IC of LIB's NAq electrolyte ( $10^{-2}$  S cm<sup>-1</sup>) as the optimistic target and the threshold common for ASSB electrolytes ( $10^{-4}$  S cm<sup>-1</sup>) as the minimum. The membrane's permeability should be

tuned in accordance with IC (they are reversibly linked), though might be approximated to be lower than  $10^{-6} \text{ cm}^2 \text{ min}^{-1}$  for NAq solvents [62]. Below, we distinguish the variety of membranes into porous, ion-exchange, dense polymeric, and inorganic types and discuss their conduction mechanisms, materials, properties, and performance.

#### *1.4.1. Types of Membrane Materials*

##### 1.4.1.1. Porous Polymer

Porous membranes (or separators) are currently used in conventional LIBs (Appendices, Table A3) and several RFB prototypes. The porous membrane itself is ionically inert — ions transfer through the liquid electrolyte penetrated into its pore system. Thereby, membrane's apparent IC and selectivity strongly depends on the pore structure, (i.e., size, tortuosity), swellability, thickness, and stability in a chosen SE [78].

In this regard, one may expect insufficient selectivity of porous membranes in NAqRFBs. Indeed, Celgard's permeability to DBBB in the DME-based electrolyte was at the order of  $10^{-4} \text{ cm}^2 \text{ min}^{-1}$  [79] (Table 1.5) — close to active molecules' diffusion in the bulk NAq solutions [80] and unacceptable for NAqRFBs. Note that in several reports on Li-HFBs, the porous membrane is used in a couple with a symmetrical design of the cell (catholyte species were in both catholyte and anode compartments [69,70,79,81]). Such a proof-of-concept approach increases the currents possible to apply, but deprives the Li-HFB from the compact architecture and excludes a crossover effect, which enhances a battery's capacity fade. This set-up is inappropriate for the next stage of prototyping, where both the simplified construction and the negligible crossover should be demonstrated.

Table 1.5. Characteristics of porous membranes employed in several NAqRFBs.

Membrane	IC, mS cm <sup>-1</sup> / Permeability, cm <sup>2</sup> min <sup>-1</sup>	Porosity, % / Pore size, μm	Electrolyte system	Ref.
Celgard 2325	0.5 / 1.7 · 10 <sup>-4</sup>	39 / <0.07	<u>Mediators</u> : 0.1 M DBBB/MePh; <u>SE</u> : 1 M LiTFSI in DME	[79]
Daramic 175	4.6 / –	57 / 0.15	<u>Mediators</u> : 0.1 M DBBB/MePh; <u>SE</u> : 1 M LiTFSI in DME	[79]
Celgard 2400 cross-linked with polysilsesquioxane	0.5 / 1.8 · 10 <sup>-6</sup>	–	<u>Mediators</u> : 0.01 M V(acac) <sub>3</sub> ; <u>SE</u> : 0.1 M TEABF <sub>4</sub> in ACN	[82]
Celgard 2400, pore-filling with PDDA	5.4 / 8.5 · 10 <sup>-9</sup>	–	<u>Mediators</u> : 0.4 M Fe(BiPy) <sub>3</sub> (BF <sub>4</sub> ) <sub>2</sub> / Ni(BiPy) <sub>3</sub> (BF <sub>4</sub> ) <sub>2</sub> ; <u>SE</u> : 0.5 M TEABF <sub>4</sub> in PC	[83]
Celgard, pore- filling with CuBTC	– / 6.9 · 10 <sup>-5</sup>	– / <0.001	<u>Mediators</u> : Li/ 0.05 M ferrocene; <u>SE</u> : 1 M LiClO <sub>4</sub> in DOL:DME	[84]
Crosslinked PIM	0.4 / 2.3 · 10 <sup>-9</sup>	– / <0.001	<u>Mediator</u> : viologen- modified oligomers; <u>SE</u> : LiPF <sub>6</sub> in ACN	[85]

There are two approaches to suppress porous membrane's permeability: (i) to modify microstructure of commercially available samples and (ii) to design the polymer from scratch tailoring its pore size to be smaller than the studied redox couples. For example, Jung et al. crosslinked the Celgard membrane with polysilsesquioxane [82] and diminished its permeability to  $V(acac)_3$  by 2 orders of magnitude (to  $1.8 \cdot 10^{-6} \text{ cm}^2 \text{ min}^{-1}$ ) comparing with pristine Celgard (Table 1.5). Kim et al. modified the Celgard membrane with mechanically stable urushi and anion-exchange PDDA polymer [83]. Retaining IC at  $5.4 \text{ mS cm}^{-1}$ , the authors suppressed the membrane's permeability by 20–200 times (to  $8.5 \cdot 10^{-9} \text{ cm}^2 \text{ min}^{-1}$ ) compared with the pristine samples. Peng et al. designed 3D MOF composed of trimesic acid and  $\text{Cu}^{2+}$  structures inside the Celgard pore system [84]. Due to the small aperture size of CuBTC (0.9 nm, Figure 1.7a-c), it easily transmits  $\text{Li}^+$  (0.15 nm) but stops ferrocene. After the Celgard modification, the Fc permeability was decreased to  $6.9 \cdot 10^{-5} \text{ cm}^2 \text{ min}^{-1}$ , whereas cell resistance kept the same. Doris et al. polymerized the membrane from modified 1,1'-spirobisindane and 2,3,5,6-tetrafluoroterephthalonitrile with the pore size of 0.4–0.8 nm fitting the viologen-based oligomeric redox couples [85]. As a result, they achieved an outstanding selectivity (ratio between permeability coefficients of  $\text{Li}^+$  and active species) of  $10^5$  and no crossover during 6-day cycling (17 cycles, Figure 1.7d, e).

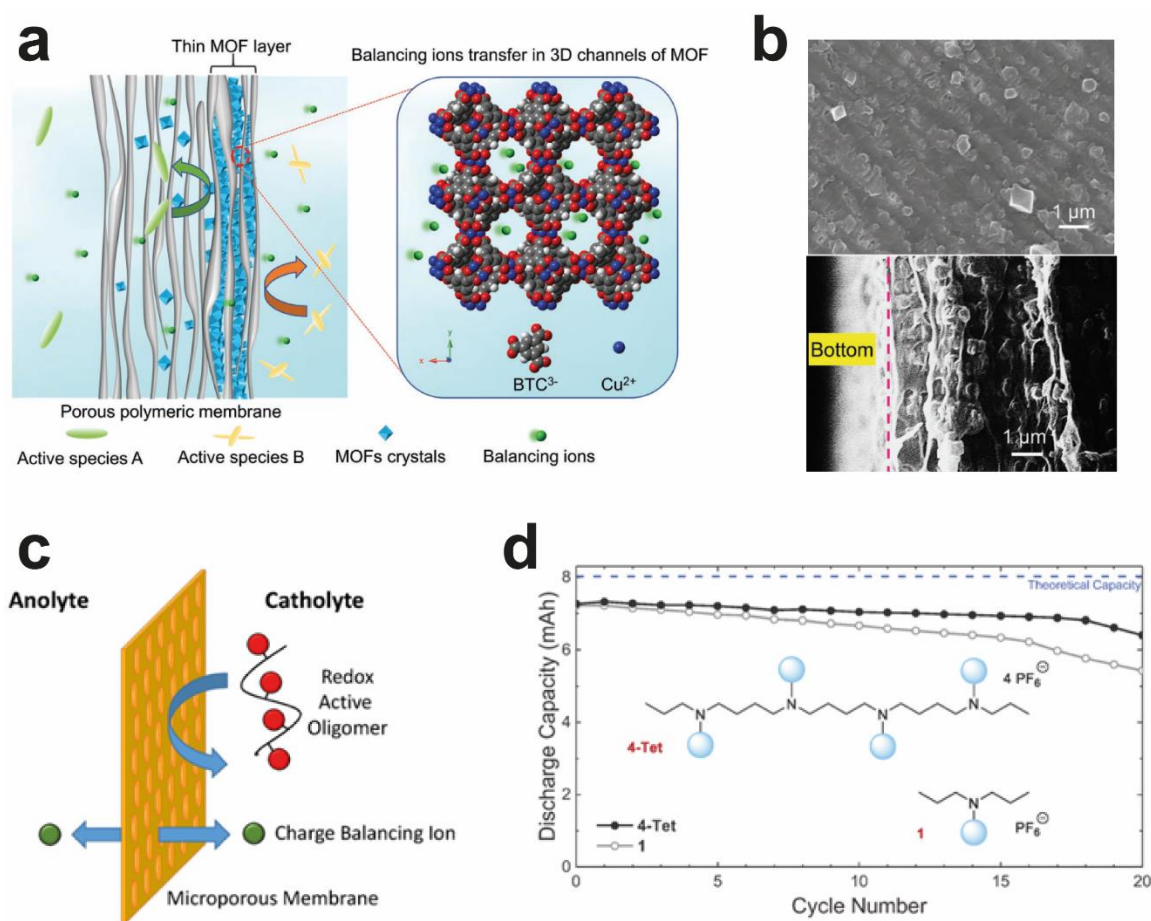


Figure 1.7. (a) Design principles of the CuBTS/Celgard membrane with a MOF gradient distribution; (b) bottom and (c) cross-section surfaces of CuBTS/Celgard; (d) representation of a microporous membrane operation in oligomer-based RFBs; (e) discharge capacity achieved for the RFB cell equipped with the most efficient catholyte redox oligomers [84,85].

Overall, commercially available porous membranes are not applicable for RFBs due to the crossover. Their pore system modification as well as the membrane synthesis from monomeric precursors provide the tunable porosity enabling the size exclusion for desired redox moieties. However, the reported IC ( $0.5\text{--}5.4\text{ mS cm}^{-1}$ ) and permeability values ( $10^{-9}\text{--}10^{-5}\text{ cm}^2\text{ min}^{-1}$ ) vary in a quite wide range that leave an uncertainty regarding the real effect of the modification approaches. Besides, there is no data regarding electrochemical stability of the mentioned polymers. The development of porous membranes still requires more attention to the material design and fabrication technology prior to their implementation in RFBs.

#### 1.4.1.2. Ion-Exchange

IEMs are already used in low-temperature fuel cells and aqueous RFBs. These membranes selectively pass only one type of ions blocking oppositely charged ones. An IEM's polymeric backbone contains charged functional groups that promote conduction of either positive (cation exchange membrane, CEM) or negative ions (anion exchange membrane, AEM). In aqueous media, considering a Nafion membrane as an example (Figure 1.8), there are three ion-transfer mechanisms: *Grotthus* (cation movement via structural diffusion), *vehicular* (transfer in bulk solution through chains), and *surface* (hoping on  $-\text{SO}_3^-$  groups), which is suppressed in water media due to high activation energy. In NAq systems, where the Grotthus and vehicular pathways are impeded (no structural diffusion, higher viscosity), the surface mechanism dominates [86], which makes the IC to be severely lower.

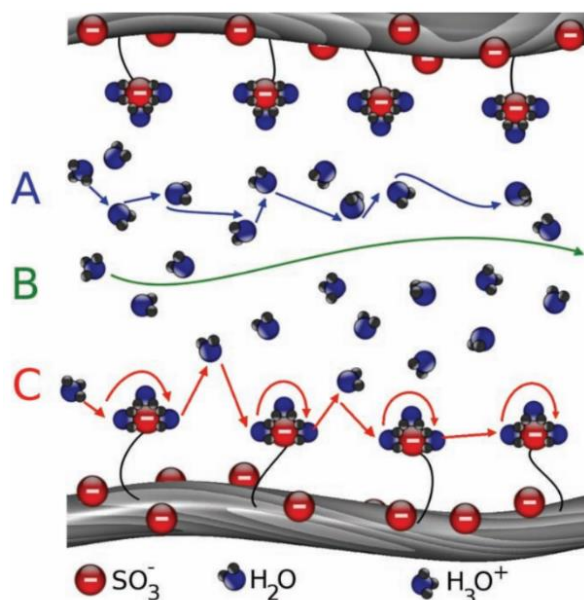


Figure 1.8. Proton conductivity mechanisms in Nafion IEM: A — Grotthuss, B — vehicular, and C — surface mechanisms [87].

CEMs, e.g., Nafion, are the most frequently used membranes for aqueous all-vanadium RFBs [88]. The pristine Nafion membranes, initially designed to conduct  $\text{H}^+$ , can be modified to transport such cations like  $\text{Li}^+$ ,  $\text{Na}^+$ ,  $\text{TBA}^+$ , or  $\text{TEA}^+$  — it makes Nafion suitable for NAqRFBs [50]. For example, Lu et al. investigated IC and permeability of the lithiated Nafion 117 membrane toward ferrocene [62] (Table 1.6). In the PC-based electrolyte, Nafion showed both low permeability ( $5.3 \cdot 10^{-8} \text{ cm}^2 \text{ min}^{-1}$ ) and IC ( $10^{-2} \text{ mS cm}^{-1}$ ), whereas the DMSO-based solution, having acceptable IC ( $5 \text{ mS cm}^{-1}$ ), demonstrated poor permeability ( $1.4 \cdot 10^{-5} \text{ cm}^2 \text{ min}^{-1}$ ). For both solvents, the minimum threshold values of  $>1 \text{ mS cm}^{-1}$  and  $<10^{-6} \text{ cm}^2 \text{ min}^{-1}$  were not achieved simultaneously.

Table 1.6. Performance of commercially available and polymerized IEMs used in NAqRFBs.

Membrane	Ionic conductivity, mS cm <sup>-1</sup>	Permeability, cm <sup>2</sup> min <sup>-1</sup>	Electrolytes	Ref.
CEM				
Nafion 117	10 <sup>-2</sup>	5.3 · 10 <sup>-8</sup>	<u>1</u> : 0.05 M Fc + 1 M LiPF <sub>6</sub> in PC	[62]
	5.0	1.4 · 10 <sup>-5</sup>	<u>2</u> : Fc + 1 M LiPF <sub>6</sub> in DMSO	
Nafion 115	5.9	2.5 · 10 <sup>-3</sup>	0.05 M V(acac) <sub>3</sub> + 0.2 M TEABF <sub>4</sub> in ACN	[89]
POATS-PPO	0.06	1.2 · 10 <sup>-7</sup>	0.1 M Fc + 1 M Li CF <sub>3</sub> SO <sub>3</sub> in DMC	[90]
AEM				
Fumasep FAP-375	1.5	–	0.1 M Fc-based + 0.5 M TEATFSI in ACN	[91]
Fumasep FAP-450	3.5	3.7 · 10 <sup>-7</sup>	0.4 M Fe(BiPy) <sub>3</sub> (BF <sub>4</sub> ) <sub>2</sub> / Ni(BiPy) <sub>3</sub> (BF <sub>4</sub> ) <sub>2</sub> + 0.5 M TEABF <sub>4</sub> in PC	[92]
Neosepta	1.0	–	<u>1</u> : 0.5 M TEABF <sub>4</sub> in ACN	[93]
AHA	0.2	5.1 · 10 <sup>-7</sup>	<u>2</u> : 0.5 M TEABF <sub>4</sub> in PC	[92]
PVC-based	0.1	2 · 10 <sup>-7</sup>	0.01 M V(acac) <sub>3</sub> + 0.1 M TEABF <sub>4</sub> in ACN	[94]
PAEK	1.5	–	0.01 M V(acac) <sub>3</sub> + 0.5 M TEABF <sub>4</sub> in ACN	[95]

Moreover, Bamgbopa et al. reported severe morphological degradation of Nafion 115 in NAq media that affected its swelling and permeability to  $V(acac)_3$  [89]. The practical use of commercial CEMs for NAqRFBs is now under question due to the instability, high cost ( $\$500\text{ m}^{-2}$  [55]) of Nafion, and insufficient IC of other CEMs — CMI-7000, Nepem-117, and Fumapem F-141 [96,97].

AEMs, originally used for seawater desalination, have been also employed in NAqRFBs. Zhen et al. reported the Fumasep FAP-375 membrane, showing good performance in all-iron NAqRFB (Table 1.6), significantly degraded after 100 cycles in the ACN-based electrolyte that enhanced the crossover [91]. Fumasep FAP-450 tested in the Ni-Fe NAqRFB demonstrated IC of  $3.5\text{ mS cm}^{-1}$ , permeability of  $3.7 \cdot 10^{-7}\text{ cm}^2\text{ min}^{-1}$ , but high extent of swelling that led to structural deformation and porosity rise [92]. Neosepta AHA, providing stable long-term cycling [98], had low IC in both ACN ( $1.0\text{ mS cm}^{-1}$ ) and PC-based electrolytes ( $0.2\text{ mS cm}^{-1}$ ) [93].

Besides commercially available IEMs, a series of samples was fabricated from scratch via the polymerization. McCornack et al. crosslinked phenoxyaniline trisulfonate with brominated PPO and obtained CEMs with highly sulfonated side chain [90]. The resulted membranes showed low swellability, ferrocene permeability ( $1.2\text{--}1.8 \cdot 10^{-7}\text{ cm}^2\text{ min}^{-1}$ ), but insufficient IC of  $0.06\text{ mS cm}^{-1}$ , which should be necessarily improved prior to the introduction into NAqRFBs. Maurya et al. fabricated the PVC-based AEMs via polymer crosslinking with 4-vinylpyridine and 1,4-dibromobutane [94]. The membrane showed IC of  $0.105\text{ mS cm}^{-1}$  and the permeability to  $V(acac)_3$  of  $2 \cdot 10^{-7}$

$7 \text{ cm}^2 \text{ min}^{-1}$  with no evident degradation and low swelling. Kwon et al. examined the PAEK membranes crosslinked with dibromobutane and employed it in  $\text{V}(\text{acac})_3$  NAqRFB [95]. The membranes showed high  $1.5 \text{ mS cm}^{-1}$  IC in  $\text{TEABF}_4$  in ACN and great stability. Unfortunately, no permeability data was reported.

Overall, commercially available IEM solutions does not suit NAqRFBs, as they do not provide the essential set of properties — they lack either high IC (CMI, Nepem, Neosepta, AMI), selectivity (Nafion), or stability (Nafion, Fumasep, Neosepta). The promising direction is, as for the porous membranes, to fabricate IEMs by polymerization. Although they exhibit much higher stability in NAq electrolytes and lower permeability than the benchmarks, their IC should be enhanced in the future.

#### 1.4.1.3. Dense Polymer

Dense polymeric membranes, proved themselves in conventional LIBs and ASSBs [99,100], can be reasonably considered promising for Li-HFBs as well. The dense polymeric structure can potentially restrict the active species crossover preventing the cell from capacity decay.

Traditionally, the polymer membranes possess extremely low intrinsic IC ( $<10^{-6} \text{ S cm}^{-1}$ ) [99,100], so their structure is reinforced by lithium salts dissolved within. The polymer's polar groups ( $-\text{O}-$ ,  $-\text{N}-$ ,  $\text{C}=\text{O}$ , etc.) can complex mobile ions, promoting the salts dissolution and boosting the polymer's IC. It is assumed that ion conduction in the polymers occurs above glass transition temperature in amorphous phase. The common conductivity mechanism can be described as follows [100]:  $\text{Li}^+$  coordinates to the polar

polymer's site  $\rightarrow$  a polymer chain experiences a segmental motion  $\rightarrow$  appeared free volume promotes  $\text{Li}^+$  migration from one site to another within or between the polymer chains. Of course, the exact process might differ from polymer to polymer depending on its nature. Often, the IC correlation with temperature can hint the predominant ion migration mechanism [101,102]. Depending on Arrhenius (1.1) or Vogel-Tamman-Fulcher models (1.2),  $\text{Li}^+$  transport occurs either via simple ion hopping or that coupled with the relaxation and segmental motion [101,103]:

$$(1.1) \quad \sigma = \sigma_0 \exp\left(\frac{-E_a}{RT}\right),$$

$$(1.2) \quad \sigma = \sigma_0 T^{-1/2} \exp\left(\frac{-B}{T-T_0}\right),$$

where  $\sigma_0$  represents the pre-exponential factor,  $E_a$  is the activation energy,  $B$  is the pseudo-activation energy, and  $T_0$  — equilibrium glass transition temperature ( $T_0 \approx T_g - 50$  K).

For conventional LIBs, a variety of polymer and salt combinations were previously tested and described in the literature; the most prominent examples are summarized in Appendices, Table A4. Among the others, we would highlight the PEO and PVdF-based membranes due to their relatively high IC, impressive stability (ESW of  $>4.3$  V), and ease of fabrication [99,100]. Surprisingly (and unfortunately), in RFB literature we have not met examples of using dense polymeric membranes with embedded salts. Perhaps, the reason might be in leaching the salt out of the polymer structure during the contact between a membrane and RFB's flowing electrolyte. We suppose the polymeric membranes' performance in NAqRFBs is in vain underestimated and should be studied in the future.

#### 1.4.1.4. Inorganic

Li-conductive inorganic materials have been extensively using as membranes in ASSBs and developing for NAqRFBs [50,99,104,105]. Currently, the most successful classes of inorganic membrane materials are lithium phosphorus oxynitride (LIPON), LISICON, perovskites, garnets, and NASICON-type ceramics [99,104] — their typical performance is summarized in Table 1.7.

Table 1.7. Performance of the common Li-conducting ceramic materials [104,105].

Material	Ionic conductivity, mS cm <sup>-1</sup>	Stability in air	Electrochemical stability window, V vs. Li/Li <sup>+</sup>	Cost
<u>LIPON</u> : Li <sub>x</sub> PO <sub>y</sub> N <sub>z</sub>	10 <sup>-3</sup> -10 <sup>-2</sup>	Mediate	<5.5	Low
<u>LISICON</u> : Li <sub>3+x</sub> M <sub>x</sub> N <sub>1-x</sub> O <sub>4</sub>	10 <sup>-2</sup> -10 <sup>-1</sup>	Mediate	<5.5	High
<u>Perovskites</u> : Li <sub>3x</sub> La <sub>2/3-x</sub> TiO <sub>3</sub>	0.2-5	Low	>1.5	High
<u>Sulfides</u> : Li <sub>6</sub> PS <sub>5</sub> X Li <sub>4-x</sub> Ge <sub>1-x</sub> P <sub>x</sub> S <sub>4</sub>	1-25	Low	<4	Mediate
<u>Garnet-type</u> : Li <sub>5</sub> La <sub>3</sub> M <sub>2</sub> O <sub>12</sub>	0.3-3	Low	<4.5	High
<u>NASICON-type</u> : LiM <sub>2</sub> (PO <sub>4</sub> ) <sub>3</sub>	0.1-1	Mediate	<4.0-6.0	High

The synthesis of LIPON compounds is performed either by magnetron sputtering [106] or beam assisted and vapor deposition [107,108], which would be costly to scale up. In spite of their low IC at RT, the synthesis techniques can produce thin LIPON layers (0.1-0.2  $\mu\text{m}$ ) of low resistance, making them more suitable for thin-film ASSBs.

LISICONs ( $\text{Li}_4\text{MO}_4$ ) possess high electrochemical stability, but insufficient IC ( $<10^{-4} \text{ S cm}^{-1}$ ) for the battery applications.

Perovskites ( $\text{Li}_{3x}\text{La}_{2/3-x}\text{TiO}_3$ ; Figure 1.9a), on the contrary, have promising IC of up to  $10^{-3} \text{ S cm}^{-1}$ , but poor stability at  $<1.5 \text{ V}$  making them incompatible with Li anodes [104].

The sulfide-type materials (thio-LISICONs, Figure 1.9b) are prospective due to the weaker interaction of  $\text{S}^{2-}$  with  $\text{Li}^+$  than  $\text{O}^{2-}$ , which gives them IC close to that of NAq liquid electrolytes [109]. Their total IC at RT ranges from  $10^{-3}$  to  $2.5 \cdot 10^{-2} \text{ S cm}^{-1}$  — the highest value ever reported for Li-conductive solid materials [110]. The main drawback for all sulfide-based compounds is instability to moisture that leads to structural changes and  $\text{H}_2\text{S}$  emission. Their high potential for ASSBs can be realized only by separating the battery from the ambient atmosphere.

The garnets,  $\text{Li}_5\text{La}_3\text{M}_2\text{O}_{12}$  ( $\text{M} = \text{Ta}, \text{Nb}$ ; Figure 1.9c), represent promising compounds for various Li-metal batteries. This material comprises  $\text{La}^{3+}$  and  $\text{M}^{5+}$  in the cubic and octahedral oxide coordination. Unusually high amount of  $\text{Li}^+$  occupies 3 trigonal, 3 tetrahedral, and 6 octahedral sites, which provides facile  $\text{Li}^+$  3D mobility and promising IC (above  $10^{-3} \text{ S cm}^{-1}$  at RT) [111]. What is more, the garnet structures are relatively stable toward metallic Li, as Ta is less reducible than other common metals (e.g., Ti, Nb). The

main disadvantage of the garnet-type materials is their catastrophic sensitivity to atmospheric moisture and CO<sub>2</sub> [112,113] that is still not suppressed. Overtaking the stability issues would lead to valuable advances in prototyping garnet-based ASSBs.

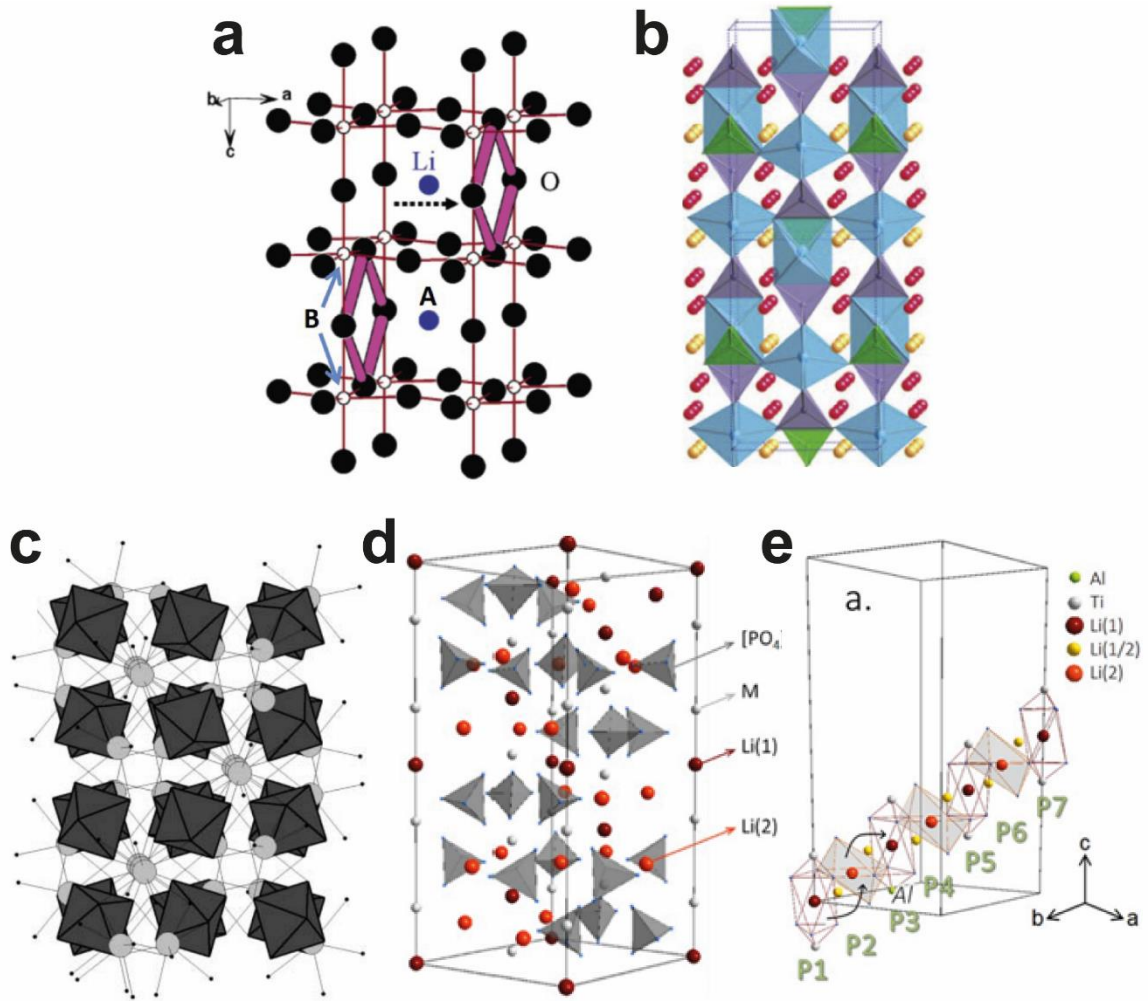


Figure 1.9. Schematic structures of (a) perovskite, (b) thio-LISICON, (c) garnet-, and (d) NASICON-type ceramics; (e) Li<sup>+</sup> easiest migration path [111,114–116].

One of the most prospective classes of inorganic Li-conducting materials is NASICON-type ceramics [104]. These materials are derived from sodium superionic conductors,  $\text{Na}_{1+x}\text{M}_2(\text{YO}_4)_3$  ( $\text{M}$  = transition metal,  $\text{Y}$  = P, Si), by replacing Na atoms to Li. In the NASICON rhombohedral structure,  $\text{MO}_6$  octahedrons and  $\text{YO}_4$  tetrahedrons, connected through oxygen, provide 3D ion diffusion within the framework (Figure 1.9d) [117]. Mobile ions are located in Li(1) and Li(2) sites and can jump between the positions (Figure 1.9e). The NASICON crystal structure is represented by different space groups depending on temperature and ions' radii [118], which determines material's IC. Varying in a broad range, the total IC value is usually higher than  $10^{-4} \text{ S cm}^{-1}$  and approach  $10^{-3} \text{ S cm}^{-1}$  [119–121]. Dense NASICONs can be synthesized via simple solid-state routines [116]. Meanwhile, these ceramics do have several issues to resolve depending on the composition. For instance, Ge-doped ceramics ( $\text{Li}_{1+x}\text{Al}_x\text{Ge}_{2-x}(\text{PO}_4)_3$ ), in spite of a higher IC, drastically increase in price [122]. The severe limitation of the Ti-contained materials ( $\text{Li}_{1+x}\text{Al}_x\text{Ti}_{2-x}(\text{PO}_4)_3$ ) is the  $\text{Ti}^{4+}$  reduction at 2.5 V that hinders its compatibility with Li anodes. The possible solutions are introduction of specific coating (deposition of a protective layer [123,124], introduction into a polymer matrix) or a total substitution of Ti.

It is assumed that the NASICON ceramics are quite stable on air, even though there is a lack of thorough quantitative analysis of structure and IC retention under exposure to ambient atmosphere (air, moisture). To shed light on the  $\text{Li}_{1.3}\text{Al}_{0.3}\text{Ti}_{1.7}(\text{PO}_4)_3$  (LATP) stability, Pogosova et al. examined the effect of air storage on ceramic's Li(1) polyhedron volume and IC [116]. After the 98-day air storage, LATP lost 76% of its initial IC (Figure

1.10a). By means of DFT modeling and XRD refinement, the authors linked the IC fall with the shrinkage of Li(1) site-involved polyhedra (Figure 1.10b). They suggested that both IC and structural degradation arose from the reaction of LATP's lithium ions with air to form  $\text{Li}_2\text{CO}_3$ . Furthermore, the destructive impact of water on LATP was specified [125]: after 2-h static soaking, ceramic's IC decreased by 64%, as well as crystallite's microcracks, formation of spherical nanoparticles, Li(1) shrinkage, and element losses were observed (Figure 1.10c, d). These results suggest that NASICON ceramics, LATP-type at least, should be designed the way to not only be protected from the Li anode, but also from moisture prior to the use in Li-metal batteries including Li-HFBs.

Evaluated the impact of Li and moisture, the behaviour of ceramics in NAq solvents should be estimated. It should be mentioned that, despite NASICON ceramics (including commercially available LICGC) are often used in NAqRFBs [65,71,73,126,127], its stability towards the battery environment was poorly addressed. Muthuraman et al. applied a sodium-ion conductor  $\text{Na-}\beta\text{-Al}_2\text{O}_3$  to  $\text{V}(\text{acac})_3$  NAqRFB [128]. The authors showed morphological and elemental stability of the material, although the cell's coulombic efficiency was extremely low (16%) that might be an attribute of a severe crossover. Neither the crossover nor IC were quantitatively evaluated in this study.

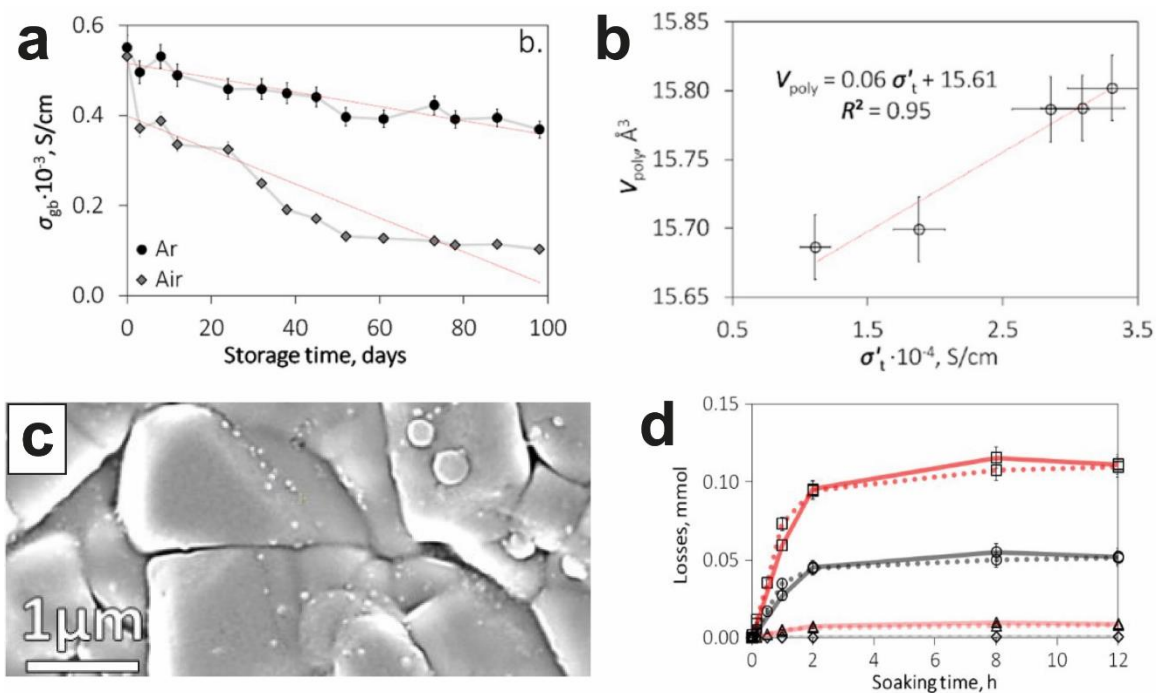


Figure 1.10. (a) LTP total IC after storage in air and in argon atmosphere; (b) relationship between the LTP's intrastructural Li(1) polyhedra volume and total IC; (c) SEM image illustrating the nanoparticles formation; (d) losses of LTP chemical elements after soaking in deionized water [116,125].

Zhang et al. examined Li-HFB based on the  $\text{Li}_{1.5}\text{Al}_{0.5}\text{Ge}_{1.5}(\text{PO}_4)_3$  membrane, BenPh active species, and LiTFSI in dimethylformamide-dichloroethane as a solvent [129]. At  $0.2 \text{ mA cm}^{-2}$ , the cell retained 78-95% coulombic efficiency and ~90% initial capacity after 50 charge/discharge cycles. Not evaluating the membrane state after the cycling tests, the authors presumably linked the limited cell efficiency with either the membrane degradation or dendritic lithium in anolyte.

Overall, the NASICON-type ceramic materials are the most promising for Li-HFBs among the inorganic classes due to promising Li-ion conductivity and simple synthesis route. At the same time, NASICON membranes demand a proper protection approach to mitigate sensitivity to Li anode, moisture, and, probably, NAq electrolytes. A prospective idea is to seal the milled ceramic material into a polymer combining the functional properties of both filler (ceramic's high IC) and matrix (polymer's stability, integrity, low cost; Table 1.8). As far as the concept of composite membranes has been recently introduced, in the next section, we are going to discuss examples of the polymer-ceramic membrane use in batteries and estimate their applicability in Li-HFBs, specifically.

Table 1.8. Qualitative performance comparison of four main membrane types.

Membrane type	Ionic				
	conductivity	Selectivity	Stability	Integrity	Cost
Porous polymer	+	-	+	++	++
Ion-exchange	-	+	-	+	-
Dense polymer	-	+	+	++	++
Inorganic (ceramic)	++	?	+ / -	-	-

++: excellent; +: good; -: unsatisfactory; ?: no reliable data

#### 1.4.2. Polymer-Ceramic Composite Membranes

Composite membranes can be distinguished by the presence/absence of a lithium salt in a matrix similar to that reported in Section 1.4.1.3. Besides traditional inorganic salts, the novel solutions for single-ion conduction (e.g., organic anions attached to the polymer backbone) are being developed [130]. At the same time, frequently used LiClO<sub>4</sub>, LiTFSI, and LiBF<sub>4</sub> are acceptable due to their electrochemical stability and solubility.

The filler can be either *inert* or *active* (involved in Li-conducting). The addition of inert fillers (clay, MOFs, etc.) promotes the formation of polymer's amorphous phase that slightly increases composite's IC [131–133]. For a more drastic IC gain, the active fillers such as Li-conducting NASICON- and garnet-type ceramics are used [134–137]. The composite membranes can be classified as “*ceramic-in-polymer*” and “*polymer-in-ceramic*” depending on the filler content (Figure 1.11a). The latter has higher rigidity, better dendrite suppression, higher IC, but poorer interfacial contact with electrodes [134].

The formation of additional Li<sup>+</sup> conduction paths in the composite fabricated with an active filler was explained by Wang et al. [135]. They showed LATP-PEO-LiClO<sub>4</sub> membrane's IC firstly increases with the LATP content, but, passing the maximum at 15 wt.% LATP ( $2 \cdot 10^{-4} \text{ S cm}^{-1}$ ), diminishes probably due to decreasing mobility of Li<sup>+</sup> in the polymer matrix. Choi et al. fabricated the composite made of Li<sub>7</sub>La<sub>3</sub>Zr<sub>2</sub>O<sub>12</sub> (LLZO), PEO, and LiClO<sub>4</sub> [136]. With no LLZO, membrane's IC was around  $6 \cdot 10^{-6} \text{ S cm}^{-1}$  at 60 °C. At optimum ceramic fraction of 52.5%, IC was  $7 \cdot 10^{-4} \text{ S cm}^{-1}$  at 60 °C and  $10^{-5} \text{ S cm}^{-1}$  at RT.

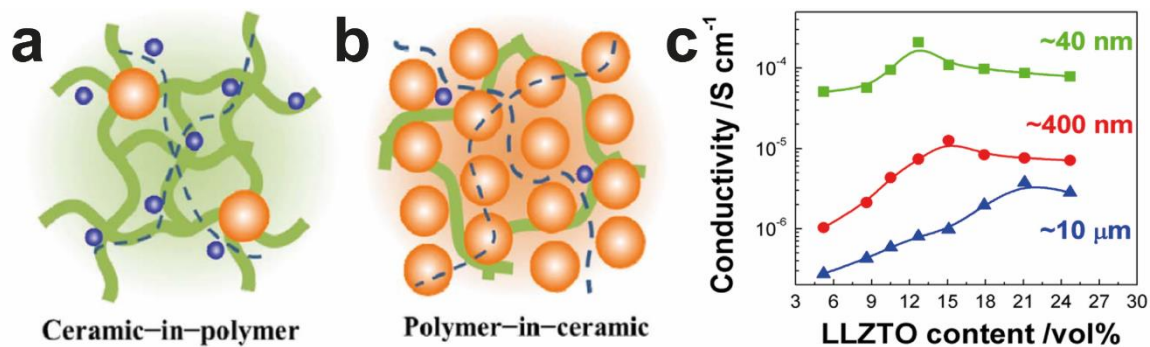


Figure 1.11. (a) Illustration of *ceramic-in-polymer* and *polymer-in-ceramic* classes of composites; (b) Effects of size and ceramic content on LLZTO-PEO's IC [137,138].

Together with the ceramic content, its particle size also plays an important role. Zhang et al. found that the 40 nm particles (in the backdrop of 400 nm and 10 μm, Figure 1.11b) provide the highest IC of  $ca. 1.1 \cdot 10^{-4} \text{ S cm}^{-1}$  in the 12.7 wt.% LLZO-PEO composite (no salt added) [137]. The smaller particles reduce the polymer crystalline phase formation and improve the polymer-ceramic interface that led to higher IC [137,139].

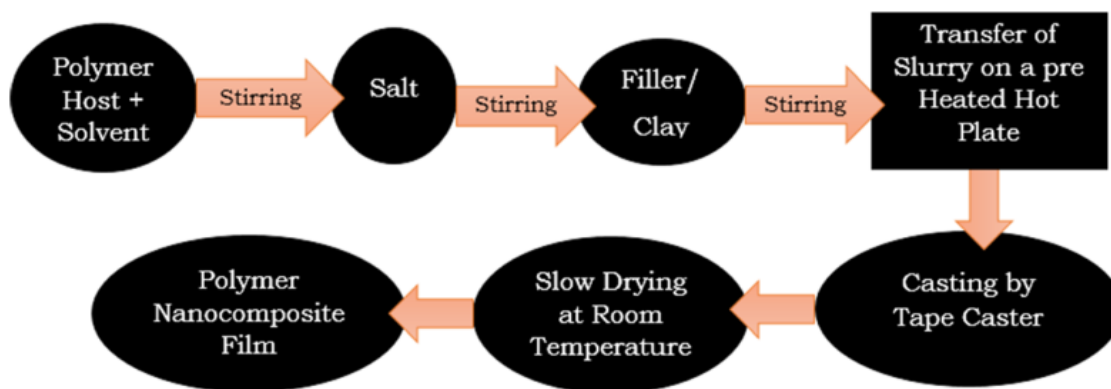
In addition to PEO, PVdF and derivatives are often used in composites due to their durability, stability, and selectivity [140,141]. Zhang et al. reported the LLZTO-PVdF-LiClO<sub>4</sub> membrane exhibited IC of  $5 \cdot 10^{-4} \text{ S cm}^{-1}$  at RT [142]. Sun et al. reported the LFP battery operated with PVdF-HFP-LLZO-LiClO<sub>4</sub> with the addition of 20 μL liquid electrolyte. The wetted membrane showed  $1.1 \cdot 10^{-4} \text{ S cm}^{-1}$ . Shi et al. obtained the stable LATP-PVdF (no salt) composite membrane that showed IC of  $10^{-3} \text{ S cm}^{-1}$ , ESW of ~5 V, and promising cycling performance in the Li|LiFePO<sub>4</sub> cell [143].

Indeed, the polymer-ceramic approach to membrane fabrication is quite promising due to the balanced integrity, IC, and stability of the systems. However, there are no reports regarding the permeability of such systems and, hence, their applicability for either all-flow RFBs or Li-HFBs. Nevertheless, we expect the polymer-ceramic composites to be prospective for Li-HFBs, as they combine good conductivity properties of active inorganic compounds with the flexibility of polymeric media. Among the large variety of choices, we will further focus on the NASICON-based LATP and PVdF combination: LATP is characterized by relatively high IC and moderate stability that, in turn, enables easy and scalable fabrication; PVdF is distinguished by its stability features and is expected to be a good protection of LATP against metallic Li-anode, ambient atmosphere, and other components of Li-HFBs. To continue, in the next section we will consider common fabrication methods of the polymer-ceramic class of composites.

#### *1.4.3. Composite Membrane Fabrication Methods*

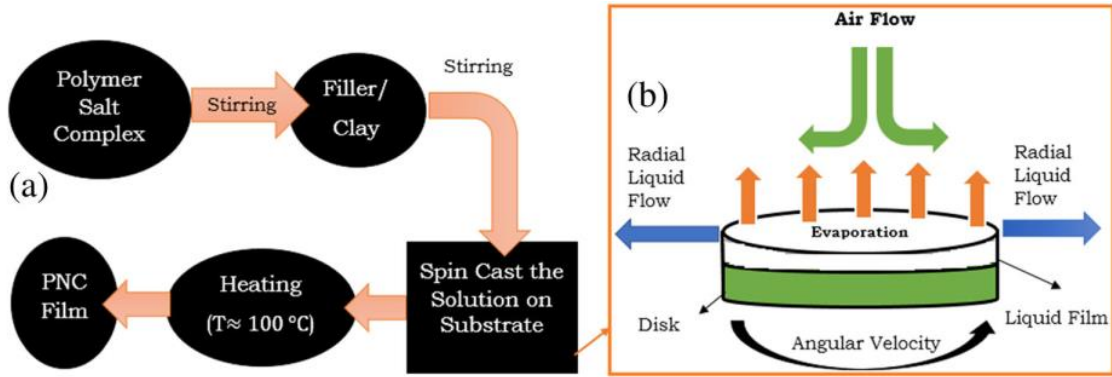
The composite preparation methods are generally similar to those for pure dense polymeric membranes. The only thing is that one should ensure the fabrication conditions and environment do not cause degradation of the filler. The main fabrication methods of the composite membranes are: 1) **solution casting/tape-casting**; 2) **spin coating**; 3) **dip coating**; 4) **hot press**; 5) **melt intercalation**.

One of the most simple and affordable, but, at the same time, effective, is the **solution casting** method:



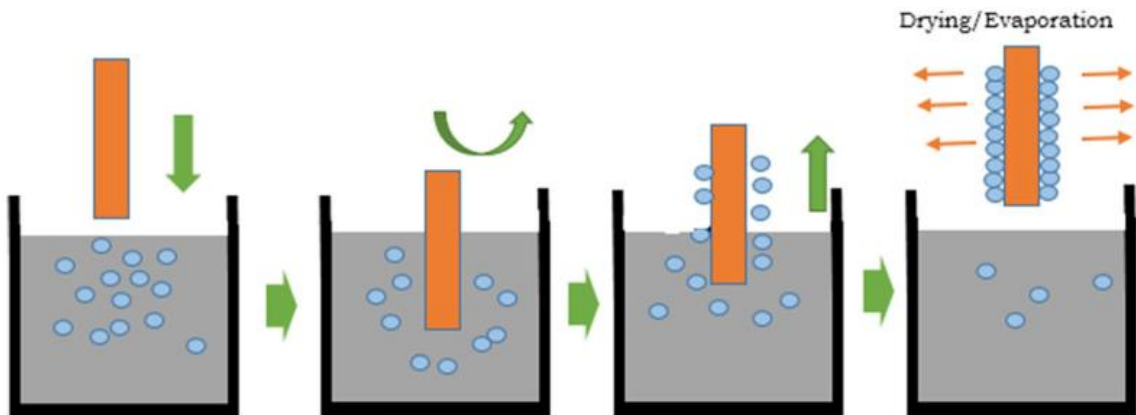
First, a polymer is dissolved in a solvent by stirring. Then, the calculated amount of salt and filler is added, and, after the suspension obtained, is intensively stirred for several hours. After that, the slurry is casted on glass or Teflon surface (often a Petri dish). In the **tape-casting** method, the stirred solution instead of pouring on the dish is transferred to a pre-heated substrate and casted by a slowly moving tape blade. Finally, the samples are left for evaporation either in air or under vacuum. This method is good to produce dense polymer-based films of various thicknesses (50–300  $\mu\text{m}$ ) with incorporated filler particles and alkaline salts. Temperatures at different fabrication stages, casting atmosphere, taping speed, etc. can significantly affect the composite's microstructure including porosity. The tape-casting method is widely used to fabricate composite membranes for ASSBs [99,130,144].

In **spin coating**, the slurry preparation is proceeded similarly as in the casting methods:



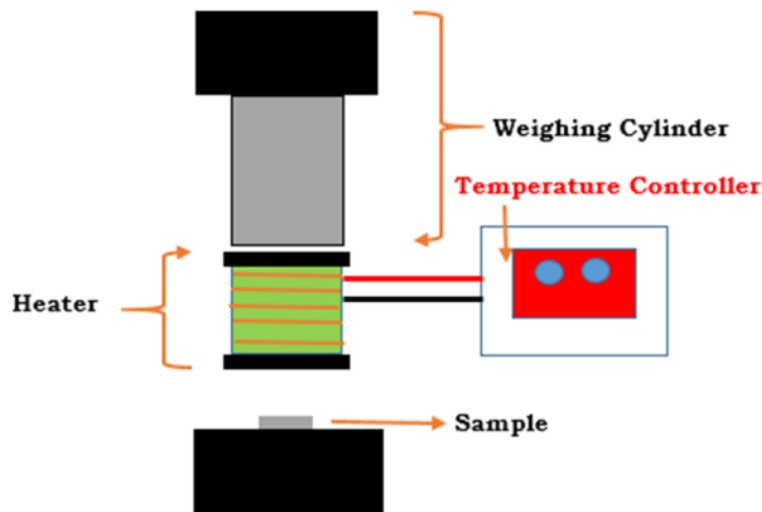
However, instead of casting, the mixture fixed on the substrate is placed into a spin coater. During the coater rotation, centripetal acceleration distributes the solution upon the substrate. After that, heat is supplied for the solvent evaporation. The spin coating allows obtaining membranes of 10 nm–10  $\mu\text{m}$  from the low-viscous solutions. Rotation speed, spin time, and surface tension can be tuned to fabricate the membrane with desired thickness and other qualities [145].

The **dip coating** process is usually performed in three steps:



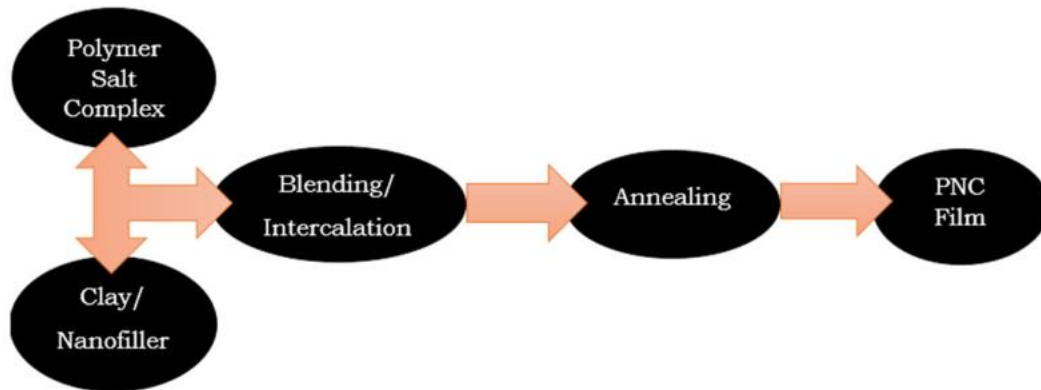
First, a special substrate is immersed into the solution — a precursor of the coating material. After a certain time, the substrate is pulled up slowly at a constant speed allowing a slurry residue to drain down leaving a thin film on the substrate surface. The thickness of the film can be tuned by varying precursor mixture density and the pulling speed [146].

The **hot press** set-up is composed of a weighing cylinder, heating chamber, and temperature controller:



The preliminarily mixed and grounded solid components (filler, polymer, salt) is firstly heated in the chamber to temperature close to the polymer's melting point. Then, the mixture is pressed by the weighing cylinder at constant pressure. The hot press method is quite promising especially for the preparation of dense multi-component membranes. Besides, it is low-cost and fast and requires no solvent [147].

Another non-solvent fabrication technique is **melt intercalation**:



First, the polymer matrix is annealed and, after the filler addition, the mixture is kneaded. After some time, the system is cooled. On one hand, the melt intercalation method is simple, cheap, and environmentally benign. On the other hand, high melting temperatures can harm the ceramic filler altering its structure and reducing its functional features (e.g., IC) [148].

Overall, the membrane fabrication methods described above are relatively cheap and simple. Among the others, the tape-casting method does not require high temperatures (compared to the hot press and melt intercalation) or complex instruments (spin coating) and allows to vary a number of parameters to improve the membrane's final properties. Porosity, one of these qualities touched in Section 1.3.3, is an extremely important parameter that influences the durability of RFBs determining its capacity retention [50,62].

#### *1.4.4. Membranes Porosity and the Ways of Its Suppression*

We have already discussed the features impacting composite membrane's IC and stability, but not permeability. The main membrane-related factor determining the

permeability is its open porosity. As it goes from Section 1.4.1.1, when one synthesizes the polymeric membranes for NAqRFBs from oligomeric precursors, the porosity can be tuned by means of a molecular design — as a result of choice of the specific polymer, crosslinking agent, plasticizer, etc. In the case of a ready polymer supplied in a powder form (PEO, PVdF, etc.), the desired porosity is regulated through the membrane fabrication conditions. In this section, we are going to discuss some membrane preparation factors that can potentially influence its porosity.

A temperature regime is among the most influential fabrication factors that can determine the polymer integrity. For instance, Li et al. investigated the impact of **substrate temperature** and ambient humidity during fabrication on PVdF's microstructure and roughness by SEM [149]. It was found that high humidity and low substrate temperature promoted the globular microstructure of the PVdF membranes. At 0% or 100 °C (Figure 1.12a,b), one can observe a smooth and dense polymer surface with no globules. Herewith, PVdF prepared at high humidity had a cloudy appearance (Figure 1.12c,d) that correlates with their morphological properties. Rinaldo investigated the correlation between PVdF membrane's casting temperature and a dominant phase of the final sample [150]. The author proved that temperatures below 70 °C result in the  $\beta$ -phase of PVdF, while at  $T > 110$  °C the  $\alpha$ -phase prevails. Based on these results, one can link the PVdF's globularity with the dominant phase — by means of the  $\alpha$  phase, the elevated casting temperatures may provide low porosity and better PVdF's density and microstructure.

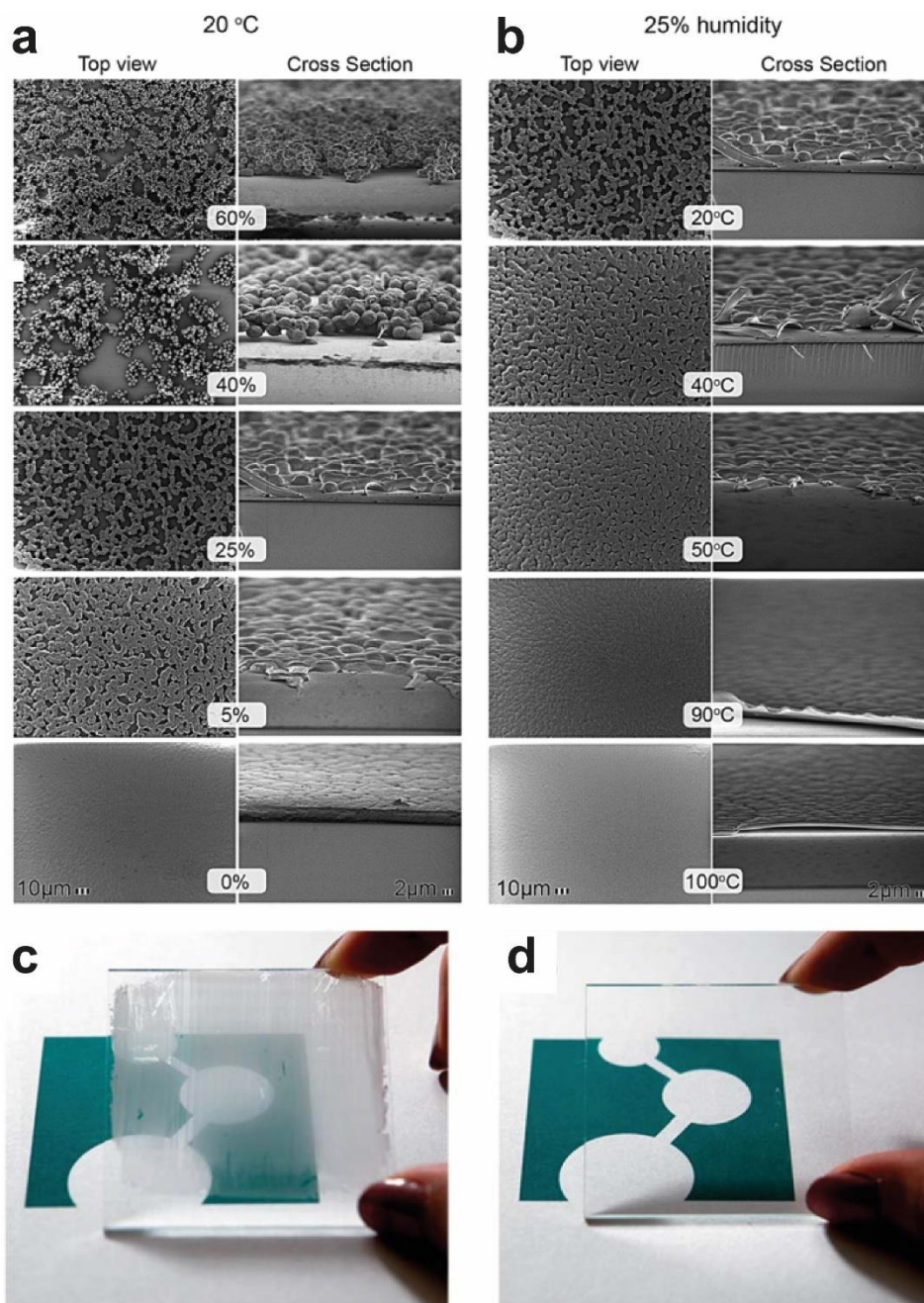


Figure 1.12. Top and cross-section views of PVdF's microstructure at different (a) relative humidity and (b) substrate temperatures. Optical properties of the PVdF films (1  $\mu\text{m}$ ) fabricated at (c) 60% and (d) 0% relative humidity [149].

Although there are a number of reports on the effect of substrate/casting temperature, nothing was published regarding the **mixing temperature** impact on PVdF microstructure during its dissolution in a solvent and subsequent homogenizing of the filler-polymer-solvent solution. However, the mixing during tape-casting usually lasts for 1-24 h — sufficient time for the components to alter their properties.

The choice of a **solvent** used during polymer dissolving is also important. The solvent affects not only a surface morphology [151], but also a polymer's internal microstructure [152]. Both characteristics can potentially influence the membrane's porosity and, hence, permeability. As was thoroughly discussed in the previous sections, permeability plays a key role defining RFB's capacity decay and cycle life.

The **filler**'s size, shape, and distribution in the polymer matrix were proved to influence the final composite's properties [144]. A size of filler particles and of their agglomerates may break polymer chains and increase a number of interceramic voids — the both can lead to the membrane's permeability enhance. Due to the lack of investigations devoted to the polymer-ceramic (filler-matrix) membranes for RFBs, there is no exact data on how the filler-related parameters correlate with the permeability. Hence, the composite's fabrication parameters (e.g., mixing temperature, casting temperature, casting solvent, filler distribution, drying conditions, components ratios, etc.) and their direct impact on membrane's functional properties should be thoroughly evaluated prior to membrane introduction into the NAqRFB prototypes.

## 1.5. Characterization Techniques: RFB Prototype and Membrane Performance Metrics

In order to prototype RFB with high performance, a series of characterization procedures are required throughout the whole development route. While there is a number of RFB *in-situ* and *ex-situ* diagnostics [48], in this chapter, we focus on the key role of materials that determine electrochemical processes: (i) redox active species, (ii) supporting electrolyte (SE), and (iii) membrane.

If new *redox active species* have been synthesized, one should firstly evaluate its chemical formula and structure to know molecular weight and estimate material's theoretical capacity. For this purpose, a complex of physico-chemical methods can be utilized, including XRD and electron microscopies (SEM or TEM) coupled with EDX; atomic absorption, atomic emission, FTIR, Raman, and nuclear magnetic resonance spectroscopies; etc. [48,153]. Then, thermodynamic and kinetic parameters of the species-involved redox reactions should be studied using CV, EIS, and other electrochemical techniques. Results would provide preliminary cell's redox potential, reaction's rate constant, diffusion coefficient, and limiting current values. After these essential data are collected and analyzed, the species structure or composition can be tuned if some of the measured parameters do not meet the target values of a desired prototype.

*SE*, in which redox mediators are dissolved and pumped through the cell, contributes to species' solubility, TCR, battery's durability, and power output. The electrolyte's resistance often correlates with its viscosity, so the dependence can be

evaluated through the screening of solvents and salts, as well as variation of a salt concentration [154]. High current densities and volumetric capacity (achieved by low SE resistance and high mediator's concentration, respectively) enhance final energy and power densities of RFB. Therefore, studying SE should definitely comprise the redox species solubility, viscosity, and IC evaluation.

The *membrane* is responsible for many RFB characteristic, e.g., TCR, cyclability, capacity retention, and price. Separating anode and cathode compartments, a membrane is not only responsible for the charge balance: the functional and mechanical stability of a solid electrolyte itself becomes the stability of the whole RFB system. Hence, we devote a little more attention to the membrane analysis. To probe the membrane's **thermal stability** and phases behavior TGA and DSC should be applied. Analyzing the heat absorption peaks, one can probe composite's components (filler, salt) interaction with the polymer [155]. **Mechanical properties** evaluation is needed to optimize the membrane's general integrity and evaluate its suitability for RFBs. Calculated Young's modulus and stress-strain tests report membrane's reliability revealing impacts of component interfaces, plasticizer's effects, and fillers [156,157].

XRD analysis is a powerful and essential non-destructive tool for crystalline and amorphous **phase** identification. Besides the polymer's phase composition, the extent of salt dissociation in the polymer matrix can be examined with XRD [158,159]. Moreover, the inorganic filler crystal structure can be solved within the composite membrane to reveal, if there are changes occurred after fabrication or other non-destructive tests.

Electron microscopies (SEM, TEM) provide a deep insight into the sample's **microstructure and morphology** by both plane and cross-section imaging. Importantly, they can reveal an extent of polymer's globularity (the plane mode) as well as ceramic agglomerates (cross-section mode). FTIR and Raman spectroscopy can show composite's **constituent groups** and hint on the **nature of interactions** between the composite's components [160]. There are other techniques to support the membrane's structural and morphological qualities such as atomic force microscopy, EDX, etc.

The membrane's IC, permeability, stability, and the associated metrics are evaluated through electrochemical methods (Table 1.9). EIS allows revealing impacts of each system's component and interface, though it is not always trivial or possible in a certain case. Decoding membrane's impedance spectra is a comprehensive task requiring much experience [161–164]. **IC**, one of the most important parameters, can be calculated relying on either a particular intercept of a Nyquist plot with the real impedance axis or a sum of several resistances estimated the same way (e.g., ceramic's bulk and grain boundaries; Figure 1.13a). Besides, EIS can probe **interfaces stability** between membrane and liquid electrolyte, Li-metal electrode and liquid electrolyte (SEI), etc. (Figure 1.13b) [124,165–167]. Other extractable parameters are **activation energy** (defines the temperature dependence of IC) and lithium **transference number**. The latter describes the  $\text{Li}^+$  share among all the charged particles (electrons, counter-ions) involved in the conductivity.

Table 1.9. Performance metrics and parameters important for RFB membranes.

Parameter	Unit	Formula	Notation description
Ionic conductivity, $\sigma$	$S\ cm^{-1}$	$\sigma = \frac{l}{R \cdot A}$	$R$ – membrane's resistance; $l$ and $A$ – membrane's thickness ( $cm$ ) and area ( $cm^2$ ), respectively
Activation energy, $E_a$	$\frac{kJ}{mol}$	$\sigma_T = \sigma_0 \exp\left(\frac{E_a}{RT}\right)$	$\sigma_T$ – membrane's ionic conductivity at temperature $T$ ; $\sigma_0$ – pre-exponential constant
Lithium transference number, $t_{Li^+}$	–	$t_{Li^+} = \frac{I_s(V - I_0R_0)}{I_0(V - I_sR_s)}$	$V$ – polarization voltage; $I_s$ and $I_0$ – current (A) before and after polarization, respectively; $R_s$ and $R_0$ – initial and steady-state resistance ( $\Omega$ )
Permeability coefficient, $P_i$	$\frac{cm^2}{min}$	$\tilde{V} \frac{dC_t}{dt} = P_i \frac{A}{l} (C_0 - C_t)$	$C_t$ – concentration (M) of active species in analyzing half-cell of volume $\tilde{V}$ (mL) at time $t$ (s); $C_0$ – initial active species concentration in another half-cell
Ionic selectivity, $IS$	–	$IS = \frac{P_s}{P_a}$	$P_s$ and $P_a$ – permeability coefficients of SE cation and active species, respectively
Swelling ratio, $SW$	%	$SW = \frac{l_w - l_d}{l_w} \cdot 100\%$	$l_w$ and $l_d$ – membrane's thickness in the soaked and dry state
Porosity, $\varepsilon$	%	$\varepsilon = 1 - \frac{m_d}{\rho_m A l} \cdot 100\%$	$\rho_m$ – true density ( $g\ mL^{-1}$ )

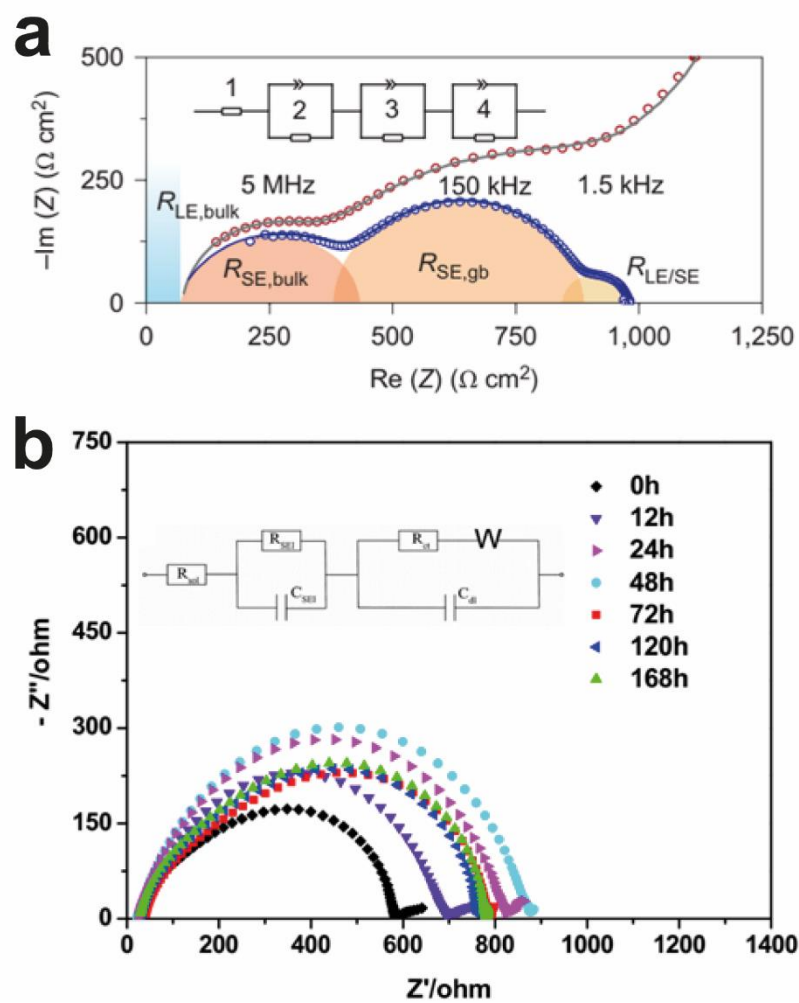


Figure 1.13. (a) Impedance spectrum measured with Au electrodes describing LAGP ceramic soaked in 1 M LiTFSI in DOL:DME; resistances:  $R_{LE,bulk}$  — liquid electrolyte,  $R_{SE,bulk}$  — bulk of ceramic,  $R_{SE,gb}$  — grain boundaries of ceramic,  $R_{LE/SE}$  — liquid electrolyte-ceramic interface. (b) Evolution of the SEI-related semicircle in Li|composite membrane|Li symmetric cell [143,167].

In order to evaluate the selectivity of ion transfer in a respect to redox moieties, the membrane's **permeability** to active species can be tracked [168,169]. Traditionally, the permeability coefficient (i.e., diffusion coefficient of transfer through the membrane) is measured using the two compartments cell: one of them is filled with active species dissolved in SE; the other one contains only SE; the membrane is placed in-between. The moieties transfer through the membrane is monitored by either CV or UV-Vis spectrometry. The redox species permeability can be related to that of SE ions (measured in a bulk solution) resulting in **ionic selectivity** (Table 1.9) [84]. Other membrane qualities, not electrochemical but linked with the permeability, are swelling ratio (electrolyte uptake) and porosity. The **swelling** represents the changes of polymer membrane's thickness after soaking in a liquid electrolyte. High swelling is undesired for RFB membranes, as thickness rise increases **pores** volume and, hence, permeability.

Membrane's **ESW** can be probed by linear sweep voltammetry, where the current response vs. voltage is monitored (Figure 1.14a). The potential region of stable and low current defines ESW. For analyzing membrane **stability to metallic Li**, required for Li-HFBs, charge/discharge cycling in the Li-symmetric cell should be performed. Uniform cycling curves with constant amplitude (Figure 1.14b) and no interruption report the stable interface formation with no short-circuiting due to the Li dendrite growth. Moreover, a good practice is to monitor the interfacial resistance changes after the cycling via EIS to semi-quantitatively illustrate their stability [124,165,166].

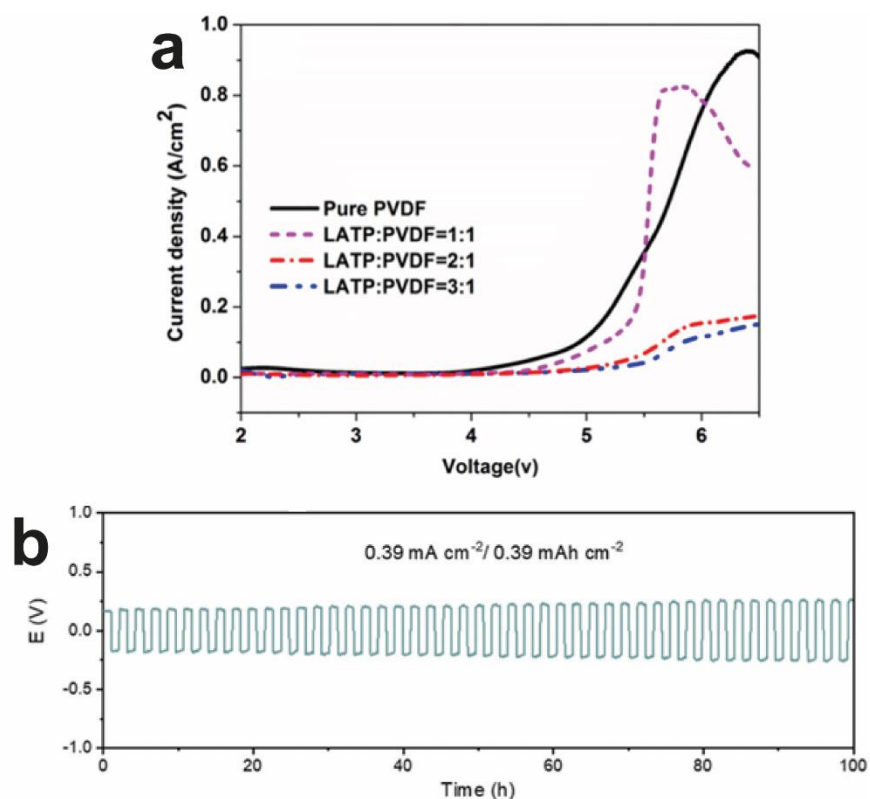


Figure 1.14. (a) Electrochemical stability window of different LATP-PVdF composite membranes. (b) Voltage profiles of membranes tested in the Li symmetric cell [124,143].

Once membrane characteristics are revealed and optimized, a cell with non-flowing electrolytes (static: coin or disassembling cell) can be assembled for a preliminary, proof-of-concept evaluation of the battery performance. First, TCR can be measured using EIS to investigate the total impact of all components and interfaces and estimate the applicable current. Then, galvanostatic cycling should be applied to evaluate cell characteristics (efficiency, initial capacity, its decay, etc.; Table 1.10) and track improvements made in materials, construction, or conditions design [170].

Table 1.10. Characteristic metrics of RFB performance that can be extracted from galvanostatic cycling analysis.

Parameter	Unit	Formula	Notation description
Theoretical capacity, $Q_{teor}$	$Ah$	$Q_{teor} = \frac{v_i n F}{3600}$	$v_i$ – amount of active component ( <i>mole</i> ); $n$ – number of electrons in redox reaction; $F$ – Faraday constant
Volumetric capacity, $Q_V$	$Ah L^{-1}$	$Q_V = \frac{Q}{\tilde{V}}$	$Q$ – charge amount ( $Ah$ ) stored in volume of $\tilde{V}$ ( $L$ )
State of charge, $SoC(t)$	%	$SoC(t) = \frac{q_{ch}(t)}{Q_{teor}} \cdot 100$	$q_{ch}(t)$ – charge stored in a battery at a certain time ( $Ah$ )
Capacity retention, $CR$	%	$CR = \frac{Q_{disch}}{Q_{teor}} \cdot 100$	$Q_{disch}$ – charge extracted during a battery discharge ( $Ah$ )
Capacity fade, $CF$	$\% cycle^{-1}$ $\% h^{-1}$	$CF = \frac{(100 - CR)}{N, t}$	$N$ – number of battery's charge/discharge cycles; $t$ – time of operation ( $h$ )
Current density, $i$	$mA cm^{-2}$	$i = \frac{I}{A}$	$I$ – applied current ( $mA$ ); $A$ – membrane's geometric area ( $cm^2$ )
Energy density, $\tilde{E}_V$	$Wh L^{-1}$	$\tilde{E}_V = \frac{Q \cdot \overline{V_{disch}}}{\tilde{V}}$	$\overline{V_{disch}}$ – an average cell potential during discharge ( $V$ )
Power density, $P$	$W cm^{-2}$	$P = i \cdot V_{cell}$	$V_{cell}$ – cell voltage ( $V$ ) measured at $SoC = 50\%$

Coulombic efficiency, $CE$	%	$CE = \frac{Q_{disch}}{Q_{ch}} \cdot 100$	$Q_{ch}, Q_{disch}$ – charge and discharge cell capacities (Ah)
Voltage efficiency, $VE$	%	$VE = \frac{\bar{V}_{disch}}{\bar{V}_{ch}} \cdot 100$	$\bar{V}_{ch}, \bar{V}_{disch}$ – average cell voltages during charge and discharge (V)
Energy efficiency, $EE$	%	$EE = \frac{CE \cdot VE}{100}$	

---

The most valuable metrics, especially for an early-stage RFB research, are capacity utilization (SoC), capacity retention, and efficiency (coulombic, volumetric, and energy) [48]. The galvanostatic cycling also provides a platform for the stability assessment of cell components [170–172] — the state of membrane, SE, and redox couples can be characterized by the techniques described above and compared with the pristine samples.

As long as the stability of the cell components is proved, an introduction of the flow system is expected for a deeper cell operation analysis. The points requiring additional optimization are electrolytes' flow rate and flow cell configuration. Their tuning should diminish TCR, which is frequently higher for the flow system than for the static. Indeed, the higher flow rates reduce the concentration polarization and enhance the convective mass transfer that lower TCR [173]. The cell optimization implies altering the thickness of carbon electrodes and membrane [173], specific Li anode design [70], etc. [174] — all of that can boost the applied current density and, hence, battery power.

## 1.6. Conclusions from Chapter 1

After thorough literature screening, here we are concluding on the main results made throughout this overview:

- 1) The use of conventional energy plants and the integration of renewable energy sources demand for efficient ESSs to mitigate production and consumption fluctuations; prevent economic, ecological, and social damages from energy overproduction; improve the overall energy distribution security.
- 2) Electrochemical devices are specifically prospective for ESSs due to their scalability and high energy efficiency. Moreover, the use of lithium ion as a charge carrier opens the platform for high-energy dense and high-power batteries due to the lightest weight and the lowest electrochemical potential of Li.
- 3) In spite of the advanced performance of the current LIBs, they have high energy-specific cost for stationary applications, suffer from the inflammation risk, and stress the environment. A prospective alternative to conventional LIBs is RFBs, which store a charge externally decoupling energy and power and providing better integrity to ESSs, durability, and safety. The main RFB's limitation is low energy density, far lower than that of LIBs. A promising solution is to combine a flow system with Li-metal anode that would boost cell voltage and bring Li-HFB's energy density closer to LIB's.
- 4) One of the main Li-HFB limitations is an absence of a membrane with suitable cell integrity, high IC and selectivity, and stability toward high potentials and Li-metal

anode. The ceramic-in-polymer composite approach in the membrane design, recently employed in ASSBs, can maintain ceramic's high IC by embedding its particles into the polymer matrix thereby protecting effective yet sensitive inorganic component from the destructing influence of ambient moisture, reactive metallic Li, and other factors. Among the whole diversity of materials, we emphasize the composite membranes based on highly conductive NASICON-type ceramic filler and stable PVdF polymer matrix. The tape-casting technique is chosen as an affordable, easy, and scalable composite membrane fabrication method.

- 5) In order to create a composite membrane suitable for Li-HFB, its functional features (IC, permeability, etc.) and stability (structural, chemical, electrochemical, and mechanical) should be assessed through solid instrumental and electrochemical analysis. This way, one can reveal the approaches for further optimization of a membrane prior to battery prototyping. After, Li-HFB cells can be assembled and tested leading to a final conclusion on the composite's compatibility with Li-HFBs.

### **1.7. Goal and Objectives of the Thesis**

The **goal** of the Thesis is to develop an ion-conductive, selective, and stable ceramic-in-polymer composite membrane for Li-metal hybrid flow batteries.

In order to accomplish this goal, a series of **objectives** were set:

- 1) To reveal the structure-property correlations for the  $\text{Li}_{1.3}\text{Al}_{0.3}\text{Ti}_{1.7}(\text{PO}_4)_3$  + poly(vinylidene fluoride) (LATP+PVdF) membranes; to estimate how the polymer's

morphology and phase, ceramic's structure, and other composite's features influence its main functional parameters: IC and permeability (selectivity to catholyte active species).

- 2) To optimize a membrane's *composition* and *fabrication conditions* to achieve the suitable structural and microstructural characteristics that would provide the composite with the best combination of the functional parameters.
- 3) To thoroughly evaluate the membrane's stability within the Li-HFB environment through comparing the composite's features before and after cycling in the hybrid battery cells.
- 4) To estimate the LATP+PVdF's applicability to the Li-HFBs by measuring performance of the Li-TEMPO hybrid cells (efficiency, durability, capacity) equipped with the developed and optimized membrane.
- 5) To summarize all the advances achieved during the composite membrane development and first attempts to prototype the Li-HFB equipped with LATP+PVdF; to discuss the explored hybrid cell's limitations and define the plan for the prototype next-stage optimization.

## Chapter 2. Experimental Details

In this chapter, we provide a description of all the experiments performed during the Thesis research. The description covers: synthesis of ceramic active filler, fabrication and properties optimization of the ceramic-in-polymer composite membranes, characterization of the studied membranes using physico-chemical and electrochemical techniques, and life tests of the fabricated membranes in NAq Li-TEMPO hybrid cells.

### 2.1. Synthesis of LATP Ceramic Filler

The two-step solid-state synthesis of the LATP ceramic filler was adopted from the routine designed in our research group by Pogosova et al [116,125,175]. The first step is responsible for the decomposition of precursors and launches NASICON phase formation. The second step completes the LATP phase formation and provides dense ceramic material.

First,  $\text{Al}_2\text{O}_3$  was prepared by calcining  $\text{Al}(\text{NO}_3)_3 \cdot 9\text{H}_2\text{O}$  ( $\geq 97\%$ , RusChem, Russia) at  $900\text{ }^\circ\text{C}$  for 2 h in a muffle furnace (Nabertherm L5/12/P330, Germany). Then, fresh  $\text{Al}_2\text{O}_3$  powder was cooled, ground, and mixed (Figure 2.1) stoichiometrically with  $\text{NH}_4\text{H}_2\text{PO}_4$  ( $\geq 98\%$ , Alfa Aesar, Japan),  $\text{TiO}_2$  ( $\geq 99.5\%$ , Sigma-Aldrich, Germany), and  $\text{Li}_2\text{CO}_3$  ( $\geq 99\%$ , Sigma-Aldrich, Chile), which was taken with the 5% excess to cover Li losses at high temperatures. The powders were milled manually in agate mortar with the addition of iso-propanol and calcined at  $750\text{ }^\circ\text{C}$  for 3 h (14 h ramp) in the muffle furnace being placed in an alumina crucible protected by the burnable separator. After sintering, a ceramic chunk was manually milled with iso-propanol and mixed with 5 wt.% solution of

polyethylene glycol (PEO,  $M_w \sim 1500$ , MO, USA) in iso-propanol during the subsequent additional milling procedure. The powder was then pressed (Carver 4350.L, IN, USA) into 0.5-g pellets, which were placed in an alumina crucible and annealed at 850 °C for 3 h (14 h ramp). Final pellets were air-quenched and thrown on the aluminum foil to complete and preserve the NASICON phase formation. The final  $\text{Li}_{1.3}\text{Al}_{0.3}\text{Ti}_{1.7}(\text{PO}_4)_3$  ceramics were further applied for the composite fabrication immediately or placed inside the Ar-filled glove box (*overall pressure* <0.4 mbar;  $c(\text{H}_2\text{O})$ ,  $c(\text{O}_2)$ , and  $c(\text{CO}_2)$  <10 ppm; MBraun, Garching bei München, Germany) and sealed in a pouch for delayed use.

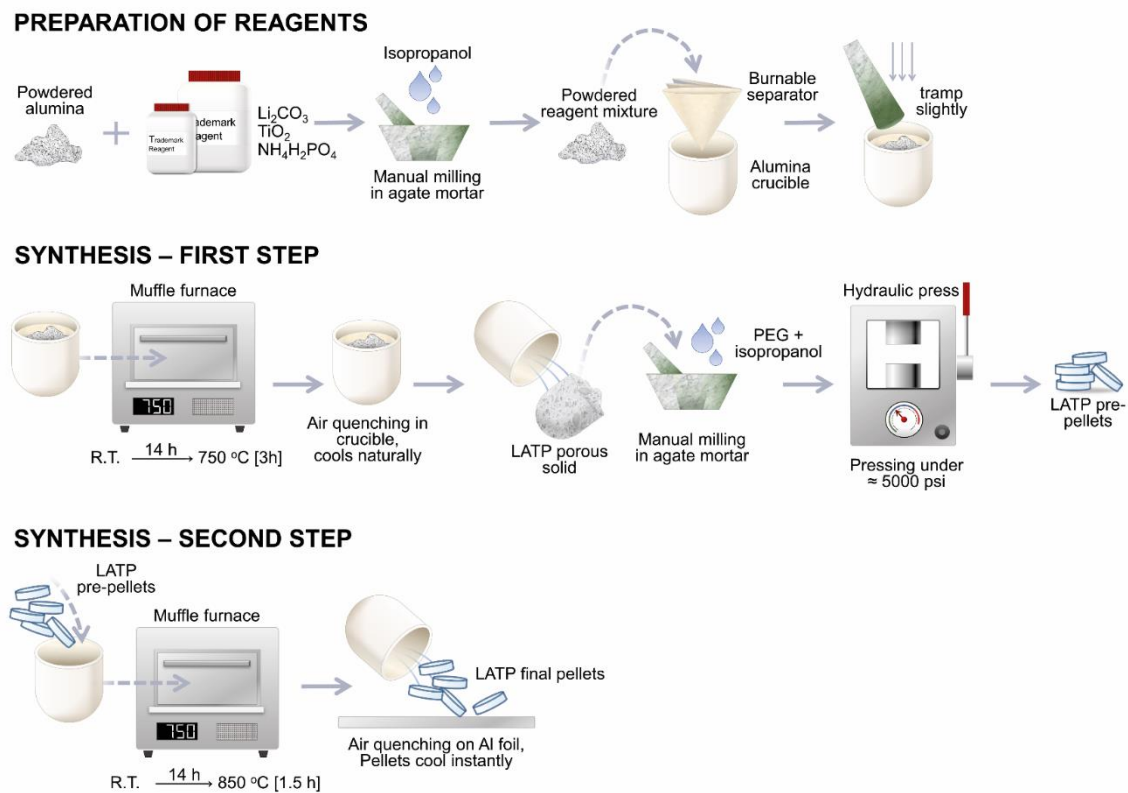


Figure 2.1. A two-step solid-state synthesis of LATP ceramic material [47].

## 2.2. Fabrication of Composite Membranes

The composite membrane fabrication routine consists of many steps and includes a large set of parameters related to materials used and procedures applied. Yet, unfortunately, there are little-to-no comprehensive studies that would evaluate the actual impact of these parameters on the final performance of a membrane and what parameters can be considered optimal for a particular system. Therefore, to obtain the most suitable morphological and functional features of the ceramic-in-polymer membrane, we thoroughly investigated and optimized a large number of fabrication-related parameters. For convenience, below they are underlined and summarized in Table 2.1. The varied parameters were divided into the membrane composition- and fabrication condition-related subgroups.

The membrane fabrication is initiated with the LATP filler treatment: manual grinding of the as-synthesized or freshly unsealed 0.5-g ceramic pellet in the agate mortar with the following intense ball-milling in the high-energy shaker (SPEX 8000, NJ, USA) for 90 min. The membranes were fabricated via the tape-casting method using LATP, LiClO<sub>4</sub> (>99.99%, Sigma-Aldrich, USA), and PVdF (M<sub>w</sub> ~534,000, Sigma-Aldrich, France) dissolved in a solvent: DMF (≥99.8%, RusChem, Russia), DMSO (≥99.7%, Acros Organics, NJ, USA), or NMP (≥99.5%, Acros Organics, NJ, USA), all dried with 3 Å sieves until  $c(\text{H}_2\text{O}) < 25$  ppm. The components were mixed in a vial in the following ratios:

- salt-to-(ceramic+polymer) — 0, 7.5 wt.%;
- polymer-to-solvent — 8–20 wt.%;
- ceramic-to-polymer — 0–60 wt.%.

Table 2.1. Summary of the optimizing parameters for composite membranes.

Optimizing parameter	Variation range	Starting point
<u>Membrane composition</u>		
Casting solvent	DMF, DMSO, NMP	DMF
Salt-(ceramic+polymer) ratio	0, 7.5 wt. %	0 wt. %
Polymer-solvent ratio	8–20 wt. %	15 wt. %
Ceramic-polymer ratio	0–60 wt. %	45 wt. %
<u>Fabrication condition</u>		
Components mixing temperature ( $T_{\text{mix}}$ )	25–130 °C	50
Solution casting temperature ( $T_{\text{sub}}$ )	70–150 °C	70
Samples drying temperature ( $T_{\text{dry}}$ )	25–130 °C	90
Samples drying atmosphere	Dynamic vacuum; atmospheric pressure	Atmospheric pressure
Components mixing protocol	A; B; C; D	A

Commonly (except for several samples studied in the components mixing protocols part, Section 3.2.4), PVdF was firstly dissolved mixing at 400 rpm for 0.5 h at the temperature ( $T_{\text{mix}}$ ) of 25–130 °C. Then, the rest composite components were added into the vial. The composite mixture was intensively stirred at 1400 rpm for 4 h with subsequent storing still for 20 h at RT for degassing. After that, the slurry was poured onto the specifically treated glass substrate. The treatment consistently includes: i) washing the

glass with acetone; ii) drying the substrate with argon flow; iii) quenching the glass with air plasma at 0.2-0.3 atm. Such procedure improves the substrate's adhesion with the polymer solution by removing the organic contaminants and activating its surface. The polymer slurry was then plated using the film applicator (Zehntner ZAA 2300, Switzerland) with the blade moved at  $15 \text{ mm s}^{-1}$  and the substrate temperature ( $T_{\text{sub}}$ ) of 70–150 °C. Finally, the samples were dried for 1 h at the drying temperature ( $T_{\text{dry}}$ ) of 25–130 °C under various ambient pressure: atmospheric or dynamic vacuum.

In Section 3.2.4, we will discuss how the components mixing approaches affect the LATP particles distribution in the composite membrane. In that experiment, we examined the composites prepared via four different mixing protocols (denoted as *Sample A–D*):

- *Sample A*, the composite is fabricated as described above;
- *Sample B*, a solvent was mixed with LATP powder to follow the DMF:LATP mass ratio of 7:1. Immediately, a proper fraction of PVdF was added to the DMF-LATP suspension under intensive stirring. The composite membrane was then processed as Sample A;
- *Sample C*, the calculated amount of LATP suspended in 1 mL of the solvent was added to PVdF dissolved in 2 mL of the same solvent under intensive stirring. The composite membrane was then processed as Sample A;
- *Sample D*, the solvent-LATP suspension was prepared as described for Sample B but with additional sonication using the VCX 130 ultrasonic processor (Sonics & Materials, CT, USA) at 20% maximum power. Then, PVdF was added and the

composite membrane was processed as Sample A. This fabrication route is illustrated in Figure 2.2.

In the next parts of the Thesis (Chapter 3, Chapter 4), unless otherwise stated, the composite membrane parameters were set according to the “starting points” from Table 2.1.

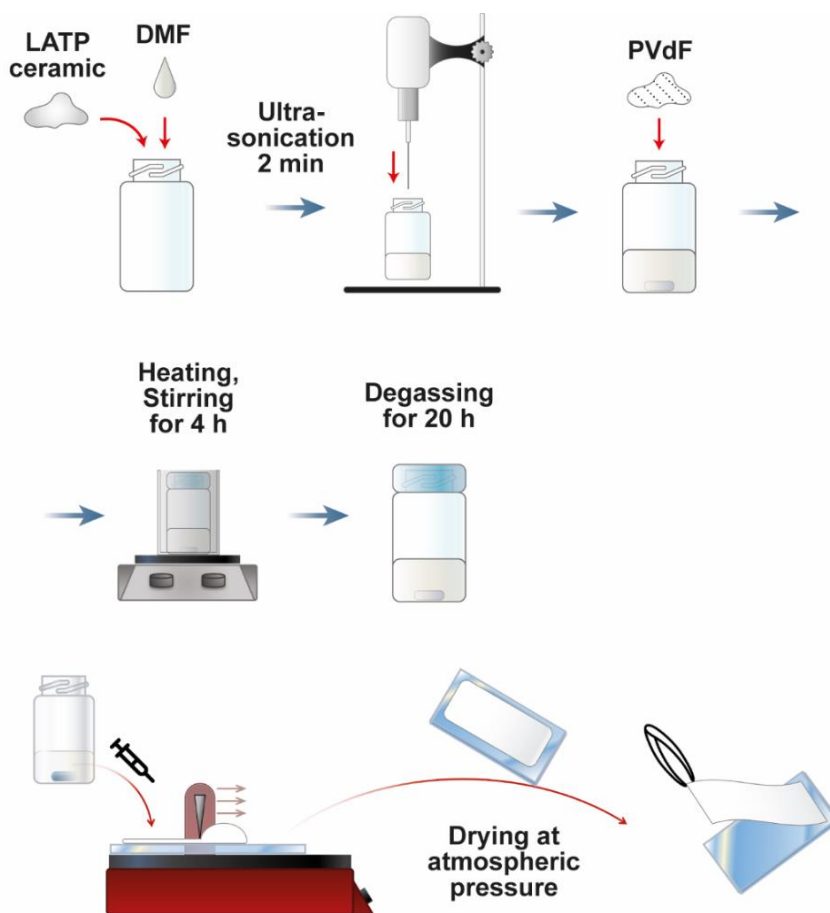


Figure 2.2. Fabrication scheme for L ATP+PVdF composite membrane prepared via the mixing protocol for *Sample D*.

### 2.3. Characterization of Composite Membranes

In this work, the membranes were investigated via a set of physicochemical and electrochemical techniques. Characterization was carried out to aim one of the following tasks:

- reveal the effect of a particular fabrication parameter and determine its optimal value;
- study the retention of a specific property after a separate process, treatment, or analysis (e.g., membrane fabrication or galvanostatic cycling in a hybrid cell).

#### 2.3.1. Physicochemical Characterization

**SEM** and **EDX** of the composite membranes and their components were performed using FEI Quattro S microscope (Thermo Fisher Scientific, MA, USA) using a low-vacuum detector to suppress artifacts due to sample charging. The acceleration voltage of 2 kV and the beam current of 0.11 nA provided sufficient lateral resolution. SEM of some polymer membrane samples was carried out using the Jeol JCM 6000 (Japan) desktop device at acceleration voltages of 10 kV. Formula units  $n_i^{unit}$  of the elements of LATP ceramic was refined according to Equation 2.1:

$$(2.1) \quad n_i^{unit} = \frac{5 \cdot C_i^{at.\%}}{\sum_i C_i^{at.\%}},$$

where  $C_i^{at.\%}$  represents the atomic percentage of the  $i$  element and “5” is a sum of theoretical units of Al, Ti, and P elements in the LATP formula (0.3+1.7+3=5).

The membrane samples for **TEM** were prepared by the focused ion beam technique using FEI Helios Xe plasma FIB (Thermo Fisher Scientific). The thickness of obtained

samples was around 100 nm. After preparation, the samples were placed into the FEI Titan Themis Z (Thermo Fisher Scientific) transmission electron microscope equipped by Super X quadrupole EDX detector. EDX mapping was performed at accelerating voltage of 200 kV and quantified in a standard way by subtracting a background.

The **XRD** patterns were registered using the Bruker D8 Advance, MA, USA (Bragg-Brentano geometry; CuK $\alpha_{1,2}$  radiation, Ni filter, circular polarization; LynXeye XE detector; 2.5 ° soller slits; 1 mm fixed divergence slit; 30 ° min<sup>-1</sup> sample holder rotation; 2 $\theta$  range from 10 ° to 120 ° for LATP ceramics and from 10 ° to 80 ° for LATP+PVdF composite membranes; 2 $\theta$  step = 0.01 °; ambient conditions, RT). Crystal structure of the obtained compounds was refined by the Rietveld method in the R3 $\bar{c}$  space group using the JANA 2006 software [176]. Two specific LeBail refinement settings — zero shift and asymmetry factors — were established by the registration, profile and structural analysis of Al<sub>2</sub>O<sub>3</sub> NIST 676a standard as described in [116]. In total, the refinement settings were as follows: background — manual in combination with the Chebyshev polynomial with 5 variables; unit cell dimensions *a* and *c*; profile — Pseudo-Voigt peak-shape function with *GW*, *LY*, anisotropic strain broadening — tensor approach accompanied by a Marquart technique mode with 0.001 Fudge factor; zero-shift (values of the alumina standard were input and fixed); vertical shift — *Sycos*; asymmetry — by divergence with HpS/L (values of the alumina NIST standard were input and fixed); Roughness — *rough1* by Pitschke, Hermann, and Matter approach. The vertical shift correction *Sycos* was involved in the general refinement to take the sample preparation features into account: the

thin layer of powder or a composite membrane sample were placed on the sample holder's flat side with no strict height control provided. The structure refinement parameters were as follows: initial atomic positions of Al, Ti, P, and O were set in accordance with neutron diffraction data presented in Ref. [177]; Al and Ti shared a joint position; Li positions were fixed); thermal displacement parameters —  $U$ , harmonic anisotropic approximation for Al and Ti, isotropic approximation for P, O, and Li (fixed for the latter one on the 0.01 value). Taking into account the XRD limitations related to the low Al concentration, similar Al<sup>3+</sup> and Ti<sup>4+</sup> electron density, and low Li<sup>+</sup> electron density, we kept the ionic occupancies fixed for all elements. The PVdF phase observed in LATP+PVdF samples was not included in refinement as a separate phase and was later qualitatively assigned in accordance with the peak positions. Selected refined structures were submitted to the CCDC database in .cif form. These XRD patterns can be found in Appendix B. XRD Refinement.

The attenuated total reflectance **FTIR** measurements were carried out using the Bruker Alpha II (MA, USA) spectrometer equipped with a diamond crystal and a KBr beamsplitter. Data were collected in the 4000–400 cm<sup>-1</sup> range within the 4 cm<sup>-1</sup> resolution and signal averaging by 20 scans.

The **Raman** spectroscopy measurements were carried out using the DXRxi Raman Imaging Microscope (Thermo Fisher Scientific) with 532-nm laser excitation. Settings of laser power, the number of counts, and exposure time were varied to overcome the signal-to-noise ratio of 50 for each particular sample.

The membrane's **swelling ratio** and **porosity** were estimated by the wet method. The membranes were soaked in PC (with the density of  $\rho_{solv}$ ) for 18 h and then their wet thickness and mass were checked ( $l_w$  and  $m_w$ ). After, the samples were placed in an oven and dried at 60 °C for 18 h followed by the thickness and mass recheck ( $l_d$  and  $m_d$ ). Membrane's swelling ratio ( $SW$ ) and porosity ( $\varepsilon$ ) were calculated using Equations 2.2, 2.3:

$$(2.2) \quad SW = \frac{l_w - l_d}{l_w} \cdot 100\%,$$

$$(2.3) \quad \varepsilon = \frac{m_w - m_d}{\rho_{solv} \cdot A \cdot l_d} \cdot 100\%.$$

Polymer-solvent solution **viscosity** was measured using the electromagnetically spinning viscometer (EMS-1000, Kyoto Electronics, Japan) at RT.

### 2.3.2. Electrochemical Characterization

To evaluate membrane's ESW, **LSV** was performed using coin cells (CR-2032) with lithium metal counter electrode and SS working electrode in the voltage range of 2–6 V and 0.6 mV s<sup>-1</sup> scan rate. The measurements were performed using the Autolab PGSTAT302N (Metrohm AG, Barendrecht, Netherlands) galvanostat-potentiostat.

In **chronoamperometry**, the membrane was stacked between either copper electrodes of the custom-made electrochemical cell (for electronic conductivity evaluation, Figure 2.3) or lithium electrodes in a coin cell (for Li<sup>+</sup> transference number calculation); voltage were 0.5 V and 0.03 V, respectively, with the application time of 9000 s. The measurements were carried out via the Autolab galvanostat-potentiostat.

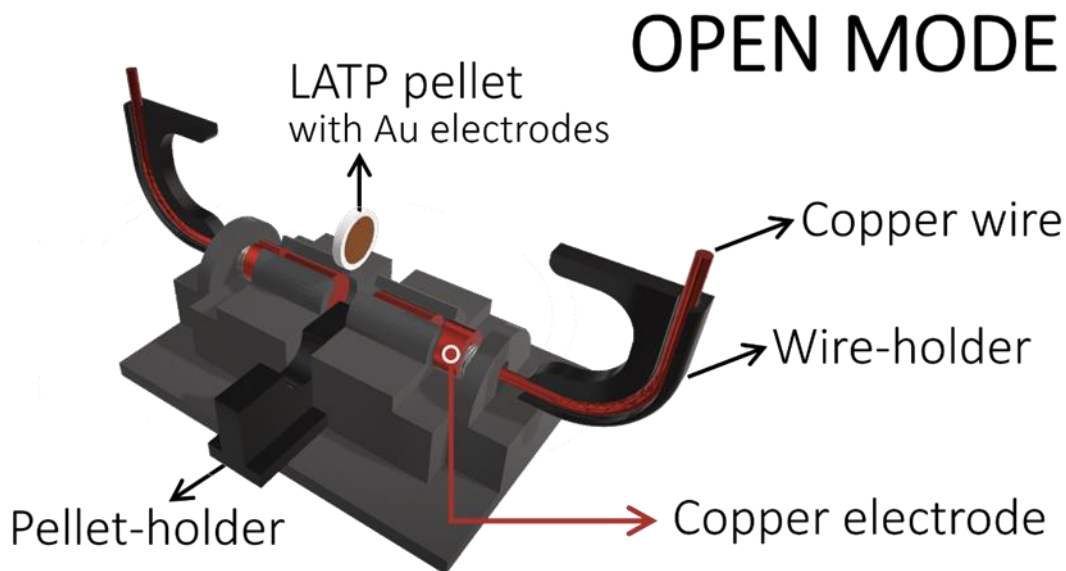


Figure 2.3. Scheme of the electrochemical cell developed in our research group used for LSV, chronoamperometry, and EIS analysis [175].

Electronic conductivity ( $\sigma_e$ ) of the membranes was calculated according to Equation 2.4:

$$(2.4) \quad \sigma_e = \frac{I_S \cdot l}{V \cdot A},$$

where  $I_S$  corresponds to the steady-state current achieved during chronoamperometry;  $V$  is the applied voltage;  $l$  and  $A$  are the membrane's thickness and area, respectively.

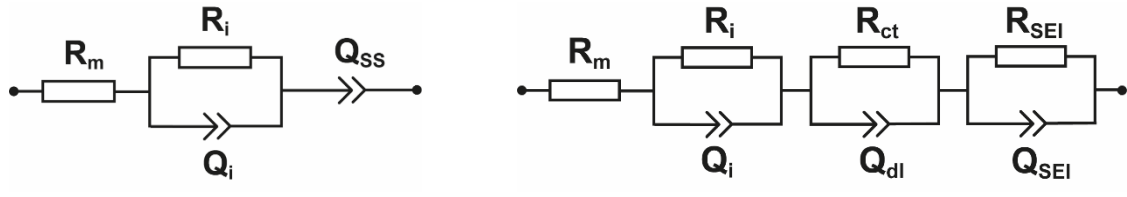
**EIS** analysis was performed in the 1 MHz–0.1 Hz frequency range with the 10-mV amplitude via the Autolab galvanostat-potentiostat. Spectra for each sample were recorded five times for better statistics and error evaluation. The mean square root approximations were performed within the Metrohm Autolab NOVA software. A Kramers–Kronig

relationship ( $\chi^2 \sim 10^{-8}$ – $10^{-6}$ ) was used to determine quality of obtained data. Sample's IC ( $\sigma_i$ ) was calculated in accordance with Equation 2.5:

$$(2.5) \quad \sigma_i = \frac{l}{R_m \cdot A},$$

where  $R_m$  is the resistance of the tested composite membrane.

The fabricated membranes were analyzed in coin cells assembled inside the Ar-filled glove box. In advance, the studied membranes were soaked in 1.0 M LiClO<sub>4</sub> in PC (Sigma-Aldrich, Budapest, Hungary; dried with 3 Å sieves until  $c(\text{H}_2\text{O})$  below 10 ppm) for 18 h. In IC measurements, symmetric coin cells were equipped with SS electrodes. The equivalent circuit used for fitting Nyquist plots of SS|membrane|SS and Li|membrane|Li cells are correspondingly illustrated below:



where  $R_m$  represents resistance of a membrane soaked in SE;  $R_i$  and  $Q_i$  are resistance and CPE related to a membrane-SE interface;  $R_{ct}$  and  $Q_{dl}$  are related to charge transfer resistance and double layer CPE;  $R_{SEI}$  and  $Q_{SEI}$  are related to a Li anode-SE interface. The CPE ( $Q$ ) instead of a capacitor was used for a more precise fit of experimental data.

Capacity ( $C$ ) of CPE was calculated via Equation 2.6:

$$(2.6) \quad C = R^{1/n-1} \cdot Q^{1/n},$$

where  $n$  is an exponent parameter.

Critical EIS data (Nyquist plots and parameters' values) are presented in Appendix C. EIS Fitting Data.

**Lithium transference number** ( $t_{Li^+}$ ) was calculated using the Bruce-Vincent methodology [178] (Equation 2.7). In this measurement, at first EIS is performed to define initial SEI resistance ( $R_0$ ). After that, the chronoamperometry was carried out until the current achieves a steady state (from  $I_0$  to  $I_s$ ). Finally, EIS was recorded to observe the change of the SEI resistance ( $R_s$ ),

$$(2.7) \quad t_{Li^+} = \frac{I_s(V - I_0 R_0)}{I_0(V - I_s R_s)}$$

**Galvanostatic stripping/plating** tests in a couple with EIS were performed to evaluate membrane's stability to metallic lithium. For this purpose, the symmetric coin cells, assembled with soaked membranes and Li electrodes, were cycled using the Biologic battery test system (France) at  $0.1 \text{ mA cm}^{-2}$ . EIS tests were carried out before and after the cycling in order to, relying on resistances behavior, estimate the interfaces degradation in a semi-quantitative manner.

**Permeability** of the membranes to TEMPO (98%, Sigma Aldrich, Germany) was estimated by CV using the PalmSens4 galvanostat-potentiostat (GA Houten, Netherlands) following the method firstly described in Ref. [169]. The custom-made two-compartment diffusion cell (Figure 2.4) was equipped with working Pt electrode (1.6 mm diameter), 3-mm glassy-carbon counter electrode, and reference electrode composed of 0.5-mm Ag wire.

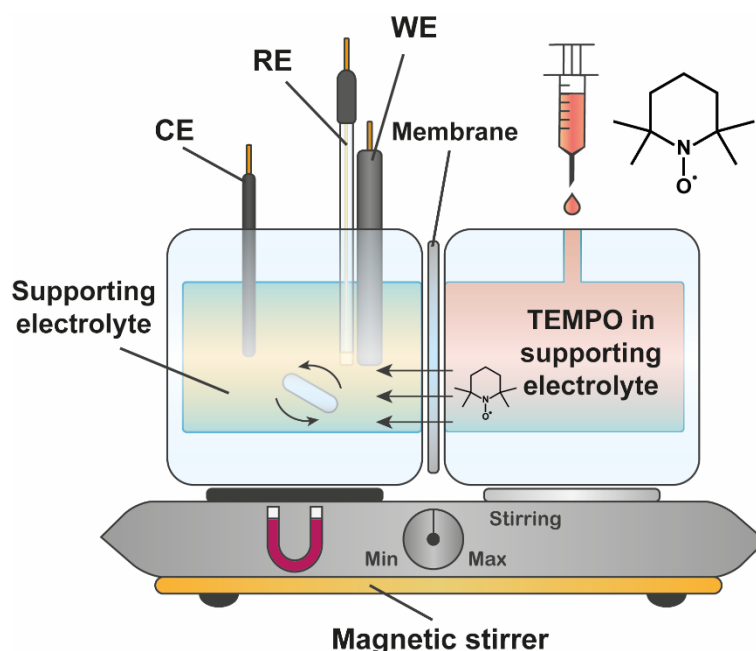


Figure 2.4. Scheme of the electrochemical cell for TEMPO permeability measurements;

CE, RE, and WE are counter, reference, and working electrodes, respectively.

The half-cell with the immersed electrodes was filled with pure SE, while another half-cell contained 0.5 M TEMPO in the same SE. The studied membrane was placed between the compartments and had an active area of *ca.* 0.785 cm<sup>2</sup>. 1.0 M LiClO<sub>4</sub> in PC was used as SE in all permeability tests. CV recording was carried out in the 0.0–0.8 V *vs.* Fc/Fc<sup>+</sup> potential range and 0.05 V s<sup>-1</sup> scan rate at RT. The obtained peak currents (*i<sub>p</sub>*) were recalculated to concentrations according to the Randles–Sevcik equation at RT (Equation 2.8):

$$(2.8) \quad i_p = 2.69 \cdot 10^5 n^{\frac{3}{2}} A D^{\frac{1}{2}} \nu^{\frac{1}{2}} C_l,$$

where  $n$  represents a number of electrons involved in the redox reaction;  $A$  is electrode area;  $D$  is the diffusion coefficient;  $v$  is the CV scan rate;  $C_l$  is the concentration of the analyzed redox active species (TEMPO).

We preliminary calibrated the peak currents using a series of TEMPO solutions with known concentrations. So, Equation 2.8 simplifies to 2.9:

$$(2.9) \quad i_p = KC_l,$$

where  $K$  is the calibration factor, constant at a certain electrolyte, cell configuration, and scan rate.

The rates of TEMPO diffusion from the right half-cell to the left (*permeability coefficients*) were calculated via the second Fick law adopted to the cylindrical cell geometry (Equation 2.10):

$$(2.10) \quad V \frac{dC_l(t)}{dt} = \frac{AP}{L} (C_r(t) - C_l(t)),$$

where  $V$  represents the volume of SE in the left half-cell;  $C_l(t)$  and  $C_r(t)$  are the TEMPO concentrations in the left and right half-cells in the particular moment ( $t$ );  $A$  and  $L$  are the membrane's active area and thickness, respectively.

By integrating (2.10) and plotting  $C_l(t)$  vs.  $t$ , one can fit the resulting linear curve and extract the permeability coefficient from a slope.

## 2.4. Membrane Life Testing in Li-TEMPO Hybrid Cells

### 2.4.1. Static Cell

To probe the composite membrane stability under the real Li-hybrid cell conditions and obtain the first performance data, life tests in the Li-TEMPO static cell (Figure 2.5) were performed. Galvanostatic cycling was carried out in the voltage range of 2.5–4.3 V and the current range of 0.25–1.25 mA cm<sup>-2</sup> using the Alians galvanostat/potentiostat (Electrochemical Instruments; Russia) inside the Ar-filled glovebox. Membrane cycling stability was evaluated at 0.5 mA cm<sup>-2</sup>. Current collectors were made of carbon felt (Sigracell, 4.6 mm thickness). Lithium metal electrode, supported by a dry carbon felt layer, after dropping 70 μL of SE on it was directly contacted with a membrane (active area of 1.13 cm<sup>2</sup>) stacked between two gaskets (Viton, 0.8 mm thickness). 600 μL of catholyte (0.1 M TEMPO + 1.0 M LiClO<sub>4</sub> in PC) was dropped into the carbon felt on the cathode side, and the cell was tightly and uniformly sealed with bolts.

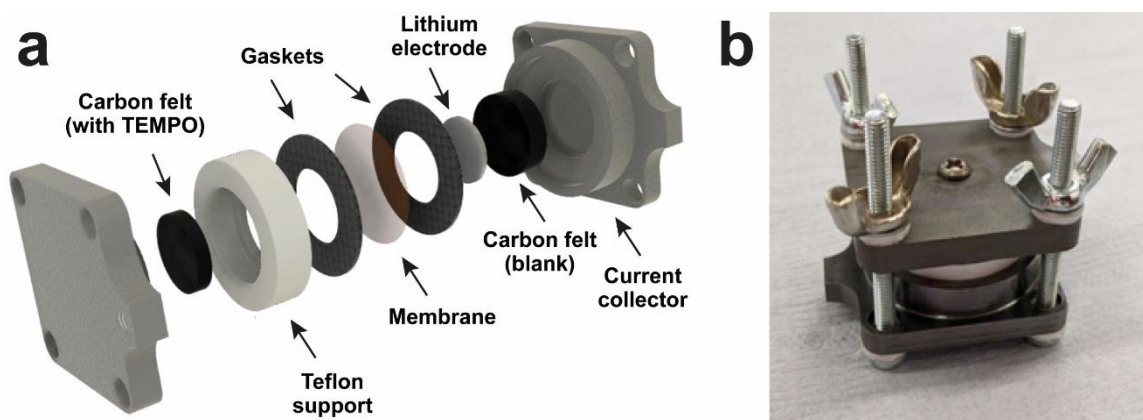


Figure 2.5. (a) Scheme and (b) image of the Li-TEMPO static cell used in cycling tests.

#### 2.4.2. Flow Cell

The Li-HFB flow cell performance tests were carried out in a custom-made electrochemical cell (Figure 2.6a) at 0.5 mA and 20 mL min<sup>-1</sup> catholyte pumping rate via the Alians galvanostat/potentiostat inside the Ar-filled glovebox. The cathode-side polar plate made of graphite contained interdigitated flow field channels. The carbon paper used (1.5×1.7 cm<sup>2</sup>, 5 layers) was preliminarily calcined at 450 °C in the air for 20 h to activate its surface. The LATP+PVdF membrane (0.03-0.04 mm thickness), soaked in SE prior to all battery assembling for 20 h, was fixed between Viton gaskets (0.7 mm thickness; NY, USA), Figure 2.6a,b. Metallic lithium as anode (0.2-0.3 mm thickness) was mechanically attached to a copper substrate using rollers. For better contact, a layer of dry carbon paper was placed between the anode and SS current collector. 100 μL of SE was dropped onto the Li anode to improve its interface with the membrane. The end-plates made of poly(tetrafluoroethylene) were fixed with bolts. The cell was connected with a peristaltic pump (Watson-Marlow, UK) via elastomeric tubes (Figure 2.6c).

TEMPO concentration in catholyte was 1 mM in all the cycling tests, whereas SE was varied so that one can specify the impact of each parameter (salt nature, salt concentration, solvent) separately.

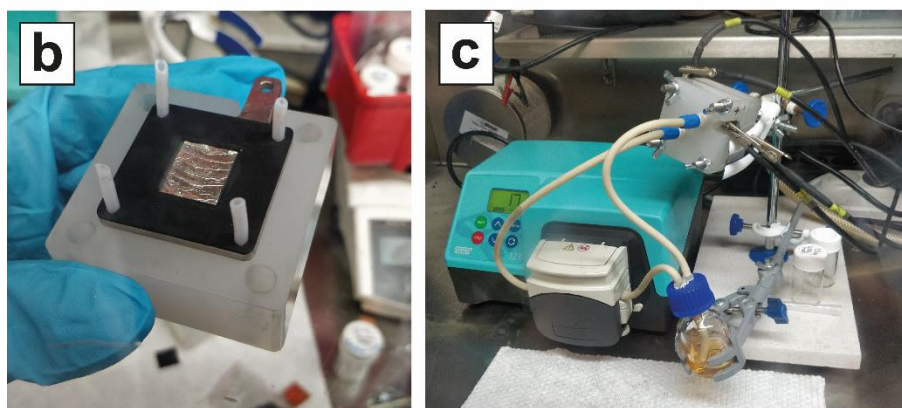
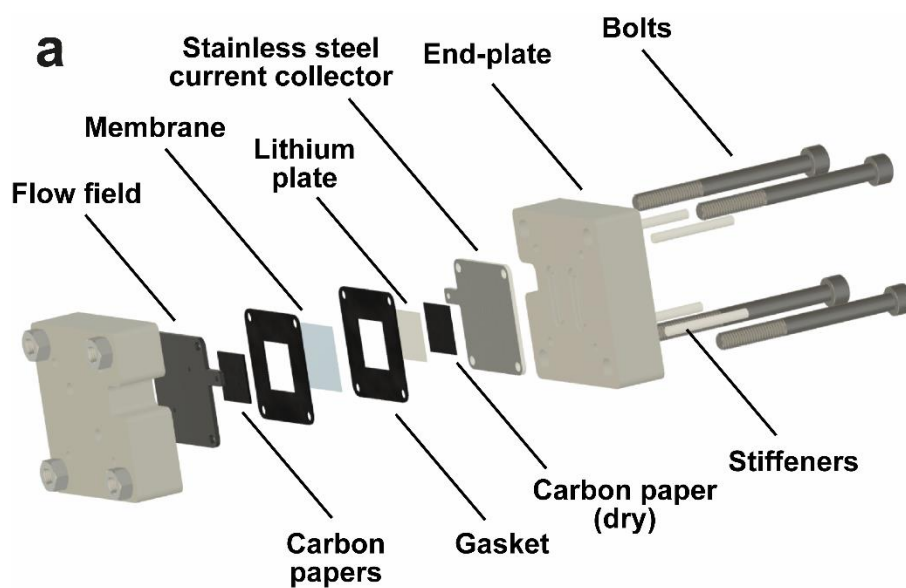


Figure 2.6. (a) Schematic of the custom-made flow cell and digital images reflecting (b) intermediate assembling stage (metallic lithium anode is visible) and (c) constructed and connected HFB cell.

The tested SEs were numbered as follows:

- (SE I) 1.0 M LiClO<sub>4</sub> in PC,
- (SE II) 1.0 M LiClO<sub>4</sub> in EC:DEC,

- (SE III) 1.0 M LiTFSI in EC:DEC,  
 (SE IV) 0.75 M LiTFSI in EC:DEC,  
 (SE V) 0.5 M LiTFSI in EC:DEC,  
 (SE VI) 0.1 M LiTFSI in EC:DEC,

where LiTFSI is lithium bis(trifluoromethanesulfonyl)imide (99.99%, Sigma-Aldrich, China), and EC:DEC — the 1:1 vol. mixture of ethylene carbonate ( $\geq 99\%$ , Sigma-Aldrich, USA) and diethyl carbonate ( $\geq 99\%$ , Sigma-Aldrich, Hungary), all additionally dried under 3 Å sieves until  $c(\text{H}_2\text{O}) < 10$  ppm).

The theoretical capacity ( $Q_{teor}$ ), experimental capacity ( $Q_{disch}$ ), state-of-the-charge ( $SoC$ ), coulombic efficiency ( $CE$ ), and energy efficiency ( $EE$ ) of both Li-TEMPO static and flow cell were calculated by Equations 2.11-2.15, respectively:

$$(2.11) \quad Q_{teor} \left( \frac{Ah}{L} \right) = \frac{C_i n F}{3600},$$

$$(2.12) \quad Q_{disch} \left( \frac{Ah}{L} \right) = \frac{\int I_{disch} dt}{V},$$

$$(2.13) \quad SoC (\%) = \frac{Q_{ch}}{Q_{teor}} \cdot 100,$$

$$(2.14) \quad CE (\%) = \frac{Q_{disch}}{Q_{ch}} \cdot 100,$$

$$(2.15) \quad EE (\%) = \frac{E_{ch}}{E_{disch}} \cdot 100,$$

where  $n$  represents a number of electrons involved in a redox reaction;  $C_i$  is a molar concentration of active species;  $F$  is the Faraday's constant;  $I_{disch}$  is the current in a certain time frame ( $t$ );  $V$  is catholyte's volume;  $E_{ch}$  and  $E_{disch}$  are charge and discharge energy, respectively.

## Chapter 3. Optimization of Composite Membrane Properties

In this chapter, we optimize the composite membrane's composition and fabrication conditions to obtain the best combination of structural, morphological, and functional (IC, selectivity, stability) properties suitable for application in Li-HFBs. Particularly, we reveal the impact of lithium salt dissolved in a polymer matrix; nature of the casting solvent; polymer-solvent and ceramic-polymer ratios. We examine the influence of solution mixing temperature; membrane casting temperature; sample drying conditions; membrane components mixing protocol.

*The results described as well as the figures and tables shown in this chapter were published in Refs. [47,172,179,180] — articles with my co-authoring.*

### 3.1. Composition Variation

#### 3.1.1. Impact of Lithium Salt

Dissolving lithium salts in the polymer-ceramic membranes is widely used to break the insufficient level of solid electrolyte's IC. At the same time, we previously assumed that the salts might be leached out from the composite structure, as the membrane is always in contact with the liquid environment in RFBs.

The basic electrochemical characteristics of LATP+PVdF and LATP+(7.5 wt.% LiClO<sub>4</sub>-PVdF) composite membranes, as well as their mass change after 1 h soaking in PC, are presented in Table 3.1. It is seen that, despite both composites demonstrate high electrochemical stability and negligible electronic conductivity, the salt-contained membrane exhibits severe mass losses after the static soaking in the solvent.

Table 3.1. Basic characterization of the composite membranes.

Membrane	ESW, V vs. Li/Li <sup>+</sup>	Electronic conductivity, S cm <sup>-1</sup>	Mass loss after PC, %
LATP+PVdF	2.2–4.8	10 <sup>-9</sup>	~0
LATP+(7.5 wt.% LiClO <sub>4</sub> -PVdF)	2.2–4.5	10 <sup>-9</sup>	~12

The SEM images of LATP+(7.5 wt.% LiClO<sub>4</sub>-PVdF) support the previous result (Figure 3.1) — after the soaking, decent voids both at the top and cross-sectional views appeared. It confirms our initial assumption regarding leaching the salt out of the polymer matrix during exposure to the liquid media.

Such degradation is unacceptable for the Li-HFB membrane, so, in further experiments, we will use the LATP+PVdF membrane with no salt added.

### 3.1.2. Solvent Variation

A tape-casting solvent was considered as an impactful factor determining the final membrane properties, specifically, its porosity that influences a crossover rate through the membrane [151,152]. Moreover, the solvent may be harmful to the composite's components, PVdF and LATP, and lead to their degradation (e.g., LATP was previously shown to be unstable toward water [125]). The DMF, DMSO, and NMP solvents, in spite of having twice lower polarity than water, solvate Li ions well that may cause ceramic's phosphate dissociation [181].

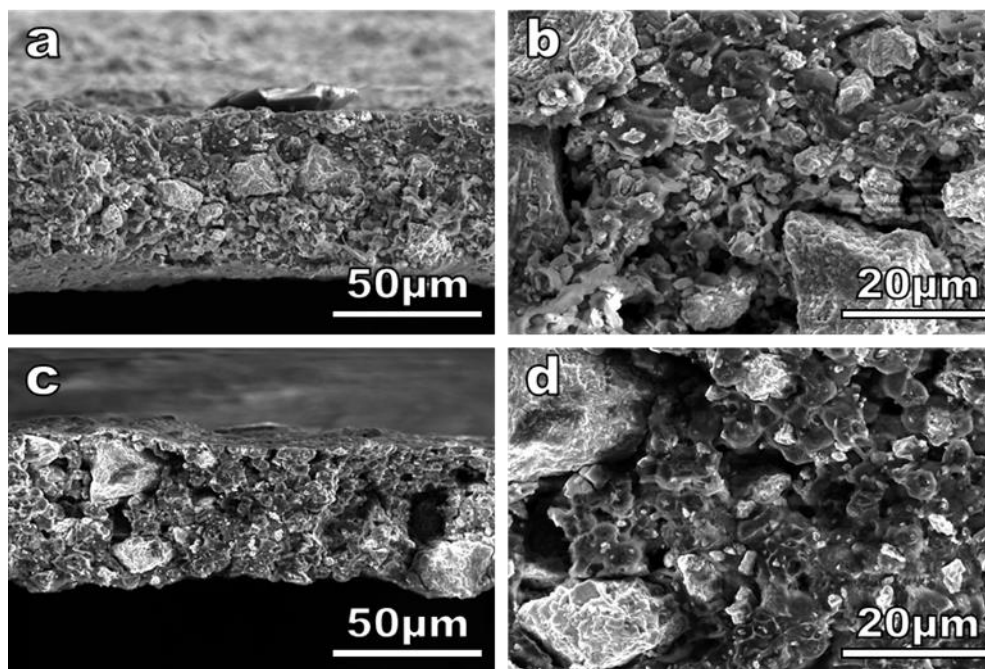


Figure 3.1. SEM images of LATP+(7.5 wt.% LiClO<sub>4</sub>-PVdF) membranes: (a) cross-section and (b) top view before soaking; (c) cross-section and (d) top view after soaking.

To analyze the behavior of LATP's crystal structure and its stability throughout the membrane fabrication process, we followed the approach previously described by our research group investigating the LATP stability toward air [116]. In that work, the authors showed that the LATP unit cell dimension and conductivity properties change with aging. A deeper analysis revealed a strong correlation between the volume of polyhedron around the Li(1) lithium position ([Li(1)O<sub>6</sub>M<sub>2</sub>]) and IC — both decreased with storage time. This makes the combination of unit cell and [Li(1)O<sub>6</sub>M<sub>2</sub>] volumes a good indicator of the structural and functional stability of LATP. Similarly, Figure 3.2a shows the LATP's cell and [Li(1)O<sub>6</sub>M<sub>2</sub>] polyhedra volumes before and after the LATP+PVdF fabrication.

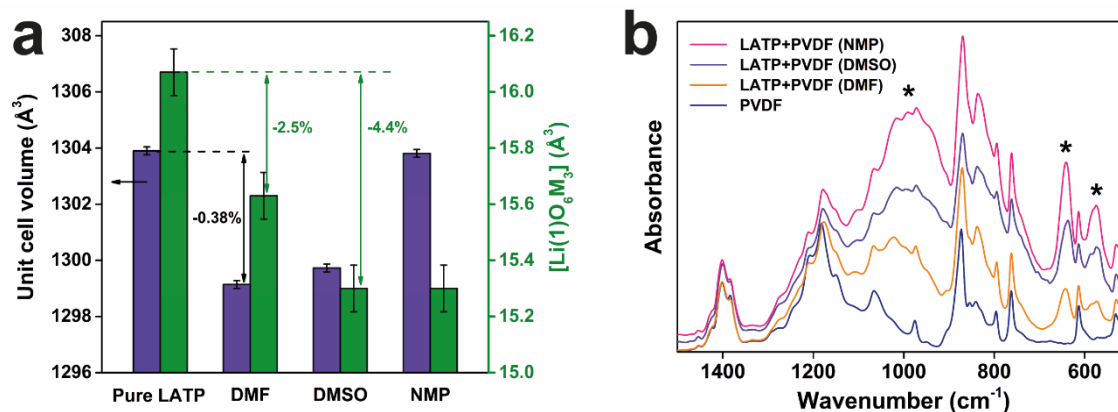


Figure 3.2. (a) Unit cell and [Li(1)O<sub>6</sub>M<sub>2</sub>] polyhedra volumes of the LATP powder and that within the LATP+PVdF composite membranes casted with DMF, DMSO, and NMP; (b) FTIR spectra of PVdF and LATP+PVdF casted with the studied solvents. Signals of LATP are marked with asterisks.

The fabrication led to the LATP's cell shrinkage from 1304 to 1299-1300 Å<sup>3</sup> for DMF- and DMSO-casted membranes (~0.38% loss). Moreover, the IC-sensitive [Li(1)O<sub>6</sub>M<sub>2</sub>] polyhedron diminishes from 16.0 to 15.6 Å<sup>3</sup> (2.5% loss) for DMF and to 15.3 Å<sup>3</sup> for DMSO and NMP (4.4% loss). The structural changes of the close extent were reported in our previous publication, where the impact of water was investigated [116,125]. In that work, the changes were accompanied with leaching the LATP elements out of the structure. Although here we did not quantitatively estimate the elemental losses, we assume the presence of slight chemical degradation similar to that for the water case. Nevertheless, regardless of the solvent nature, XRD phase analysis showed no new crystallized compounds as well as depicted the maintenance of the initial NASICON phase of LATP.

In addition, the solvent impact was investigated by FTIR to analyze the polymer's phases. In Figure 3.2b, one can see the characteristic bands of LATP (P–O stretching vibrations near  $1000\text{ cm}^{-1}$  and O–P–O bending vibrations at  $640$  and  $570\text{ cm}^{-1}$ ) and PVdF (mainly  $\alpha$ -phase:  $614, 762, 975\text{ cm}^{-1}$ ; and  $\beta$ -phase:  $877, 1272\text{ cm}^{-1}$  [182,183]). We observe no qualitative difference in the spectra — there are no signals ascribed to either residual solvent or side products. Therefore, speaking about the phase composition, both LATP and PVdF phases maintain their initial features after the membrane fabrication.

To study the solvent impact on the membranes' morphology, we performed SEM and EDX. For all solvents, the membrane's surface was quite smooth, ceramic filler particles were uniformly distributed (Figure 3.3), and element ratios roughly corresponded to the theoretical formula units (Table 3.2). However, in comparison to DMF, the membranes created with the application of DMSO and NMP possess a larger number of pores visible on their surface (Figure 3.4). The open pores are undesired, as might be the cause of the membrane's permeability to redox species (crossover) [50].

Nevertheless, the calculated permeability coefficients were quite close to each other:  $3.0, 2.7,$  and  $3.1 \cdot 10^{-7}\text{ cm}^2\text{ min}^{-1}$  for DMF, DMSO, and NMP, respectively (Figure 3.5). In spite of the structural and mild morphological changes occurred during membrane fabrication, LATP+PVdF's permeability does not depend much on the studied solvents. Composite's IC diminished from  $(3.1\pm 0.5) \cdot 10^{-4}\text{ S cm}^{-1}$  (for pure ceramic pellet) to  $(1.45\pm 0.44), (1.0\pm 0.3),$  and  $(1.7\pm 0.5) \cdot 10^{-4}\text{ S cm}^{-1}$  for the same row of the solvents (Figure 3.5) due to its in-matrix embedment and the slight impact of solvent.

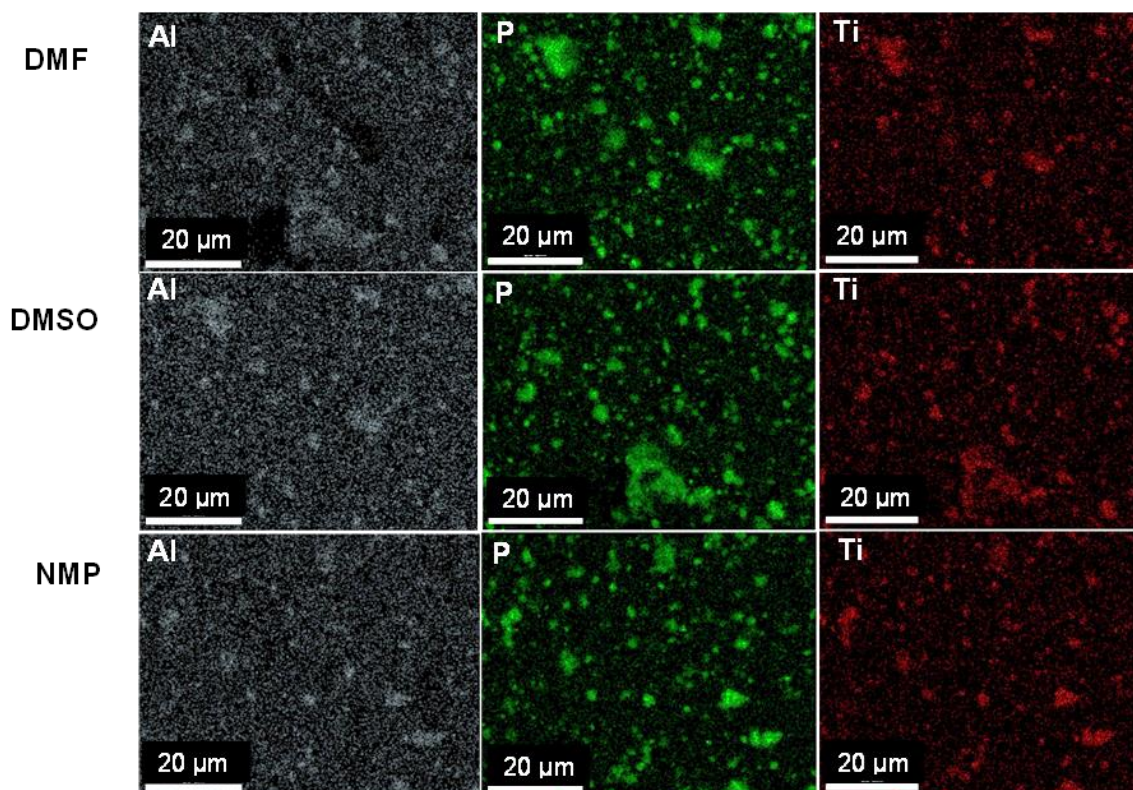


Figure 3.3. EDX of LATP+PVdF membranes casted with DMF, DMSO, and NMP.

Table 3.2. EDX elemental distribution of LATP+PVdF membranes fabricated using the DMF, DMSO, and NMP solvents. LATP =  $\text{Li}_{1.3}\text{Al}_{0.3}\text{Ti}_{1.7}(\text{PO}_4)_3$ .

Solvent	Atomic fraction			Formula unit		
	Al	Ti	P	Al	Ti	P
DMF	2.1±0.3	4.4±0.8	11.8±0.9	0.6±0.1	1.2±0.2	3.2±0.2
DMSO	1.9±0.3	4.9±0.8	12.1±0.8	0.6±0.1	1.3±0.2	3.2±0.2
NMP	1.8±0.3	4.7±0.8	11.1±0.9	0.5±0.1	1.3±0.2	3.2±0.2

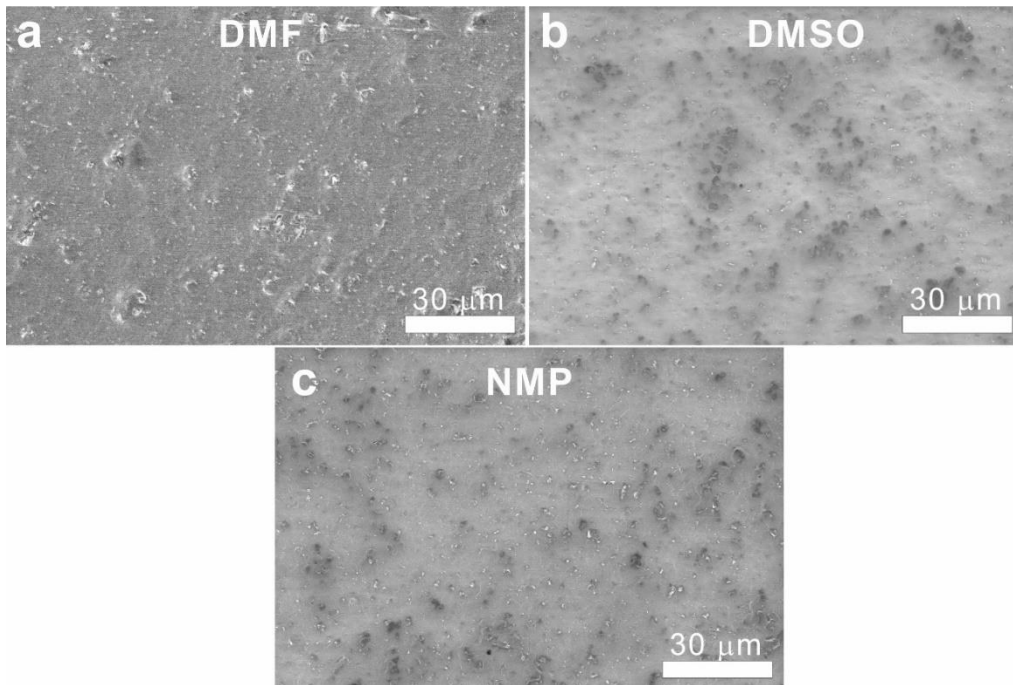


Figure 3.4. Top view SEM images of LATP+PVdF fabricated using (a) DMF, (b) DMSO, and (c) NMP solvents.

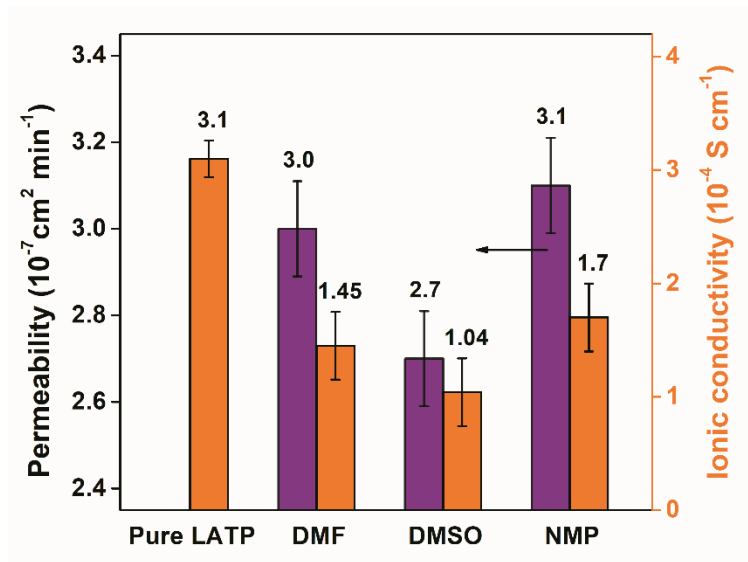


Figure 3.5. A correlation between permeability (purple bar) and IC (orange bar) of LATP+PVdF fabricated using different solvents.

Worth noting, the IC values correlate with the permeability data (Figure 3.5): LATP+PVdF casted with DMSO possesses the lowest permeability and IC simultaneously, whereas the NMP-casted composites have the highest values. It confirms the connection between membrane's IC and permeability through their open porosity.

To sum up, the investigation of the solvent nature impact led us to the conclusion that not only pure LATP ceramics are unstable toward ambient atmosphere and water, but also towards pre-dried dipolar aprotic media. This observation was made for the first time. Nevertheless, either DMF, DMSO, or NMP can be used for fabricating the LATP+PVdF composite membranes, as all the membranes showed close and acceptable values of both permeability and IC. For convenience, all further investigations were performed using DMF.

### *3.1.3. Polymer-Solvent Ratio*

The polymer-solvent ratio used in the composite fabrication determines viscosity of the intermediate solution, processing convenience, and the final membrane's thickness. At viscosity of  $>2000$  mPa s, it is hard to take the DMF-PVdF solution out of the mixing vial due to the lack of continuous flowing. At the same time, diluted samples ( $<500$  mPa s) were too diffuent or led to the formation of overly thin membranes. Within this viscosity region, 15 wt.% of PVdF in DMF was fixed as an optimum composition for uniform and robust membrane fabrication (Figure 3.6). Worth noting, a membrane thickness can also be controlled by altering the blade gap of the applicator machine — no need to change the solution's viscosity, if thinner or thicker samples are needed.

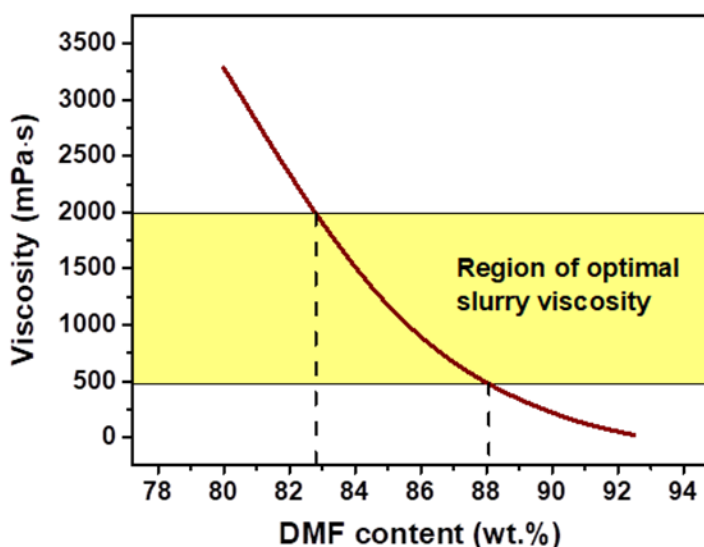


Figure 3.6. Dependence of DMF-PVdF solution's viscosity on DMF content within.

#### 3.1.4. Ceramic-Polymer Ratio

The filler content is one of the most important parameters determining polymer-ceramic membrane's robustness, IC, and permeability. Presumably, composite's IC should rise with the fraction of an ion-conducting material. Permeability is affected by the filler-matrix interface, which can be different for the membranes with low and high content of the ceramics. Too high fractions may promote membrane's fragility and porosity due to the increase of voids in ceramic agglomerations.

To investigate the impact of LATP content, we firstly performed XRD, FTIR, and SEM analysis of the membranes with 0, 15, 30, 45, and 60 wt.% of LATP (further denoted as PVdF and 15, 30, 45, and 60LATP+PVdF, respectively). XRD pattern of a pure polymeric membrane contains wide reflexes typical for PVdF (Figure

3.7a) — characteristic peaks within 18–20° with a moderate crystallization level [184,185]. Reflexes of the composite's patterns can be assigned to either LATP or PVdF with relative intensity proportional to their content in the composite.

All the observed infrared bands of the LATP+PVdF membranes belong to either LATP or PVdF (Figure 3.7b). Absorption bands near 842, 1235 and 1275  $\text{cm}^{-1}$  imply the presence of crystalline  $\beta$ - and  $\gamma$ -PVdF in both pure polymer and composite membranes [185]. The characteristic vibrations of LATP's  $\text{PO}_4$  group (bending at 845  $\text{cm}^{-1}$  and stretching in 1000–1230  $\text{cm}^{-1}$ ) are blue-shifted compared to the initial pure LATP powder and possess a gradual bathochromic shift with the increase of LATP content (Figure 3.7b, inset).

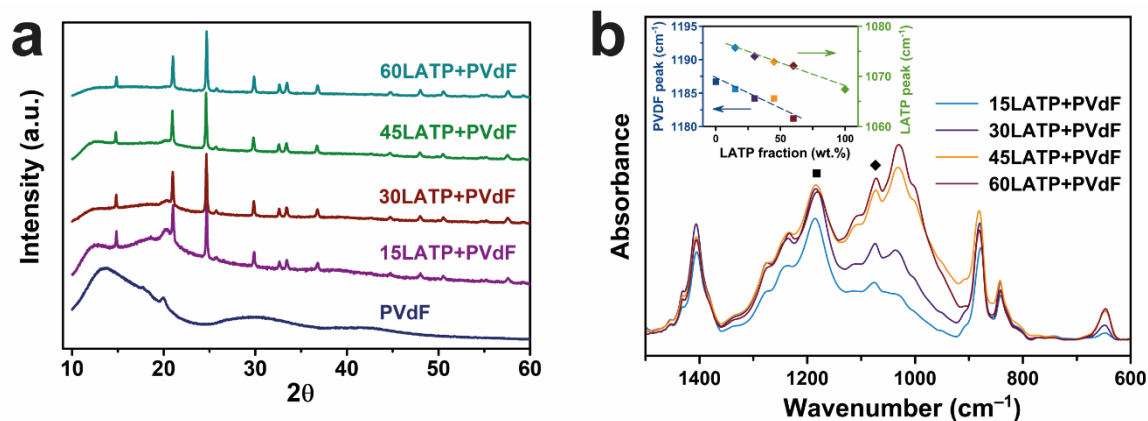


Figure 3.7. XRD patterns of (a) LATP+PVdF composite membranes with LATP content varied from 0 to 60 wt.%. (b) Effect of LATP content on FTIR spectra of composite membranes; inset — dependence of  $\text{CF}_2$  and  $\text{PO}_4$  vibration peak positions of PVdF and LATP on ceramic content in LATP+PVdF.

Moreover, the frequency of PVdF's  $\text{CF}_2$  vibrations ( $1180\text{--}1190\text{ cm}^{-1}$ ) decreases with the increase of LATP content. The described results might be attributed to a certain interaction between LATP and PVdF. As far as the fluor ion has the highest electronegativity, one may expect F to coordinate either ceramic filler particles (featured with the oxidized surface [125]) or separate lithium ions of LATP.

To analyze the membrane's microstructure, we applied SEM. Two planar surfaces of a membrane have morphological differences: *smooth side* touches substrate during drying (Figure 3.8b,c); *rough side* is in contact with air (Figure 3.8d,e). This morphological feature is typical for both pure polymeric and composite membranes. Worth noting that LATP ceramic slightly increases membrane's porosity (Figure 3.8b,d) that was confirmed by the soaking tests (Table 3.3): with LATP introduction, the porosity increased from 21 to 33%. Such growth can be attributed to the ceramic agglomeration. Indeed, the cross-section image of LATP+PVdF shows that LATP particles tend to form agglomerates of up to  $20\text{ }\mu\text{m}$  (Figure 3.8f) in size. At the same time, the ceramic-polymer contact is visibly tight, which, in turn, can provide a durable structure. Indeed, the composite membrane's swelling in the PC solvent was around zero unlike the pure PVdF membrane, whose thickness increased by  $\sim 18\%$  (Table 3.3). Apparently, the LATP filler when combined with PVdF chains, provides the composite with rigidity and suppresses the thickness change. These results are in agreement with the FTIR data discussed above confirming the assumption of an interaction between the polymeric and inorganic components.

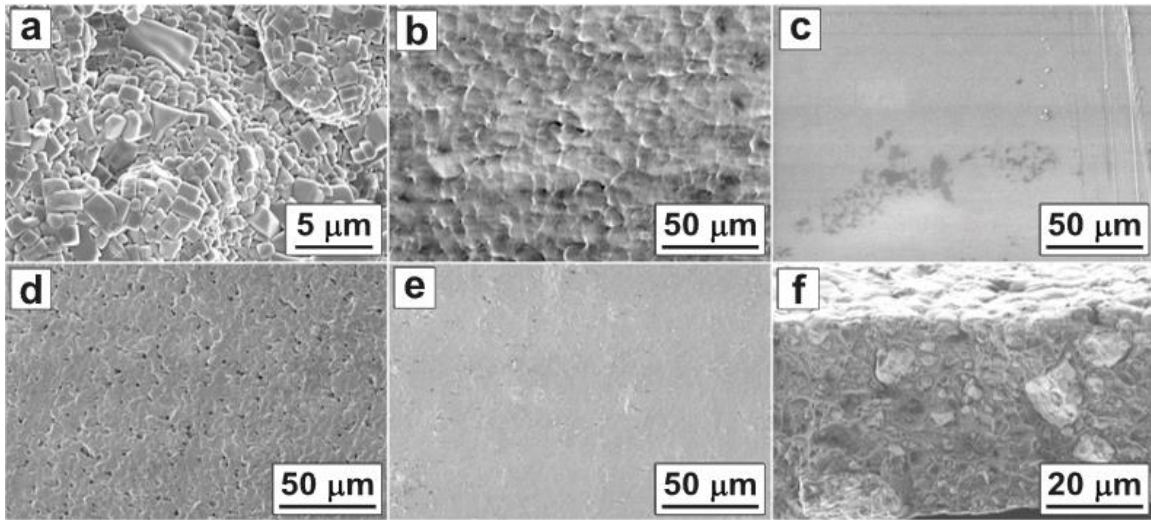


Figure 3.8. SEM images of (a) LATP ceramic; (b) rough and (c) smooth planes of PVdF membrane; (d) rough, (e) smooth, and (f) cross-section planes of 45LATP+PVdF composite.

Table 3.3. Swelling ration and porosity of the studied membranes.

Membrane	Swelling ratio, %	Porosity, %
PVdF	$18 \pm 4$	$21 \pm 4$
45LATP+PVdF	$\sim 0$	$33 \pm 3$
45Al <sub>2</sub> O <sub>3</sub> +PVdF	$\sim 0$	$31 \pm 6$

After morphological and structural investigation, we evaluated the membranes IC. The 0-60LATP+PVdF membranes were compared with the reference samples — 45Al<sub>2</sub>O<sub>3</sub>+PVdF (inert filler), Neosepta AHA, and Li-Nafion (see pretreatment description of the commercial membranes in Appendices, D). It is seen (Figure 3.9), with addition of LATP, membrane's IC grew from  $3.8 \cdot 10^{-5}$  for pure PVdF to  $4.6 \cdot 10^{-4}$  S cm<sup>-1</sup> for 60LATP+PVdF (electronic conductivity was negligible,  $6.1 \cdot 10^{-8}$  S cm<sup>-1</sup>), which is a good result assuming the previously stated IC threshold of  $10^{-4}$  S cm<sup>-1</sup>.

In order to distinguish the impact of porosity and filler's IC, we examined the composite with inert Al<sub>2</sub>O<sub>3</sub> powder (1 μm size, 45 wt.% content) instead of Li-conductive LATP (Table 3.3). In fact, IC of 45Al<sub>2</sub>O<sub>3</sub>+PVdF was only ~20% higher than of the PVdF membrane ( $4.5 \cdot 10^{-5}$  vs.  $3.8 \cdot 10^{-5}$  S cm<sup>-1</sup>; Figure 3.9), which is attributed to the pure effect of the porosity growth. Hence, ~98% of the LATP+PVdF's IC growth (from 0.38 to  $3.4 \cdot 10^{-4}$  S cm<sup>-1</sup>) is explained by the ceramic impact and 2% — by the porosity increment.

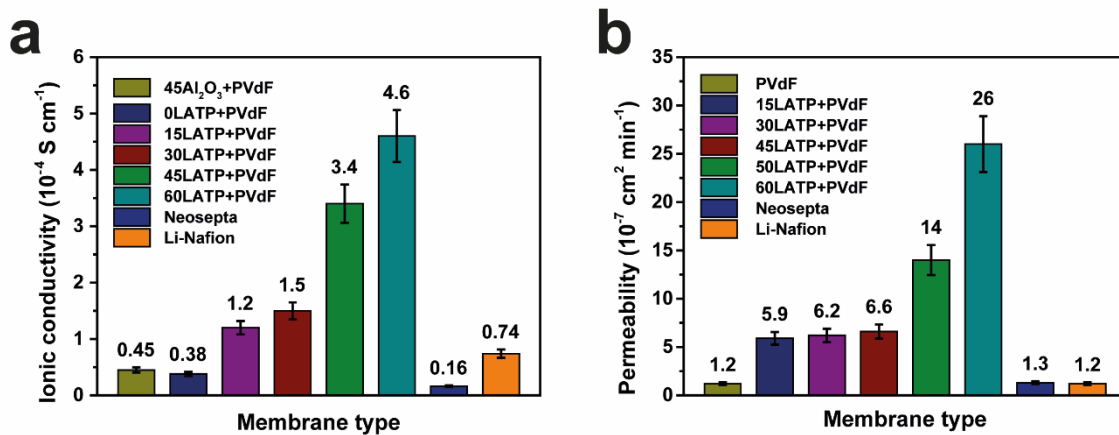


Figure 3.9. (a) Ionic conductivity and (b) permeability of 0-60LATP+PVdF, reference 45Al<sub>2</sub>O<sub>3</sub>+PVdF, and commercially available Neosepta AHA and Li-Nafion membranes.

Benchmarking the composite membranes with Neosepta and Li-Nafion, we observed IC of commercial samples were much lower —  $1.6 \cdot 10^{-5}$  and  $7.4 \cdot 10^{-5}$  S cm<sup>-1</sup>, respectively. Neosepta’s IC is about one order of magnitude lower than in other PC-based electrolytes ( $1.6\text{-}2.1 \cdot 10^{-4}$  S cm<sup>-1</sup>) [93,94]. Li-Nafion’s IC is close to that reported for the dry state ( $6.3 \cdot 10^{-5}$  S cm<sup>-1</sup>) [186], but higher than soaked in pure PC ( $2.2 \cdot 10^{-5}$  S cm<sup>-1</sup>) [187] and 1.0 M LiFSI in DMC ( $10^{-5}$  S cm<sup>-1</sup>) [90].

The calculated membranes’ transference numbers ( $t_{Li+}$ , Table 3.4) were relatively far from unity due to the membrane’s porosity filled with SE. The composite membrane shows the highest  $t_{Li+}$  among other materials, which supports the dominant role of LATP ceramic in LATP+PVdF’s IC. Moderate  $t_{Li+}$  of Li-Nafion can be caused by the incomplete lithiation state. The low  $t_{Li+}$  value for Neosepta AHA is understandable — this membrane has anion-exchange nature.

Table 3.4. Lithium transference number ( $t_{Li+}$ ) of the studied membranes.

Membrane	$t_{Li+}$
45LATP+PVdF	$0.7 \pm 0.1$
PVdF	$0.57 \pm 0.09$
Li-Nafion	$0.62 \pm 0.09$
Neosepta	$0.33 \pm 0.05$

Along with IC, it is essential to evaluate the impact of LATP filler on membrane's permeability. Figure 3.9b illustrates that the permeability coefficient gradually grows with the LATP content: being  $1.2 \cdot 10^{-7} \text{ cm}^2 \text{ min}^{-1}$  for pure PVdF membrane, it reaches the plateau at  $5.9\text{-}6.6 \cdot 10^{-7} \text{ cm}^2 \text{ min}^{-1}$  for 15–45LATP+PVdF and then drastically increases to  $2.6 \cdot 10^{-6} \text{ cm}^2 \text{ min}^{-1}$  for 60 wt.% of LATP. The studied composite membranes showed higher permeability coefficients than commercially available Li-Nafion and Neosepta membranes ( $1.2\text{--}1.3 \cdot 10^{-7} \text{ cm}^2 \text{ min}^{-1}$ ; Figure 3.9b). The dramatic permeability rise, according to the results above, might be attributed to the porosity increase with addition of ceramic filler. Despite the 15–45LATP+PVdF composites meet the formal permeability requirement of  $<10^{-6} \text{ cm}^2 \text{ min}^{-1}$  (Table 1.4), it can be further suppressed to approach that for commercial membranes, unless it is at the expense of IC.

Overall, the LATP filler integration into the polymer matrix has not altered much the components' phases, but implies the polymer-ceramic interaction in the LATP+PVdF system. Composite's IC increases with the ceramic content and was significantly higher than for the Nafion and Neosepta commercial membranes. At the same time, with addition of LATP, the membrane's porosity increases probably due to the void formation within ceramic agglomerates. This, together with visible pores on a membrane surface, is assumed to cause the membrane's permeability to the catholyte active species. It rises with the LATP introduction and was larger than that of the commercially available samples. At this stage, the optimum 45 wt.% LATP+PVdF membranes demonstrated the best trade-off between IC and permeability, so this composition will be used in further membrane optimization

stages. Yet, it is desired to reach the permeability of commercial level-samples ( $10^{-7} \text{ cm}^2 \text{ min}^{-1}$ ) with the insignificant damage to IC.

## **3.2. Fabrication Conditions Variation**

### *3.2.1. Solution Mixing Temperature*

After considering the influence of composition on membrane's properties, we are moving to fabrication conditions and, particularly, solution mixing temperature ( $T_{\text{mix}}$ ). As it was mentioned in Section 1.4.4, the prolonged exposure of a pre-membrane solution (that contains solvent, polymer, etc.) to heating have not been evaluated yet, though might influence the qualities of the final sample. To evaluate this, we varied  $T_{\text{mix}}$  of pure polymer PVdF membranes (to exclude interfering impacts) within 25–130 °C (Set P.1) and compared samples' morphology, phase composition, and permeability.

Figure 3.10 shows roughness of the membranes' top surfaces. Being completely smooth for the sample mixed at 25 °C, the PVdF's plane side becomes more globular at 50–90 °C and obtains the maximum roughness at 130 °C. Simultaneously, we report the thickness growth for *ca.* 5  $\mu\text{m}$  (>25% of the 25 °C sample) with the increase of  $T_{\text{mix}}$  likely due to the porosity rise.

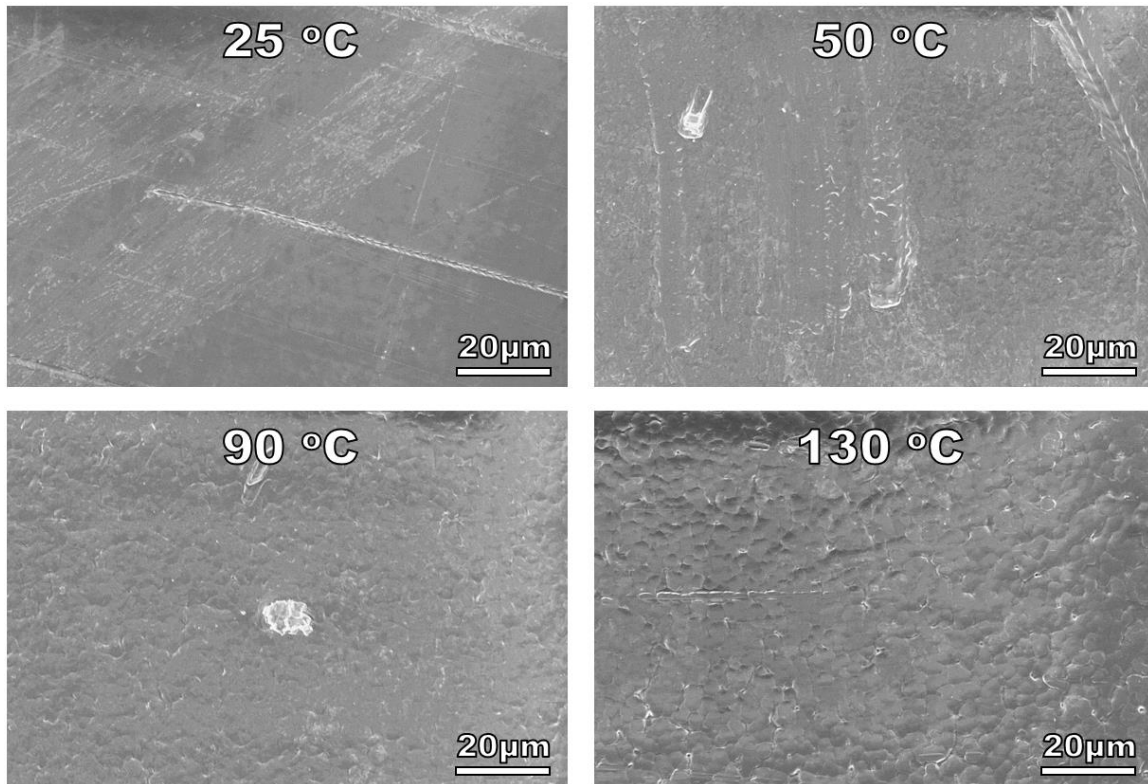


Figure 3.10. SEM microphotographs of the top PVdF surface of membranes fabricated at  $T_{\text{mix}}$  of 25, 50, 90, and 130 °C.

Then, we explored the PVdF membranes' phase composition by vibrational spectroscopies. Based on the FTIR results (Figure 3.11a), the dominant crystalline phase at  $T_{\text{mix}} = 25$  °C was *alfa* (975, 762, and 614  $\text{cm}^{-1}$ ). With the temperature increase to 90 °C, the  $\alpha$ -phase slightly gives the way to the  $\beta$ -phase (bands at 1272 and 877  $\text{cm}^{-1}$ ). In the case of further heating to 130 °C, the  $\alpha$ -phase almost diminishes, whereas the  $\beta$ -phase becomes dominant. Worth to mention, the *gamma* PVdF phase is also present on the spectra (at 1234 and 811  $\text{cm}^{-1}$ ), however its content was low.

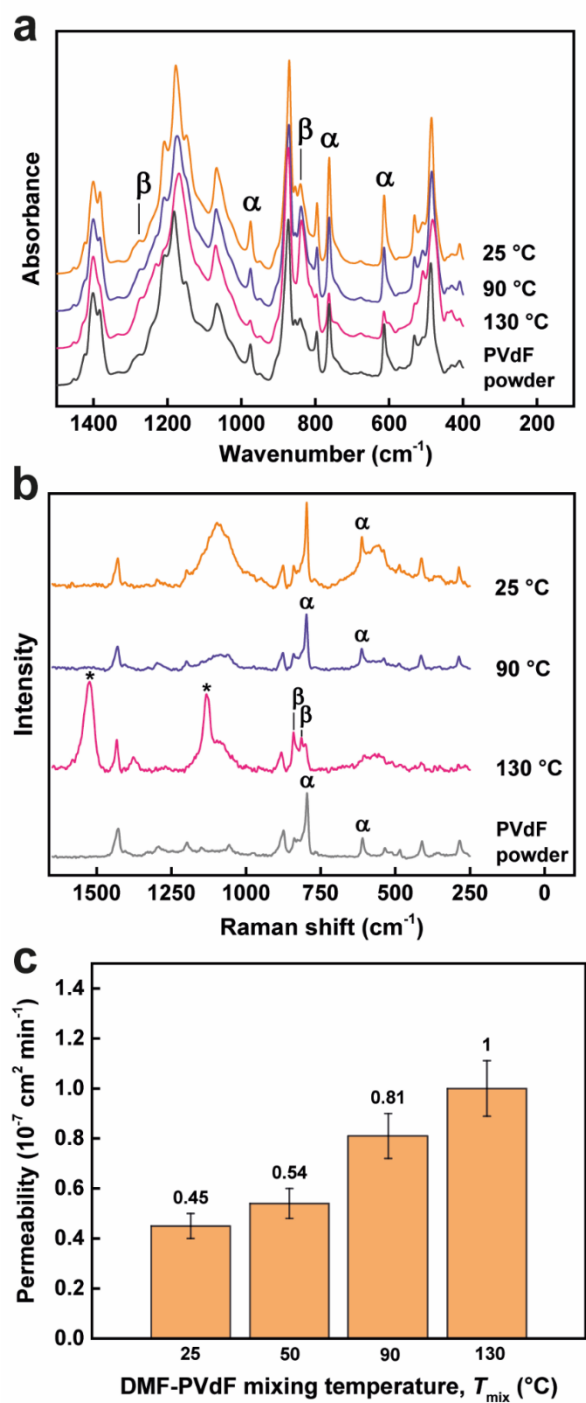


Figure 3.11. (a) FTIR spectra, (b) Raman spectra, and (c) permeability coefficients of the PVdF membranes fabricated at various  $T_{mix}$ .

All the studied PVdF membranes were multi-phased — each membrane contained  $\alpha$ -,  $\beta$ -, and  $\gamma$ -PVdF at least in a small amount. Raman spectroscopy confirmed the prevalence of  $\alpha$  phase (bands at 611 and 797  $\text{cm}^{-1}$ ) at  $T_{\text{mix}}$  of 25–90 °C and the  $\beta$ -phase formation (813 and 841  $\text{cm}^{-1}$ ) at 130 °C (Figure 3.11b). The nature of the bands marked with the \*-symbol (1132 and 1525  $\text{cm}^{-1}$ ) is still unclear, but they are likely attributed to the  $-\text{CH}=\text{CH}-$  vibrations that might appear due to the PVdF degradation observed in Ref. [188].

Finally, the membranes' permeability raises from 0.45 to  $1.00 \cdot 10^{-7} \text{ cm}^2 \text{ min}^{-1}$  with  $T_{\text{mix}}$  increasing from 25 to 130 °C (Figure 3.11c). Taking such growth into account, we conclude on the strong temperature-phase-globularity-permeability correlation. High  $T_{\text{mix}}$  promotes the  $\beta$ -PVdF formation with a more globular morphology that promotes permeability. Lower  $T_{\text{mix}}$ , which causes  $\alpha$ -PVdF with a smooth surface, are more beneficial for the PVdF-based membranes, as they provide lower permeability. From now on, membrane's  $T_{\text{mix}}$  will be maintained at 25 °C.

### 3.2.2. Solution Casting Temperature

As it goes from Section 1.4.3, substrate temperature ( $T_{\text{sub}}$ ) in the stage of casting the free-standing membrane may influence its microstructure and final phase composition. To estimate the impact of  $T_{\text{sub}}$ , we studied four PVdF membrane samples casted at 70, 110, and 150 °C (Set P.2). It is seen (SEM images; Figure 3.12), the membrane exhibits evident microporosity at  $T_{\text{sub}}$  of 70 °C that gradually disappears with the further elevation.

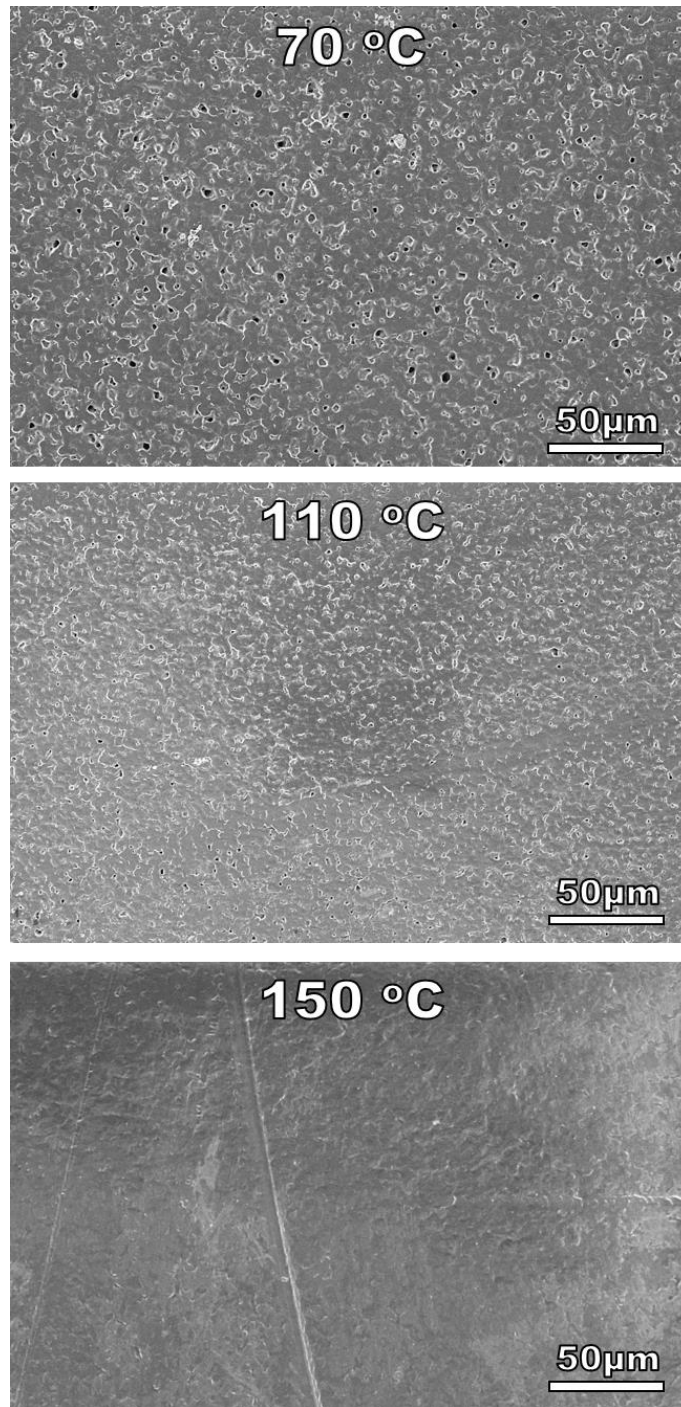


Figure 3.12. SEM microphotographs of the top face of PVdF membranes fabricated at

$T_{\text{sub}}$  of 70, 110, and 150 °C;  $T_{\text{mix}} = 25$  °C;  $T_{\text{dry}} = 90$  °C.

The membrane prepared at  $T_{\text{sub}} = 150$  °C shows a denser and glossier plane, the globularity is merged. The observed changes are in agreement with porosity measured for these samples (Table 3.5): with rise of  $T_{\text{sub}}$  from 70 to 150 °C, it decreased from 27 to 10%.

Then, as it is seen at Raman spectra (Figure 3.13), with the  $T_{\text{sub}}$  growth, the content of PVdF's  $\beta$  phase gradually decreases. The sample fabricated at  $T_{\text{sub}} = 150$  °C has almost pure  $\alpha$  phase that correlates with the lower globularity, as well as it was observed for the  $T_{\text{mix}}$  variation experiments. This supports the previously described globularity-microstructure interrelation and confirms the globularity's negative impact on the membrane's porosity. The findings are in accordance with literature: higher  $T_{\text{sub}}$  diminishes the PVdF's globularity leading to the smoother and denser planes [149].

Table 3.5. Dry-measured porosity of PVdF polymer membrane samples.

Temperature varied, °C	Porosity, %
<u>Set P.2</u> ( $T_{\text{sub}}$ variation)	
70	$27 \pm 7$
110	$10 \pm 9$
150	$10 \pm 9$
<u>Set P.3</u> ( $T_{\text{dry}}$ variation)	
70	$25 \pm 7$
90	$19 \pm 8$
110	$20 \pm 8$
150	$25 \pm 7$

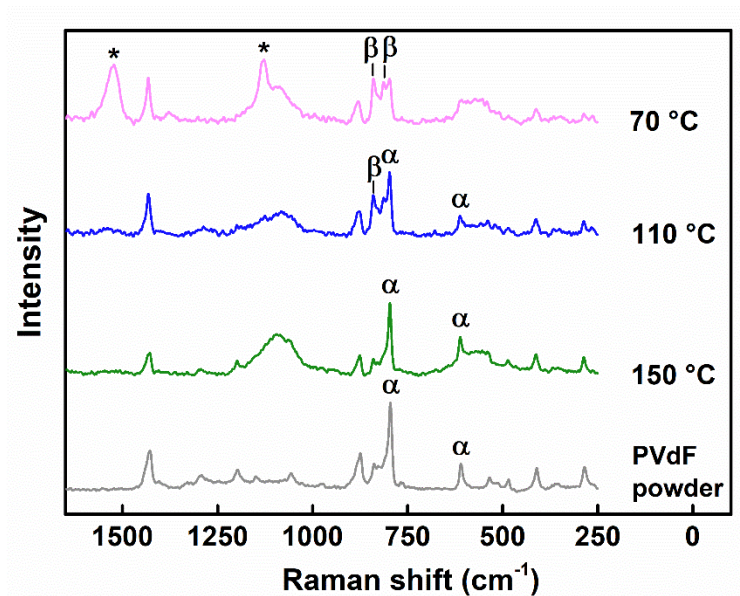


Figure 3.13. Raman spectra of the PVdF membranes fabricated at various  $T_{\text{sub}}$ .

Overall, higher  $T_{\text{sub}}$  reduces both the globular morphology and porosity of the PVdF membrane. We ensured that the PVdF's  $\beta$  phase promotes the globular structure formation. Hence, optimal  $T_{\text{sub}}$  of 150 °C will be used further in the PVdF-based membrane fabrication.

### 3.2.3. Samples Drying Conditions

After a fresh membrane is casted on a substrate, it should be carried to an oven for drying. The drying process should provide complete but gentle solvent removal resulting in a smooth and non-globular membrane's microstructure. The most influential drying conditions are temperature ( $T_{\text{dry}}$ ) and atmosphere, i.e., vacuum or ambient pressure. At elevated temperatures, polymer chains can rearrange, aligning the structure and decreasing

porosity; while the dynamic vacuum accelerates solvent evaporation [189]. Below, we investigate the influence of  $T_{\text{dry}}$  and vacuum on the final PVdF membrane's morphology.

Figure 3.14 contains the SEM images of PVdF membranes dried at different regimes: 80-90 °C + atmospheric pressure (denoted as *only T*), 80-90 °C + dynamic vacuum (*T+vac*), and 25 °C + dynamic vacuum (*only vac*). It is seen (Figure 3.14a-c) that *only T* and *T+vac* membranes have acceptable smooth appearance in contrast to the *only vac* sample. The latter sample has evident polymer disruptions that cause deep, likely open, pores (Figure 3.14d) totally unsuitable for Li-HFB purposes.

To evaluate the impact of  $T_{\text{dry}}$  on the PVdF microstructure, we fabricated four samples (Set P.3) dried at 70, 90, 110, and 150 °C (atmospheric pressure). The semi-quantitative evaluation showed the close porosity characteristics for all the studied membranes (Table 3.5). It was also barely possible to see any difference in polymers' appearance either visually or instrumentally. Therefore, we decided to leave  $T_{\text{dry}}$  equalled ~90 °C as an optimum temperature that provides quick solvent evaporation and no samples destruction.

The drying temperature range of 70–150 °C does not influence much on the membrane's morphology unlike to the drying pressure that must be atmospheric for efficient, non-destructive solvent evaporation from the samples.

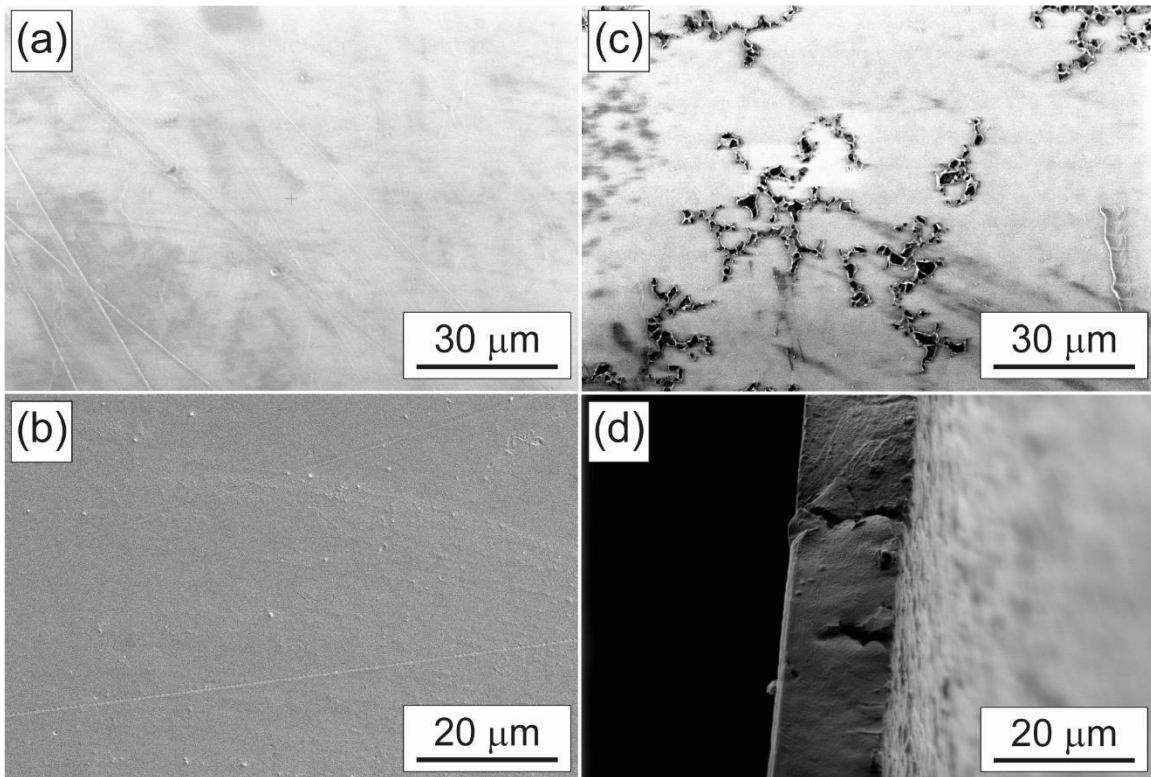


Figure 3.14. Plane-side SEM microphotographs of PVdF membranes dried at different regimes: (a) *only T*, (b) *T+vac*, and (c) *only vac*. (d) Cross-section image of the PVdF membrane dried with *only vac*. demonstrating high probability of open pores.

#### 3.2.4. Effect of Filler Distribution

As assumed in Section 1.4.4, large and/or agglomerated filler particles may trap pores in the composite, thereby increasing a number of interceramic voids and, hence, permeability. Indeed, in Section 3.1.4, we observed sufficient LATP agglomerates of up to 20  $\mu\text{m}$  in the LATP+PVdF membranes, although the mean ceramic particle size was about 1  $\mu\text{m}$  (90-min ball milling; Figure 3.15).

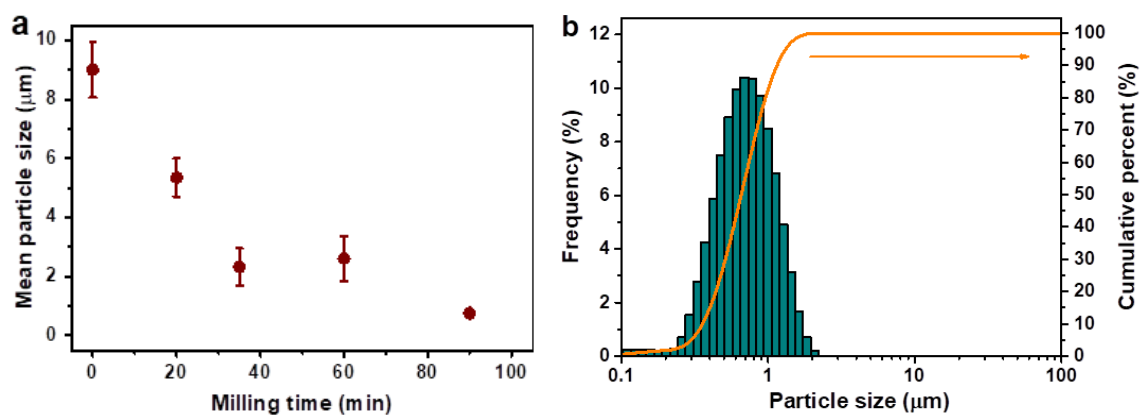


Figure 3.15. (a) Dependence of the mean particle size of LATP on milling time.

(b) Particle size distribution of LATP ball-milled for 90 min.

To achieve better distribution uniformity, we examined the composite membranes fabricated via three different mixing protocols (*Sample A-D*; see preparation description in Section 2.2). The LATP+PVdF membranes fabricated via the *A-C* methods, differed only by the subsequence of components addition, did not show any functional difference — their permeability coefficients were close to each other (Table 3.6). *Sample D* was fabricated with additional ultrasonic treatment of the DMF-LATP suspension to improve the LATP particles dissociation and, therefore, suppress filler agglomeration.

Table 3.6. Permeability coefficients of *Sample A-D*.

<i>Sample</i>	Brief description	Permeability, $10^{-7} \text{ cm}^2 \text{ min}^{-1}$
<i>A</i>	LATP filler added into DMF-PVdF solution	$2.19 \pm 0.24$
<i>B</i>	PVdF powder added into DMF-LATP suspension	$2.27 \pm 0.25$
<i>C</i>	DMF-LATP suspension added into DMF-PVdF solution	$2.59 \pm 0.29$
<i>D</i>	PVdF powder added into <i>ultrasonicated</i> DMF-LATP suspension	$0.86 \pm 0.09$

In Figure 3.16, we compare the plane and cross-sectional sides of the *original* LATP+PVdF membrane ( $T_{\text{mix}} = 50 \text{ }^\circ\text{C}$ ,  $T_{\text{sub}} = 70 \text{ }^\circ\text{C}$ , no DMF-LATP sonication) and *modified* LATP+PVdF ( $T_{\text{mix}} = 25 \text{ }^\circ\text{C}$ ,  $T_{\text{sub}} = 150 \text{ }^\circ\text{C}$ , DMF-LATP sonicated). One can observe that the modification of the composite's fabrication route not only improved the surface, but also diminished the size of filler agglomerates from 20 to *ca.* 5  $\mu\text{m}$  and likely suppressed voids within the agglomerates (Figure 3.16a).

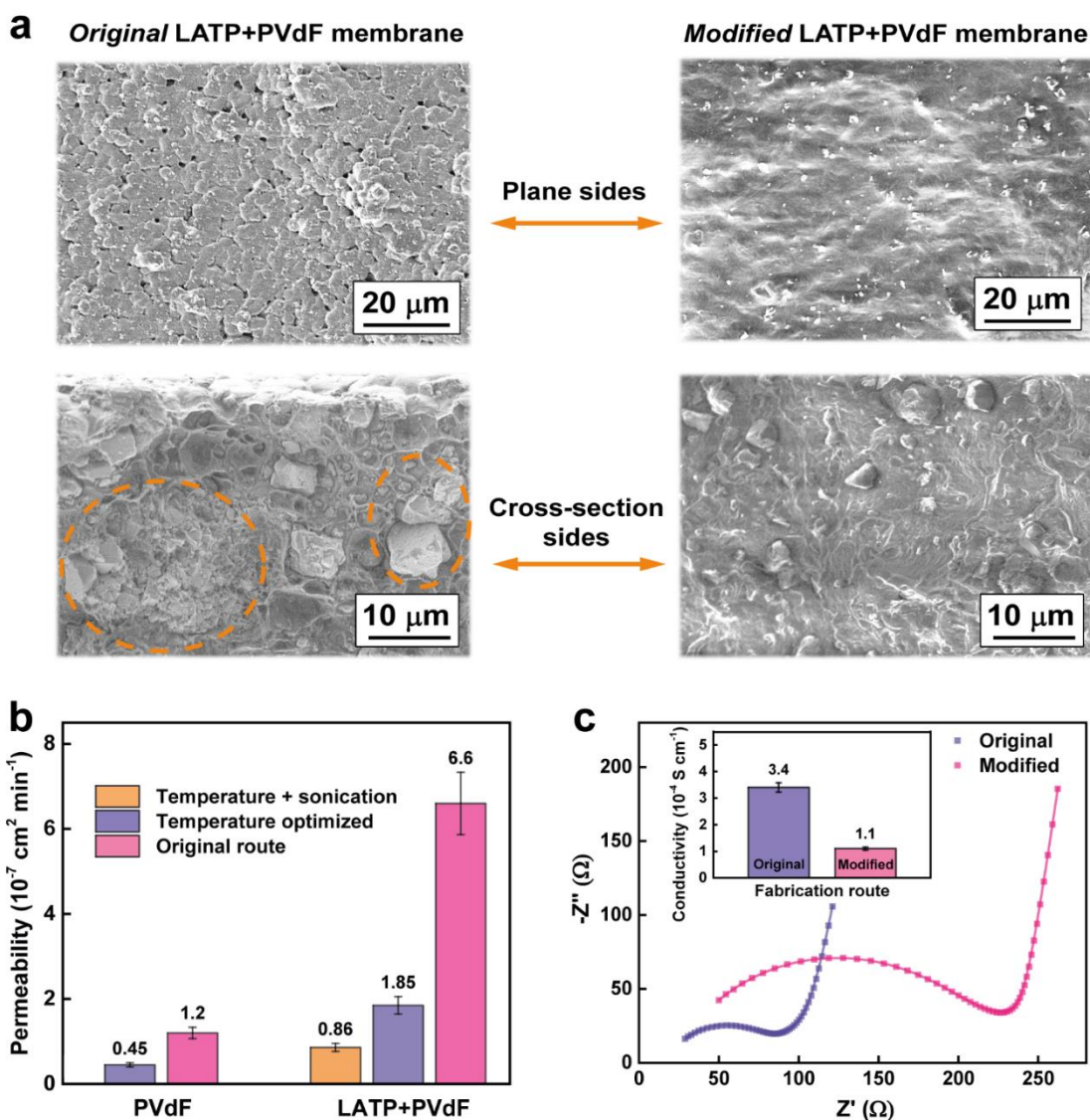


Figure 3.16. (a) SEM images of plane and cross-section morphology of *original* ( $T_{\text{mix}} = 50 \text{ }^{\circ}\text{C}$ ;  $T_{\text{sub}} = 70 \text{ }^{\circ}\text{C}$ ; no DMF-LATP sonication) and *modified* ( $T_{\text{mix}} = 25 \text{ }^{\circ}\text{C}$ ;  $T_{\text{sub}} = 150 \text{ }^{\circ}\text{C}$ ; DMF-LATP sonicated) LATP+PVdF membranes. (b) Permeability coefficients of PVdF and LATP+PVdF fabricated via the *original* route, after temperature refinement, and via the final *modified* technique. (c) Nyquist plots and ionic conductivity data (inset) of LATP+PVdF prepared via the *original* and *modified* routes.

To quantify the advances above, we compared the permeabilities of pure polymeric and composite LATP+PVdF membranes prepared through the *original route*; with the only temperature-optimized route; and with both optimized temperatures and ultrasonication applied (i.e., fully *modified* route; Figure 3.16b). One can see the permeability drop of both PVdF polymer and LATP+PVdF membranes — the coefficients decreased from 1.2 to 0.45 and from  $6.6$  to  $1.85 \cdot 10^{-7} \text{ cm}^2 \text{ min}^{-1}$ , respectively. The DMF-LATP ultrasonication suppressed the composite's permeability further: down to  $0.86 \cdot 10^{-7} \text{ cm}^2 \text{ min}^{-1}$ , the value even lower than of some commercial samples (Figure 3.9b). Therefore, the whole tape-casting routine optimization reduced the LATP+PVdF's permeability by  $\sim 7.5$  times.

Important to highlight, the membrane's porosity and filler distribution do not only define permeability, but also IC. As it was discussed above (Section 3.1.4), the presence of a through porosity system filled with SE solution would also contribute to the IC of a soaked membrane. Hence, the porosity elimination is reasonably expected to suppress the final IC to some extent. Indeed, after the 7.5-fold permeability suppression, membrane's IC drops from  $3.4$  to  $1.1 \cdot 10^{-4} \text{ S cm}^{-1}$  (Figure 3.9c). Even though the desired IC values for a NAqRFB membrane are recommended to reach  $10^{-3} \text{ S cm}^{-1}$  [62], the final IC achieved in our study meets the requirement for solid-state electrolytes ( $>10^{-4} \text{ S cm}^{-1}$ ; Table 1.4). In general, a trade-off between permeability and IC should be chosen individually for each particular system.

In total, the LATP ceramic distribution within the PVdF matrix largely influences the composite's porosity and, hence, it's crucial functional features — permeability and

IC. Among the considered protocols, the preliminary ultrasonic treatment of the DMF-LATP suspension provides the minimal permeability likely due to suppressing the interceramic voids and improving the polymer-ceramic interface.

### 3.3. Conclusions from Chapter 3

In this chapter, we have optimized a number of parameters (associated with composite membrane's composition and fabrication conditions) affecting LATP+PVdF membrane's properties. The summary of these parameters is provided in Table 3.7.

Table 3.7. Parameter values after LATP+PVdF optimization,

Optimizing parameter	Optimal value	Effect
<u>Membrane composition</u>		
Salt-(ceramic+polymer) ratio	0	<i>Salt leaches from polymer matrix</i>
Casting solvent	DMF	LATP cell parameters
Polymer-solvent ratio	15 wt. %	Ease of processing
Ceramic-polymer ratio	45 wt. %	Porosity; IC and permeability
<u>Fabrication condition</u>		
Solution mixing temperature ( $T_{\text{mix}}$ )	25 °C	PVdF phase, morphology, porosity; permeability
Casting temperature ( $T_{\text{sub}}$ )	150 °C	PVdF phase, morphology, porosity; permeability
Drying temperature ( $T_{\text{dry}}$ )	90 °C	No visible effect
Components mixing protocol	<i>D</i>	LATP agglomerate size

After the LATP+PVdF optimization procedure, we can draw the following conclusions:

- 1) An affordable and scalable tape-casting method allows to fabricate the robust composite membranes, consisting of LATP ceramic filler and PVdF polymer matrix, with flexibility, high-voltage stability, and other promising properties, which should be adopted for a certain battery type.
- 2) The LATP ceramic plays a crucial role in defining the composite membrane properties. Despite a slight degradation during the fabrication process (likely due to the leaching of  $\text{Li}^+$  out), the ceramic provides the membrane with competitive Li-ion conductivity of  $>10^{-4} \text{ S cm}^{-1}$  — higher than commercially available samples show in the same conditions (Li-Nafion and Neosepta in SE). The LATP ceramic filler interacts with the polymer matrix and reinforces it suppressing the membrane swelling.
- 3) The LATP filler negatively impacts the composite's porosity and, hence, permeability due to forming agglomerates and interceramic voids. An introduced solvent-ceramic preliminary sonication step successfully diminished agglomerate size (by  $\sim 4$  times) and made the LATP+PVdF's permeability ( $<10^{-7} \text{ cm}^2 \text{ min}^{-1}$ ) lower than that of some commercial samples.
- 4) PVdF's globularity is the main matrix-related factor that impacts the composite's porosity — this was not investigated before. It was found that the  $\beta$  phase of PVdF promotes rough and globular microstructure increasing the number of pores and

promoting permeability. By the precise temperature control during each LATP+PVdF fabrication step (components mixing, membrane casting, and sample drying), almost pure  $\alpha$ -PVdF is obtained that provides dense, non-porous membrane with an extremely low permeability level.

- 5) All the advances made throughout the membrane optimization process are expected to improve the performance and durability of RFB cells equipped with LATP+PVdF. The results described in this Chapter provide a strong impetus to launch the prototyping of the Li-hybrid flow cell.

## **Chapter 4. Prototyping Li-Hybrid Flow Cell Equipped with Composite Membrane**

In this chapter, we examine the performance of LATP+PVdF composite membranes within Li-HFB cells. First, we probe stability of the membrane and adjacent interfaces toward metallic Li. Then, we evaluate performance of the static-mode Li-TEMPO cell equipped with the membrane and analyze its stability during cycling. Finally, we assemble and test a flow-mode Li-TEMPO HFB cell and complement the picture of LATP+PVdF behavior within.

*The results described as well as the figures and tables shown in this chapter were published in Refs. [172,180] — articles with my co-authoring.*

### **4.1. Evaluation of Membranes Stability to Metallic Lithium**

Prior to start composite membrane life tests, we should ensure in its tolerance to metallic lithium anodes, i.e., how effectively the polymer matrix protects the sensitive LATP and provides robustness and integrity to the whole system. For this purpose, we carried out galvanostatic stripping/plating tests in Li-Li symmetric coin cells. We analyzed the LATP+PVdF state before and after the cycling (EIS, instrumental methods) and compare it with several commercially available samples — Li-Nafion and Neosepta AHA.

As one can see (Figure 4.1a), now the system comprises two semicircles related to interfaces. Despite EIS decoding of such systems is not trivial and varies in different publications, here we adopt the description from Refs. [186,190,191].

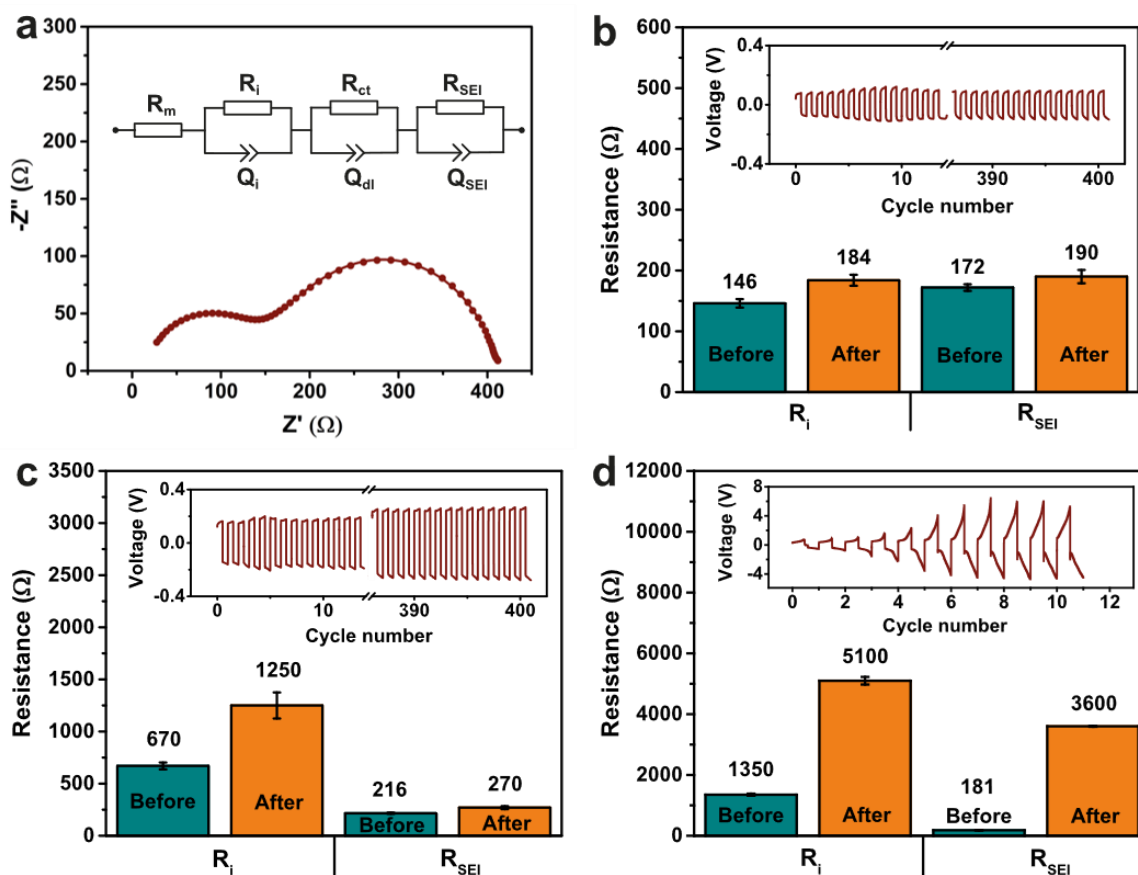


Figure 4.1. (a) Example Nyquist plot with experimental (dots) and fitting data (line) of Li/membrane/Li cells; inset — equivalent circuit used for approximation. Voltage profiles of the Li/membrane/Li cells, as well as interface resistances ( $R_i$  and  $R_{SEI}$ ) before and after stripping/plating tests at  $0.1 \text{ mA cm}^{-2}$  of (b) LATP+PVdF, (c) Li-Nafion, and (d) Neosepta AHA membranes. SE — 1.0 M  $\text{LiClO}_4$  in PC.

The first semicircle was attributed to the membrane-liquid electrolyte interface ( $R_i-Q_i$ ; parameters are close to that of blocking electrodes; Table C2,C3, Appendices), whereas the second one contains the charge transfer ( $R_{ct}-Q_{dl}$ ) and SEI ( $R_{SEI}-Q_{SEI}$ ) impacts (according to Ref. [192]).

Figure 4.1b–d illustrates the stripping/plating voltage profiles and interface resistances for LATP+PVdF, Li-Nafion, and Neosepta. The LATP+PVdF composite and Nafion membranes showed 400 stable charge/discharge cycles with no short-circuiting — no rapid rise of a voltage amplitude [186,193], although the LATP+PVdF's amplitude is smaller (~100 vs. 260 mV; Figure 4.1b–c). Furthermore, interface resistances of the LATP+PVdF cell do not change significantly after the cycling:  $R_i$  grew from only 146 to 184  $\Omega$ , whereas  $R_{SEI}$  increased from 172 to 190  $\Omega$ . In contrast, while the Li-Nafion's  $R_{SEI}$  parameter increased insignificantly (from 216 to 270  $\Omega$ ), the  $R_i$  value rose by more than 85% (from 670 to 1250  $\Omega$ ) that might indicate the interface degradation between Li-Nafion and Li metal [124]. The Neosepta membrane demonstrated even lower stability: the polarization amplitude, extremely high since the first cycle (1 V; Figure 4.1d), grew to 4 V after 8 cycles that might indicate enhancing cell resistances. Indeed,  $R_i$  and  $R_{SEI}$  grew from 1350 and 131  $\Omega$  to 5100 and 3600  $\Omega$ , correspondingly.

As it goes from the stripping/plating and EIS results, only the LATP+PVdF membrane is tolerant to metallic Li and, thus, is suitable for testing within Li-HFB cells. Li-Nafion and Neosepta membranes showed severe interface degradation, so there is no need to exploit them in Li-HFB prototyping.

## 4.2. Performance of Li-TEMPO Static Cell

To continue adopting the composite membrane for Li-HFBs, we assembled the cell with Li in the anode side and a static TEMPO solution at the cathode side (Figure 2.5). Such a simplified cell architecture is acceptable for initial system characterization (e.g., probing overall stability and durability), as it avoids high catholyte volumes, neglects bulk diffusion, etc. These preliminary tests were carried out prior to the final optimization of the membrane described in Chapter 3, therefore, the *original* LATP+PVdF samples (see “Starting Point”; Table 2.1) were applied. Although these samples do not possess improved permeability levels, this application was considered acceptable at this early stage, as we focus on the first evaluation of the general membrane’s cycling stability inside the hybrid cell environment.

Figure 4.2 illustrates the cycling performance of the Li-TEMPO static cell equipped with the LATP+PVdF membrane. It is seen (Figure 4.2b) that coulombic and energy efficiencies exceed 95 and 73% correspondingly during 100 charge/discharge cycles. The initial discharge capacity is  $2.50 \text{ Ah L}^{-1}$ , SoC of *ca.* 93% — almost all TEMPO can be utilized at  $0.5 \text{ mA cm}^{-2}$ . At the same time, the cell’s capacity gradually decreases (first, exponentially, then, linearly) to  $1.37 \text{ Ah L}^{-1}$  by the speed of  $\sim 0.8\% \text{ h}^{-1}$ . Such a trend is quite similar to an ordinary capacity fade of RFBs due to crossover [194]. As far as the porosity of the initial composite was *ca.* 33% (Table 3.3), we can reasonably expect LATP+PVdF to be partially penetrable for TEMPO molecules.

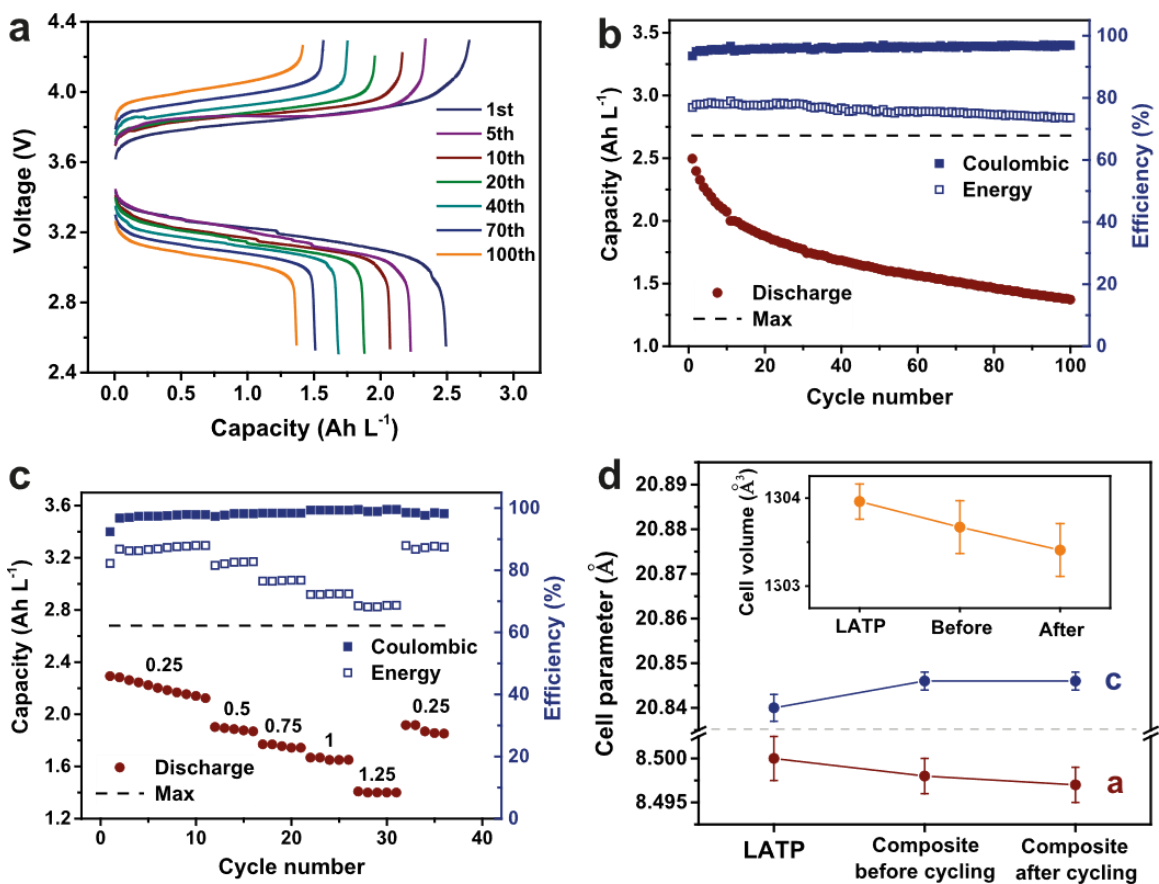


Figure 4.2. Performance of Li-TEMPO HFB cell equipped with LATP+PVdF composite membrane. (a) Charge/discharge profiles at 0.5 mA cm<sup>-2</sup>. (b) Discharge capacity with coulombic and energy efficiencies at 0.5 mA cm<sup>-2</sup>. (c) Rate performance at 0.25–1.25 mA cm<sup>-2</sup>. (d) Unit cell parameters and (inset) cell volume of LATP ceramic as a pristine powder, in as-synthesized LATP+PVdF, and in the membrane after 100 charge/discharge cycles in the Li-TEMPO static cell.

Catholyte — 0.5 M TEMPO + 1.0 M LiClO<sub>4</sub> in PC.

At first cycles, the TEMPO concentration in the anode part is close to zero, so the concentration gradient is high and TEMPO species go through the membrane rapidly. The more TEMPO transferred, the lower is the gradient, and, hence, the capacity fade decelerates (the linear region in Figure 4.2b). With the increase of current density (Figure 4.2c), coulombic efficiency grows slightly, whereas the capacity decreases slower, which might be attributed to the TEMPO crossover as well.

To evaluate the LATP+PVdF's stability, we applied a set of XRD, FTIR, and SEM analyzes both before and after the cycling. From Figure 4.3a,b, it is seen there are neither admixture phases nor signs of serious composite degradation appeared after 100 cycles. Furthermore, the unit cell dimensions and cell volume of the LATP filler did not change significantly during membrane fabrication and subsequent cycling tests (Figure 4.2d). The SEM images state no morphology degradation as well (Figure 4.3c-f).

The LATP+PVdF composite membrane demonstrated the promising performance in the static Li-TEMPO cell: high coulombic (>95%) and energy efficiency (>73%), as well as ambitious cycling durability primarily due to the high phase and interfaces stability of LATP+PVdF. The main drawback as expected is the TEMPO species crossover through the membrane led to severe cell's capacity decay ( $0.8\% \text{ h}^{-1}$ ). We hope that the permeability suppression advances shown in Chapter 3 will decrease the capacity decay. Therefore, in the next section, we tested the fully optimized LATP+PVdF in the designed Li-TEMPO flow cell.

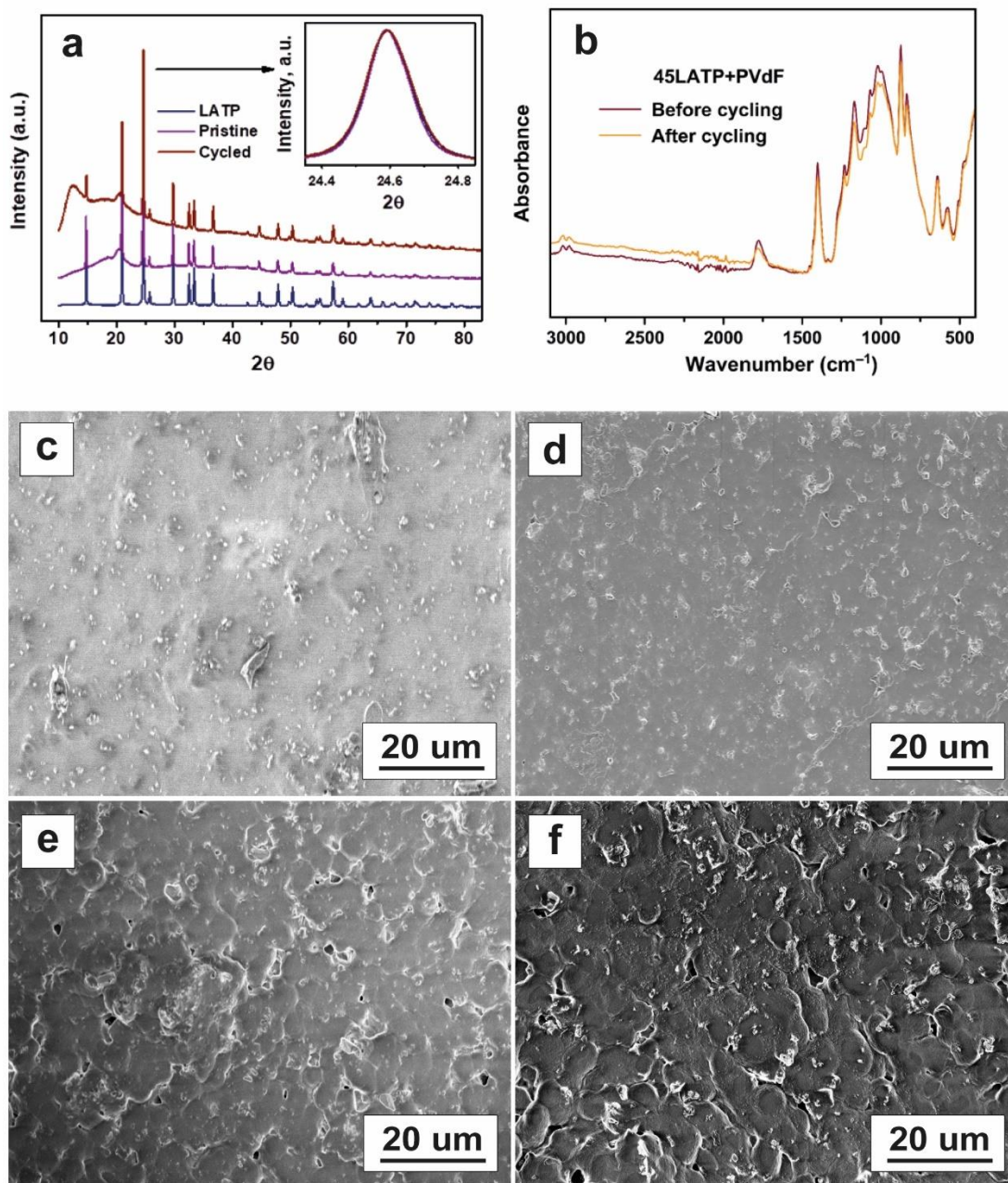


Figure 4.3. State of LAMP+PVdF membrane before and after 100 charge/discharge cycles in the Li-TEMPO static cell. Comparative (a) XRD patterns, (b) FTIR spectra, and SEM images of (c, d) smooth and (e, f) rough membrane sides.

### 4.3. Performance of Li-TEMPO Flow Cell

The *flow*-mode cell operates with much higher volumes of catholyte and hides other pitfalls, so its prototyping requires much more effort than for the *static* cell. In this section, besides probing optimized membrane's performance, we discuss Li-HFB cell's TCR — a complex parameter that defines the highest applicable current and, hence, energy density. Here, we also discuss Li-HFBs' capacity retention and membrane's state after cycling.

Besides a membrane, catholyte's SE composition impacts Li-HFB's TCR. To find a suitable candidate, we examined a set of SEs (see the list in Section 2.2) that allows to reveal the impact of a supporting salt, its concentration, and a solvent separately. SE I (1.0 M LiClO<sub>4</sub> in PC) is a common composition previously used in our electrochemical analysis as well as in RFB testing from literature [66,70,195]. However, in the flow operation mode, it shows non-uniform charge/discharge trends with evident “shoulders” at first cycles, capacity shrinkage, and the ohmic drop increase (Figure 4.4a). Such an unstable operation of PC-based SEs might be attributed to specific PC-derived subproducts hindering the generation of suitable SEI for metallic Li anodes [196–198].

To improve the cycling stability, we substituted PC with EC:DEC (SE II). EC solvates Li<sup>+</sup> ions in a lower extent than PC that leads to a more proper initiation of stable SEI [198,199]. DEC, facilitating ionic transportation, is frequently used in combination with EC for Li-ion batteries [199]. However, substituted the solvent to EC:DEC, we observed a similar trend — unidentified sharp inflections of the charge/discharge curves and even more drastic capacity shrinkage (Figure 4.4b).

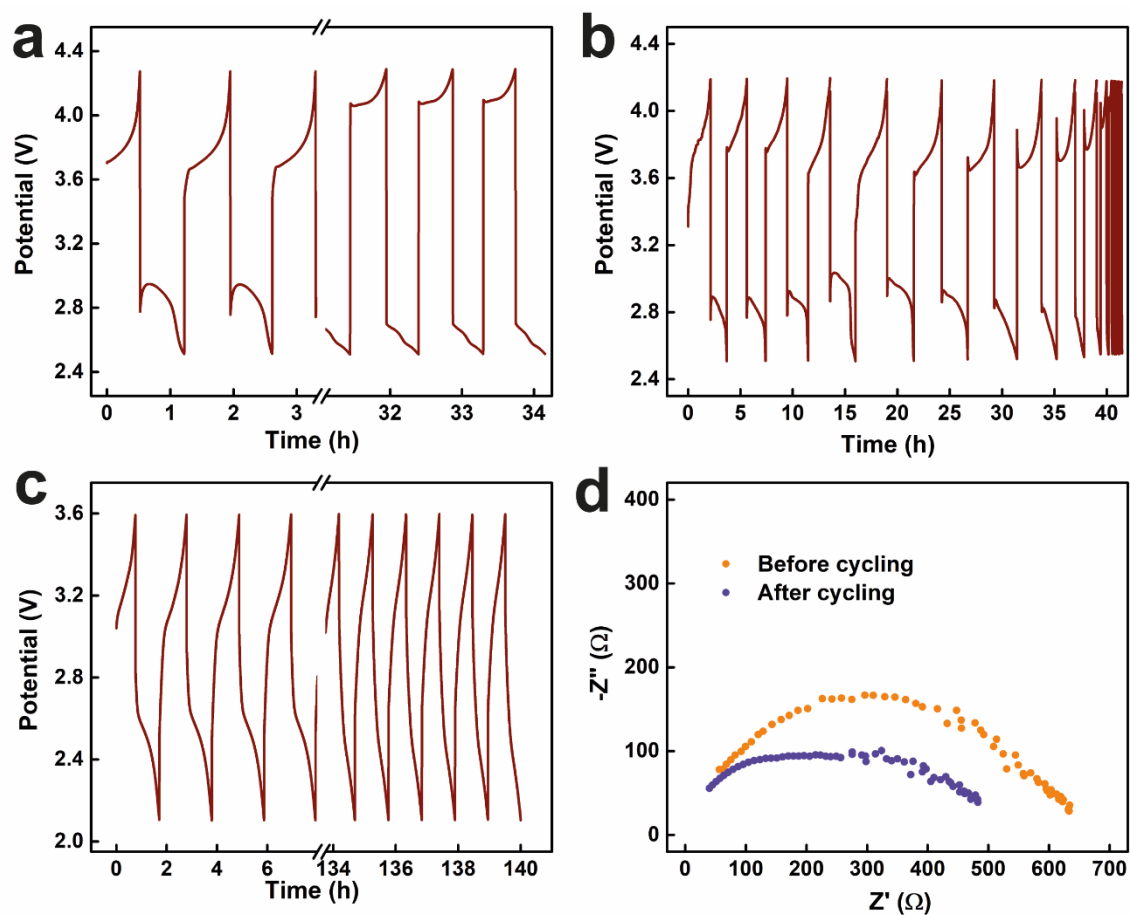


Figure 4.4. Cycling performance of Li-TEMPO HFB cell operating with (a) 1.0 M LiClO<sub>4</sub> in PC, SE I; (b) 1.0 M LiClO<sub>4</sub> in EC:DEC, SE II; and (c) 1.0 M LiTFSI in EC:DEC, SE III; (d) Nyquist plots obtained for the Li-HFB cell before and after 100 cycles using SE III. Current — 0.5 mA, active area — 2.55 cm<sup>2</sup>.

At the next step, we changed the  $\text{LiClO}_4$  salt to LiTFSI, which is better for SEI formation and more tolerant for carbon electrodes [199,200]. Resulting SE **III** gave more gradual and stable cycling than previous SE **I–II** (operation for 140 vs. 40 h, Figure 4.4c). Likely, the  $\text{LiClO}_4$  salt was the main reason for SE **I–II** poor cyclability, although the nature of this effect is unknown and should be evaluated.

TCR measurements before and after cycling supports the observed SE **I–III** behavior. Indeed, TCRs of SE **I–II**, initially quite high (790 and 650  $\Omega$ ), increase to 950 and 900  $\Omega$ , respectively, after the cycling (Figure 4.5a). TCR of SE **III**, initially quite close to SE **II**, on the contrary, diminishes from 640 to 550  $\Omega$ . This TCR decrease might be associated with the better SEI stabilization, for which LiTFSI is responsible. These TCR results imply two points: i) EC:DEC solvent is more favorable than PC in terms of TCR; ii) unlike to  $\text{LiClO}_4$ , the LiTFSI salt provides the long-term cycling probably due to the less-resistant SEI formed.

Next, we investigate the effect of LiTFSI concentration on TCR (SE **III–VI**; Figure 4.5b). The 0.75 M LiTFSI concentration provides the lowest TCR value among the studied SEs — 510  $\Omega$ . At concentrations below 0.75 M, TCR decreases due to the  $\text{Li}^+$  concentration lowering; whereas above 0.75 M, it likely increases due to the raise of electrolyte viscosity. Overall, SE **IV** turned up to be the least resistive electrolyte, so it will be used further to perform the durability tests and evaluate the cell characteristics.

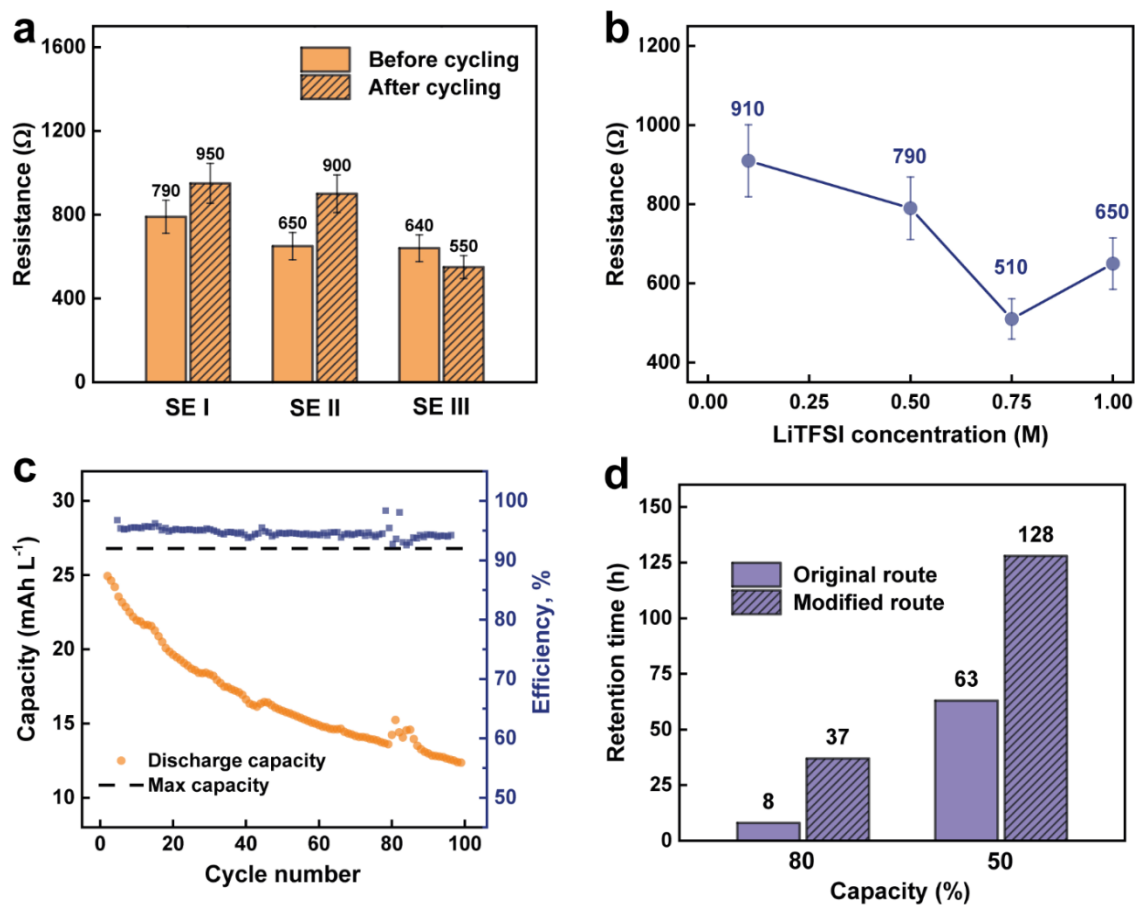


Figure 4.5. (a) Cell resistance before and after cycling tests of the Li-TEMPO flow cell operated with SE I–III. (b) Dependence of initial TCR on LiTFSI salt concentration in SE III–VI; (c) Discharge capacity and coulombic efficiency of the Li-TEMPO cell at 0.5 mA (2.55 cm<sup>2</sup> active area) using SE IV-based catholyte — 1 mM TEMPO + 0.75 M LiTFSI in EC:DEC; (d) Cell capacity retention times,  $t_{80}$  and  $t_{50}$ , of LATP+PVdF membranes fabricated via the *original* and *modified* routes.

From Figure 4.5c it is seen that coulombic efficiency of the SE **IV**-based cell was ~95% for 100 cycles. However, initial capacity of 24.9 mAh L<sup>-1</sup> (93% of theoretical) gradually decreases to 12.4 mAh L<sup>-1</sup> — the fade is close to that observed for the *original* membrane (~50%; Section 4.2). From the first sight, it might seem the membrane's permeability optimization did not affect the capacity fade rate. However, the *original* LATP+PVdF was tested in the static cell, where a single charge\discharge cycle takes much less time than in the flow one. Therefore, to compare the performance of the *original* and *modified* membranes properly, we introduce the  $t_{80}$  and  $t_{50}$  parameters that characterize how much time the battery retains 80 and 50% of its initial capacity, respectively. In these terms, the Li-HFB cell with the *modified* membrane maintains 80 and 50% capacity for 37 and 128 h against 8 and 63 h for *original* LATP+PVdF (Figure 4.5d). The cell with the *modified* membrane exhibits the capacity losses of *ca.* 0.4% h<sup>-1</sup> vs. 0.8% h<sup>-1</sup> for the original sample (Section 4.2). Among the publications devoted to Li-HFBs [65,67,70–73,195,201], according to our knowledge, only a few explicitly discuss capacity retention. In the current work, we achieved the ~68% capacity retention after 50 cycles, which is quite close to the reported literature data (Table 4.1).

Table 4.1. Comparison of Li-hybrid flow cells performance reported in literature.

Catholyte redox species / Concentration	Supporting electrolyte	Capacity retention, % / N cycles	Coulombic efficiency, % / Current, mA cm <sup>-2</sup>	Membrane	Limitations	Ref.
TEMPO / 1 mM	0.75 M LiTFSI in EC:DEC	68 / 50 50 / 100	94 / 0.2	Composite: LATP+PVdF	Low TEMPO initial availability; high cell resistance	This work
Methoxymethyl ferrocene / 100 mM	1 M LiTFSI in DME	30 / 100	91 / 20	Porous: Daramic	DME volatizes in 100 cycles	[201]
DB-1 / 80 mM	1 M LiTFSI in DMSO	100 / 50	99 / 20	IEM: Nafion 115	Low solubility and affordability of active species	[72]
TEMPO / 50 mM	1 M LiPF <sub>6</sub> in PC	70 / 50	97 / 5	Porous: Celgard	TEMPO degradation during cycling	[195]

Methyl-phenothiazine / 50 mM	1 M LiPF <sub>6</sub> in EC:DEC	95 / 1000	99 / 0.2	Ceramic: LAGP	Low catholyte volume – 4 mL	[73]
MeO-TEMPO	LiTFSI + 17 wt.% H <sub>2</sub> O ionic liquid	84 / 20	– / 0.2	Ceramic: LICGC	Low catholyte volume – 50 μL	[71]
TEMPO / 100 mM	1.0 M LiPF <sub>6</sub> in EC:PC:EMC + 15 wt.% FEC	99 / 100	99 / 5	Porous: polyethylene-based	Highly corrosive LiPF <sub>6</sub>	[70]
Anthraquinone / 250 mM	1 M LiPF <sub>6</sub> in PC	70 / 40	93 / 0.1	Porous: Celgard	Low cell voltage	[67]
Benzoquinone / 10 mM	1 M LiClO <sub>4</sub> in GBL	77 / 25 50 / 100	– / 0.05	Ceramic: LICGC	Fast capacity decay	[65]

---

After prolonged cycling of the membrane, we analyzed the LATP structural changes to ensure its stability in the real conditions of operating Li-HFB cell. Discussing the LATP structure, we compared ceramic's unit cell volumes ( $V$ ) and intrastructural polyhedron  $[\text{Li}(1)\text{O}_6\text{M}_2]$  volume following Refs. [116,125]. Initial LATP represents a well-crystallized and pure NASICON phase;  $V$  and  $[\text{Li}(1)\text{O}_6\text{M}_2]$  values (Appendices, Figure B1) were close to that previously reported [125]. After the LATP+PVdF fabrication, one can observe two phases (Appendices, Figure B2): LATP (refined) and  $\alpha$ -PVdF (identified qualitatively based on Ref. [202]). LATP filler's  $V$  shrank by 0.25%, whereas  $[\text{Li}(1)\text{O}_6\text{M}_2]$  grew by 4.22%. We expect these changes were caused by the Li losses accompanied by the Al/Ti ratio shift that occurred during the intense ball-milling and prolonged ceramic exposure to DMF [47]. After the cycling, LATP+PVdF still contained the same distinguishable phases (Appendices, Figure B3). However, we see the shift of both  $V$  and  $[\text{Li}(1)\text{O}_6\text{M}_2]$  toward the initial values of LATP. The  $V$  loss diminishes from 0.25% to 0.11%, while the  $[\text{Li}(1)\text{O}_6\text{M}_2]$  decreases by 1.60% opposite to the 4.22% growth for the as-prepared membrane (Figure 4.6). Such behavior might only be caused by the LATP active involvement in  $\text{Li}^+$  migration processes, despite it is embedded in a PVdF matrix. This conclusion supports our previous results (Section 3.1.4): IC of the membrane with the inert  $\text{Al}_2\text{O}_3$  filler was  $\sim 8$  times lower compared to that for LATP+PVdF.

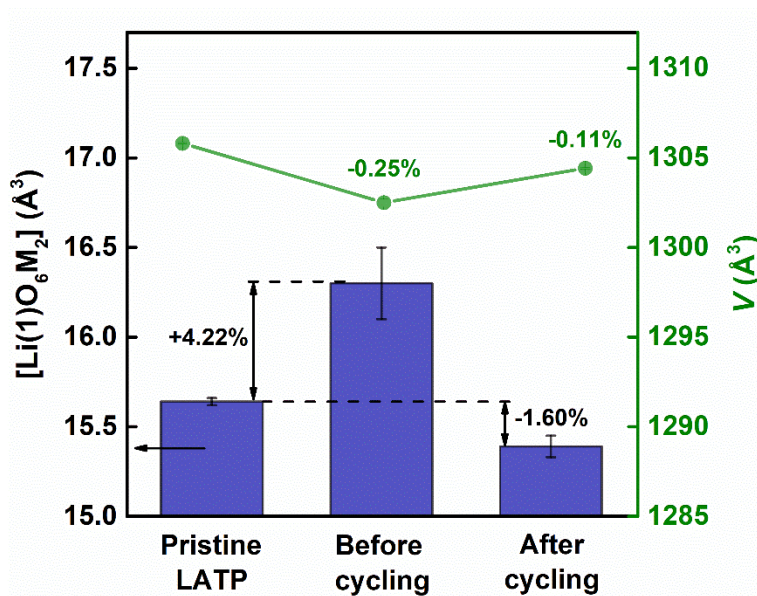


Figure 4.6. L ATP cell volume ( $V$ ) and  $[\text{Li}(1)\text{O}_6\text{M}_2]$  polyhedron volume of pristine ceramic and inside L ATP+PVdF membrane before and after 100 cycles in Li-HFB cell.

As far as the surface of ceramic grains is mostly covered with oxygen [125], we did not expect PVdF to be coordinated to L ATP by fluorine. Indeed, F atoms are distributed homogeneously within the PVdF matrix in the as-fabricated composite membrane (Figure 4.7). However, after cycling one can see the prominent excess of F right around a filler particle. Assuming PVdF is the only F-contained component in the system (LiTFSI was washed out), we can associate the accumulated F atoms with Li counterions both involved in polymer-ceramic interface formation. Although the  $-\text{F}\cdots\text{Li}$  coordination should elongate the C–F bond, the vibration frequency shift at  $1180\text{ cm}^{-1}$  is not observed in FTIR spectra (Figure 4.8). More comprehensive interface analysis is needed to explain the influence of cycling on L ATP+PVdF.

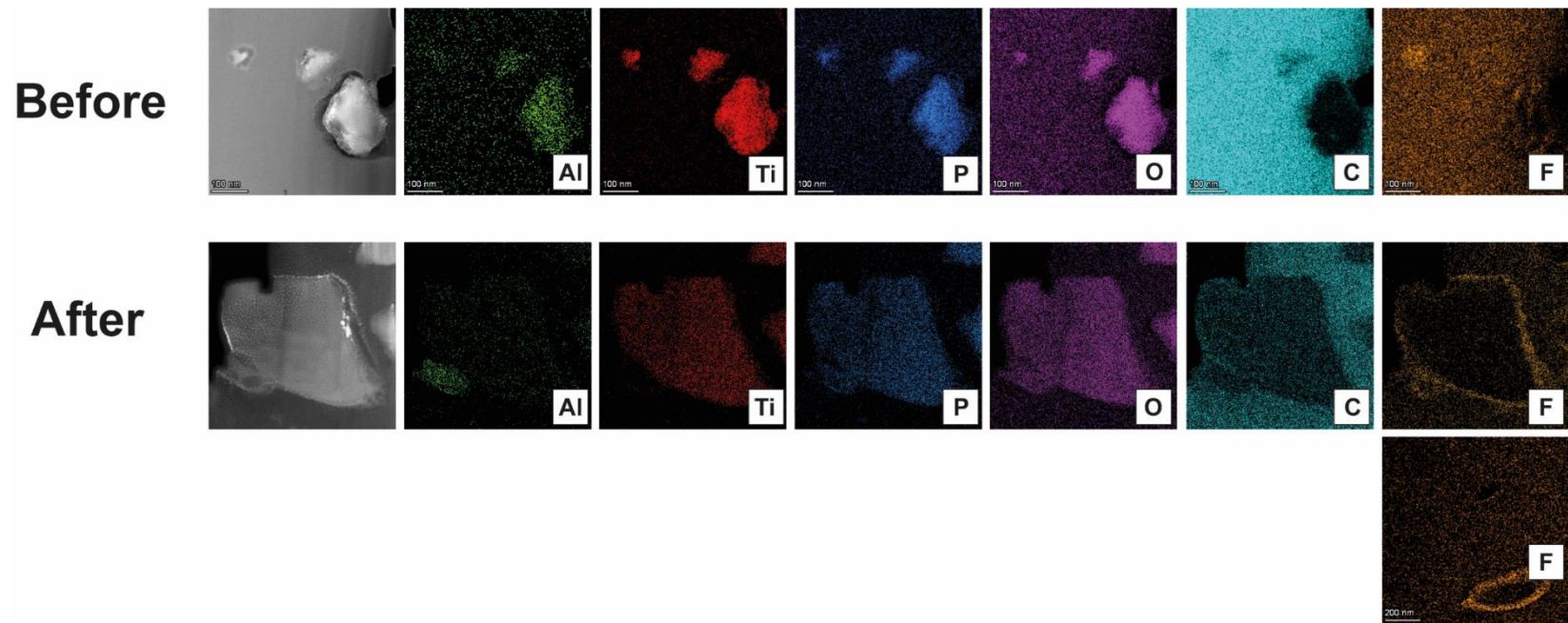


Figure 4.7. TEM-EDX images of LATP ceramic particles blended in a PVdF matrix within a composite membrane before and after 100 cycles in the Li-HFB cell.

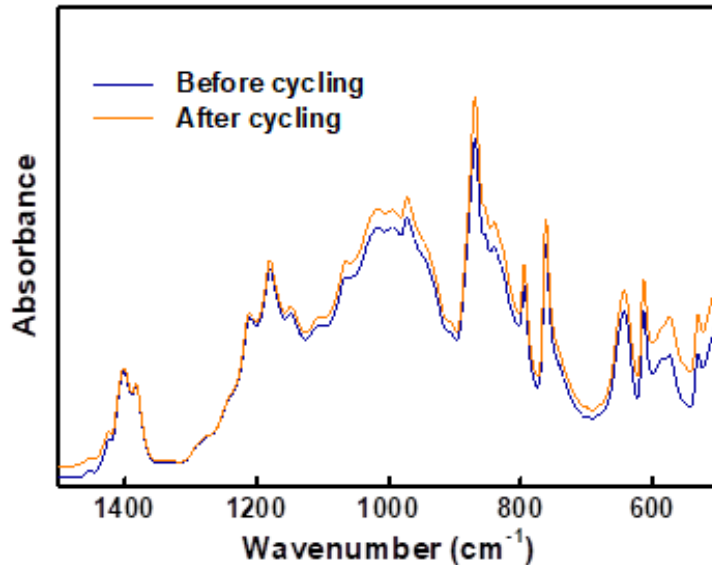


Figure 4.8. FTIR spectra of LATP+PVdF after 100 cycles in the Li-HFB cell.

The designed Li-TEMPO HFB cell, operated with the modified composite membrane and cyclable SE, showed >95% coulombic efficiency during 100 cycles. The cell's capacity decay still exists, though halved (0.4 vs. 0.8% h<sup>-1</sup>) comparing to the non-optimized membranes. After the cycling, LATP+PVdF showed excellent phase and composition stability — neither impurity, decomposition, or etching were observed. The LATP cell volume parameters,  $V$  and  $[\text{Li}(1)\text{O}_6\text{M}_2]$ , indicated the filler active involvement in electrochemical processes — the Li-ion transfer significantly impacts the LATP structure and the filler-matrix interface. Although the composite membrane proved to be very promising for Li-HFBs, configuration of the catholyte, flow cell, etc. should be further optimized to move the Li-HFB forward to the next prototyping stage.

#### 4.4. Conclusions from Chapter 4

Evaluated the performance of the Li-TEMPO HFB cells and the LATP+PVdF membrane's stability within, we summarize the main results achieved in this chapter:

- 1) The composite membrane, as well as the adjacent interfaces, were probed to be stable toward metallic Li, unlike the common commercially available samples (Nafion, Neosepta). The first LATP+PVdF's life tests within the Li-TEMPO static cell did not show any signs of a severe morphology, phase, or structural degradation.
- 2) The main problem occurred during the primary cycling tests was a cell's capacity decay due to sufficient crossover through the composite membrane. The introduced LATP+PVdF modification (Chapter 3) enhanced the cell's capacity stability diminishing the fade twice: from 0.8 to 0.4% h<sup>-1</sup>. Besides, the optimal SE composition (0.75 M LiTFSI in EC+DEC) provided the Li-TEMPO flow cell with ~93% initial capacity and >95% coulombic efficiency during 100 charge/discharge cycles.
- 3) The volume changes of the Li-involved LATP's polyhedron supported our previous assumption — ceramic particles actively participate in the ion-conductivity process within the composite membrane. Moreover, the microscopy analysis confirmed the presence of an interaction between the PVdF matrix and LATP filler that likely enhances during the cell operation; though, internal interfaces' behavior should later be thoroughly studied.

## **Chapter 5. Conclusions and Future Perspective**

In the final chapter, we discuss the results of developing the hybrid battery system — Li-TEMPO HFB cell equipped with the LATP+PVdF composite membrane. We summarize all the advances achieved and define the limitations one should focus on for further development of the system to the next stage of prototyping. In the end, we draw final conclusions of the Thesis.

### **5.1. System Advances and Paths for Improvement**

In the previous chapters, we worked with a large variety of different aspects and pitfalls of Li-HFB cells and its components. Relying on the literature data and following own experience, we collected important features and requirements (Table 5.1) of the Li-HFB concept. We also provide a list of recommendations to solve a number of Li-HFB-related issues. We identify them into the Membrane, Catholyte, and Design Problems. To each problem, the value threshold, related Li-HFB's characteristics, our personal outcome, and practical recommendations correspond.

Table 5.1. Parameters crucial for Li-HFB cell high performance related to Membrane, Catholyte, and Design Problems.

Parameter	Value or quality threshold / Impact	Our value / <u>Perspective</u>	Recommendation
1. Membrane Problems			
1.1. Ionic conductivity	$10^{-4}$ – $10^{-2}$ S cm <sup>-1</sup> / Current density	$1.1 \cdot 10^{-4}$ S cm <sup>-1</sup> / <u>To be improved</u>	<ul style="list-style-type: none"> <li>- Improve membrane's internal interfaces: ceramic-polymer, ceramic-ceramic, etc.;</li> <li>- Introduce conductive but stable additives;</li> <li>- Evaluate the impact of each fabrication step on components and final composite;</li> <li>- Tune volume fraction of conductive filler;</li> <li>- Evaluate other materials and designs;</li> </ul>
1.2 Permeability	$<10^{-6}$ cm <sup>2</sup> min <sup>-1</sup> (depends on solvent) / Capacity decay rate	$0.86 \cdot 10^{-7}$ cm <sup>2</sup> min <sup>-1</sup> / <u>Good</u>	<ul style="list-style-type: none"> <li>- Improve membrane's internal interfaces;</li> <li>- Tune membranes porosity;</li> <li>- Consider effects of matrix phase and microstructure</li> <li>- Consider the size of redox-active species;</li> <li>- Evaluate the impact of each fabrication step;</li> <li>- Post-treatment to collapse porosity;</li> </ul>

1.3 Chemical stability of components and interfaces	Neither membrane nor interfaces degradation / Cell resistance, battery lifetime	400 cycles with no drastic increase of interfacial resistances and cell short-circuit / <u>Good</u>	<ul style="list-style-type: none"> <li>- Improve membrane's internal interfaces;</li> <li>- Estimate stability of phase, structure, and functional features of both, components and final composite;</li> <li>- In case of a sensitive filler, consider a matrix that acts as protective sealing;</li> </ul>
---	---	---	--

---

## 2. Catholyte Problems

2.1 Active species: stability; concentration	No degradation during cycling; >1 M / Energy density, battery lifetime	1 mM / <u>To be estimated;</u> <u>improved</u>	<ul style="list-style-type: none"> <li>- Find the concentration-solubility trade-off;</li> <li>- Improve the solubility through SE modifying;</li> <li>- Tailor the structure (easily applied for organic molecules) for a more suitable size/stability;</li> </ul>
2.2 Supporting electrolyte: resistance; capability with SEI	The lower resistance, the better / Current density, battery lifetime	0.75 M LiTFSI in EC:DEC; 100 cycles / <u>To be improved</u>	<ul style="list-style-type: none"> <li>- Optimize SE composition to achieve cell components stability, low viscosity, and resistance;</li> <li>- Consider cyclable F-contained salts;</li> <li>- Apply electrolyte enhancers (e.g., FEC, VC);</li> </ul>

---

---

### 3. Design Problems

3.1 Interfacial resistances	Cell resistance of $<100 \Omega$ / Current density	Total cell resistance of $\sim 600 \Omega$ / <u>To be improved</u>	- Evaluate cell components to form stable and low-resistant interfaces; - Emphasize anode design — one of the most crucial part responsible for Li-HFB operation;
3.2 Cell architecture and other parameters	General impact on cell resistance, capacity availability, stability, etc.	<u>To be improved</u>	- Work on the design optimization of electrodes, current collectors, pumping system, catholyte circulation, etc.

---

1. Membrane Problems. Research usually starts with identifying promising components: supporting Li salt ( $\text{LiClO}_4$ , LiTFSI, if applicable), polymer matrix (PAN, PEO, PVdF, etc.) and filler (LZTO, LATP, etc.) [203]. We have followed the same strategy: we started with optimization of the LATP ceramic [116,125] and chose PVdF and  $\text{LiClO}_4$  as prospective matrix-salt basis. Then, we continued with setting the LATP+PVdF fabrication routine: varied a number of composite's composition and fabrication parameters and measured the sample's IC, permeability, stability, and cyclability. Although we have broken the initial threshold for IC ( $10^{-4} \text{ S cm}^{-1}$ ; 1.1, Table 5.1), it should be further increased to  $10^{-3} \text{ S cm}^{-1}$  and higher to show the performance close to that of conventional LIBs. The further increase of the membrane's IC can be implemented by improving the inner interfaces through modifying the components, introducing linking and conductive agents, and developing alternative fabrication procedures. The membrane's permeability feature (1.2) is dictated by its porosity and interfacial behavior. Working on the porosity, one should consider the connection between IC and permeability, relevant for the RFB membranes, open pores of which are filled with SE. For the Li-HFB membranes, stability toward metallic Li anode should be evaluated to exclude the degradation of interfaces or the growth of Li dendrites (1.3). In sum, the membrane's performance depends on its components and their interrelations.

2. Catholyte Problems can be distinguished into the issues related to active species (2.1; Table 5.1) and SE (2.2). A RFB capacity loss can be affected by the size of redox-active compounds through the crossover. Bigger molecules harder diffuse through

the membrane, so show lower permeability. At the same time, the solubility of larger species is frequently lower, and one should follow a trade-off in the size design [66]. TEMPO utilized in this work possesses high solubility in carbonate SEs (~2 M), but has a small size [70]. As a result, TEMPO still goes through LATP+PVdF even after the membrane optimization, although twice less than it used to be (Figure 4.5d). Permeability can be suppressed even more by the substitution of redox-active moieties to larger molecules, for instance, quinoxalines (e.g., DBBB), triarylaminines, and other. [204,205]. Additionally, the species stability should be evaluated to exclude the degradation as a source of cell's capacity fade. The SE issues (2.2) impact battery's total resistance and lifetime. Bulky salts or highly concentrated solutions can hinder the  $\text{Li}^+$  diffusion. Finally, to improve the cell cyclability and stabilize SEI, fluorine-contained salts (e.g., LiTFSI and family) and small amounts of specific solvent additives (VC, FEC [206]) can be used.

3. The cell Design also defines TCR. In addition to membrane and SE impacts, TCR also contains the contributing interface resistances (3.1), such as current collector-Li, Li-liquid electrolyte (SEI), and catholyte-carbon felt. Ideally, to decrease TCR, each interface should be separately optimized. A special attention should be devoted to the Li-HFB's anode compartment. Here, we place the membrane directly onto the metallic Li anode because of its proven stability. This allows us to avoid additional intermediate layers of Celgard [67,126] or carbon papers [70,195,201] that are frequently used in the literature. Before, we have already mentioned adding catholyte species to the anode cell compartment (Section 1.3.3). From one hand, it boosts the applied current density, but neglects the

membrane’s permeability and deprives the Li-HFB’s simplified architecture. Another design problem that we personally faced is a low TEMPO concentration in the catholyte during the flow cell cycling. At the concentrations higher than 1 mM, the initially available cell capacity drastically fell down (Table 5.2) — currently, it cannot be explained. So far, such low concentrations might be acceptable, as we have focused mainly on the *membrane* development. This issue should be resolved during further steps of Li-HFB prototyping.

The current Thesis work shows the complexity and versatility of developing a Li-HFB and, particularly, a membrane applicable for this type of batteries. Nevertheless, through the thorny optimization path, we configured the composite membrane with acceptable IC, low permeability, and superior stability within the Li-HFB environment. In our notation, we have solved the vast majority of the Membrane Problems toward the creation of a Li-HFB prototype. To step forward, from now on, the main attention should be devoted to overtaking the Catholyte and cell Design issues. We would like to particularly emphasize the TCR diminish, anode compartment modification, and active species availability resolution as the starting points for the next research.

Table 5.2. Dependence of Li-TEMPO flow cell capacity on TEMPO concentration.

Concentration, mM	Initial capacity, % of theoretical
1	93
10	12
100	~1

## 5.2. Conclusions of the Thesis

- 1) Through a combination of physico-chemical and electrochemical techniques, we revealed that easily fabricated ceramic-in-polymer composite membranes are promising for Li-HFBs — prospective electrochemical devices for large-scale energy storage.
- 2) We found that the PVdF's phase and microstructure significantly affect the membrane's porosity, which eventually defines its permeability to the catholyte's redox-active species. By applying the proper temperature regime during the fabrication (components mixing at RT, film casting at 150 °C, samples drying under atmospheric pressure), we suppressed the membrane's permeability from 6.6 to  $1.85 \cdot 10^{-7} \text{ cm}^2 \text{ min}^{-1}$ .
- 3) We elucidated that the ceramic filler affects both the composite's permeability and IC. The added LATP particles tend to form large agglomerates ( $\sim 20 \mu\text{m}$ ) comprising severe intragranular voids that promote the membrane's permeability. The preliminary ultrasonic treatment of the solvent-ceramic suspension destroys major agglomerates and further diminishes the permeability — from 1.85 to  $0.86 \cdot 10^{-7} \text{ cm}^2 \text{ min}^{-1}$ . By means of blending inert particles into the matrix, we showed that the Li-conductive ceramic filler mostly contributes to the IC of the composite membranes: the addition of 45 wt.% LATP to PVdF enhances its IC from 0.38 to  $3.4 \cdot 10^{-4} \text{ S cm}^{-1}$ , whereas the same amount of  $\text{Al}_2\text{O}_3$  provides only  $0.45 \cdot 10^{-4} \text{ S cm}^{-1}$ . What is more, the volume

fluctuations of Li-contained polyhedra before and after membrane cycling confirm the active participation of LATP filler in the conductivity process.

- 4) The LATP+PVdF composites showed superior bulk and interfacial stability toward metallic Li. By cycling the membrane within the Li-TEMPO static cell, we ensured the system was capable of providing competitive efficiency, durability, and specific capacity with neither phase nor morphological changes. The main disadvantage is the rapid capacity decay likely caused by a crossover — one of the problems we mainly address during the Thesis.
- 5) The designed Li-TEMPO HFB cell, equipped with the developed membrane, demonstrates high coulombic efficiency (>95%) during 100 charge/discharge cycles and a high initial capacity (>93%). After the LATP+PVdF optimization, the capacity decay rate was reduced by half from 0.8 to 0.4% h<sup>-1</sup>. After the significant advances made in membrane development, for further Li-HFB prototyping, we emphasize solving the issues related to the catholyte and electrochemical cell design through a TCR decrease, active species upgrade or substitution, etc.

## Bibliography

1. What Is Energy Transition? Available online: <https://www.spglobal.com/en/research-insights/articles/what-is-energy-transition> (accessed on 24 January 2023).
2. Martins, F.; Felgueiras, C.; Smitkova, M.; Caetano, N. Analysis of Fossil Fuel Energy Consumption and Environmental Impacts in European Countries. *Energies (Basel)* **2019**, *12*, 964, doi:10.3390/en12060964.
3. Blanc, P.; Zafar, M.; Levy, J.; Gupta, P. Five Steps to Energy Storage. Innovation Insights Brief 2020. *World Energy Council* **2020**, 62.
4. Ibrahim, H.; Ilinca, A.; Perron, J. Energy Storage Systems-Characteristics and Comparisons. *Renewable and Sustainable Energy Reviews* 2008, *12*, 1221–1250.
5. Palizban, O.; Kauhaniemi, K. Energy Storage Systems in Modern Grids—Matrix of Technologies and Applications. *J Energy Storage* 2016, *6*, 248–259.
6. Energy Storage Systems Market Size Report, 2030 Available online: <https://www.grandviewresearch.com/industry-analysis/energy-storage-systems-market> (accessed on 27 January 2023).
7. Chen, H.; Cong, T.N.; Yang, W.; Tan, C.; Li, Y.; Ding, Y. Progress in Electrical Energy Storage System: A Critical Review. *Progress in Natural Science* **2009**, *19*, 291–312, doi:10.1016/j.pnsc.2008.07.014.
8. Zohuri, B.; Mossavar-Rahmani, F.; Behgounia, F. Energy Storage Technologies and Their Role in Renewable Integration. In *Knowledge is Power in Four Dimensions: Models to Forecast Future Paradigm*; 2022; pp. 529–570.
9. Ibrahim, H.; Ilinca, A.; Perron, J. Energy Storage Systems-Characteristics and Comparisons. *Renewable and Sustainable Energy Reviews* **2008**, *12*, 1221–1250, doi:10.1016/j.rser.2007.01.023.
10. Abbas A. Akhil, Georgianne Huff, Aileen B. Currier, Benjamin C. Kaun, D.M.R.; Stella Bingqing Chen, Andrew L. Cotter, Dale T. Bradshaw, and W.D.G. DOE/EPRI 2013 Electricity Storage Handbook in Collaboration with NRECA Available online: <https://www.academia.edu/download/49323464/SAND2013-5131.pdf> (accessed on 6 April 2023).
11. Song, W.J.; Yoo, S.; Song, G.; Lee, S.; Kong, M.; Rim, J.; Jeong, U.; Park, S. Recent Progress in Stretchable Batteries for Wearable Electronics. *Batter Supercaps* **2019**, *2*, 181–199, doi:10.1002/batt.201800140.
12. Thielmann, A.; Sauer, A.; Isenmann, R.; Wietschel, M. Technology Roadmap Energy Storage for Electric Mobility 2030. *Fraunhofer Institute for Systems and Innovation Research ISI* **2013**, 32.
13. Kebede, A.A.; Kalogiannis, T.; van Mierlo, J.; Bercibar, M. A Comprehensive Review of Stationary Energy Storage Devices for Large Scale Renewable Energy Sources Grid Integration. *Renewable and Sustainable Energy Reviews* 2022, *159*, 112213.

14. Liang, Y.; Zhao, C.Z.; Yuan, H.; Chen, Y.; Zhang, W.; Huang, J.Q.; Yu, D.; Liu, Y.; Titirici, M.M.; Chueh, Y.L.; et al. A Review of Rechargeable Batteries for Portable Electronic Devices. *InfoMat* 2019, *1*, 6–32.
15. Blomgren, G.E. The Development and Future of Lithium Ion Batteries. *J Electrochem Soc* **2017**, *164*, A5019–A5025, doi:10.1149/2.0251701jes.
16. Wang, X.; Ding, Y.L.; Deng, Y.P.; Chen, Z. Ni-Rich/Co-Poor Layered Cathode for Automotive Li-Ion Batteries: Promises and Challenges. *Adv Energy Mater* 2020, *10*, 1903864.
17. Liu, L.; Li, M.; Chu, L.; Jiang, B.; Lin, R.; Zhu, X.; Cao, G. Layered Ternary Metal Oxides: Performance Degradation Mechanisms as Cathodes, and Design Strategies for High-Performance Batteries. *Prog Mater Sci* 2020, *111*, 100655.
18. Luo, X.; Wang, J.; Dooner, M.; Clarke, J. Overview of Current Development in Electrical Energy Storage Technologies and the Application Potential in Power System Operation. *Appl Energy* **2015**, *137*, 511–536, doi:10.1016/j.apenergy.2014.09.081.
19. Mongrid, K. *HydroWIRES: Energy Storage Technology and Cost Report*; 2019;
20. Kumar, D.; Rajouria, S.K.; Kuhar, S.B.; Kanchan, D.K. Progress and Prospects of Sodium-Sulfur Batteries: A Review. *Solid State Ion* **2017**, *312*, 8–16, doi:10.1016/j.ssi.2017.10.004.
21. Mizushima, K.; Jones, P.C.; Wiseman, P.J.; Goodenough, J.B.  $\text{Li}_x\text{CoO}_2$  ( $0 < x < 1$ ): A New Cathode Material for Batteries of High Energy Density. *Mater Res Bull* **1980**, *15*, 783–789, doi:10.1016/0025-5408(80)90012-4.
22. Padhi, A.K.; Nanjundaswamy, K.S.; Goodenough, J.B. Phospho-Olivines as Positive-Electrode Materials for Rechargeable Lithium Batteries. *J Electrochem Soc* **1997**, *144*, 1188–1194, doi:10.1149/1.1837571.
23. Whittingham, M.S. The Role of Ternary Phases in Cathode Reactions. *J Electrochem Soc* **1976**, *123*, 315–320, doi:10.1149/1.2132817.
24. Whittingham, M.S. Electrical Energy Storage and Intercalation Chemistry. *Science (1979)* **1976**, *192*, 1126–1127, doi:10.1126/science.192.4244.1126.
25. Miao, Y.; Hynan, P.; von Jouanne, A.; Yokochi, A. Current Li-Ion Battery Technologies in Electric Vehicles and Opportunities for Advancements. *Energies (Basel)* 2019, *12*, 1074.
26. Julien, C.M.; Mauger, A.; Zaghbi, K.; Groult, H. Comparative Issues of Cathode Materials for Li-Ion Batteries. *Inorganics (Basel)* **2014**, *2*, 132–154, doi:10.3390/inorganics2010132.
27. Chen, Y.; Kang, Y.; Zhao, Y.; Wang, L.; Liu, J.; Li, Y.; Liang, Z.; He, X.; Li, X.; Tavajohi, N.; et al. A Review of Lithium-Ion Battery Safety Concerns: The Issues, Strategies, and Testing Standards. *Journal of Energy Chemistry* 2021, *59*, 83–99.
28. Zheng, F.; Kotobuki, M.; Song, S.; Lai, M.O.; Lu, L. Review on Solid Electrolytes for All-Solid-State Lithium-Ion Batteries. *J Power Sources* **2018**, *389*, 198–213, doi:10.1016/j.jpowsour.2018.04.022.

29. Liang, J.; Luo, J.; Sun, Q.; Yang, X.; Li, R.; Sun, X. Recent Progress on Solid-State Hybrid Electrolytes for Solid-State Lithium Batteries. *Energy Storage Mater* **2019**, *21*, 308–334, doi:10.1016/j.ensm.2019.06.021.
30. Birkel, C.R.; Roberts, M.R.; McTurk, E.; Bruce, P.G.; Howey, D.A. Degradation Diagnostics for Lithium Ion Cells. *J Power Sources* **2017**, *341*, 373–386, doi:10.1016/j.jpowsour.2016.12.011.
31. Han, X.; Lu, L.; Zheng, Y.; Feng, X.; Li, Z.; Li, J.; Ouyang, M. A Review on the Key Issues of the Lithium Ion Battery Degradation among the Whole Life Cycle. *eTransportation* 2019, *1*, 100005.
32. Tomaszewska, A.; Chu, Z.; Feng, X.; O’Kane, S.; Liu, X.; Chen, J.; Ji, C.; Endler, E.; Li, R.; Liu, L.; et al. Lithium-Ion Battery Fast Charging: A Review. *eTransportation* 2019, *1*.
33. U.S. Geological Survey 2022 *Final List of Critical Minerals: U.S. Geological Survey*; 2022;
34. Harper, G.; Sommerville, R.; Kendrick, E.; Driscoll, L.; Slater, P.; Stolkin, R.; Walton, A.; Christensen, P.; Heidrich, O.; Lambert, S.; et al. Recycling Lithium-Ion Batteries from Electric Vehicles. *Nature* **2019**, *575*, 75.
35. Bae, H.; Kim, Y. Technologies of Lithium Recycling from Waste Lithium Ion Batteries: A Review. *Mater Adv* **2021**, *2*, 3234.
36. Meng, F.; McNeice, J.; Zadeh, S.S.; Ghahreman, A. Review of Lithium Production and Recovery from Minerals, Brines, and Lithium-Ion Batteries. *Mineral Processing and Extractive Metallurgy Review* **2021**, *42*, 123.
37. IEA *Global EV Outlook 2020: Technology Report*; 2020;
38. Kim, J.G.; Son, B.; Mukherjee, S.; Schuppert, N.; Bates, A.; Kwon, O.; Choi, M.J.; Chung, H.Y.; Park, S. A Review of Lithium and Non-Lithium Based Solid State Batteries. *J Power Sources* **2015**, *282*, 299–322, doi:10.1016/j.jpowsour.2015.02.054.
39. Pissort, P.A. No Title 1933.
40. Bartolozzi, M. Development of Redox Flow Batteries. A Historical Bibliography. *J Power Sources* **1989**, *27*, 219–234, doi:10.1016/0378-7753(89)80037-0.
41. Thaller, L.H. ELECTRICALLY RECHARGEABLE REDOX FLOW CELLS. In Proceedings of the iece; 1974; pp. 924–928.
42. THALLER, L. Redox Flow Cell Energy Storage Systems.; American Institute of Aeronautics and Astronautics (AIAA), June 4 1979.
43. T., T.; T., S.; N., M.; K., M.; T., S. Development of a Redox Flow Battery. In Proceedings of the SEI Technical Review; 1990; p. 191.
44. Pelligri, A.; P.M., S. To Oronzio de Nori Impianti Elettrochimici S.p.A. 1978.
45. Sum, E.; Skyllas-Kazacos, M. A Study of the V(II)/V(III) Redox Couple for Redox Flow Cell Applications. *J Power Sources* **1985**, *15*, 179–190, doi:10.1016/0378-7753(85)80071-9.

46. Rychcik, M.; Skyllas-Kazacos, M. Characteristics of a New All-Vanadium Redox Flow Battery. *J Power Sources* **1988**, *22*, 59–67, doi:10.1016/0378-7753(88)80005-3.
47. Waris, Z.; Akhmetov, N.O.; Pogosova, M.A.; Lipovskikh, S.A.; Ryazantsev, S. V.; Stevenson, K.J. A Complex Investigation of LATP Ceramic Stability and LATP+PVDF Composite Membrane Performance: The Effect of Solvent in Tape-Casting Fabrication. *Membranes (Basel)* **2023**, *13*, 155, doi:10.3390/membranes13020155.
48. Gandomi, Y.A.; Aaron, D.S.; Houser, J.R.; Daugherty, M.C.; Clement, J.T.; Pezeshki, A.M.; Ertugrul, T.Y.; Moseley, D.P.; Mench, M.M. Critical Review—Experimental Diagnostics and Material Characterization Techniques Used on Redox Flow Batteries. *J Electrochem Soc* **2018**, *165*, A970–A1010, doi:10.1149/2.0601805jes.
49. Bortolotti, M. Joint EASE/EERA Recommendations for a European Energy Storage Technology Development Road Map 2017 Update. **2017**, 1–128.
50. Yuan, J.; Pan, Z.-Z.Z.; Jin, Y.; Qiu, Q.; Zhang, C.; Zhao, Y.; Li, Y. Membranes in Non-Aqueous Redox Flow Battery: A Review. *J Power Sources* **2021**, *500*, 229983, doi:10.1016/j.jpowsour.2021.229983.
51. First Phase of 800MWh World Biggest Flow Battery Commissioned in China - Energy Storage News Available online: <https://www.energy-storage.news/first-phase-of-800mwh-world-biggest-flow-battery-commissioned-in-china/> (accessed on 9 March 2023).
52. Butler, P.; Eidler, P.; Grimes, P.; ... S.K.-H. of; 2001, U. *Zinc/Bromine Batteries*;
53. Sánchez-Díez, E.; Ventosa, E.; Guarnieri, M.; Trovò, A.; Flox, C.; Marcilla, R.; Soavi, F.; Mazur, P.; Aranzabe, E.; Ferret, R. Redox Flow Batteries: Status and Perspective towards Sustainable Stationary Energy Storage. *J Power Sources* **2021**, *481*, 228804, doi:10.1016/j.jpowsour.2020.228804.
54. Leung, P.; Li, X.; Ponce De León, C.; Berlouis, L.; Low, C.T.J.; Walsh, F.C. Progress in Redox Flow Batteries, Remaining Challenges and Their Applications in Energy Storage. *RSC Adv* **2012**, *2*, 10125–10156, doi:10.1039/c2ra21342g.
55. Zhang, M.; Moore, M.; Watson, J.S.; Zawodzinski, T.A.; Counce, R.M. Capital Cost Sensitivity Analysis of an All-Vanadium Redox-Flow Battery. *J Electrochem Soc* **2012**, *159*, A1183–A1188, doi:10.1149/2.041208jes.
56. Lynn, K.; Parks, W.; Handa, R.; Kannberg, L.; Hearne, S.; Waldrip, K.; Braccio, R. Acknowledgements.
57. Biswas, S.; Senju, A.; Mohr, R.; Hodson, T.; Karthikeyan, N.; Knehr, K.W.; Hsieh, A.G.; Yang, X.; Koel, B.E.; Steingart, D.A. Minimal Architecture Zinc-Bromine Battery for Low Cost Electrochemical Energy Storage. *Energy Environ Sci* **2017**, *10*, 114–120, doi:10.1039/c6ee02782b.
58. Wang, W.; Sprenkle, V. Energy Storage: Redox Flow Batteries Go Organic. *Nat Chem* **2016**, *8*, 204–206, doi:10.1038/nchem.2466.

59. Matsuda, Y.; Tanaka, K.; Okada, M.; Takasu, Y.; Morita, M.; Matsumura-Inoue, T. A Rechargeable Redox Battery Utilizing Ruthenium Complexes with Non-Aqueous Organic Electrolyte. *J Appl Electrochem* **1988**, *18*, 909–914, doi:10.1007/BF01016050.
60. Liu, Q.; Sleightholme, A.E.S.; Shinkle, A.A.; Li, Y.; Thompson, L.T. Non-Aqueous Vanadium Acetylacetonate Electrolyte for Redox Flow Batteries. *Electrochem commun* **2009**, *11*, 2312–2315, doi:10.1016/j.elecom.2009.10.006.
61. Li, Z.; Li, S.; Liu, S.; Huang, K.; Fang, D.; Wang, F.; Peng, S. Electrochemical Properties of an All-Organic Redox Flow Battery Using 2,2,6,6-Tetramethyl-1-Piperidinyloxy and N-Methylphthalimide. *Electrochemical and Solid-State Letters* **2011**, *14*, A171, doi:10.1149/2.012112esl.
62. Su, L.; Darling, R.M.; Gallagher, K.G.; Xie, W.; Thelen, J.L.; Badel, A.F.; Barton, J.L.; Cheng, K.J.; Balsara, N.P.; Moore, J.S.; et al. An Investigation of the Ionic Conductivity and Species Crossover of Lithiated Nafion 117 in Nonaqueous Electrolytes. *J Electrochem Soc* **2016**, *163*, A5253–A5262, doi:10.1149/2.03211601jes.
63. Wei, X.; Xu, W.; Huang, J.; Zhang, L.; Walter, E.; Lawrence, C.; Vijayakumar, M.; Henderson, W.A.; Liu, T.; Cosimbescu, L.; et al. Radical Compatibility with Nonaqueous Electrolytes and Its Impact on an All-Organic Redox Flow Battery. *Angewandte Chemie - International Edition* **2015**, *54*, 8684–8687, doi:10.1002/anie.201501443.
64. Wei, X.; Duan, W.; Huang, J.; Zhang, L.; Li, B.; Reed, D.; Xu, W.; Sprenkle, V.; Wang, W. A High-Current, Stable Nonaqueous Organic Redox Flow Battery. *ACS Energy Lett* **2016**, *1*, 705–711, doi:10.1021/acsenerylett.6b00255.
65. Senoh, H.; Yao, M.; Sakaebe, H.; Yasuda, K.; Siroma, Z. A Two-Compartment Cell for Using Soluble Benzoquinone Derivatives as Active Materials in Lithium Secondary Batteries. *Electrochim Acta* **2011**, *56*, 10145–10150, doi:10.1016/j.electacta.2011.08.115.
66. Leung, P.; Shah, A.A.; Sanz, L.; Flox, C.; Morante, J.R.; Xu, Q.; Mohamed, M.R.; Ponce de León, C.; Walsh, F.C. Recent Developments in Organic Redox Flow Batteries: A Critical Review. *J Power Sources* **2017**, *360*, 243–283, doi:10.1016/j.jpowsour.2017.05.057.
67. Wang, W.; Xu, W.; Cosimbescu, L.; Choi, D.; Li, L.; Yang, Z. Anthraquinone with Tailored Structure for a Nonaqueous Metal-Organic Redox Flow Batter. *Chemical Communications* **2012**, *48*, 6669–6671, doi:10.1039/c2cc32466k.
68. Huang, J.; Cheng, L.; Assary, R.S.; Wang, P.; Xue, Z.; Burrell, A.K.; Curtiss, L.A.; Zhang, L. Liquid Catholyte Molecules for Nonaqueous Redox Flow Batteries. *Adv Energy Mater* **2015**, *5*, 1401782, doi:10.1002/aenm.201401782.
69. Huang, J.; Pan, B.; Duan, W.; Wei, X.; Assary, R.S.; Su, L.; Brushett, F.R.; Cheng, L.; Liao, C.; Ferrandon, M.S.; et al. The Lightest Organic Radical Cation for Charge Storage in Redox Flow Batteries. *Sci Rep* **2016**, *6*, 1–9, doi:10.1038/srep32102.

70. Wei, X.; Xu, W.; Vijayakumar, M.; Cosimbescu, L.; Liu, T.; Sprenkle, V.; Wang, W. TEMPO-Based Catholyte for High-Energy Density Nonaqueous Redox Flow Batteries. *Advanced Materials* **2014**, *26*, 7649–7653, doi:10.1002/adma.201403746.
71. Takechi, K.; Kato, Y.; Hase, Y. A Highly Concentrated Catholyte Based on a Solvate Ionic Liquid for Rechargeable Flow Batteries. *Advanced Materials* **2015**, *27*, 2501–2506, doi:10.1002/adma.201405840.
72. Pahlevaninezhad, M.; Leung, P.; Velasco, P.Q.; Pahlevani, M.; Walsh, F.C.; Roberts, E.P.L.; Ponce de León, C. A Nonaqueous Organic Redox Flow Battery Using Multi-Electron Quinone Molecules. *J Power Sources* **2021**, *500*, doi:10.1016/j.jpowsour.2021.229942.
73. Chen, H.; Zhou, Y.; Lu, Y.C. Lithium-Organic Nanocomposite Suspension for High-Energy-Density Redox Flow Batteries. *ACS Energy Lett* **2018**, *3*, 1991–1997, doi:10.1021/acsenergylett.8b01257.
74. Buhrmester, C.; Moshurchak, L.M.; Wang, R.L.; Dahn, J.R. The Use of 2,2,6,6-Tetramethylpiperinyl-Oxides and Derivatives for Redox Shuttle Additives in Li-Ion Cells. *J Electrochem Soc* **2006**, *153*, A1800, doi:10.1149/1.2221860.
75. Duduta, M.; Ho, B.; Wood, V.C.; Limthongkul, P.; Brunini, V.E.; Carter, W.C.; Chiang, Y.M. Semi-Solid Lithium Rechargeable Flow Battery. *Adv Energy Mater* **2011**, *1*, 511–516, doi:10.1002/aenm.201100152.
76. Gentil, S.; Reynard, D.; Girault, H.H. Aqueous Organic and Redox-Mediated Redox Flow Batteries: A Review. *Curr Opin Electrochem* **2020**, *21*, 7–13, doi:10.1016/j.coelec.2019.12.006.
77. Lee, H.; Yanilmaz, M.; Toprakci, O.; Fu, K.; Zhang, X. A Review of Recent Developments in Membrane Separators for Rechargeable Lithium-Ion Batteries. *Energy Environ Sci* **2014**, *7*, 3857–3886, doi:10.1039/c4ee01432d.
78. Costa, C.M.; Lee, Y.H.; Kim, J.H.; Lee, S.Y.; Lanceros-Méndez, S. Recent Advances on Separator Membranes for Lithium-Ion Battery Applications: From Porous Membranes to Solid Electrolytes. *Energy Storage Mater* **2019**, *22*, 346–375, doi:10.1016/j.ensm.2019.07.024.
79. Wei, X.; Duan, W.; Huang, J.; Zhang, L.; Li, B.; Reed, D.; Xu, W.; Sprenkle, V.; Wang, W. A High-Current, Stable Nonaqueous Organic Redox Flow Battery. *ACS Energy Lett* **2016**, *1*, 705–711, doi:10.1021/acsenergylett.6b00255.
80. Ma, T.; Pan, Z.; Miao, L.; Chen, C.; Han, M.; Shang, Z.; Chen, J. Porphyrin-Based Symmetric Redox-Flow Batteries towards Cold-Climate Energy Storage. *Angewandte Chemie - International Edition* **2018**, *57*, 3158–3162, doi:10.1002/anie.201713423.
81. Liu, T.; Wei, X.; Nie, Z.; Sprenkle, V.; Wang, W. A Total Organic Aqueous Redox Flow Battery Employing a Low Cost and Sustainable Methyl Viologen Anolyte and 4-HO-TEMPO Catholyte. *Adv Energy Mater* **2016**, *6*, 1501449, doi:10.1002/aenm.201501449.

82. Jung, J.; Won, J.; Hwang, S.S. Highly Selective Composite Membranes Using Ladder-like Structured Polysilsesquioxane for a Non-Aqueous Redox Flow Battery. *J Memb Sci* **2020**, *595*, 117520, doi:10.1016/j.memsci.2019.117520.
83. Kim, D.; Song, J.; Won, J. Structural Effects of Anion Exchange Composite Membranes in Non-Aqueous Redox Flow Batteries. *J Memb Sci* **2018**, *564*, 523–531, doi:10.1016/j.memsci.2018.07.061.
84. Peng, S.; Zhang, L.; Zhang, C.; Ding, Y.; Guo, X.; He, G.; Yu, G. Gradient-Distributed Metal–Organic Framework–Based Porous Membranes for Nonaqueous Redox Flow Batteries. *Adv Energy Mater* **2018**, *8*, 1802533, doi:10.1002/aenm.201802533.
85. Doris, S.E.; Ward, A.L.; Baskin, A.; Frischmann, P.D.; Gavvalapalli, N.; Chénard, E.; Sevov, C.S.; Prendergast, D.; Moore, J.S.; Helms, B.A. Macromolecular Design Strategies for Preventing Active-Material Crossover in Non-Aqueous All-Organic Redox-Flow Batteries. *Angewandte Chemie - International Edition* **2017**, *56*, 1617–1621, doi:10.1002/ange.201610582.
86. Eikerling, M.; Kornyshev, A.A. Proton Transfer in a Single Pore of a Polymer Electrolyte Membrane. *Journal of Electroanalytical Chemistry* **2001**, *502*, 1–14, doi:10.1016/S0022-0728(00)00368-5.
87. Peckham, T.J.; Holdcroft, S. Structure-Morphology-Property Relationships of Non-Perfluorinated Proton-Conducting Membranes. *Advanced Materials* **2010**, *22*, 4667–4690, doi:10.1002/adma.201001164.
88. Doan, T.N.L.; Hoang, T.K.A.; Chen, P. Recent Development of Polymer Membranes as Separators for All-Vanadium Redox Flow Batteries. *RSC Adv* **2015**, *5*, 72805–72815, doi:10.1039/c5ra05914c.
89. Bamgbopa, M.O.; Almheiri, S. Influence of Solvents on Species Crossover and Capacity Decay in Non-Aqueous Vanadium Redox Flow Batteries: Characterization of Acetonitrile and 1, 3 Dioxolane Solvent Mixture. *J Power Sources* **2017**, *342*, 371–381, doi:10.1016/j.jpowsour.2016.12.050.
90. McCormack, P.M.; Luo, H.; Geise, G.M.; Koenig, G.M. Conductivity, Permeability, and Stability Properties of Chemically Tailored Poly(Phenylene Oxide) Membranes for Li<sup>+</sup> Conductive Non-Aqueous Redox Flow Battery Separators. *J Power Sources* **2020**, *460*, 228107, doi:10.1016/j.jpowsour.2020.228107.
91. Zhen, Y.; Zhang, C.; Yuan, J.; Zhao, Y.; Li, Y. A High-Performance All-Iron Non-Aqueous Redox Flow Battery. *J Power Sources* **2020**, *445*, 227331, doi:10.1016/j.jpowsour.2019.227331.
92. Gong, S.J.; Kim, D.; Cho, E.; Hwang, S.S.; Won, J. A Chitosan/Urushi Anion Exchange Membrane for a Non–Aqueous Redox Flow Battery. *ChemistrySelect* **2017**, *2*, 1843–1849, doi:10.1002/slct.201601772.
93. Hudak, N.S.; Small, L.J.; Pratt, H.D.; Anderson, T.M. Through-Plane Conductivities of Membranes for Nonaqueous Redox Flow Batteries. *J Electrochem Soc* **2015**, *162*, A2188–A2194, doi:10.1149/2.0901510jes.

94. Maurya, S.; Shin, S.H.; Sung, K.W.; Moon, S.H. Anion Exchange Membrane Prepared from Simultaneous Polymerization and Quaternization of 4-Vinyl Pyridine for Non-Aqueous Vanadium Redox Flow Battery Applications. *J Power Sources* **2014**, *255*, 325–334, doi:10.1016/j.jpowsour.2014.01.047.
95. Kwon, H.G.; Bae, I.; Choi, S.H. Crosslinked Poly(Arylene Ether Ketone) Membrane with High Anion Conductivity and Selectivity for Non-Aqueous Redox Flow Batteries. *J Memb Sci* **2021**, *620*, 118928, doi:10.1016/j.memsci.2020.118928.
96. Li, Z.; Li, S.; Liu, S.; Huang, K.; Fang, D.; Wang, F.; Peng, S. Electrochemical Properties of an All-Organic Redox Flow Battery Using 2,2,6,6-Tetramethyl-1-Piperidinyloxy and N-Methylphthalimide. *Electrochemical and Solid-State Letters* **2011**, *14*, A171, doi:10.1149/2.012112esl.
97. Kosswataarachchi, A.M.; Cook, T.R. Mixed-Component Catholyte and Anolyte Solutions for High-Energy Density Non-Aqueous Redox Flow Batteries. *J Electrochem Soc* **2018**, *165*, A194–A200, doi:10.1149/2.0751802jes.
98. Stauber, J.M.; Zhang, S.; Gvozdk, N.; Jiang, Y.; Avena, L.; Stevenson, K.J.; Cummins, C.C. Cobalt and Vanadium Trimetaphosphate Polyanions: Synthesis, Characterization, and Electrochemical Evaluation for Non-Aqueous Redox-Flow Battery Applications. *J Am Chem Soc* **2018**, *140*, 538–541, doi:10.1021/jacs.7b08751.
99. Ding, Z.; Li, J.J.; Li, J.J.; An, C. Review—Interfaces: Key Issue to Be Solved for All Solid-State Lithium Battery Technologies. *J Electrochem Soc* **2020**, *167*, 070541, doi:10.1149/1945-7111/ab7f84.
100. Long, L.; Wang, S.; Xiao, M.; Meng, Y. Polymer Electrolytes for Lithium Polymer Batteries. *J Mater Chem A Mater* **2016**, *4*, 10038–10039, doi:10.1039/c6ta02621d.
101. Ratner, M.A.; Johansson, P.; Shriver, D.F. Polymer Electrolytes: Ionic Transport Mechanisms and Relaxation Coupling. *MRS Bull* **2000**, *25*, 31–37, doi:10.1557/mrs2000.16.
102. Quartarone, E.; Mustarelli, P. Electrolytes for Solid-State Lithium Rechargeable Batteries: Recent Advances and Perspectives. *Chem Soc Rev* **2011**, *40*, 2525–2540, doi:10.1039/c0cs00081g.
103. Agrawal, R.C.; Pandey, G.P. Solid Polymer Electrolytes: Materials Designing and All-Solid-State Battery Applications: An Overview. *J Phys D Appl Phys* **2008**, *41*, 223001, doi:10.1088/0022-3727/41/22/223001.
104. Zheng, F.; Kotobuki, M.; Song, S.; Lai, M.O.; Lu, L. Review on Solid Electrolytes for All-Solid-State Lithium-Ion Batteries. *J Power Sources* **2018**, *389*, 198–213, doi:10.1016/j.jpowsour.2018.04.022.
105. Reddy, M. V.; Julien, C.M.; Mauger, A.; Zaghbi, K. Sulfide and Oxide Inorganic Solid Electrolytes for All-Solid-State Li Batteries: A Review. *Nanomaterials* **2020**, *10*, 1–80, doi:10.3390/nano10081606.
106. Bates, J.B.; Dudney, N.J.; Gruzalski, G.R.; Zuh, R.A.; Choudhury, A.; Luck, C.F.; Robertson, J.D. Fabrication and Characterization of Amorphous Lithium Electrolyte

- Thin Films and Rechargeable Thin-Film Batteries. *J Power Sources* **1993**, *43*, 103–110, doi:10.1016/0378-7753(93)80106-Y.
107. Li, G.; Li, M.; Dong, L.; Li, X.; Li, D. Low Energy Ion Beam Assisted Deposition of Controllable Solid State Electrolyte LiPON with Increased Mechanical Properties and Ionic Conductivity. *Int J Hydrogen Energy* **2014**, *39*, 17466–17472, doi:10.1016/j.ijhydene.2014.01.012.
  108. Fujibayashi, T.; Kubota, Y.; Iwabuchi, K.; Yoshii, N. Highly Conformal and High-Ionic Conductivity Thin-Film Electrolyte for 3D-Structured Micro Batteries: Characterization of LiPON Film Deposited by MOCVD Method. *AIP Adv* **2017**, *7*, doi:10.1063/1.4999915.
  109. Tatsumisago, M.; Hayashi, A. Sulfide Glass-Ceramic Electrolytes for All-Solid-State Lithium and Sodium Batteries. *Int J Appl Glass Sci* **2014**, *5*, 226–235, doi:10.1111/ijag.12084.
  110. Kato, Y.; Hori, S.; Saito, T.; Suzuki, K.; Hirayama, M.; Mitsui, A.; Yonemura, M.; Iba, H.; Kanno, R. High-Power All-Solid-State Batteries Using Sulfide Superionic Conductors. *Nat Energy* **2016**, *1*, 1–7, doi:10.1038/nenergy.2016.30.
  111. Cussen, E.J. The Structure of Lithium Garnets: Cation Disorder and Clustering in a New Family of Fast Li<sup>+</sup> Conductors. *Chemical Communications* **2006**, 412–413, doi:10.1039/b514640b.
  112. Larraz, G.; Orera, A.; Sanjuán, M.L. Cubic Phases of Garnet-Type Li<sub>7</sub>La<sub>3</sub>Zr<sub>2</sub>O<sub>12</sub>: The Role of Hydration. *J Mater Chem A Mater* **2013**, *1*, 11419–11428, doi:10.1039/c3ta11996c.
  113. Xia, W.; Xu, B.; Duan, H.; Tang, X.; Guo, Y.; Kang, H.; Li, H.; Liu, H. Reaction Mechanisms of Lithium Garnet Pellets in Ambient Air: The Effect of Humidity and CO<sub>2</sub>. *Journal of the American Ceramic Society* **2017**, *100*, 2832–2839, doi:10.1111/jace.14865.
  114. Stramare, S.; Thangadurai, V.; Weppner, W. Lithium Lanthanum Titanates: A Review. *Chemistry of Materials* **2003**, *15*, 3974–3990, doi:10.1021/cm0300516.
  115. Kamaya, N.; Homma, K.; Yamakawa, Y.; Hirayama, M.; Kanno, R.; Yonemura, M.; Kamiyama, T.; Kato, Y.; Hama, S.; Kawamoto, K.; et al. A Lithium Superionic Conductor. *Nat Mater* **2011**, *10*, 682–686, doi:10.1038/nmat3066.
  116. Pogosova, M.; Krasnikova, I.; Sergeev, A.; Zhugayevych, A.; Stevenson, K. Correlating Structure and Transport Properties in Pristine and Environmentally-Aged Superionic Conductors Based on Li<sub>1.3</sub>Al<sub>0.3</sub>Ti<sub>1.7</sub>(PO<sub>4</sub>)<sub>3</sub> Ceramics. *J Power Sources* **2020**, *448*, doi:10.1016/j.jpowsour.2019.227367.
  117. Hong, H.Y.P. Crystal Structures and Crystal Chemistry in the System Na<sub>1+x</sub>Zr<sub>2</sub>SixP<sub>3</sub>-XO<sub>12</sub>. *Mater Res Bull* **1976**, *11*, 173–182, doi:10.1016/0025-5408(76)90073-8.
  118. Hong, H.Y.P. Crystal Structures and Crystal Chemistry in the System Na<sub>1+x</sub>Zr<sub>2</sub>SixP<sub>3</sub>-XO<sub>12</sub>. *Mater Res Bull* **1976**, *11*, 173–182, doi:10.1016/0025-5408(76)90073-8.

119. Aono, H.; Imanaka, N.; Adachi, G. ya High Li<sup>+</sup> Conducting Ceramics. *Acc Chem Res* **1994**, *27*, 265–270, doi:10.1021/ar00045a002.
120. Fu, J. Fast Li<sup>+</sup> Ion Conducting Glass-Ceramics in the System Li<sub>2</sub>O-Al<sub>2</sub>O<sub>3</sub>-GeO<sub>2</sub>-P<sub>2</sub>O<sub>5</sub>. *Solid State Ion* **1997**, *104*, 191–194, doi:10.1016/s0167-2738(97)00434-7.
121. Thokchom, J.S.; Gupta, N.; Kumar, B. Superionic Conductivity in a Lithium Aluminum Germanium Phosphate Glass–Ceramic. *J Electrochem Soc* **2008**, *155*, A915, doi:10.1149/1.2988731.
122. Zhao, E.; Ma, F.; Guo, Y.; Jin, Y. Stable LATP/LAGP Double-Layer Solid Electrolyte Prepared: Via a Simple Dry-Pressing Method for Solid State Lithium Ion Batteries. *RSC Adv* **2016**, *6*, 92579–92585, doi:10.1039/c6ra19415j.
123. Hao, X.; Zhao, Q.; Su, S.; Zhang, S.; Ma, J.; Shen, L.; Yu, Q.; Zhao, L.; Liu, Y.; Kang, F.; et al. Constructing Multifunctional Interphase between Li<sub>1.4</sub>Al<sub>0.4</sub>Ti<sub>1.6</sub>(PO<sub>4</sub>)<sub>3</sub> and Li Metal by Magnetron Sputtering for Highly Stable Solid-State Lithium Metal Batteries. *Adv Energy Mater* **2019**, *9*, 1–8, doi:10.1002/aenm.201901604.
124. Yang, L.; Song, Y.; Liu, H.; Wang, Z.; Yang, K.; Zhao, Q.; Cui, Y.; Wen, J.; Luo, W.; Pan, F. Stable Interface between Lithium and Electrolyte Facilitated by a Nanocomposite Protective Layer. *Small Methods* **2020**, *4*, 1–7, doi:10.1002/smt.201900751.
125. Pogosova, M.A.; Krasnikova, I. V.; Sanin, A.O.; Lipovskikh, S.A.; Eliseev, A.A.; Sergeev, A. V.; Stevenson, K.J. Complex Investigation of Water Impact on Li-Ion Conductivity of Li<sub>1.3</sub>Al<sub>0.3</sub>Ti<sub>1.7</sub>(PO<sub>4</sub>)<sub>3</sub>- Electrochemical, Chemical, Structural, and Morphological Aspects. *Chemistry of Materials* **2020**, *32*, 3723–3732, doi:10.1021/acs.chemmater.9b04419.
126. Lu, Y.; Goodenough, J.B. Rechargeable Alkali-Ion Cathode-Flow Battery. *J Mater Chem* **2011**, *21*, 10113–10117, doi:10.1039/c0jm04222f.
127. Ding, Y.; Zhao, Y.; Li, Y.; Goodenough, J.B.; Yu, G. A High-Performance All-Metallocene-Based, Non-Aqueous Redox Flow Battery. *Energy Environ Sci* **2017**, *10*, 491–497, doi:10.1039/c6ee02057g.
128. Muthuraman, G.; Boyeol, L.; Il-Shik, M. Na-β-Alumina as a Separator in the Development of All-Vanadium Non-Aqueous Tubular Redox Flow Batteries: An Electrochemical and Charging-Discharging Examination Using a Prototype Tubular Redox Flow Cell. *J Electrochem Soc* **2018**, *165*, A1920–A1924, doi:10.1149/2.1461809jes.
129. Zhang, C.; Niu, Z.; Ding, Y.; Zhang, L.; Zhou, Y.; Guo, X.; Zhang, X.; Zhao, Y.; Yu, G. Highly Concentrated Phthalimide-Based Anolytes for Organic Redox Flow Batteries with Enhanced Reversibility. *Chem* **2018**, *4*, 2814–2825, doi:10.1016/j.chempr.2018.08.024.
130. Arya, A.; Sharma, A.L. *Polymer Electrolytes for Lithium Ion Batteries: A Critical Study*; Ionics, 2017; Vol. 23; ISBN 1158101619.

131. Croce, F.; Persi, L.; Ronci, F.; Scrosati, B. Nanocomposite Polymer Electrolytes and Their Impact on the Lithium Battery Technology. *Solid State Ion* **2000**, *135*, 47–52, doi:10.1016/S0167-2738(00)00329-5.
132. Wang, Z.; Wang, S.; Wang, A.; Liu, X.; Chen, J.; Zeng, Q.; Zhang, L.L.; Liu, W.; Zhang, L.L. Covalently Linked Metal-Organic Framework (MOF)-Polymer All-Solid-State Electrolyte Membranes for Room Temperature High Performance Lithium Batteries. *J Mater Chem A Mater* **2018**, *6*, 17227–17234, doi:10.1039/c8ta05642k.
133. Yuan, C.; Li, J.; Han, P.; Lai, Y.; Zhang, Z.; Liu, J. Enhanced Electrochemical Performance of Poly(Ethylene Oxide) Based Composite Polymer Electrolyte by Incorporation of Nano-Sized Metal-Organic Framework. *J Power Sources* **2013**, *240*, 653–658, doi:10.1016/j.jpowsour.2013.05.030.
134. Huo, H.; Chen, Y.; Luo, J.; Yang, X.; Guo, X.; Sun, X. Rational Design of Hierarchical “Ceramic-in-Polymer” and “Polymer-in-Ceramic” Electrolytes for Dendrite-Free Solid-State Batteries. *Adv Energy Mater* **2019**, *9*, 1804004, doi:10.1002/aenm.201804004.
135. Wang, Y.J.; Pan, Y.; Kim, D. Conductivity Studies on Ceramic Li<sub>1.3</sub>Al<sub>0.3</sub>Ti<sub>1.7</sub>(PO<sub>4</sub>)<sub>3</sub>-Filled PEO-Based Solid Composite Polymer Electrolytes. *J Power Sources* **2006**, *159*, 690–701, doi:10.1016/j.jpowsour.2005.10.104.
136. Choi, J.H.; Lee, C.H.; Yu, J.H.; Doh, C.H.; Lee, S.M. Enhancement of Ionic Conductivity of Composite Membranes for All-Solid-State Lithium Rechargeable Batteries Incorporating Tetragonal Li<sub>7</sub>La<sub>3</sub>Zr<sub>2</sub>O<sub>12</sub> into a Polyethylene Oxide Matrix. *J Power Sources* **2015**, *274*, 458–463, doi:10.1016/j.jpowsour.2014.10.078.
137. Zhang, J.; Zhao, N.; Zhang, M.; Li, Y.; Chu, P.K.; Guo, X.; Di, Z.; Wang, X.; Li, H. Flexible and Ion-Conducting Membrane Electrolytes for Solid-State Lithium Batteries: Dispersion of Garnet Nanoparticles in Insulating Polyethylene Oxide. *Nano Energy* **2016**, *28*, 447–454, doi:10.1016/j.nanoen.2016.09.002.
138. Chen, L.; Li, Y.; Li, S.P.; Fan, L.Z.; Nan, C.W.; Goodenough, J.B. PEO/Garnet Composite Electrolytes for Solid-State Lithium Batteries: From “Ceramic-in-Polymer” to “Polymer-in-Ceramic.” *Nano Energy* **2018**, *46*, 176–184, doi:10.1016/j.nanoen.2017.12.037.
139. Gang, W.; Roos, J.; Brinkmann, D.; Capuano, F.; Croce, F.; Scrosati, B. Comparison of NMR and Conductivity in (PEP)<sub>8</sub>LiClO<sub>4</sub>+ $\gamma$ -LiAlO<sub>2</sub>. *Solid State Ion* **1992**, *53–56*, 1102–1105, doi:10.1016/0167-2738(92)90297-3.
140. He, Z.; Chen, L.; Zhang, B.; Liu, Y.; Fan, L.Z. Flexible Poly(Ethylene Carbonate)/Garnet Composite Solid Electrolyte Reinforced by Poly(Vinylidene Fluoride-Hexafluoropropylene) for Lithium Metal Batteries. *J Power Sources* **2018**, *392*, 232–238, doi:10.1016/j.jpowsour.2018.05.006.
141. Zhang, J.; Zang, X.; Wen, H.; Dong, T.; Chai, J.; Li, Y.; Chen, B.; Zhao, J.; Dong, S.; Ma, J.; et al. High-Voltage and Free-Standing Poly(Propylene Carbonate)/Li<sub>6.75</sub>La<sub>3</sub>Zr<sub>1.75</sub>Ta<sub>0.25</sub>O<sub>12</sub> Composite Solid Electrolyte for Wide

- Temperature Range and Flexible Solid Lithium Ion Battery. *J Mater Chem A Mater* **2017**, *5*, 4940–4948, doi:10.1039/c6ta10066j.
142. Zhang, X.; Liu, T.; Zhang, S.; Huang, X.; Xu, B.B.; Lin, Y.; Xu, B.B.; Li, L.; Nan, C.W.; Shen, Y. Synergistic Coupling between Li<sub>6.75</sub>La<sub>3</sub>Zr<sub>175</sub>Ta<sub>0.25</sub>O<sub>12</sub> and Poly(Vinylidene Fluoride) Induces High Ionic Conductivity, Mechanical Strength, and Thermal Stability of Solid Composite Electrolytes. *J Am Chem Soc* **2017**, *139*, 13779–13785, doi:10.1021/jacs.7b06364.
  143. Shi, X.; Ma, N.; Wu, Y.; Lu, Y.; Xiao, Q.; Li, Z.; Lei, G. Fabrication and Electrochemical Properties of LATP/PVDF Composite Electrolytes for Rechargeable Lithium-Ion Battery. *Solid State Ion* **2018**, *325*, 112–119, doi:10.1016/j.ssi.2018.08.010.
  144. Liang, J.; Luo, J.; Sun, Q.; Yang, X.; Li, R.; Sun, X. Recent Progress on Solid-State Hybrid Electrolytes for Solid-State Lithium Batteries. *Energy Storage Mater* **2019**, *21*, 308–334, doi:10.1016/j.ensm.2019.06.021.
  145. Park, C.H.; Park, M.; Yoo, S.I.; Joo, S.K. A Spin-Coated Solid Polymer Electrolyte for All-Solid-State Rechargeable Thin-Film Lithium Polymer Batteries. *J Power Sources* **2006**, *158*, 1442–1446, doi:10.1016/j.jpowsour.2005.10.022.
  146. Brinker, C.J.; Hurd, A.J. Fundamentals of Sol-Gel Dip-Coating. *Journal de physique. III* **1994**, *4*, 1231–1242, doi:10.1051/jp3:1994198.
  147. Chandra, A. Hot-Pressed Ag<sup>+</sup> Ion Conducting Glass-Polymer Electrolytes: Synthesis and Battery Application. *Portugaliae Electrochimica Acta* **2012**, *30*, 261–266, doi:10.4152/pea.201204261.
  148. Pavlidou, S.; Papaspyrides, C.D. A Review on Polymer-Layered Silicate Nanocomposites. *Progress in Polymer Science (Oxford)* **2008**, *33*, 1119–1198, doi:10.1016/j.progpolymsci.2008.07.008.
  149. Li, M.; Katsouras, I.; Piliago, C.; Glasser, G.; Lieberwirth, I.; Blom, P.W.M.; De Leeuw, D.M. Controlling the Microstructure of Poly(Vinylidene-Fluoride) (PVDF) Thin Films for Microelectronics. *J Mater Chem C Mater* **2013**, *1*, 7695–7702, doi:10.1039/c3tc31774a.
  150. Gregorio, R.; Ueno, E.M. Effect of Crystalline Phase, Orientation and Temperature on the Dielectric Properties of Poly (Vinylidene Fluoride) (PVDF). *J Mater Sci* **1999**, *34*, 4489–4500, doi:10.1023/A:1004689205706.
  151. Dong, X.; Lu, D.; Harris, T.A.L.; Escobar, I.C. Polymers and Solvents Used in Membrane Fabrication: A Review Focusing on Sustainable Membrane Development. *Membranes (Basel)* **2021**, *11*.
  152. Huang, X. Cellular Porous Polyvinylidene Fluoride Composite Membranes for Lithium-Ion Batteries. *Journal of Solid State Electrochemistry* **2013**, *17*, 591–597, doi:10.1007/s10008-012-1891-4.
  153. Nolte, O.; Volodin, I.A.; Stolze, C.; Hager, M.D.; Schubert, U.S. Trust Is Good, Control Is Better: A Review on Monitoring and Characterization Techniques for Flow Battery Electrolytes. *Mater Horiz* **2021**, *8*, 1866–1925, doi:10.1039/d0mh01632b.

154. Murugesan, V.; Wei, X.; Hollas, A.; Nie, Z.; Li, B.; Sprenkle, V.; Reed, D.; Wang, W. Redox Flow Battery Electrolyte Design Formulations: Molecular Screening and Engineering. In Proceedings of the ECS Meeting Abstracts; IOP Publishing, April 13 2018; Vol. MA2018-01, pp. 216–216.
155. Li, W.; Xing, Y.; Wu, Y.; Wang, J.; Chen, L.; Yang, G.; Tang, B. Study the Effect of Ion-Complex on the Properties of Composite Gel Polymer Electrolyte Based on Electrospun PVdF Nanofibrous Membrane. *Electrochim Acta* **2015**, *151*, 289–296, doi:10.1016/j.electacta.2014.11.083.
156. Ramesh, S.; Winie, T.; Arof, A.K. Investigation of Mechanical Properties of Polyvinyl Chloride-Polyethylene Oxide (PVC-PEO) Based Polymer Electrolytes for Lithium Polymer Cells. *Eur Polym J* **2007**, *43*, 1963–1968, doi:10.1016/j.eurpolymj.2007.02.006.
157. Aji, A. Morphology and Mechanical Properties of Virgin and Recycled Polyethylene/Polyvinyl Chloride Blends. *Polym Eng Sci* **1995**, *35*, 64–71, doi:10.1002/pen.760350109.
158. Hashmi, S.A.; Chandra, S. Experimental Investigations on a Sodium-Ion-Conducting Polymer Electrolyte Based on Poly(Ethylene Oxide) Complexed with NaPF<sub>6</sub>. *Materials Science and Engineering B* **1995**, *34*, 18–26, doi:10.1016/0921-5107(95)01219-2.
159. Kiran Kumar, K.; Ravi, M.; Pavani, Y.; Bhavani, S.; Sharma, A.K.; Narasimha Rao, V.V.R. Investigations on the Effect of Complexation of NaF Salt with Polymer Blend (PEO/PVP) Electrolytes on Ionic Conductivity and Optical Energy Band Gaps. *Physica B Condens Matter* **2011**, *406*, 1706–1712, doi:10.1016/j.physb.2011.02.010.
160. Sharma, A.L.; Shukla, N.; Thakur, A.K. Studies on Structure Property Relationship in a Polymer-Clay Nanocomposite Film Based on (Pan)8LiClO<sub>4</sub>. *J Polym Sci B Polym Phys* **2008**, *46*, 2577–2592, doi:10.1002/polb.21583.
161. Vadhva, P.; Hu, J.; Johnson, M.J.; Stocker, R.; Braglia, M.; Brett, D.J.L.; Rettie, A.J.E. Electrochemical Impedance Spectroscopy for All-Solid-State Batteries: Theory, Methods and Future Outlook. *ChemElectroChem* **2021**, *8*, 1930–1947, doi:10.1002/celec.202100108.
162. Wang, S.; Zhang, J.; Gharbi, O.; Vivier, V.; Gao, M.; Orazem, M.E. Electrochemical Impedance Spectroscopy. *Nature Reviews Methods Primers* **2021**, *1*, 1–21, doi:10.1038/s43586-021-00039-w.
163. García-Sánchez, M.F.; M'Peko, J.C.; Ruiz-Salvador, A.R.; Rodríguez-Gattorno, G.; Echevarría, Y.; Fernández-Gutierrez, F.; Delgado, A. An Elementary Picture of Dielectric Spectroscopy in Solids: Physical Basis. *J Chem Educ* **2003**, *80*, 1062–1073, doi:10.1021/ed080p1062.
164. Kidner, N.J.; Perry, N.H.; Mason, T.O.; Garboczi, E.J. The Brick Layer Model Revisited: Introducing the Nano-Grain Composite Model. *Journal of the American Ceramic Society* **2008**, *91*, 1733–1746, doi:10.1111/j.1551-2916.2008.02445.x.

165. Cheng, X.B.; Zhang, R.; Zhao, C.Z.; Wei, F.; Zhang, J.G.; Zhang, Q. A Review of Solid Electrolyte Interphases on Lithium Metal Anode. *Advanced Science* **2015**, *3*, 1–20, doi:10.1002/advs.201500213.
166. Park, M.S.; Ma, S.B.; Lee, D.J.; Im, D.; Doo, S.G.; Yamamoto, O. A Highly Reversible Lithium Metal Anode. *Sci Rep* **2014**, *4*, 1–8, doi:10.1038/srep03815.
167. Busche, M.R.; Drossel, T.; Leichtweiss, T.; Weber, D.A.; Falk, M.; Schneider, M.; Reich, M.L.; Sommer, H.; Adelhelm, P.; Janek, J. Dynamic Formation of a Solid-Liquid Electrolyte Interphase and Its Consequences for Hybrid-Battery Concepts. *Nat Chem* **2016**, *8*, 426–434, doi:10.1038/nchem.2470.
168. Cho, E.; Won, J. Novel Composite Membrane Coated with a Poly(Diallyldimethylammonium Chloride)/Urushi Semi-Interpenetrating Polymer Network for Non-Aqueous Redox Flow Battery Application. *J Power Sources* **2016**, *335*, 12–19, doi:10.1016/j.jpowsour.2016.10.020.
169. Karpushkin, E.A.; Gvozdik, N.A.; Levitskiy, O.A.; Stevenson, K.J.; Sergeyeve, V.G.; Magdesieva, T. V. Sol-Gel-Modified Membranes for All-Organic Battery Based on Bis-(Tert-Butylphenyl)Nitroxide. *Colloid Polym Sci* **2019**, *297*, 317–323, doi:10.1007/S00396-018-4387-7.
170. Yao, Y.; Lei, J.; Shi, Y.; Ai, F.; Lu, Y.C. Assessment Methods and Performance Metrics for Redox Flow Batteries. *Nat Energy* **2021**, doi:10.1038/s41560-020-00772-8.
171. Gandomi, Y.A.; Aaron, D.S.; Nolan, Z.B.; Ahmadi, A.; Mench, M.M. Direct Measurement of Crossover and Interfacial Resistance of Ion-Exchange Membranes in All-Vanadium Redox Flow Batteries. *Membranes (Basel)* **2020**, *10*, 1–21, doi:10.3390/membranes10060126.
172. Akhmetov, N.; Ovsyannikov, N.; Gvozdik, N.; Pogosova, M.; Ryazantsev, S.; Lipovskikh, S.; Krasnikova, I.; Stevenson, K. Composite Lithium-Conductive LATP+PVdF Membranes: Development, Optimization, and Applicability for Li-TEMPO Hybrid Redox Flow Batteries. *J Memb Sci* **2022**, *643*, 120002, doi:10.1016/j.memsci.2021.120002.
173. Khataee, A.; Dražević, E.; Catalano, J.; Bentien, A. Performance Optimization of Differential PH Quinone-Bromide Redox Flow Battery. *J Electrochem Soc* **2018**, *165*, A3918–A3924, doi:10.1149/2.0681816jes.
174. Arenas, L.F.; Ponce de León, C.; Walsh, F.C. Redox Flow Batteries for Energy Storage: Their Promise, Achievements and Challenges. *Curr Opin Electrochem* **2019**, *16*, 117–126.
175. Krasnikova, I. V.; Pogosova, M.A.; Sanin, A.O.; Stevenson, K.J. Toward Standardization of Electrochemical Impedance Spectroscopy Studies of Li-Ion Conductive Ceramics. *Chemistry of Materials* **2020**, *32*, 2232–2241, doi:10.1021/acs.chemmater.9b04899.
176. Petříček, V.; Dušek, M. THE CRYSTALLOGRAPHIC COMPUTING SYSTEM. *www.xray.fzu.cz* **2000**.

177. Redhammer, G.J.; Rettenwander, D.; Pristat, S.; Dashjav, E.; Kumar, C.M.N.; Topa, D.; Tietz, F. A Single Crystal X-Ray and Powder Neutron Diffraction Study on NASICON-Type  $\text{Li}_{1+x}\text{Al}_x\text{Ti}_{2-x}(\text{PO}_4)_3$  ( $0 \leq x \leq 0.5$ ) Crystals: Implications on Ionic Conductivity. *Solid State Sci* **2016**, *60*, 99–107, doi:10.1016/j.solidstatesciences.2016.08.011.
178. Bruce, P.G.; Evans, J.; Vincent, C.A. Conductivity and Transference Number Measurements on Polymer Electrolytes. *Solid State Ion* **1988**, *28–30*, 918–922, doi:10.1016/0167-2738(88)90304-9.
179. Ashraf Gandomi, Y.; Krasnikova, I. V.; Akhmetov, N.O.; Ovsyannikov, N.A.; Pogosova, M.A.; Matteucci, N.J.; Mallia, C.T.; Neyhouse, B.J.; Fenton, A.M.; Brushett, F.R.; et al. Synthesis and Characterization of Lithium-Conducting Composite Polymer-Ceramic Membranes for Use in Nonaqueous Redox Flow Batteries. *ACS Appl Mater Interfaces* **2021**, *13*, 53746–53757, doi:10.1021/acsami.1c13759.
180. Akhmetov, N.; Waris, Z.; Ryazantsev, S.; Lipovskikh, S.; Gvozdik, N.; Pogosova, M.; Stevenson, K. Towards Durable Li-Hybrid Flow Batteries: Composite Membrane Development, Cell Performance, and Perspective. *J Mater Chem A Mater* **2023**, *11*, 19656–19668, doi:10.1039/D3TA02501B.
181. Parker, A.J. The Effects of Solvation on the Properties of Anions in Dipolar Aprotic Solvents. *Quarterly Reviews, Chemical Society* **1962**, *16*, 163–187, doi:10.1039/qr9621600163.
182. Peng, Y.; Wu, P. A Two Dimensional Infrared Correlation Spectroscopic Study on the Structure Changes of PVDF during the Melting Process. *Polymer (Guildf)* **2004**, *45*, 5295–5299, doi:10.1016/j.polymer.2004.05.034.
183. Bachmann, M.A.; Gordon, W.L.; Koenig, J.L.; Lando, J.B. An Infrared Study of Phase-III Poly(Vinylidene Fluoride). *J Appl Phys* **1979**, *50*, 6106–6112, doi:10.1063/1.325780.
184. Pareek, T.; Dwivedi, S.; Ahmad, S.A.; Badole, M.; Kumar, S. Effect of NASICON-Type  $\text{LiSnZr}(\text{PO}_4)_3$  Ceramic Filler on the Ionic Conductivity and Electrochemical Behavior of PVDF Based Composite Electrolyte. *J Alloys Compd* **2020**, *824*, 153991, doi:10.1016/j.jallcom.2020.153991.
185. Cai, X.; Lei, T.; Sun, D.; Lin, L. A Critical Analysis of the  $\alpha$ ,  $\beta$  and  $\gamma$  Phases in Poly(Vinylidene Fluoride) Using FTIR. *RSC Adv* **2017**, *7*, 15382–15389, doi:10.1039/c7ra01267e.
186. Gao, J.; Shao, Q.; Chen, J. Lithiated Nafion-Garnet Ceramic Composite Electrolyte Membrane for Solid-State Lithium Metal Battery. *Journal of Energy Chemistry* **2020**, *46*, 237–247, doi:10.1016/j.jechem.2019.11.012.
187. Doyle, M.; Lewittes, M.E.; Roelofs, M.G.; Perusich, S.A.; Lowrey, R.E. Relationship between Ionic Conductivity of Perfluorinated Ionomeric Membranes and Nonaqueous Solvent Properties. *J Memb Sci* **2001**, *184*, 257–273, doi:10.1016/S0376-7388(00)00642-6.

188. Papp, J.K.; Forster, J.D.; Burke, C.M.; Kim, H.W.; Luntz, A.C.; Shelby, R.M.; Urban, J.J.; McCloskey, B.D. Poly(Vinylidene Fluoride) (PVDF) Binder Degradation in Li-O<sub>2</sub> Batteries: A Consideration for the Characterization of Lithium Superoxide. *Journal of Physical Chemistry Letters* **2017**, *8*, 1169–1174, doi:10.1021/acs.jpcclett.7b00040.
189. Ferreira, J.C.C.; Monteiro, T.S.; Lopes, A.C.; Costa, C.M.; Silva, M.M.; Machado, A. V.; Lanceros-Mendez, S. Variation of the Physicochemical and Morphological Characteristics of Solvent Casted Poly(Vinylidene Fluoride) along Its Binary Phase Diagram with Dimethylformamide. *J Non Cryst Solids* **2015**, *412*, 16–23, doi:10.1016/j.jnoncrysol.2015.01.003.
190. Ye, J.; Zhao, X.; Ma, Y.; Su, J.; Xiang, C.; Zhao, K.; Ding, M.; Jia, C.; Sun, L. Hybrid Membranes Dispersed with Superhydrophilic TiO<sub>2</sub> Nanotubes Toward Ultra-Stable and High-Performance Vanadium Redox Flow Batteries. *Adv Energy Mater* **2020**, *10*, 1–7, doi:10.1002/aenm.201904041.
191. Boyle, D.T.; Kong, X.; Pei, A.; Rudnicki, P.E.; Shi, F.; Huang, W.; Bao, Z.; Qin, J.; Cui, Y. Transient Voltammetry with Ultramicroelectrodes Reveals the Electron Transfer Kinetics of Lithium Metal Anodes. *ACS Energy Lett* **2020**, *5*, 701–709, doi:10.1021/acseenergylett.0c00031.
192. Zaban, A.; Zinigrad, E.; Aurbach, D. Impedance Spectroscopy of Li Electrodes. 4. A General Simple Model of the Li-Solution Interphase in Polar Aprotic Systems. *Journal of Physical Chemistry* **1996**, *100*, 3089–3101, doi:10.1021/jp9514279.
193. Yang, L.; Wang, Z.Z.; Feng, Y.; Tan, R.; Zuo, Y.; Gao, R.; Zhao, Y.; Han, L.; Wang, Z.Z.; Pan, F. Flexible Composite Solid Electrolyte Facilitating Highly Stable “Soft Contacting” Li–Electrolyte Interface for Solid State Lithium-Ion Batteries. *Adv Energy Mater* **2017**, *7*, 1–9, doi:10.1002/aenm.201701437.
194. Rodby, K.E.; Carney, T.J.; Ashraf Gandomi, Y.; Barton, J.L.; Darling, R.M.; Brushett, F.R. Assessing the Levelized Cost of Vanadium Redox Flow Batteries with Capacity Fade and Rebalancing. *J Power Sources* **2020**, *460*, 227958, doi:10.1016/j.jpowsour.2020.227958.
195. Ok, B.; Na, W.; Kwon, T.H.; Kwon, Y.W.; Cho, S.; Hong, S.M.; Lee, A.S.; Lee, J.H.; Koo, C.M. Understanding the Enhanced Electrochemical Performance of TEMPO Derivatives in Non-Aqueous Lithium Ion Redox Flow Batteries. *Journal of Industrial and Engineering Chemistry* **2019**, *80*, 545–550, doi:10.1016/j.jiec.2019.08.027.
196. Aurbach, D.; Zinigrad, E.; Cohen, Y.; Teller, H. A Short Review of Failure Mechanisms of Lithium Metal and Lithiated Graphite Anodes in Liquid Electrolyte Solutions. In Proceedings of the Solid State Ionics; Elsevier, June 2 2002; Vol. 148, pp. 405–416.
197. Wang, X.J.; Lee, H.S.; Li, H.; Yang, X.Q.; Huang, X.J. The Effects of Substituting Groups in Cyclic Carbonates for Stable SEI Formation on Graphite Anode of Lithium Batteries. *Electrochem Commun* **2010**, *12*, 386–389, doi:10.1016/j.elecom.2009.12.041.

198. Xing, L.; Zheng, X.; Schroeder, M.; Alvarado, J.; Von Wald Cresce, A.; Xu, K.; Li, Q.; Li, W. Deciphering the Ethylene Carbonate-Propylene Carbonate Mystery in Li-Ion Batteries. *Acc Chem Res* **2018**, *51*, 282–289, doi:10.1021/acs.accounts.7b00474.
199. Luo, D.; Li, M.; Zheng, Y.; Ma, Q.; Gao, R.; Zhang, Z.; Dou, H.; Wen, G.; Shui, L.; Yu, A.; et al. Electrolyte Design for Lithium Metal Anode-Based Batteries Toward Extreme Temperature Application. *Advanced Science* **2021**, *8*, 2101051.
200. Metzger, M.; Walke, P.; Solchenbach, S.; Salitra, G.; Aurbach, D.; Gasteiger, H.A. Evaluating the High-Voltage Stability of Conductive Carbon and Ethylene Carbonate with Various Lithium Salts. *J Electrochem Soc* **2020**, *167*, 160522, doi:10.1149/1945-7111/abcabd.
201. Zhang, C.; Chen, H.; Qian, Y.; Dai, G.; Zhao, Y.; Yu, G. General Design Methodology for Organic Eutectic Electrolytes toward High-Energy-Density Redox Flow Batteries. *Advanced Materials* **2021**, *33*, 1–8, doi:10.1002/adma.202008560.
202. Jurczuk, K.; Galeski, A.; Mackey, M.; Hiltner, A.; Baer, E. Orientation of PVDF  $\alpha$  and  $\gamma$  Crystals in Nanolayered Films. *Colloid Polym Sci* **2015**, *293*, 1289–1297, doi:10.1007/s00396-015-3542-7.
203. Grundish, N.S.; Goodenough, J.B.; Khani, H. Designing Composite Polymer Electrolytes for All-Solid-State Lithium Batteries. *Curr Opin Electrochem* **2021**, *30*, 100828, doi:10.1016/j.coelec.2021.100828.
204. Brushett, F.R.; Vaughey, J.T.; Jansen, A.N. An All-Organic Non-Aqueous Lithium-Ion Redox Flow Battery. *Adv Energy Mater* **2012**, *2*, 1390–1396, doi:10.1002/aenm.201200322.
205. Romadina, E.I.; Volodin, I.A.; Stevenson, K.J.; Troshin, P.A. New Highly Soluble Triarylamine-Based Materials as Promising Catholytes for Redox Flow Batteries. *J Mater Chem A Mater* **2021**, *9*, 8303–8307, doi:10.1039/d0ta11860e.
206. Liu, B.; Zhang, J.G.; Xu, W. Advancing Lithium Metal Batteries. *Joule* **2018**, *2*, 833–845.
207. Skyllas-Kazacos, M.; Grossmith, F. Efficient Vanadium Redox Flow Cell. *J Electrochem Soc* **1987**, *134*, 2950–2953, doi:10.1149/1.2100321.
208. Skyllas-Kazacos, M. Novel Vanadium Chloride/Polyhalide Redox Flow Battery. *J Power Sources* **2003**, *124*, 299–302, doi:10.1016/S0378-7753(03)00621-9.
209. Risbud, M.; Menictas, C.; Skyllas-Kazacos, M.; Noack, J. Vanadium Oxygen Fuel Cell Utilising High Concentration Electrolyte. *Batteries* **2019**, *5*, 24, doi:10.3390/batteries5010024.
210. Cho, K.T.; Ridgway, P.; Weber, A.Z.; Haussener, S.; Battaglia, V.; Srinivasan, V. High Performance Hydrogen/Bromine Redox Flow Battery for Grid-Scale Energy Storage. *J Electrochem Soc* **2012**, *159*, A1806–A1815, doi:10.1149/2.018211jes.
211. Cathro, K.J.; Cedzynska, K.; Constable, D.C. Preparation and Performance of Plastic-Bonded-Carbon Bromine Electrodes. *J Power Sources* **1987**, *19*, 337–356, doi:10.1016/0378-7753(87)87009-X.
212. Salkind, A.J.; Hammel, R.O.; Cannone, A.G.; Trumbure, F.A.; Linden, D.; Reddy, T.B. *Handbook of Batteries*; 2002; ISBN 0071359788.

213. Yang, B.; Hooper-Burkhardt, L.; Krishnamoorthy, S.; Murali, A.; Prakash, G.K.S.; Narayanan, S.R. High-Performance Aqueous Organic Flow Battery with Quinone-Based Redox Couples at Both Electrodes. *J Electrochem Soc* **2016**, *163*, A1442–A1449, doi:10.1149/2.1371607jes.
214. Brushett, F.R.; Jansen, A.N.; Vaughey, J.T.; Su, L.; Milshtein, J.D. Materials for Use with Aqueous Redox Flow Batteries and Related Methods and Systems. *Google Patents* 2015, *133*, 1–38.
215. Xu, Y.; Wen, Y.; Cheng, J.; Cao, G.; Yang, Y. Study on a Single Flow Acid Cd-Chloranil Battery. *Electrochem commun* **2009**, *11*, 1422–1424, doi:10.1016/j.elecom.2009.05.021.
216. Chen, Q.; Gerhardt, M.R.; Hartle, L.; Aziz, M.J. A Quinone-Bromide Flow Battery with 1 W/Cm<sup>2</sup> Power Density. *J Electrochem Soc* **2016**, *163*, A5010–A5013, doi:10.1149/2.0021601jes.
217. Lin, K.; Chen, Q.; Gerhardt, M.R.; Tong, L.; Kim, S.B.; Eisenach, L.; Valle, A.W.; Hardee, D.; Gordon, R.G.; Aziz, M.J.; et al. Alkaline Quinone Flow Battery. *Science (1979)* **2015**, *349*, 1529–1532, doi:10.1126/science.aab3033.
218. Winsberg, J.; Janoschka, T.; Morgenstern, S.; Hagemann, T.; Muench, S.; Hauffman, G.; Gohy, J.F.; Hager, M.D.; Schubert, U.S. Poly(TEMPO)/Zinc Hybrid-Flow Battery: A Novel, “Green,” High Voltage, and Safe Energy Storage System. *Advanced Materials* **2016**, *28*, 2238–2243, doi:10.1002/adma.201505000.
219. Robert Lewis Clarke, Orinda, C.; (US); Brian Dougherty, Menlo Park, CA (US); Stephen Harrison, Benicia, CA (US); Peter J. Millington, Weaverham (GB); Samaresh Mohanta, Fremont, C. (US) Cerium Batteries. *US 2004/0202925 A1* 2002.
220. Matsuda, Y.; Tanaka, K.; Okada, M.; Takasu, Y.; Morita, M.; Matsumura-Inoue, T. A Rechargeable Redox Battery Utilizing Ruthenium Complexes with Non-Aqueous Organic Electrolyte. *J Appl Electrochem* **1988**, *18*, 909–914, doi:10.1007/BF01016050.
221. Sleightholme, A.E.S.; Shinkle, A.A.; Liu, Q.; Li, Y.; Monroe, C.W.; Thompson, L.T. Non-Aqueous Manganese Acetylacetonate Electrolyte for Redox Flow Batteries. *J Power Sources* **2011**, *196*, 5742–5745, doi:10.1016/j.jpowsour.2011.02.020.
222. Park, S.K.; Shim, J.; Yang, J.H.; Shin, K.H.; Jin, C.S.; Lee, B.S.; Lee, Y.S.; Jeon, J.D. Electrochemical Properties of a Non-Aqueous Redox Battery with All-Organic Redox Couples. *Electrochem commun* **2015**, *59*, 68–71, doi:10.1016/j.elecom.2015.07.013.
223. Potash, R.A.; McKone, J.R.; Conte, S.; Abruña, H.D. On the Benefits of a Symmetric Redox Flow Battery. *J Electrochem Soc* **2016**, *163*, A338–A344, doi:10.1149/2.0971602jes.
224. Winsberg, J.; Muench, S.; Hagemann, T.; Morgenstern, S.; Janoschka, T.; Billing, M.; Schacher, F.H.; Hauffman, G.; Gohy, J.F.; Hoepfener, S.; et al. Polymer/Zinc Hybrid-Flow Battery Using Block Copolymer Micelles Featuring a TEMPO Corona as Catholyte. *Polym Chem* **2016**, *7*, 1711–1718, doi:10.1039/c5py02036k.

225. Jiang, F.; Nie, Y.; Yin, L.; Feng, Y.; Yu, Q.; Zhong, C. Core-Shell-Structured Nanofibrous Membrane as Advanced Separator for Lithium-Ion Batteries. *J Memb Sci* **2016**, *510*, 1–9, doi:10.1016/j.memsci.2016.02.067.
226. Zhang, H.; Zhang, Y.; Xu, T.; John, A.E.; Li, Y.; Li, W.; Zhu, B. Poly(m-Phenylene Isophthalamide) Separator for Improving the Heat Resistance and Power Density of Lithium-Ion Batteries. *J Power Sources* **2016**, *329*, 8–16, doi:10.1016/j.jpowsour.2016.08.036.
227. Xiao, W.; Zhang, K.; Liu, J.; Yan, C. Preparation of Poly(Vinyl Alcohol)-Based Separator with Pore-Forming Additive for Lithium-Ion Batteries. *Journal of Materials Science: Materials in Electronics* **2017**, *28*, 17516–17525, doi:10.1007/s10854-017-7687-7.
228. Le Mong, A.; Kim, D. Tailor-Made Pore Controlled Poly (Arylene Ether Ketone) Membranes as a Lithium-Ion Battery Separator. *J Power Sources* **2016**, *304*, 301–310, doi:10.1016/j.jpowsour.2015.11.051.
229. Liang, H. qing; Wan, L. shu; Xu, Z. kang Poly(Vinylidene Fluoride) Separators with Dual-Asymmetric Structure for High-Performance Lithium Ion Batteries. *Chinese Journal of Polymer Science (English Edition)* **2016**, *34*, 1423–1435, doi:10.1007/s10118-016-1860-y.
230. Zhang, H.; Zhang, Y.; Yao, Z.; John, A.E.; Li, Y.; Li, W.; Zhu, B. Novel Configuration of Polyimide Matrix-Enhanced Cross-Linked Gel Separator for High Performance Lithium Ion Batteries. *Electrochim Acta* **2016**, *204*, 176–182, doi:10.1016/j.electacta.2016.03.189.
231. Heo, J.; Choi, Y.; Chung, K.Y.; Park, J.H. Controlled Pore Evolution during Phase Inversion from the Combinatorial Non-Solvent Approach: Application to Battery Separators. *J Mater Chem A Mater* **2016**, *4*, 9496–9501, doi:10.1039/c6ta02472f.
232. Wen, H.; Zhang, J.; Chai, J.; Ma, J.; Yue, L.; Dong, T.; Zang, X.; Liu, Z.; Zhang, B.; Cui, G. Sustainable and Superior Heat-Resistant Alginate Nonwoven Separator of LiNi<sub>0.5</sub>Mn<sub>1.5</sub>O<sub>4</sub>/Li Batteries Operated at 55 °C. *ACS Appl Mater Interfaces* **2017**, *9*, 3694–3701, doi:10.1021/acsami.6b14352.
233. Zhang, C.; Tian, W.; Li, D.; Quan, L.; Zhu, C. The High Performances of SiO<sub>2</sub>-Coated Melt-Blown Non-Woven Fabric for Lithium-Ion Battery Separator. <https://doi.org/10.1080/00405000.2017.1423004> **2018**, *109*, 1254–1261, doi:10.1080/00405000.2017.1423004.
234. Fang, C.; Yang, S.; Zhao, X.; Du, P.; Xiong, J. Electrospun Montmorillonite Modified Poly(Vinylidene Fluoride) Nanocomposite Separators for Lithium-Ion Batteries. *Mater Res Bull* **2016**, *79*, 1–7, doi:10.1016/j.materresbull.2016.02.015.
235. Wu, Y.S.; Yang, C.C.; Luo, S.P.; Chen, Y.L.; Wei, C.N.; Lue, S.J. PVDF-HFP/PET/PVDF-HFP Composite Membrane for Lithium-Ion Power Batteries. *Int J Hydrogen Energy* **2017**, *42*, 6862–6875, doi:10.1016/j.ijhydene.2016.11.201.
236. Rohan, R.; Kuo, T.C.; Chen, M.W.; Lee, J.T. Nanofiber Single-Ion Conducting Electrolytes: An Approach for High-Performance Lithium Batteries at Ambient

- Temperature. *ChemElectroChem* **2017**, *4*, 2178–2183, doi:10.1002/celec.201700389.
237. Kong, L.; Yuan, L.; Liu, B.; Tian, G.; Qi, S.; Wu, D. Crosslinked Polyimide Nanofiber Membrane Prepared via Ammonia Pretreatment and Its Application as a Superior Thermally Stable Separator for Li-Ion Batteries. *J Electrochem Soc* **2017**, *164*, A1328–A1332, doi:10.1149/2.0141707jes.
238. Oh, Y.S.; Jung, G.Y.; Kim, J.H.; Kim, J.H.; Kim, S.H.; Kwak, S.K.; Lee, S.Y. Janus-Faced, Dual-Conductive/Chemically Active Battery Separator Membranes. *Adv Funct Mater* **2016**, *26*, 7074–7083, doi:10.1002/adfm.201602734.
239. Sharma, A.L.; Thakur, A.K. Improvement in Voltage, Thermal, Mechanical Stability and Ion Transport Properties in Polymer-Clay Nanocomposites. *J Appl Polym Sci* **2010**, *118*, 2743–2753, doi:10.1002/app.32677.
240. Lin, D.; Liu, W.; Liu, Y.; Lee, H.R.; Hsu, P.C.; Liu, K.; Cui, Y. High Ionic Conductivity of Composite Solid Polymer Electrolyte via in Situ Synthesis of Monodispersed SiO<sub>2</sub> Nanospheres in Poly(Ethylene Oxide). *Nano Lett* **2016**, *16*, 459–465, doi:10.1021/acs.nanolett.5b04117.
241. Choi, S.W.; Jo, S.M.; Lee, W.S.; Kim, Y.R. An Electrospun Poly(Vinylidene Fluoride) Nanofibrous Membrane and Its Battery Applications. *Advanced Materials* **2003**, *15*, 2027–2032, doi:10.1002/adma.200304617.
242. Wang, X.; Gong, C.; He, D.; Xue, Z.; Chen, C.; Liao, Y.; Xie, X. Gelled Microporous Polymer Electrolyte with Low Liquid Leakage for Lithium-Ion Batteries. *J Memb Sci* **2014**, *454*, 298–304, doi:10.1016/j.memsci.2013.12.016.
243. Liang, B.; Tang, S.; Jiang, Q.; Chen, C.; Chen, X.; Li, S.; Yan, X. Preparation and Characterization of PEO-PMMA Polymer Composite Electrolytes Doped with Nano-Al<sub>2</sub>O<sub>3</sub>. *Electrochim Acta* **2015**, *169*, 334–341, doi:10.1016/j.electacta.2015.04.039.
244. Sharma, A.L.; Thakur, A.K. Plastic Separators with Improved Properties for Portable Power Device Applications. *Ionics (Kiel)* **2013**, *19*, 795–809, doi:10.1007/s11581-012-0760-6.
245. Zhang, H.; Liu, C.; Zheng, L.; Xu, F.; Feng, W.; Li, H.; Huang, X.; Armand, M.; Nie, J.; Zhou, Z. Lithium Bis(Fluorosulfonyl)Imide/Poly(Ethylene Oxide) Polymer Electrolyte. *Electrochim Acta* **2014**, *133*, 529–538, doi:10.1016/j.electacta.2014.04.099.

## Appendices

### A. Data Supporting Literature Overview

Table A1. Main battery parameters used for performance analysis.

Parameter	Unit	Description
Energy density	Wh L <sup>-1</sup>	Specifies amount of energy stored per litre
Specific energy	Wh kg <sup>-1</sup>	(kilogram). Important when selecting a battery technology where space (mass) is critical
Power density	W L <sup>-1</sup>	Characterize a power output of a battery; how fast it releases its energy
Specific power	W kg <sup>-1</sup>	
Specific capacity	Ah kg <sup>-1</sup>	A storage unit expressed in elemental charge and normalized to mass or volume; defines time needed for a battery to be (dis)charged at a certain current
Volumetric capacity	Ah L <sup>-1</sup>	
Cycle life	Number	A number of charge/discharge cycles a battery experiences until achieves a critical capacity value
Coulombic (energy) efficiency	%	Ratio between supplied and released charge (energy) within a cycle
Self-discharge	% Time <sup>-1</sup>	Reduction of battery capacity per hour (day etc.) at open circuit potential (no current load)
Depth of discharge	%	Level of capacity relative to maximum allowed for a battery type to be discharged to avoiding damage
State of charge	%	Characterizes amount of capacity currently stored relative to a total battery capacity

Table A2. Variety of aqueous RFBs.

Class	Type	Positive; negative redox couples	OCV, V	Energy density, Wh L <sup>-1</sup> / power density, W L <sup>-1</sup>	Energy efficiency, %	Ref.
All-inorganic	All-Vanadium	VO <sup>2+</sup> /VO <sub>2</sub> <sup>+</sup> ; V <sup>2+</sup> /V <sup>3+</sup>	1.26	25-40 / 60-100	70-85	[207]
	Vanadium-Bromine	Cl <sup>-</sup> /ClBr <sub>2</sub> <sup>-</sup> ; VBr <sub>2</sub> /VBr <sub>3</sub>	1.30	35-70 / –	65	[208]
	Vanadium-Oxygen	H <sub>2</sub> O/O <sub>2</sub> ; V <sup>2+</sup> /V <sup>3+</sup>	1.49	14 / 35 (mW cm <sup>-2</sup> )	46	[209]
	Hydrogen-Bromine	Br <sup>-</sup> /Br <sub>2</sub> ; H <sub>2</sub> /H <sup>+</sup>	1.09	200 / 1.4 (W cm <sup>-2</sup> )	90	[210]
	Zinc-Bromine	Br <sup>-</sup> /Br <sub>2</sub> ; Zn/Zn <sup>2+</sup>	1.85	60-90 / 40	65-75	[211]
	Lead-acid (soluble)	Pb <sup>2+</sup> /PbO <sub>2</sub> ; Pb/Pb <sup>2+</sup>	1.69	46 / 46	65	[212]
	Lithium-Ferrocene (isolated)	Fe(CN) <sub>6</sub> <sup>4-</sup> /Fe(CN) <sub>6</sub> <sup>3-</sup> ; Li/Li <sup>+</sup>	3.4	– / 17 (mW cm <sup>-2</sup> )	–	[126]

All-organic	Anthraquinone- benzoquinone		0.76	16 / 0.1 (W cm <sup>-2</sup> )	80	[213]
	Quinoxaline- Benzoquinone		1.35	- / -	63	[214]
	Methyl viologen- hydroxyl-TEMPO		1.25	8.4 / -	62	[81]

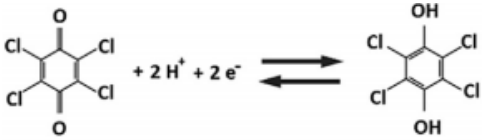
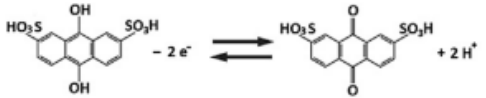
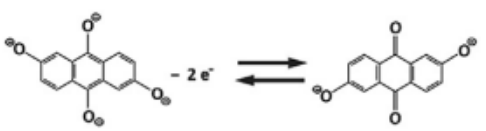
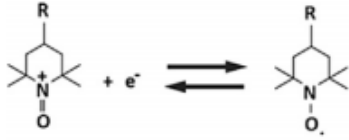
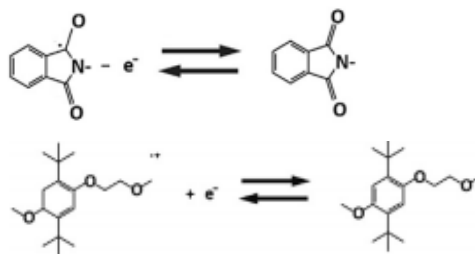
Organic- inorganic	Cadmium-chloro- benzoquinone	$\text{Cd}/\text{Cd}^{2+};$ 	1.13	–	82	[215]
	Anthraquinone- bromide	 $\text{Br}^-/\text{Br}_2$	1.00	50 / 1.0 ( $\text{W cm}^{-2}$ )	–	[216]
	Anthraquinone- ferricyanide	 $\text{Fe}(\text{CN})_6^{4-}/\text{Fe}(\text{CN})_6^{3-}$	1.01	6.8 / 0.45 ( $\text{W cm}^{-2}$ )	84	[217]
	Zinc-polymeric TEMPO	$\text{Zn}/\text{Zn}^{2+}$ 	1.66	8.1 / –	80	[218]

Table A3. Variety of NAqRFBs.

Class	Type	Positive; negative redox couples	OCV, V	Energy density, Wh L <sup>-1</sup> / current density, mA cm <sup>-2</sup>	Energy efficiency, %	Ref.
All-Inorganic	Zinc/Cerium	Ce <sup>3+</sup> /Ce <sup>4+</sup> ; Zn/Zn <sup>2+</sup>	2.5	- / 0.1	-	[219]
	Ruthenium	[Ru(bpy) <sub>3</sub> ] <sup>+</sup> /[Ru(bpy) <sub>3</sub> ] <sup>2+</sup> ; [Ru(bpy) <sub>3</sub> ] <sup>2+</sup> /[Ru(bpy) <sub>3</sub> ] <sup>3+</sup>	2.6	- / 5	-	[220]
	Chromium	Cr <sup>+</sup> /Cr <sup>3+</sup> ; Cr <sup>3+</sup> /Cr <sup>5+</sup>	3.4	- / 0.14	22	[221]
All-Organic	N-methylphtalimide-TEMPO		1.6	- / 0.35	60	[96]



N-methylphthalimide-  
DBBB

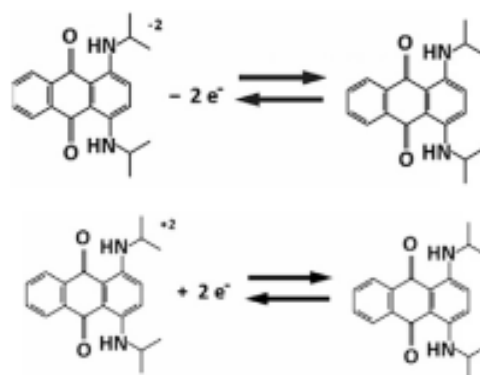


2.3 - / 35

69

[64]

Diamino  
anthraquinone



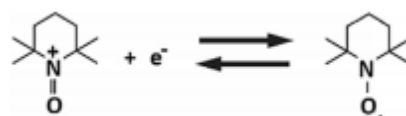
1.1 - / 0.66

40

[223]

Organic- Zinc-polymeric  
inorganic TEMPO

Zn/Zn<sup>2+</sup>



1.5 - / 1

65

[224]

Table A4. Characteristics of porous membranes applied in conventional LIBs [78].

Membrane / Material	IC, mS cm <sup>-1</sup>	Porosity, % / Pore size, μm	Electrolyte system	Ref.
<u>Single polymers</u>				
Celgard 2325	1.0	39 / <0.07	1 M LiPF <sub>6</sub> in EC:DEC;	[225]
<u>Microporous:</u> PVdF, PAEK, PMIA, PVA	1-2	50-60 / <2	1 M LiPF <sub>6</sub> in EC:DMC:EMC	[226–229]
<u>Nonwoven:</u> alginate, PI, PVdF- HFP, PP/SiO <sub>2</sub>	1.4-4.3	60-75 / >5		[230–233]
<u>Electrospun:</u> PI, PAN, PVdF/POSS	3.4-8.4	>75 / >5		[234–237]
<u>Modified polymers</u>				
PVP/PAN + MWCNT	4.9	–	1 M LiPF <sub>6</sub> in EC:DMC	[238]
Cellulose matrix + SiO <sub>2</sub> filler	6.5	–	1 M LiPF <sub>6</sub> in EC:DEC	[225]

Table A5. Properties of dense polymeric membranes applied in conventional LIBs.

Polymer	Salt	Fabrication solvent	Ionic conductivity, mS cm <sup>-1</sup>	Electrochemical stability, V vs. Li/Li <sup>+</sup>	Ref.
PEO	LiFSI	ACN	1.3	5.7	[143]
	LiClO <sub>4</sub>	ACN	1.2	5.5	[144]
	LiCF <sub>3</sub> SO <sub>3</sub>	–	0.8	–	[145]
PAN	LiClO <sub>4</sub>	DMF	0.2	4.8	[146]
	LiPF <sub>6</sub>	DMF	3.7	4.3	[239]
	LiCF <sub>3</sub> SO <sub>3</sub>	DMF	1.0	5.6	[240]
PVdF	LiPF <sub>6</sub>	–	1.0	4.5	[241]
	LiClO <sub>4</sub>	–	1.4	4.5	[242]
PVA-PVdF	LiClO <sub>4</sub>	DMF	0.03	–	[243]
	LiTFSI	DMF	0.4	4.7	[244]
	LiCF <sub>3</sub> SO <sub>3</sub>	DMF	2.7	3.4	[245]

## B. XRD Refinement

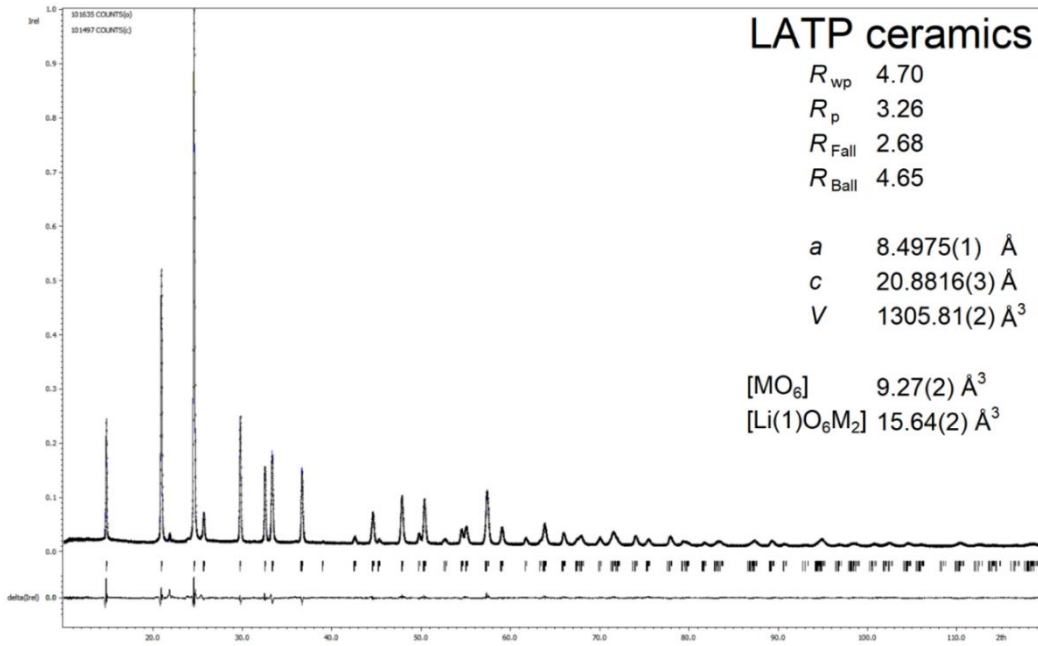


Figure B1. Experimental, refined, and differential XRD patterns of the **LATP ceramics** sample, as well as R-factors, calculated cell ( $a$ ,  $c$ ,  $V$ ) parameters, and intrastructural polyhedra volumes ( $[MO_6]$ ,  $[Li(1)O_6M_2]$ ). CCDC deposition number: 2243668.

Table B1. Atomic positions, occupancies ( $a_i$ ), coordinates ( $x$ ,  $y$ ,  $z$ ), and thermal displacement parameters ( $U_{iso}$ ,  $U_{11}$ ,  $U_{22}$ ,  $U_{33}$ ,  $U_{12}$ ,  $U_{13}$ ,  $U_{23}$ ) for the **LATP ceramic** sample.

Wyckoff Position	$a_i$	$x$	$y$	$z$	$U_{iso}$	$U_{11}$	$U_{22}$	$U_{33}$	$U_{12}$	$U_{13}$	$U_{23}$
Al 12c	0.15	0	0	0.14156(4)	0.0122(3)	0.0130(4)	0.0130(4)	0.0105(6)	0.0065(2)	0	0
Ti 12c	0.85	0	0	0.14156(4)	0.0122(3)	0.0130(4)	0.0130(4)	0.0105(6)	0.0065(2)	0	0
P 18e	1	0.2886(1)	0	0.25	0.0169(3)						
O1 36f	1	0.1817(2)	0.9915(2)	0.19000(6)	0.0142(5)						
O2 36f	1	0.1861(2)	0.1630(1)	0.0822(1)	0.0089(5)						
Li1 6b	1	0	0	0	0.01						
Li2 36f	0.05	0.073	0.34	0.091	0.01						

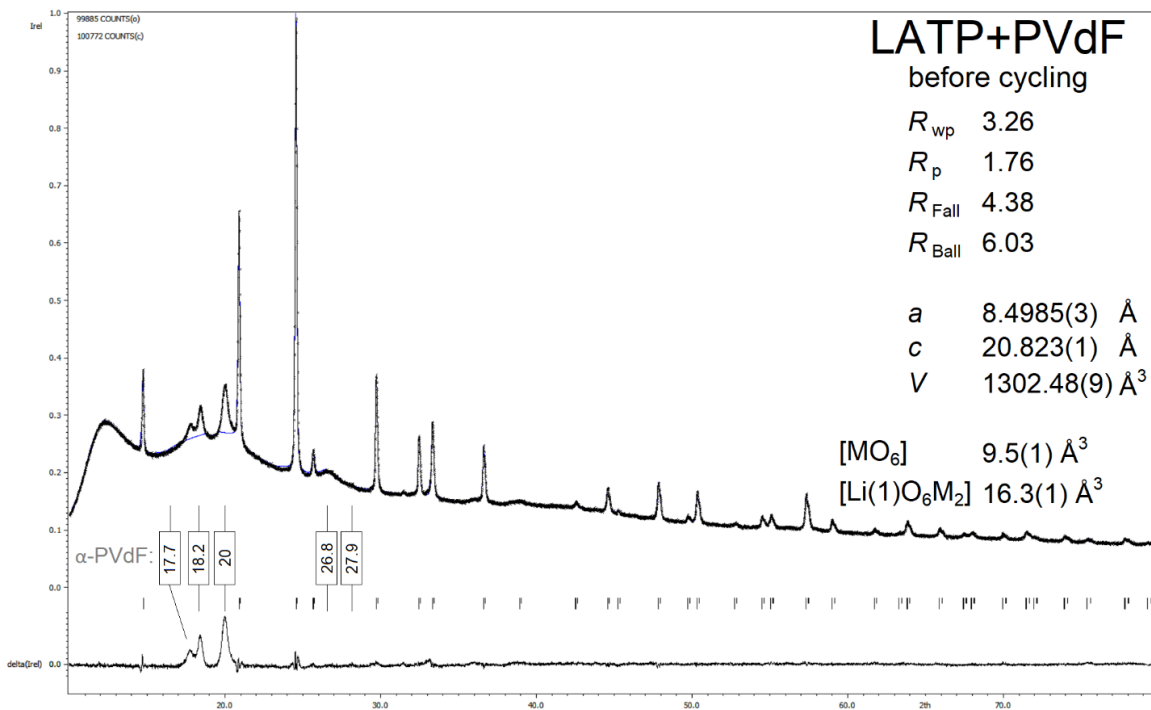


Figure B2. Experimental, refined, and differential PXR patterns of the **LATP+PVdF membrane** sample *before* cycling; R-factors, cell parameters ( $a$ ,  $c$ ,  $V$ ), and intrastructural polyhedra volumes ( $[\text{MO}_6]$ ,  $[\text{Li}(1)\text{O}_6\text{M}_2]$ ). CCDC deposition number: 2243666.

Table B2. Atomic positions, occupancies ( $a_i$ ), coordinates ( $x$ ,  $y$ ,  $z$ ), and thermal displacement parameters for the **LATP+PVdF membrane** *before* cycling.

Wyckoff	Position	Position	$a_i$	$x$	$y$	$z$	$U_{\text{iso}}$	$U_{11}$	$U_{22}$	$U_{33}$	$U_{12}$	$U_{13}$	$U_{23}$
Al 12c	Al		0.15	0	0	0.1417(3)	0.041(3)	0.040(3)	0.040(3)	0.044(7)	0.020(1)	0	0
Ti 12c	Ti		0.85	0	0	0.1417(3)	0.041(3)	0.040(3)	0.040(3)	0.044(7)	0.020(1)	0	0
P 18e	P		1	0.2921(8)	0	0.25	0.050(3)						
O1 36f	O2		1	0.189(1)	0.1653(8)	0.0838(9)	0.040(4)						
O2 36f	O1		1	0.183(1)	0.9812(9)	0.1888(4)	0.032(3)						
Li1 6b	Li1		1	0	0	0	0.01						
Li2 36f	Li2		0.05	0.073	0.34	0.091	0.01						

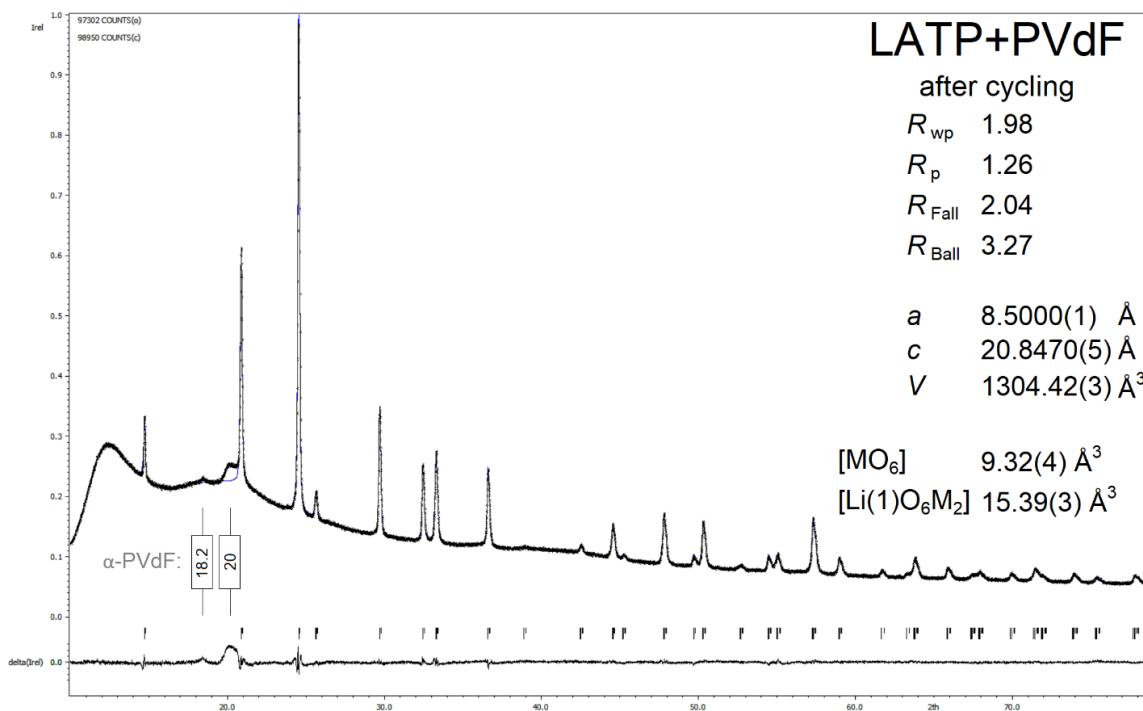


Figure B3. Experimental, refined, and differential PXRD patterns of the **LATP+PVdF membrane** sample *after cycling*; R-factors, cell parameters ( $a$ ,  $c$ ,  $V$ ), and intrastructural polyhedra volumes ( $[\text{MO}_6]$ ,  $[\text{Li}(1)\text{O}_6\text{M}_2]$ ). CCDC deposition number: 2243667.

Table B3. Atomic positions, occupancies ( $a_i$ ), coordinates ( $x$ ,  $y$ ,  $z$ ), and thermal displacement parameters for the **LATP+PVdF membrane** sample *after cycling*.

Wyckoff												
Position	Position	$a_i$	$x$	$y$	$z$	$U_{\text{iso}}$	$U_{11}$	$U_{22}$	$U_{33}$	$U_{12}$	$U_{13}$	$U_{23}$
Al 12c	Al	0.15	0	0	0.14126(7)	0.0242(9)	0.0264(9)	0.0264(9)	0.020(2)	0.0132(4)	0	0
Ti 12c	Ti	0.85	0	0	0.14126(7)	0.0242(9)	0.0264(9)	0.0264(9)	0.020(2)	0.0132(4)	0	0
P 18e	P	1	0.2888(2)	0	0.25	0.031(1)						
O1 36f	O1	1	0.1829(3)	0.9893(3)	0.1885(1)	0.029(1)						
O2 36f	O2	1	0.1846(3)	0.1636(3)	0.0813(2)	0.020(1)						
Li1 6b	Li1	1	0	0	0	0.01						
Li2 36f	Li2	0.05	0.073	0.34	0.091	0.01						

## C. EIS Fitting Data

### *Solvent variation*

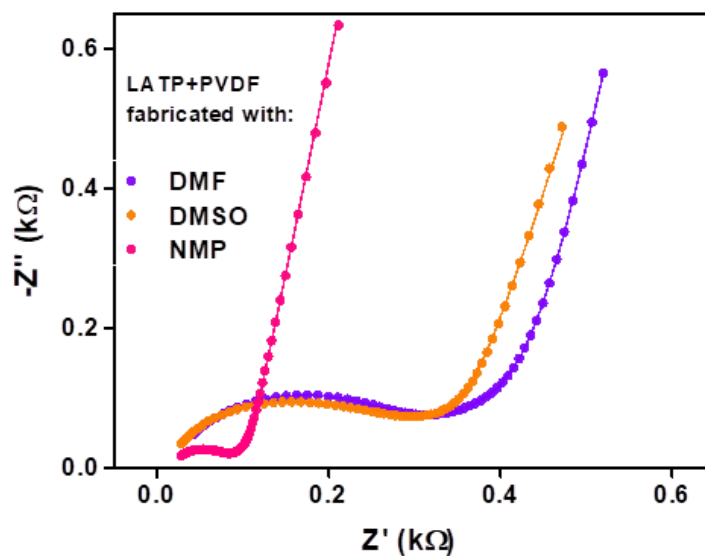


Figure C1. Nyquist plots of the LATP+PVdF membranes casted with DMF, DMSO, and NMP solvent; dots relate to experimental data and lines — to the fitting curves.

Table C1. Equivalent circuit parameters for each fit of SS/LATP+PVdF/SS cells. LATP+PVdF fabricated via different solvents (in brackets).

Membrane	$R_m, \Omega$	$R_i$	$Q_i, F s^{n-1}$	$n_i$	$Q_{ss}$	$n_{ss}$
LATP+PVDF (DMF)	12.7	360	$5.33 \cdot 10^{-7}$	0.65	$1.23 \cdot 10^{-5}$	0.77
LATP+PVDF (DMSO)	10.9	322	$5.52 \cdot 10^{-7}$	0.67	$1.39 \cdot 10^{-5}$	0.77
LATP+PVDF (NMP)	15.5	221	$2.5 \cdot 10^{-7}$	0.72	$4.30 \cdot 10^{-6}$	0.91

Ceramic-polymer variation

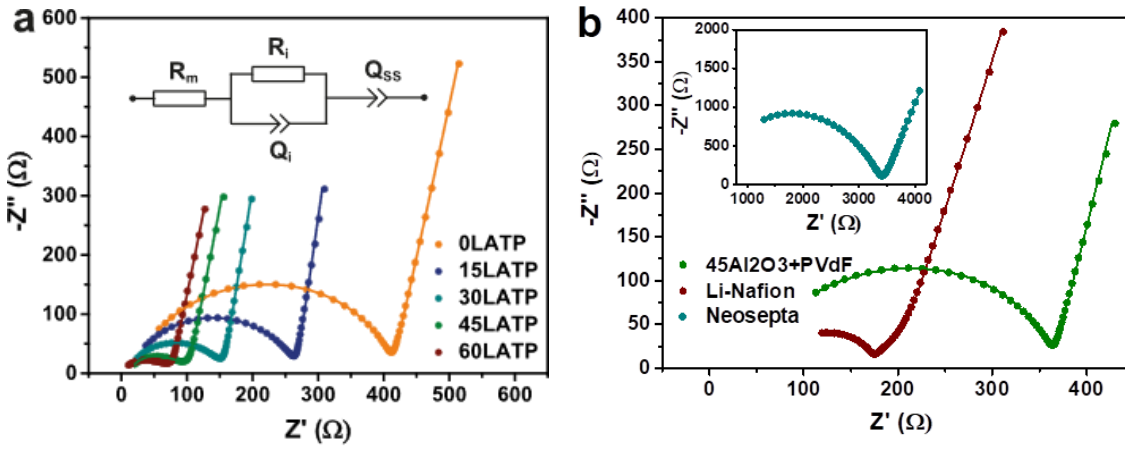


Figure C1. Nyquist plots of (a) LATP+PVdF membranes of various LATP content and of (b) 45Al<sub>2</sub>O<sub>3</sub>+PVdF, Li-Nafion, and Neosepta AHA reference samples.

Table C2. Equivalent circuit parameters for each fit of the SS/membrane/SS cells.

Membrane	$R_m, \Omega$	$R_i$	$Q_i, F s^{n-1}$	$n_i$	$Q_{ss}$	$n_{ss}$
45Al <sub>2</sub> O <sub>3</sub> +PVdF	41	323	$3.2 \cdot 10^{-8}$	0.806	$7.1 \cdot 10^{-6}$	0.859
PVdF	18.1	395	$3.4 \cdot 10^{-8}$	0.827	$6.6 \cdot 10^{-6}$	0.872
15LATP+PVdF	11.1	256	$6.2 \cdot 10^{-8}$	0.801	$4.8 \cdot 10^{-6}$	0.919
30LATP+PVdF	8.69	146	$1.6 \cdot 10^{-7}$	0.776	$4.7 \cdot 10^{-6}$	0.906
45LATP+PVdF	5.10	90.7	$9.2 \cdot 10^{-7}$	0.684	$1.0 \cdot 10^{-5}$	0.785
60LATP+PVdF	6.00	80.1	$2.0 \cdot 10^{-6}$	0.639	$8.0 \cdot 10^{-6}$	0.888
Li-Nafion	47	151	$9.6 \cdot 10^{-8}$	0.714	$1.3 \cdot 10^{-5}$	0.820
Neosepta AHA	643	3203	$2.1 \cdot 10^{-8}$	0.661	$4.4 \cdot 10^{-5}$	0.677

*Li-membrane interface probe*

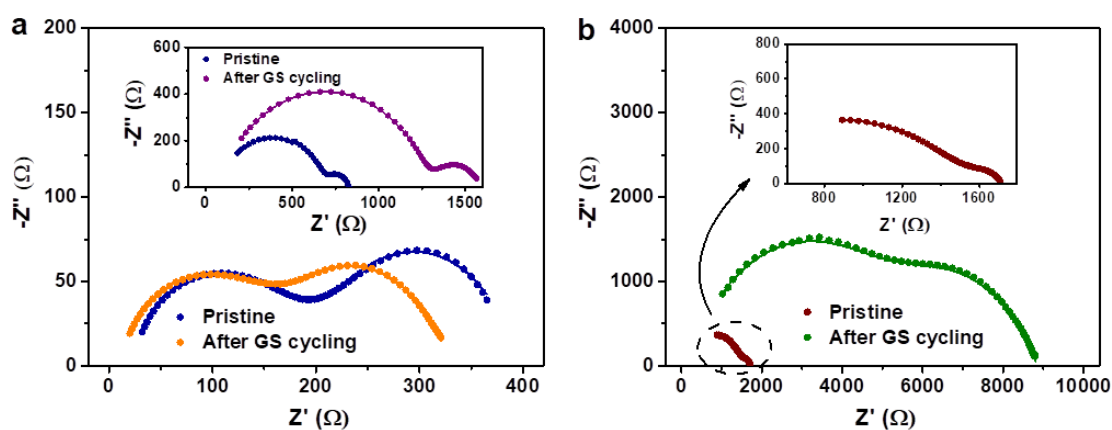


Figure C3. Nyquist plots of Li|membrane|Li cells before and after 400 cycles of stripping/plating at  $0.1 \text{ mA cm}^{-2}$  for (a) LATP+PVdF (inset — Li-Nafion) and (b) Neosepta membranes. Dots are related to experimental data, lines — to fitted curves.

Table C3. Equivalent circuit parameters for each fit of the Li/membrane/Li cells.

Membrane	Cycling	$R_m, \Omega$	$R_i$	$Q_i, \text{F s}^{n-1}$	$n_i$	$R_{\text{SEI}}$	$Q_{\text{SEI}}$	$n_{\text{SEI}}$
LATP+PV	Before	11.9	146	$3.3 \cdot 10^{-7}$	0.752	172	$1.4 \cdot 10^{-5}$	0.680
dF	After	15.8	184	$4.4 \cdot 10^{-7}$	0.724	190	$4.6 \cdot 10^{-5}$	0.642
Li-Nafion	Before	42.7	667	$2.0 \cdot 10^{-8}$	0.796	216	$5.5 \cdot 10^{-5}$	0.859
	After	62.1	1246	$3.4 \cdot 10^{-8}$	0.739	274	$2.5 \cdot 10^{-5}$	0.735
Neosepta	Before	538	1351	$5.7 \cdot 10^{-8}$	0.629	181	$7.0 \cdot 10^{-6}$	0.714
AHA	After	502	5141	$6.5 \cdot 10^{-8}$	0.594	3619	$1.8 \cdot 10^{-5}$	0.578

#### D. Pre-Treatment and Performance of Commercial Membranes

Commercial Nafion 112 (Sigma-Aldrich; dry thickness of  $\sim 50 \mu\text{m}$ ) was chosen to prepare the lithiated cation-exchange membrane (Li-Nafion). The “112” model was chosen because of its close thickness to our composite membranes (*ca.* 50 vs. 40  $\mu\text{m}$ , respectively). Prior to use, the Li-Nafion membrane was boiled within the following aqueous solutions subsequently:  $\text{H}_2\text{O}$  (deionized) for 0.5 h  $\rightarrow$  0.1 M  $\text{H}_2\text{O}_2$  for 1 h  $\rightarrow$   $\text{H}_2\text{O}$  for 0.5 h  $\rightarrow$  0.1 M HCl for 1 h  $\rightarrow$   $\text{H}_2\text{O}$  for 0.5 h  $\rightarrow$  0.1 M LiOH for 1 h  $\rightarrow$   $\text{H}_2\text{O}$  for 0.5 h. After that, the membrane was dried at 75 °C under dynamic vacuum for 12 h and then soaked in 1.0 M  $\text{LiClO}_4$  in PC for 18 h.

Anion-exchange Neosepta AHA (Astom; dry thickness of  $\sim 200 \mu\text{m}$ , stored in deionized water) was dried at 75 °C under dynamic vacuum for 12 h. After that, it was immersed in pure PC for 1 h and then soaked in 1.0 M  $\text{LiClO}_4$  in PC for 18 h.

As it might be expected, commercial membranes demonstrated no stable cycling due to the instability toward Li metal (Section 4.1) and low IC (Section 3.1.4). Discharge capacities of the Li-TEMPO cell with Li-Nafion and Neosepta were initially 0.91 and 0.50  $\text{Ah L}^{-1}$  (SoC of 33 and 20%, respectively) and drastically decreased within 5 cycles to 0.017 and 0.029  $\text{Ah L}^{-1}$ , respectively (SoC of  $\sim 1\%$ , Figure D1). Furthermore, the maximum current density achieved for Nafion and Neosepta is an order of magnitude lower than for LATP+PVdF (0.05 vs. 0.5  $\text{mA cm}^{-2}$ , correspondingly) due to their too high IC.

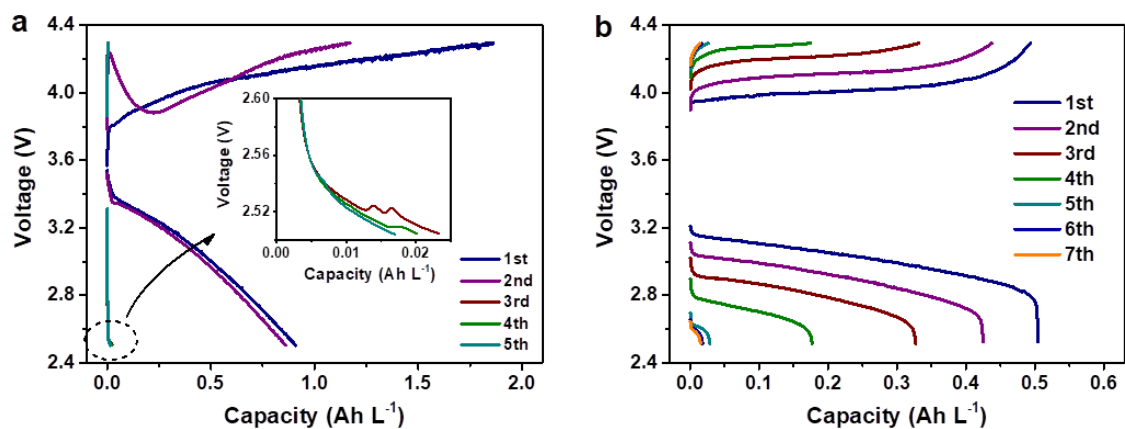


Figure D1. Charge/discharge of Li-TEMPO static cell equipped with (a) Li-Nafion and (b) Neosepta AHA membranes.  $0.05 \text{ mA cm}^{-2}$ . Catholyte —  $0.5 \text{ M TEMPO} + 1.0 \text{ M LiClO}_4$  in PC.